SYNTHESIS AND CHARACTERISATION OF MESOPOROUS TRANSITION METAL ION MODIFIED SILICA-ZIRCONIA AND SILICA-SULFATED ZIRCONIA MATERIALS TOWARDS NO_X CATALYSIS

A THESIS
SUBMITTED TO THE DEPARTMENT OF CHEMISTRY
AND THE INSTITUTE OF ENGENEERING AND SCIENCES
OF BILKENT UNIVERSITY
IN PARTIAL FULFILLMENT OF THE REQUIREMENTS
FOR THE DEGREE OF
DOCTOR OF PHILOSOPHY

By
OLGA SAMARSKAYA
September 2006

I certify that I have read this thesis and that in my opinion it is fully adequate, in scope and quality, as a dissertation for the degree of doctor of philosophy.

_____

Assoc. Prof. Dr. Ömer Dağ (Supervisor)

I certify that I have read this thesis and that in my opinion it is fully adequate, in scope and quality, as a dissertation for the degree of doctor of philosophy.

_____

Assoc. Prof. Dr. Margarita Kantcheva (Co-supervisor)

I certify that I have read this thesis and that in my opinion it is fully adequate, in scope and quality, as a dissertation for the degree of doctor of philosophy.

_____

Prof. Dr. Şefik Süzer

I certify that I have read this thesis and that in my opinion it is fully adequate, in scope and quality, as a dissertation for the degree of doctor of philosophy.

Assoc. Prof. Dr. Gürkan Karakaş

I certify that I have read this thesis and that in my opinion it is fully adequate, in scope and quality, as a dissertation for the degree of doctor of philosophy.

Assoc. Prof. Dr. Oğuz Gülseren

Approved for the Institute of Engineering and Science:

Prof. Dr. Mehmet Baray
Director of the Institute

ABSTRACT

SYNTHESIS AND CHARACTERISATION OF MESOPOROUS TRANSITION METAL ION MODIFIED SILICA-ZIRCONIA AND SILICA-SULFATED ZIRCONIA MATERIALS TOWARDS NO_X CATALYSIS

OLGA SAMARSKAYA

Ph.D. in Chemistry

Supervisor: Assoc. Prof. Dr. Ömer Dağ

Co-Supervisor: Assoc. Prof. Dr. Margarita Kantcheva

September 2006

The purpose of this work is to design and investigate mesostructured material as a potential support for the reaction of the methane with surface NO_x species. Several objectives have been pursued in achievement of the goals. The first objective is to develop a facile procedure for the synthesis of mesoporous silica-zirconia mixed oxide supports that are modified with the sulphate (SO_4^{2-}), cobalt (Co^{2+}) and palladium (Pd^{2+}) ions. The support with requisite catalytic properties was obtained through the adjustment of the synthetic steps and optimisation of the composition. The second objective is to explore the effect of cobalt and zirconia loading in the reaction of the NO_x species with methane over the Co-, Pd-, and Co-Pd-silica-sulfated zirconia (Si-SZr).

A one-pot synthesis procedure has been developed to prepare the mesoporous silica-zirconia (Si-Zr), Si-SZr supports and the supermicroporous Co(II) incorporated Si-SZr catalysts with a wide range of zirconia loadings. Introduction of the Co(II) active sites by various post-synthesis methods leads to the modification of the surface, whereas the direct (co-precipitation) techniques have provided the modification of both surface and bulk of the supports. The palladium ions were introduced by the conventional impregnation methods onto the calcined solid materials. The detailed

analysis of the materials has revealed that the silica and zirconia are well mixed in the framework, whereas the cobalt and sulfate ions are uniformly dispersed on the internal surface of the silica-zirconia supports.

The materials prepared in this thesis possess sufficient stability, requisite catalytic properties, as well as good Bronsted and Lewis acidity. However, the high cobalt loading renders the catalytic performance of the Pd-Si-SZr catalysts. Among the investigated catalysts, the interaction of the NO_x species with the CH_4 takes place at the lowest temperature over the Co-, Pd-, Co-Pd-supported zirconia rich (Zr/Si = 28) Si-SZr catalysts.

Key words: Mesostructure, Mesoporous Silica-Zirconia, Mesoporous Silica-Sulfated Zirconia, Co-preciapitation, Impregnation, Surface Modification, Co(II), Pd(II), NO_x Catalyst, Interaction of NO_x with the Methane.

ÖZET

NO_X KATALİZLEMEYE YÖNELİK MEZOGÖZENEKLİ GEÇİŞ METAL İYON KATKILI SİLİKA-ZİRKONYA VE SİLİKA-SÜLFATLANMIŞ ZİRKONYA MALZEMELERİNİN SENTEZİ VE KARAKTERİZASYONU

OLGA SAMARSKAYA

Danışman: Doç. Dr. Ömer Dağ
Yardımcı Danışman: Doç. Dr. Margarita Kantcheva

Eylül 2006

Bu çalışmanın amacı, metan ile yüzey NO_x bileşiklerinin tepkimelerine potansiyel oluşturacak mezoyapılı malzemeleri tasarlamak ve çalışmaktır. Amaca ulaşmak için bir kaç hedef tasarlanmıştır. Birinci hedef, sülfat (SO_4^{2-}), kobalt (Co^{2+}) ve paladium (Pd^{2+}) iyonu katkılandırılmış mezogözenekli silica-zirkonya oksit alt-taşı için uygun bir sentez yönteminin geliştirilmesidir. Uygun katalitik özelliğe sahip alt-taşlar, sentez aşamalarının ayarlanması ve kompozisyonun optimizasyonu ile elde edilmiştir. İkinici hedef ise Co-, Pd- ve Co-Pd-silika-sülfatlanmış zirkonya (Si-SZr) malzemelerinde kobalt ve zirkonya miktarının NO_x bileşikleri ile metan arasındaki tepkimelere etkisinin aydınlatılması hedefler.

Mezogözenekli silika-zirkonya (Si-Zr), Si-SZr ve süpermikrogözenekli Co(II) katkılandırılmış Si-SZr katalizörleri bir çok değişik zirkonya içeriğinde hazırlanması için tek aşamalı sentez yöntemi geliştirilmiştir. Co(II) aktif birimlerinin katkılandırılması için, uygulanan sonradan ekleme-sentez yöntemleriyle sadece yüzeyin katkılandırildığı fakat, doğrudan, sentez esnasında ekleme yöntemiyle, alt-taşların hem yüzeyleri hemde külçe yapılarının katkılandığı tespit edilmiştir. Palladiyum iyonları, bilinen sonradan katkılandırma yöntemiyle oksijen ortamında yakılarak temizlenmiş katı malzemelere eklenmiştir. Detaylı analizler silika ve

zirkonyanın mezoyapı içerisinde çok iyi karıştığını, kobalt ve sülfat iyonlarının ise silika-zirkonya alt-taşalarının yüzeyinde çok iyi dağıldığını göstermiştir.

Bu tez çerçevesinde hazırlanmış malzemeler, yeterli kararlılık, istenen katalitik özellik ve aynı zamanda iyi Bronsted ve Lewis asitlik göstermektedir. Fakat, yüksek kobalt miktarlarında Pd-Si-SZr katalizörlerinin katalitik performanslarının azaldığı tespit edilmiştir. Çalışılan katalizörler arasında Co-, Pd-, Co-Pd-içeren zirkonyumca zengin (Zr/Si = 28) Si-SZr katalizörlerinin NO_x metan tepkimelerini en düşük sıcaklıklarda gerçekleştiği saptanmıştır.

Anahtar Kelimeler: Mezoyapı, Mezogözenekli Silika-Zirkonya, Mezogözenekli Silika-Sülfatlanmış Zirkonya, Doğrudan Çöktürme, Sonradan Katkılandırma, Yüzey Desenlenmesi, Co(II), Pd(II), NO_x Katalizörleri, NO_x Metan Etkileşimi.

.

ACKNOWLEDGEMENTS

I would like to thank Assoc. Prof. Dr. Ömer Dağ for giving me freedom in choosing the subject and working on it, for his help and encouragement. I would like to thank Assoc. Prof. Dr. Margarita Kantcheva for fruitful discussions and collaboration.

I am indebted to the former and present members of Chemistry Department, Bilkent University.

I would like to thank Assoc. Prof. Dr. Gurkan Karakaş and Dr. Burcu Mirkelamoğlu for their help in N_2 sorption measurements. I would like to acknowledge Dr. Neil Coombs for TEM images.

I would like to express my gratitude to Prof. Alexander S. Shumovsky and Mrs. Natalya E. Shumovskaya for their help, endless support, encouragement, and understanding.

Last but not least thanks go to my dearest friends, among whom I give my special gratitude to Prof. A.A. Klyachko, Prof. I.V. Ostrovskii, Mrs. Larisa Kudyna, Adnan Hazar, Alexander P., Ludmila and Mariya Goncharov, Alex and Ayşe Degtyarev, Lori Russell-Dağ, Natalya and Kostya Zheltukhin, Ilknur Çayirtepe, Ilknur Tunc, Cemal Albayrak, Oğuzhan Celebi, Űnsal Koldemir.

TABLE OF CONTENTS

LIST OF TABLES

LIST OF FIGURES

1. INTRODUCTION

1.1 Meso & Nano

The burgeoning science of mesostructured materials spans chemistry, materials science, physics, biology, and engineering. Reviewing existing literature in this area, we will encounter term nano-materials (nanoclusters, nanowires, nanoparticles etc.) together with meso-materials (mesophase, mesostructured, mesoporous, mesocrystal etc.) albeit both of the notations imply a nanometer scale. Nanomaterials, as finely divided forms of bulk matter, exhibit characteristic physical and chemical properties because they have at least one spatial dimension in the size range of 1 – 100 nm. For instance, solid-state properties such as melting point and conductivity show strong dependence on the scale of some nanometers. Porosity is designated by the International Union of Pure and Applied Chemistry in three length scales, microporous < 2 nm, mesoporous 2 – 50 nm and macroporous > 50 nm. However, the dimension of the material between pores is not specified [1]. In the case of mesophases, which are soft matters utilized as structure directing templates and characterized by their order and mode of self-organization, have sizes between 2 – 50 nm [2]. A mesocrystal is defined as a superstructure of crystalline nanoparticles with external crystal faces on the scale of some hundred nanometers to micrometers [3]. Thus, “nano” is strictly a scale alone, but “meso” has a wider meaning. The contemporary model for understanding “meso” is delineated by G.A. Ozin and M. Antonietty as follows: “meso” is not directly related to a length scale, but to a principle of operation: it is “in-between”, that is in-between molecular and solid-state chemistry, in-between molecular and continuum approach, in-between covalent chemistry and micromolecular techniques, in-between the lines, fields and the limits of currently “make-able” [4].

Mesoscale chemistry can be regarded as controlled generation of meso-objects (in the nano- and micro-range) with especially designed for this level of molecular assembly chemical strategies and principles. The targets to control within the mesoscale context are: (i) size, shape, surface area and curvature; (ii) surface and interface chemistry and texture; (iii) mutual arrangement, morphology and order; topological defects. On a molecular scale meso-objects are glassy-disordered, crystalline or nanocrystalline species which on the mesoscale form hybrid structure or porous system, which, in turn, can adopt from completely disordered to a partially ordered, to a perfectly ordered state of matter. The mesoscale morphology leads to a finely divided particulate, fiber, film, monolith, sphere, superlattice and patterned forms. Numerous control opportunities, multimodal morphologies and structures, broad composition scope, potentially provide mesomaterials with particular properties for versatile applications.

1.1.1. Fabrication of the Mesostructure

Currently, the so-called top-down and bottom-up approaches or their combination are used to organize nano-structured building blocks into ordered superstructures. The top-down approach is based on physical methods such as patterning. Solid-state synthesis of finely powdered inorganic materials is also described as “shake-and-bake” or “heat-and-beat”. The latter one uses soft chemistry processes [5] (“chimie douce”) i.e. chemistry at low temperatures and pressures from molecular or colloidal precursors. In the latest studies concerning mesomaterials, more and more similarities to biominerals are pointed out. Biosilicates, where processes of “chimie douce” occur with participation of bacteria, have been known to scientific community for a long time. In nature, the formation of ordered mesostructures is based on templated self-assembly process in which pre-organized organic surfaces regulate the nucleation, growth, morphology and orientation of inorganic crystals. One, therefore, might assume that synthetic steps for preparation of mesostructures, especially

meso-silicates, are guided by those occurring during biomineralization [6]. In reality, the possibility to tailor material in nano-scale with so many controllable parameters and unique properties has not been uncovered until after the break through in early 90's. The scientists in Mobil Oil Corporation [7] synthesized mesoporous silica and alumosilicates denoted as M41S.

In general, the combination of appropriate amounts of four major components: inorganic precursor, surfactant, a base or acid and water lead to the formation of mesoporous framework. The surfactant molecules can self-organise into a mesophase, which, in turn, can act as a template for creation of solid inorganic replicates. The synthesis strategy presents a specific interest because it addresses the questions of control of composition, structure, property and function. This is a ground level understanding of which would allow us to make desired mesomaterial. Through in-situ and post-synthesis investigations of meso-structure and property evolution as a function of synthesis parameters as well as available up-to-date equipment to some extant revealed the formation mechanism of mesomaterials. The formation of mesoarchetecture is accomplished by a synergy of self-assembly and sol-gel chemistry processes (note, these are soft chemistry procedures). The growth of siliceous mesostructures begins with formation of a seed [8]. This soft seed around 50 nm in size is a co-assembly of silicates and about ten surfactant aggregates in each direction. The shape of the seed relies on the synthesis conditions and the equality of surface and bulk elastic energy. Aspects of evolution of this nano-meso unit in time have not been exactly understood yet. It is apparent that the growth is connected to colloidal interactions operating between the evolving seed and accreting surfactant-silicate micelles. It is proposed that interplay of colloidal and elastic forces leads to meso-structure organization and sophisticated curved shapes (rods, gyroids,

toroids, spirals and spheres) observed for surfactant templated mesoporous silica and organo-silica molecules.

During aging due to hydrolytic poly-condensation of silicatropic mesophase gradual rigidification takes place. At this stage formation of buckling patterns and other curved patterns [9] on mesoporous silica were observed, apparently, as a result of contraction-induced stress by polymerization of silicate species. Thus, all textural parameters and properties of mesomaterial spring from processes that take place on the framework-template inter-phase.

1.1.2. Race towards Order

The chemical generation of structures on the nano- or mesoscale is complex, unconstrained by scale and not restricted to just chemical bonding forces. Formation of nanoscale units and their association employs self-assembly, template technique, physical binding. Self-assembly [10] is generally defined as the spontaneous organization of materials through noncovalent interactions (hydrogen bonding, Van der Waals forces, dipole-dipole, ion-dipole, amphiphilicity etc.) with no external intervention. Large units, called building blocks or tectons, assemble to form mesomaterials.

Table 1.1 Methods of self-assembly [11]

Type of interaction	Strength [kJmol^{-1}]	Range	Character
Van der Waals	51	short	non-selective, non-directional
H-bonding	5 – 56	short	selective, directional
Coordination binding	50 - 200	short	directional
“fit interaction”	10 - 100	short	very selective
“amphiphilic”	5 – 50	short	non-selective
ionic	50 – 250[a]	long	non-selective
covalent	350	short	irreversible

[a] dependent on solvent and ion solution, data are for organic media.

The type of mutual order is encoded in the shape and chemical functionality of the objects involved and in the strength and directionality of interaction. In their nature, interactions are strong enough to provide sufficient stability, but not so strong that first contacts are irreversible (Table 1.1 [11]). This "flexibility" provides self-optimization of the mesophase, which is a delicate balance of competing structural and energy states. Self-assembly is an integral part of many mesochemical processes, for example, when surfactants or block co-polymers (BCs) are structure-directing agents. The amphiphilic surfactants with lyophilic head groups and lyophobic tails aggregate in solvents where one of these domains is insoluble, to form isotropic normal or inverted spherical or rod-like micelles in dilute solutions, and liquid crystalline phases at high surfactant concentrations. The formation of liquid crystal is driven by combination of molecular geometry and intermolecular and entropic interaction.

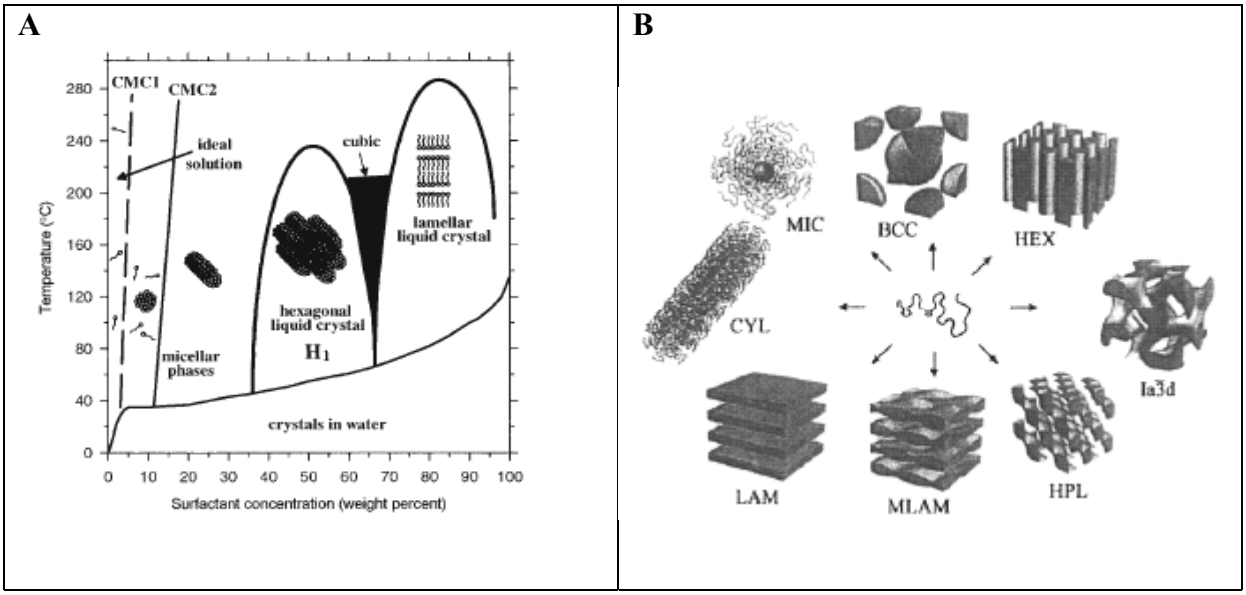

Figure 1.1. A - Schematic phase diagram for cationic surfactant C_{16}TMABr in water, CMC stands for the critical micelle concentration [12]; B - Common morphologies of ABCs: body centered cubic (BCC), hexagonally ordered cylinders (HEX), gyroid (Ia3d), hexagonally perforated layers (HPL), modulated lamellae (MLAM), lamellae (LAM), cylindrical micelles (CYL), and spherical micelles (MIC) [2].

Depending on the nature and morphology of discrete molecules, surfactants usually assemble into hexagonal, cubic or lamellar phases (Fig. 1.1 A [12]), while block co-polymers form more sophisticated structures (Fig.1.1 B [2]).

Stronger and irreversible covalent and ionic bonding are also utilised in the template technique. In this case, the templates are introduced either as ligands covalently bonded to silica or react with inorganic polymers during synthesis. Amphiphilic alkyloxysilanes alone or with other silica species can be organised into a liquid crystal-like arrays. For instance, both MCM-41 and MCM-48 can be prepared with n-tetradecyldimethyl(3-dimethoxysililpropyl) ammonium chloride as covalently bonded surfactant-silica source [13]. Free fatty acids can react with hydrolyzed silicon alkoxide species; as a result inorganic-organic hybrids are formed [14]. The covalent bonding forces provide close association of template and framework, which limits independent organization of organic and inorganic moieties, and imparts functionality to the siloxane network

Meso-objects can also be bound together by adhesion layers or electrostatic binding layers. This method allows formation of heterojoints of unusual composition and creation layer-by-layer films on different surfaces [15].

1.1.3. Synthesis of Mesoporous Silicates

Siliceous mesoporous materials are the most numerous and widely investigated class of mesostructured materials. In 1990 Yanagisawa et al. [16] reported the synthesis of a three-dimensional structure with nanoscale pores. This so-called FSM-16 material is formed through intercalation of ammonium surfactant ($C_nH_{2n+1}NMe_3$) in the layers of kanemite structure (hydrated sodium silicate $NaHSi_2O_5 \cdot 3H_2O$ composed of sheets). After the surfactants

ion-exchanged into the single-layered silica, the later one is thought to fold around the surfactant and then is converted into hexagonal structure during heating. However, worldwide attention to mesoporous materials has been driven two years later, when MCM-41 (hexagonal, a 2-D system of hexagonally arrayed cylindrical pores), MCM-48 (cubic, a 3-D bicontinuous system of pores) and MCM-50 (lamella, 2-D system of metal oxide sheets interleaved by surfactant bilayers) mesoporous molecular sieves were disclosed [7]. These materials were prepared by basic hydropolycondensation of silica/aluminosilicate in the presence of cetyltrimethylammonium halides [$C_{16}H_{33}(CH_3)_3NX$, X = Cl, Br] as a template in the temperature range between 70 and 150^0C. Research in this area was rapidly evolving and it has been demonstrated that materials with MCM-41 characteristics can be prepared by using a broad spectrum of surfactants and a wide range of synthesis conditions (e.g., temperature, pH, reaction time etc.). Targeted experimental attempts resulted in various types of mesostructured silica (Table 1.2), helped to envisage synthesis parameter-structure correlation and, more importantly, provided insight on the synthetic mechanisms.

1.1.3.1. Synthesis Methodologies

A close structural resemblance of inorganic framework to that of a surfactant-solvent (template) led scientists to assume that the formation of a liquid crystalline (LC) phase is an essential step in the synthesis. In order surfactant to self-assemble into LC phase in certain solvent, its concentration (c) should be in the range CMC 2 < c = LC. However, soft chemistry processes make possible to tailor mesostructure when the surfactant molecules initially are in a form of a spherical micelle (CMC 1 < c < CMC2), a cylindrical micelle (CMC 2 < c < LC) or a liquid crystalline phase (c = LC). Several synthesis strategies based on reaction conditions and initial nature of reagents provide plausible explanation for mesostructure formation.

Table 1.2. Families of mesoporous silica

Family	Structuring agent (S or N)	Inorganic source (I)	pH	Interaction type		Structure	Comments/Ref.
M41S (MCM – Mobil Corporation Matter)	$C_nH_{2n+1}(CH_3)_3N^+$ C_nTMACl (8< n < 18)	TEOS, Ludox, fumed silica, sodium silicate	basic	S^+I^- (electrostatic)	MCM-41 MCM-48 MCM-50	2D hexagonal 3D cubic Lamellar	Long-range order [7]
FSM (Folded Sheet Mesoporous)	C_{16}TMABr	kanemite	~8.5		FSM-16	hexagonal	[16]
SBA - n (Santa Barbara)	$C_nH_{2n+1}(C_2H_5)_3N^+$ C_{n-s-1}^* $C_{20}H_{41}(C_2H_5)_3N^+$ $C_{16}EO_{10}$ $C_{18}EO_{10}$ $C_{12}EO_4$ P123 F127	TMOS TEOS	< 1	$S^+X^-I^+$ (X=Cl) $N^0X^-I^+$ $(N^0H^+)(X^-I^+)$	SBA-1 SBA-2 SBA-3 SBA-11 SBA-12 SBA-14 SBA-15 SBA-16	Cubic Pm3m 3D hexagonal hexagonal cubic Pm3m 3D hexagonal cubic hexagonal cubic Im3n	Cage type pores [13, 17] [18] Bimodal network [19] [18]
HMS (Hexagonal Mesoporous Silica)	$C_nH_{2n+1}NH_2$ (alkylamine)	TEOS	neutral	S^0I^0 (hydrogen bonding)		3D	Wormhole pore-packing motif [20]
MSU-X (Michigan State University) (mesoporous silica, X refers to surfactant type)	Alkyl PEO Alkylaryl PEO PPO PEO (ABC) Tween	TEOS, sodium silicate	2 - 4	N^0I^0, $(N^0(F^-)\,I^0)$	MSU-1 MSU-2 MSU-3 MSU-4	3D	Wormhole pores [21]
FDU (Fudan University)	$EO_{39}BO_{47}EO_{39}$ (B50-6600)	TEOS	acidic	$N^0X^-I^+$ (X=Cl)	FDU-1	Cubic Fm3m with 3D hexagonal intergrowth	Large cage-like pores [22]

TUD (Technishe Universiteit Delft)	TEA, TMAOH	TEOS	basic		TUD - 1	3D sponge-like	Surfactant free one pot synthesis, hydrother-mally stable [23]
KIT (Korean Advanced Institute of Science and Technology)	HTACl & $EDTANa_4$	Sodium silicate	basic	S^+I^- (electrostatic)	KIT-1	3D short wormlike channels	Disordered channels with uniform pore width [24]
MCF (Mesostructured Cellular Foam)	P123 + TMB (1, 3, 5-trimethylbenzene)	TEOS	acidic			Continuous 3D pore system	Uniformly sized large spherical cells interconnected by uniform windows [25]
PMO (Periodic Mesoporous Organosilica)	CTMABr	TEOS & silsesquioxa nes	basic			3D hexagonal 2D hexagonal cubic Pm3n	[26]
HOM-n (Highly Ordered silica Monolith)	Brij 56 ($C_{16}EO_{10}$) + alkane P123 + alkane	TMOS	~ 1	$S^0X^-I^+$ (X^-=Cl)	HOM-1 HOM-2 HOM-3 HOM-4 HOM-5 HOM-7 HOM-10	Cubic Im3m 2D hexagonal 3D hexagonal cubic Pm3m cubic Ia3d cubic Pn3m cubic Fm3m	Large cage cubic structures, long range order [27]

*)$C_nH_{2n+1}N(CH_3)_2(CH_2)_sN(CH_3)_3$

1.1.3.1.1. Precipitation Based Methods

Concentration of surfactant in initial solution is c < LC, i.e., there is no liquid crystalline phase prior to addition of silica. Silica precursor, when added to the system, cooperatively organizes with surfactant into an inorganic-organic liquid-crystalline phase. Firouzi et al. [28] called this phase silicatropic liquid crystal (SLC) and proved by ^{2}H and ^{29}Si NMR that uncondensed $Si_8O_{20}^{8-}$ cubic octamers and micelle solution of CTMAB transform into SLC phase. Heating of the SLC phase results in the formation of meso-silicate. The sequence of steps is illustrated in detail in Fig. 1.2. [28].

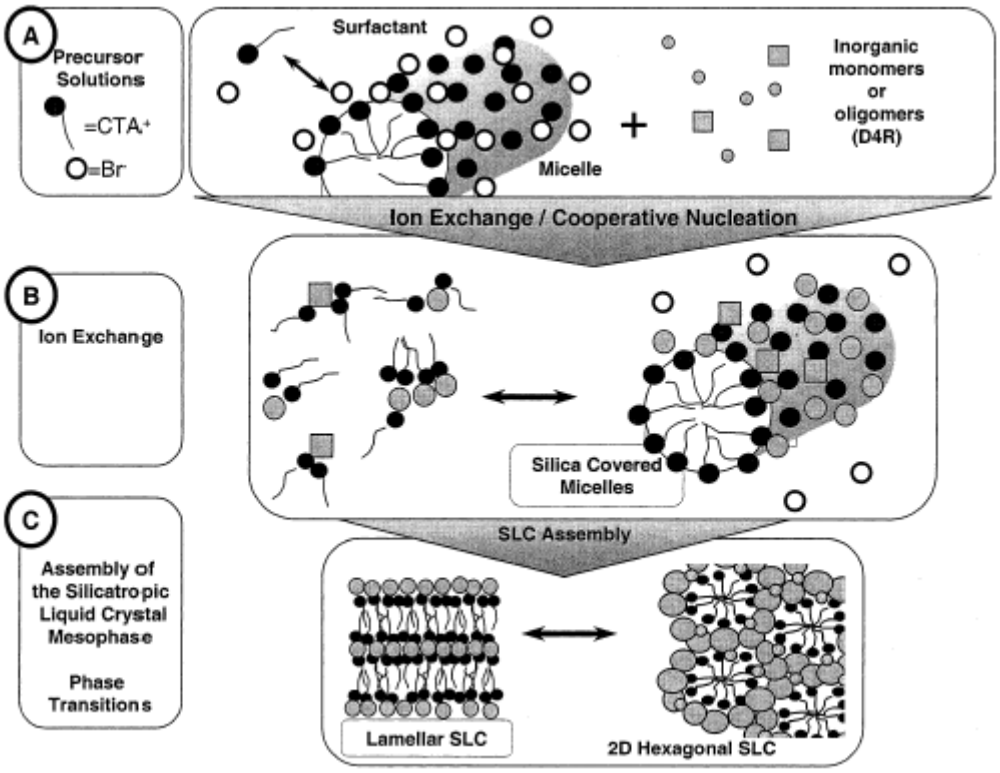

Figure 1.2. Schematic mechanism of the "surfactant-silica" cooperative organization [28].

Three models, following precipitation from solution route, were postulated: puckering layered model (Steel et al. [29]), silicate rod assembly (Chen et al. [30]) and cooperative charge density matching (Monnier et al. [31]). M41S (prepared in basic medium) and SBA-n (synthesized at low pH) families are examples of this methodology.

1.1.3.1.2. True Liquid Crystalline Templating (TLCT)

As the name implies lyotropic liquid crystals (LLC) exist in the initial solution (c = LC). The LLC surfactant array is infiltrated with molecular silicate (i.e., alkoxide), which undergoes hydrolysis and polymerization in the lyophilic region of the template and/or in the aqueous domains between the packed micellar aggregates (Fig. 1.3 [32]). The polymerisation-condensation of inorganic species into solid amorphous framework is completed during heat treatment. In this approach, proposed by Attard et al. [33], the surfactant array works as a cast or mold in which the inorganic precursor polymerizes and the formation of ordered mesophase is effectively independent of surfactant:silicate interfacial interactions. These meso-composites can be tuned to any structure via adjustment of the fraction of hydrophilic and hydrophobic parts and content.

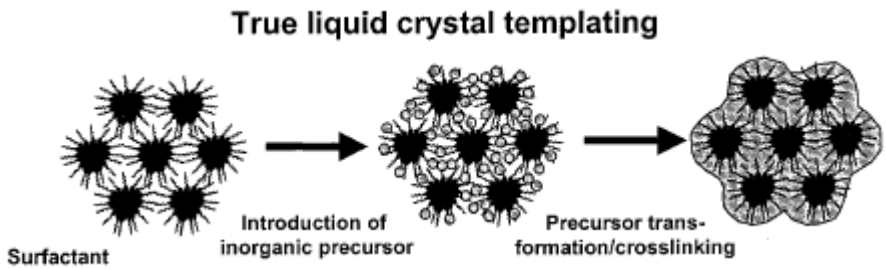

Figure 1.3. Schematic mechanism of silica framework formation, when c = LC [32].

1.1.3.1.3. Evaporation-Induced Self-Assembly

General principles of templating utilized in making monoliths, powders or bulk are also the bases in the formation of organized films by means of "evaporation-induced self-assembly" (EISA) process [10, 35], which includes dip-coating, spin coating and spraying techniques. The EISA leads to ordered inorganic mesophases from homogeneous dilute solutions of soluble silica and surfactant (c « CMC) prepared in large amounts of volatile low viscosity solvent. High dilution and pH close to isoelectric point of silica delays inorganic polymerization and allows unimpeded cooperative silica-surfactant self-assembly. Preferential evaporation of volatile solvent progressively leads to high concentration of incipient silica-surfactant moieties and results in organized LC mesophases. Throughout drying the LC domains grow inward from the solid-liquid and liquid-vapor interphases, the latter is enhanced by directional drying pressure (e.g. spin coating). Thus, thin films generated by the EISA have high degree of preferred orientation. Subsequent aging in the presence of acid or base catalyst or thermal treatment solidifies the silicon skeleton into the desired mesostructures.

1.1.4. Hybrid Interface between the Organics and Inorganics

There are two main processes to synthesize a mesomaterial, which take place either simultaneously or subsequently. These are (a) the creation of the organized texture due to the self-assembly of the template; it leads to the microphase separation, which divides the space into two domains: hydrophilic hydrophobic; (b) the formation of an inorganic framework; the inorganic precursors are placed into one of the spatially separated parts of these

nanoheterogeneously separated systems and condensation reactions will give rise to an extended inorganic matrix.

Three fundamental interaction types are essential in tailoring of the final structure. Two of the interactions – surfactant-surfactant (S-S) and inorganic-inorganic (I-I) – take place in microsegregated domains, while surfactant-inorganic (S-I) interaction operates in the inorganic-template hybrid interface (HI). Monnier et al. [31], has introduced thermodynamic factors, which most likely operate during the formation of the interface, these were later used by Huo et al. [13] for the description of cooperative assembly model. Four terms contribute to the free energy of mesostructure formation (ΔG_{ms}) Eq. 1.1:

$$\Delta G_{ms} = \Delta G_{inter} + \Delta G_{inorg} + \Delta G_{org} + \Delta G_{solv} \quad (1.1)$$

Here, ΔG_{org} represents self-assembly of the organic template leading to segregation of solvophobic regions; ΔG_{inorg} is related to inorganic framework; ΔG_{inter} is associated with creation of a well-defined and compatible HI between inorganic walls and organic template, and ΔG_{solv} is a contribution of the solvent. In TLCT mechanism [33], for instance, the aspect of template self-arrangement ΔG_{org} prevails over other interactions, while ΔG_{inter} is central in the cooperative self-assembly route [28].

In terms of kinetics, the adjustment of two competitive processes – phase separation of the template and polymerisation of inorganic component – are crucial. The overwhelming parameter is determined by the reaction conditions. In highly basic or acidic media it is condensation of silica (k_{inorg}), since it is fast, when on the other hand condensation of the inorganic precursor is slow, the kinetic constants of different processes are arranged in the following order: $k_{inter} > k_{org} > k_{inorg}$. Thus, two central points to fine-tune the self-assembly and the construction of inorganic matrix are the reactivity of inorganic precursors and S-I interfacial interactions.

The formation of inorganic framework proceeds through gelation, aging, drying, and calcination steps. These sol-gel chemistry processes can be controlled by reaction conditions, in particular, by the relative rates of hydrolysis (Eq. 1.2) and condensation (Eq.1.3 and 1.4).

(a) Hydrolysis

$$Si(OR)_4 + xH_2O \rightarrow (RO)_{3-x}\text{-}Si\text{-}(OH)_x + xROH \quad (1.2)$$

(b) Condensation

$$\text{-}Si\text{-}OR + \text{-}Si\text{-}OH \rightarrow \text{-}Si\text{-}O\text{-}Si\text{-} + ROH \quad (1.3)$$

$$\text{-}Si\text{-}OH + \text{-}Si\text{-}OH \rightarrow \text{-}Si\text{-}O\text{-}Si\text{-} + HOH \quad (1.4)$$

It is well known [34] that silica polymeric units formed in basic conditions are different from those, which form at low pH values. The acid catalysis promotes the hydrolysis and end-off chain condensation leading to the production of small polymeric entities, which during gelation cross-link into tenuous open structures tending to collapse upon drying to produce a microporous textures. The basic hydrolysis, on the other hand, promotes the cross-linking and formation of ramified polymers that are converted into a dense material by heat treatment. Since rates of the hydrolysis and the condensation influence the nature of I-I interactions, it also correlates with the order of the meso-framework [35]. In mild acidic media, pH = 2 - 4 ($pH_{iep\ silica} \approx 2$), the condensation rate of silica is slower, this should permit a higher order in the framework. At higher pH = 5 - 7 fast silica polymerization prevails, so that only worm-like materials are produced. The synthesis performed at higher ($pH > pH_{iep}$) or lower ($pH < pH_{iep}$) pH values, where silica condensation is fast, lead to less ordered materials. Fluoride is a well-known catalyst for hydrolysis and condensation of silica species [34]. It has also been effectively used to obtain highly ordered mesostructures [36] in a wide pH range (pH = 0 - 9). Sodium silicate can be used as an alternative source of silica [37]. Control over network formation is achieved by means of Na^+ amount and pH: at pH = 2 - 3 polysilicic acid is

formed and polycondensation rate is the slowest, while at pH values between 3 - 10.5 the reaction catalyzed by OH^- takes place.

Organic porogen is another important side of the hybrid interface. The surfactants, polymers, colloids, biological (viruses, proteins) systems are reported to template the mesostructure. Ionic surfactants i.e., species with charged head groups, such as S^+ alkyl trimethylammonium, $C_nH_{2n+1}N(CH_3)_3^+$ n = 8 – 18; S^- alkyl sulfonate, $C_nH_{2n+1}OSO_3^{2-}$, n = 12 – 18, alkyl phosphates C_nH_{2n+1} OPO_3^{2-} were the first templates to produce mesostructured materials. The ability of these surfactants to self-assemble is driven by hydrophobic interactions of the surfactant tail groups and electrostatic repulsion between charged head groups. The non-ionic surfactants, for instance, alkyl amine, S^0, or alkyl polyethylene oxides, N^0, form more stable arrays, since polar chains are weakly if at all protonated in the solvent medium, diminishing the Columbic repulsion. Many reports [38] showed that surfactants with a short alkyl chain $n \leq 7$, where n is the number of carbon atoms, do not form micelles and as the surfactant concentration increases in an aqueous solution, the phases always change in the following sequence: “normal” spheres, “normal” cylinders, lamellae, “inverse” cylinders, “inverse” spheres. Israelachvili and colleagues [39] explained phase transitions based on geometrical considerations, which rely on the ratio of the polar head surface, a_0, to the hydrophobic volume v/l, here v and l is the volume and the length of alkyl chain, respectively. Under this view, the amphiphilic molecules can be modeled as canonical fragments Fig. 1.4 [39] in the shape of ice-cream cone (one alkyl tail) or champagne cork (two hydrophobic chains).

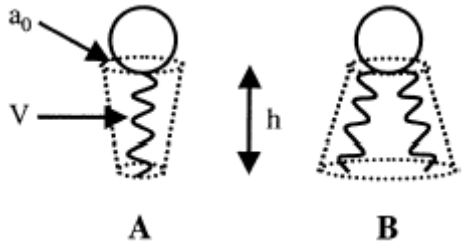

Figure 1.4. Canonical shapes of amphiphilic surfactants: A ice-cream cone; B champagne cork [39]

The architecture of aggregates is determined by the value of packing parameter g, Eq. 1.5. The larger is the g value, the smaller the curvature of the micelle motif.

$$g = v/l_c a_0 \quad (1.5)$$

where l_c is the length of fully extended hydrophobic chain, it can be estimated as $l_c \leq 1.5 + 1.265n$ Å. Table 1.3 [39] represents expected micelle structures according to g values.

Table 1.3. g parameter of different micelle structures [39]

$g = v/I_c a_0$	structures	examples
$g < 0.33$	spherical micelles	single chain with a large polar head (soaps, detergents)
$g = 0.33 - 0.5$	cylindrical or rod shaped micelles	simple surfactants with small head groups; ionic detergents in concentrated electrolyte solutions
$g = 0.5 - 1$	bilayer structures, vesicles	double chains with large head groups
$g = 1 – 2$	bilayer, membranes	
$g = 2 – 3$	inverse cylindrical micelles	double chain with small polar heads
$g > 3$	inverse spherical micelles	

The value of g increases as: a_0 decreases, v increases, and l decreases. Hence, the phase transitions reflect a decrease in surface curvature from cubic through vesicular to lamellae. Surfactants with large polar head groups associate in a spherical structure and pack into a

cubic mesophase, if, on the other hand, the head groups pack tightly, the aggregation number will increase, and the rod or lamella packing will be favoured. The value of g between 1/2 - 2/3, which corresponds to a cubic Ia3d space group depends upon the volume fraction of the surfactant chains [40].

Amphiphilic block copolymers (ABCs) are good alternatives to the low-weight surfactants and extend the templating boundaries. Table 1.4 [35] delineates intrinsic characteristic of the surfactants and block copolymers in a binary solvent-specie system and as a structure directing agents.

Table 1.4. Characteristics of surfactants and block copolymers [35]

Surfactant	Block copolymer
Solution and mesophase behavior	
Molecular/monodisperse Head + chain structure object shape, controlled by the g packing parameter	Polymeric/can be polydisperse Wide range of architectures: linear, branched, star, gyroid… shaped, controlled by the Z aggregation parameter
Simple micelle-like or bicontinuous mesostructures Micellization driven by slovophilic/phobic character, interaction between head groups	Possibility of complex multiscale mesostructures Micellization driven by solvophilic/phobic character, block size and conformation
Used in the design of mesostructured materials	
Well-defined HI	Blurry interface, swollen by the inorganic phase
Thin walls (1 – 1.5 nm); walls not entangled with template	Thick walls (2 – 10 nm); walls entangled with template (‘multiphase’)
Pore size limited by micelle size	Pore size tailorable by modifying the polymerization degree, monomer nature or polymer fraction

The micelle assemblies of the ABCs are defined by aggregation number Z, Eq. 1.6 [2] i.e., the number of block copolymers in a micelle.

$$Z = Z_0 N_A N_B^{-0.8} \quad (1.6)$$

N_A and N_B are the degree of polymerization of a soluble and an insoluble block, respectively. The parameter Z_0 is related to the interaction parameter χ, monomer volume and packing parameter Eq. 1.7:

$$Z_0 = 36\pi N_B^{6\varepsilon} (v/(al))^3 \quad (1.7)$$

The shape transitions from spherical to cylindrical to lamella in ABC solutions can be induced by increasing the ionic strength of the medium or by the relative length of the core block. This might be explained in terms of the surfactant parameter, v/al, which increases along the shape transition sequence from 1/3 to 1/2 to 1, respectively. It is because the increase in ionic strength decreases the area per head group, a, while increase in the second factor results in decrease of the contour length, l. For instance, in polyethylene oxide- polypropylene oxide-polyethylene oxide (PEO_x-PPO_y-PEO_x) aqueous solution at given PPO block length (insoluble part) a decrease in PEO block length (soluble part) destabilizes the hexagonal phase, so that the lamella phase dominates [41]. A similar behaviour has been observed in the case of non-ionic alkyl poly(glycol ether)s under the same conditions. Lyotropic phase behavior of Pluronics (PEO_x-PPO_y-PEO_x) is sensitive to temperature, which affects dehydration of the blocks: PPO chain dehydrates between 20 and 50^0C, PEO part at temperature ca. 80^0C. Salt-induced phase transitions take place at equilibrium conditions. However, exact nature and prerequisites for shape transitions are still unclear.

The dimension and shape of pores in the silica framework is closely related to the intrinsic properties of the template. Pore size mediation or pore remodeling of templeted silicates can be achieved if surfactants with different length of alkyl tails or their mixtures are used [42], or if auxiliary species or co-solvent is added to swell either corona or core of the

micelle [18, 20, 42a, 43], and when ex-situ hydrothermal treatment is employed [44]. The binary and ternary template systems may behave differently in the presence of inorganic precursor due to co-assembly of surfactant (S) and inorganic species (I). The interactions at HI are modeled as S^+I^- or S^-I^+ ion pairs, $S^+X^-I^+$ or $S^-M^+I^-$ ion-clusters, and S^0I^0/N^0I^0 hydrogen bonded pairs, where X and M are charge balancing anion and cation, respectively (Table 1.2). Hence, the porogen-matrix interaction is dictated by the nature of reagents and synthetic conditions. For $S^+X^-I^+$ route a cationic surfactant is chosen and pH is set far below the isoelectronic point of silica, so that inorganic species will be positively charged $[SiOH_2]^+$. In the case of S^0I^0 pathway the reaction is done at near neutral pH, which means silicate ions are partially charged and amine or ethylene oxide head groups of the surfactant are neutral. The S-I interactions are particularly important for the surfactant/BC dilute systems (c < LC). The experimental results showed that the BC weight fractions higher than 40% templates an ordered mesostructure. Formation of a disordered gel at lower F127 ($PEO_{106}PPO_{70}PEO_{106}$) concentrations is explained by the fact that stronger Si-O/PPO (I-S) than PPO/PPO (S-S) interactions prevent microsegregation of PPO blocks [45]. Association between Si-O-Si double four-rings forming inorganic skeleton and PEO chain of Pluronics led to the additional structural microporosity, i.e., bimodal framework in SBA-n type materials [46]. The PEO units are compatible with silica and interpenetrate into inorganic walls [47] thereby appraisal of pore size and geometry based on packing parameter, g, is somewhat violated. The $[H_2O]/[Si]$ ratio [48] alternates the morphology expected regarding the BC phase diagram [49] by modifying HI. The effect of water is two fold: template adopts more curved forms and it generates more hydrophilic silanol ends. This hydrophilic HI tends to maximize interactions with the hydrophilic block and enhanced the curvature. The hybrid interface has particularly important effect on the synthesis pathway, structure type and order of mesomaterials.

A new class of nanocomposite materials has emerged from a fusion of organic synthesis, sol-gel chemistry, and supramolecular chemistry. The “chimie douce” synthesis methodology, which provides flexibility and self-optimization, together with judicious choice of the structure directing agent, solvent, co-solvent, temperature, pH, reaction time, added salts, swelling agent, precursor enables control over structure type, pore size, composition and morphology. Materials with pore diameters in the 2 – 10 nm range, high surface area and myriad of pore and channel textures are typically characterized by the Transmission Electron Microscopy (TEM), Scanning Electron Microscopy (SEM), small angle X-ray diffraction and gas adsorption isotherms. The microstructure of mesostructured materials can be defined by the Magic Angle Spinning Nuclear Magnetic Resonance (MAS-NMR), vibrational Infrared (IR) and Raman spectroscopy, and Extended X-ray Absorption Fine Structure (EXAFS) analysis.

1.2. Multifunctional Silica Based and Non-Siliceous Mesoporous Oxides

The mesoporous materials based on the amphiphilic supramolecular templates contribute to intrapore chemistry by giving solids with myriad of controllable architectures and morphologies. Mesoporous hosts possess highly ordered or wormlike, isolated or interconnected channels with large pores and pore openings, large surface area, amorphous pore walls, and scarce acidity. In addition to structural versatility, amorphous siliceous framework can be modified either only on the surface of mesopores or in bulk or both giving rise to multifunctional materials. Multifunctionality implies that each component provides a different contribution necessary to meet the requirements of intended final product. For instance, incorporation of heteroatoms improves such properties of a material as thermal and hydrothermal stability, surface acidity/basicity.

Zirconia as a catalyst or support has received considerable attention. However, low thermal stability, small surface area, microporous structure, lack of Brønsted acidity (surface protons) in pure oxide limit its application. High activity of zirconia requires both stable highly porous or dispersed ZrO_2 phase to increase the surface area and functionality to circumvent insufficient acidity. Therefore, zirconia combined with high surface area silica and if necessary doped with other elements is expected to overcome the drawbacks of pristine constituents. The pore walls of mixed siliceous oxides tend to be amorphous, while the single non-siliceous oxides crystallize at relatively low temperatures. The amorphous nature makes structure less defined when compared to crystalline phase. On the other hand, it imposes fewer restrictions on the structures, which is expected to provide wider opportunities in tailoring of such properties like pore size and pore connectivity to create architectures that are unprecedented in materials science. In catalysis, nano-particles (size between 1 – 10 nm) will provide more active sites due to greater accessibility of all surface atoms and their low coordination number. However, dispersion and embedding of nano-particles into mesoporous silica framework will to some extent limit their accessibility and lower the activity.

Further, we have reviewed existing methodologies for the synthesis of mixed siliceous oxides, namely, silica-zirconia and functionalized silica-zirconia as well as non-siliceous oxides, in particular, zirconia to be able to find a suitable method to design material for catalytic application.

1.2.1 Incorporation of Heteroelements into Mesoporous Silicates

The internal surface reactivity of mesoporous hosts can be modified directly and by post-synthesis methods. Inclusion, ion exchange, covalent grafting are examples of the latter

approach. The former methodologies are based on sol-gel and co-precipitation procedures and may lead to the modification of both surface and bulk.

1.2.1.1. Isomorphous Substitution of Zirconium into Silica. Sol-Gel Chemistry

The sol-gel technique is a versatile solution process initially used for the preparation of inorganic materials such as glasses and ceramics with a high porosity and homogeneity [50-51]. The sol-gel synthesis of the mixed oxides generally involves an acid or base hydrolysis of the component alkoxide precursors, either in the presence or absence of a complexing or templating agent, gelation by condensation, polymerization and drying followed by calcination at higher temperatures to remove organics. The alkoxides are first dissolved in a solvent and then hydrolyzed to provide better mixing. Very often one of the inorganic precursors is more reactive then the other and segregation of one of the oxides occurs. Therefore, less reactive alkoxide is pre-hydrolyzed prior to mixing with another alkoxide and in the next step the mixture is hydrolyzed together. An alternative way to prevent inhomogeneouty is to use the so-called complexing agent, which reacts with the more reactive precursor and reduces the rate of its hydrolysis and condensation.

The sol-gel derived silica-zirconia with pores in the range of 33 - 68 Å has been successfully synthesized [52]. Tetramethyl orthosilicate (TMOS) or tetraethyl orthosilicate (TEOS) and zirconium isopropoxide are the most widely used reagents of silica and zirconia, respectively. The overall reactions leading to the formation of silica-zirconia gel from component alkoxides can be schematically represented as follows:

$$\equiv Si\text{-}OR + HOH \leftrightarrow \equiv SiOH + ROH \qquad (1.8)$$

$$(\equiv SiOH)_x + Zr(OPr)_4 \rightarrow (\equiv Si\text{-}O\text{-})_x Zr(OPr)_{4-x} + xHOPr \qquad (1.9)$$

In this case, the resulting materials are usually microporous. However, it has been reported by several authors [53] that utilization of sulfuric acid as a hydrolysis catalyst generates mesoporosity. It is known that zirconium alkoxides hydrolyze much faster than those of silica, therefore, two-step hydrolysis [54] or complexing agents (e.g. 2, 4-pentanedione, acetylacetonate) [55] have been used to prepare silica-zirconia systems with high degree of heteroatom mixing. Modified sol-gel method employs salts of inorganic precursors, which undergo slow hydrolysis and condensation in aqueous medium and are cheaper than conventional alkoxides [56]. When the sol-gel processes are used for the formation of mesostructured materials organic additives (e.g. tetrapropyl ammonium hydroxide (TPAOH)) [57] as well as surfactants [58], which may play a role of gelling/templating agent and /or pore filler are added to the synthesis mixture.

The sol-gel synthesized silica-zirconias with low Zr content (ca. 23 mol% Zr/Si) favor mesoporosity but exhibit only type IV isotherms with type II hysteresys loop. Incorporation of high amount of zirconia into the silica framework destroys the meso-structure and microporous solids with tetragonal or monoclinic crystalline ZrO_2 phase and small surface area is formed.

The building block approach differs from the sol-gel method only by the nature of precursors. Organic-inorganic hybrids, which do not break down during synthesis, are designated as building blocks. The octameric $Si_8O_{20}^{8-}$ silicate anions i.e. inorganic moieties of building units polymerize to form solid framework, while hydrophobic organic tails of the building units fill the core of the micelle and are removed by calcination to obtain highly porous material. Hasegawa et al. [59] used (2-hydroxyethyl) trimethylammonium silicate and zirconium tetrakis(2,4-pentandione) as building blocks to prepare mesoporous SiO_2-ZrO_2

oxide. Although this approach yields materials with higher surface area, it is limited to small amounts of incorporated zirconium; here the highest possible Si/Zr atomic ratio was 7.2.

1.2.1.2. Supramolecular Templating

An alternative in situ pathway to create mesoporous multifunctional and silica free oxides is to adopt the routes successful in the synthesis of mesoporous silicas. The most widely used mechanism is surfactant/inorganic self-assembly. The true liquid crystal templating method has found much less application.

In materials abbreviated Zr-MCM-41 [60], Zr-MCM-48 [61], Zr-SBA-15 [62], Zr-HMS [63], the synthesis methodologies for MCM-41, MCM-48 and SBA-15 are closely followed. The order of addition of zirconium and silicon precursors to the synthesis mixture is crucial for the integrity of material and depends on their origin. In the case of alkoxides, the reagents are either initially mixed in a solvent [64] or zirconium source is added to silica-template mixture in the last step [65], so that the rate of hydrolysis of alkoxides is balanced. When zirconium salt (e.g. $Zr(NO_3)_2$ $2H_2O$, $Zr(SO_4)_2$ $4H_2O$, $ZrOCl_2$ 8 H_2O) is used, the silica source (e.g. alkoxide, aerosil, sodium silicate) is added to the final blend of all components. The mixtures containing structure-directing agents, template, solvent and acid/base are subjected to hydrothermal treatment at temperatures between 80 and 100^0C for 2 – 4 days. The resulting precipitate is recovered by filtering, washing, draying and calcined to remove the template and stiffen the framework. Characterization of the co-precipitated zirconia-silica revealed that materials with low zirconium concentrations closely resemble their siliceous parent in terms of structure and morphology, and have amorphous pore walls confirming good

mixing of components on the atomic level. As the zirconium amount gradually increases, the textural parameters such as surface area, pore size and pore volume decrease substantially and the tetragonal ZrO_2 phase emerges. Zirconium rich samples are microporous partially crystalline disordered solids. Based on the literature data it is not possible to specify the range of Si/Zr values to determine the threshold when meso structure collapses [66].

Hydrothermal synthesis is usually long and tedious. Wei et al. [67] have reported that zirconium containing mesoporous silicates structurally analogous to MCM-41 could be templated by hexadecylpyridinium chloride at room temperature (RT) in basic medium. Under basic condition, sodium silicate and zirconium oxinitrate form mesostructure in 3 days. Materials with Si/Zr molar ratio values as low as 0.33 have been prepared by artrane route [68]. Here, the CTAB surfactant plays a role of template, complexing polyalchohol (2, 2', 2'' nitriletriethanol or triethanolamine) is used as hydrolysis retarding agent to produce zirconatrane and silatrane derivatives of inorganic precursors, which form mesostructured solid in aqueous basic medium during 24 hours of aging at RT. This route gives materials with narrow pore size distribution, good homogeneity; however, parameters related to meso properties greatly depend on the zirconium content. Non-conventional microwave-hydrothermal synthesis was applied by Kamarneni et al. [62] to obtain Zr-SBA-15 with bulk Si/Zr mole ratio up to 20. In highly acidic medium using P123, TEOS, zirconium oxychloride and water at 373 K in 2 hours. A bimodal network has been formed with average pore size of about 72 Å and additional smaller pores of about 33 Å.

Comparing the supramolecular templating and sol-gel synthetic routes, it is noteworthy to mention that the former technique gives materials with versatile architectures, more ordered framework, better textural parameters, less amount of zirconium in final

material (lower than that in the initial mixture), and allows utilization of various inorganic precursors. In order to successfully synthesize a mesoporous mixed oxide in situ, the following general guidences should be considered:

- The nature of inorganic species and surfactant (block copolymer) should favor interaction with each other (strong Coulomb interaction, hydrogen bonding, hydrophilic/hydrophobic interaction), because it renders long-range order;
- Mixing of precursors in a solvent prior to hydrolysis results in the formation of M-O-M' heterolinkages. In the case of oxides of different reactivity the less reactive component is pre-hydrolyzed or the more reactive one is combined with a capping agent to achieve the homogeneity;
- The inorganic species need to have a sufficiently high tendency to condense to an extended framework;
- The template removal should be possible without structural collapse.

1.2.1.3. Post Synthesis Incorporation of Zirconium

Inclusion chemistry techniques have been widely used to functionalize the surface of a material. For instance, impregnation and ion exchange are usually used to modify zeolites with various metal ions. Walls of mesoporous materials are covered with surface silanol groups, which would favor covalent grafting of various species. For example, the following entities $\{C_2H_4(1\text{-indenyl})_2\}ZrCl_4$ [69], $Zr(OPr)_4$[61, 70], $ZrOCl_2$ 8 H_2O [71], $ZrCl_4$ [72], $Zr(NO_3)_2$ [73] have been firstly anchored onto the pore surface of mesoporous silica, in the next step the surface zirconium species are converted into $Zr(OH)_4$ groups. Zirconium propoxide has proved to be a better source than zirconium salts in this type of reaction. Since the former reagent gives isolated and accessible zirconium centers on the silica surface with

minor constriction of pores, while the latter results in the formation of ZrO_2 clusters and may lead to a collapse of the initial meso structure due to strong basic medium required for the hydrolysis of salt [61, 70]. The grafting approach was successfully used to obtain uniform single particle cubic zirconia shell on the external surface of monodisperse spherical mesoporous silica [74]. Gao et al. [75] used incipient wetness method to functionalize preformed SBA-15. Characterisation of the final materials has shown that only 10 wt% of zirconium can be monolayerly dispersed on the pore surface, and crystalline ZrO_2 phase appears when zirconia loading was about 20 wt%. High dispersion of $Zr(OH)_4$ on the surface of MCM-41 up to 36.7 wt% of ZrO_2 was achieved through a chemical liquid deposition and subsequent hydrolysis of zirconium propoxide.

The analysis of inclusion chemistry schemes for the preparation of zirconia supported silica addresses the following issues:

- The initial structure of the substrate is preserved;
- The dopant species are at the surface or near to it and, therefore, are accessible;
- Only limited amount of zirconia is highly dispersed;
- The crystalline ZrO_2 phase forms at moderate heteroatom loading and leads to decrease in surface area, pore size and pore volume and eventually blockage of pores;
- The support should have accessible, evenly dietributed anchoring sites;
- The internal as well as external surfaces can be modified;
- The process can be repeated several times to achieve higher loadings.

1.2.2. Insertion of Sulfate into Silica-Zirconia

The presence of sulfate ions is expected, on one hand, to further enhance the acidity and possibly induce super acid catalytic properties as well as to improve the thermal stability of the silica-zirconia. On the other hand, it is used to promote the activity of sulfated zirconia phase due to its fine dispersion over the high surface area silica.

The conventional sulfation method is the wet impregnation of calcined silica-zirconia substrate with aqueous sulfuric acid (0.1 – 0.5 M) followed by high temperature treatment [76]. It has been noticed that during the thermal decomposition process zirconium atoms are extracted from the bulk and amorphous zirconia clusters form on the surface of the substrate [77]. Thus, the impregnation induces segregation at the surface and sulfated silica-zirconia is addressed as sulfated zirconia dispersed on silica. One-step incipient wetness impregnation route was exploited to disperse aqueous solution of zirconium sulfate onto the preformed MCM-41 [78]. However, investigations have shown that zirconium sulfate is not a good precursor. It is because in addition to segregation of amorphous zirconia, which may block the pores, it also limits the amount of incorporated ions of zirconia, and MCM-41 framework does not withstand under strong acidic synthetic conditions. Chung-Yuan Mou et al. [79] has impregnated zirconium sulfate onto the as-synthesized surfactant/silicate composite. This process appeared to be an efficient way to introduce large amount of species, while the mesostructure remains intact. The complete filling of the pores with the impregnated species is prevented, because of the space-occupying template inside the pores. In the next step, remaining in the pores template is burned off and the zirconium sulfate is dispersed into MCM-41 host by solid-state dispersion method. The pore size and pore volume uniformly decrease upon zirconia loading up to 50 wt%, while at higher concentrations ca. 70 wt%

ZrO_2, decrease in the textural parameters levels off. These observations indicate that 50 wt% is a threshold of ZrO_2 dispersion inside the MCM-41 pores and the large ZrO_2 particles grow outside the pores at higher concentrations.

In order to overcome the formation of both the amorphous sulfated zirconia phase at the surface of the pores and the ZrO_2 particles on the external surface, direct sulfation methods have been applied. For instance, the sol-gel synthesis was performed with sulfuric acid as a hydrolysis catalyst [80]. In an another work ammonium sulfate has been mixed with CTMAB to produce sulfated silica-zirconia by the hydrothermal organic/inorganic self-assembly technique [81]. Here, Si/Zr molar ratio equal to 20 was kept constant, while the amount of sulfate was varied. It was noticed that the concentration of SO_4^{2-} should be controlled, because it induces structural disorder in the liquid crystal mesophase.

1.2.3. Mesostructured Zirconia and Sulfated Zirconia

As it has already been mentioned, zirconia is a good catalyst and catalytic support. Arata and Hino [82] reported that sulfated zirconia exhibits acidity 10^4 times stronger than 100% sulfuric acid characterized by Hammet acid function, therefore, it is recognized as a super acid. Moreover, sulfated zirconia has higher thermal stability than the pure oxide [83].

In contrast to the silica-zirconia and silica-sulfated zirconia, early attempts to prepare mesostructured zirconia (Zr) and sulfated zirconia (SZr) by sol-gel and conventional precipitation methods resulted in microporous materials with low surface area [84]. However, Signoretto et al. [85] recently prepared the mesostructured sulfated zirconia by precipitation under reflux conditions at 90^0C.

So much efforts have been directed to optimize the synthetic conditions of novel supramolecular templating route for the preparation of mesoporous Zr and SZr. Wong and Ying [86] have exploited amphiphilic templating pathway based on the covalent bond approach and modified sol-gel method. The best results have been obtained with alkyl phosphates as a structure directing agents. Calcination of this material at 400^0C led to, although XRD amorphous, but highly porous materials with surface area < 300 m^2/g and pore size distribution centered at 25 Å. Amphiphiles with carboxylate head groups also yielded mesostructure, but it collapsed upon template removal. Formation of the mesostructured zirconia has not been observed when zirconium alkoxide is mixed with surfactants containing sulfate groups. In the presence of primary ammine only a disordered ZrO_2 mesostructure has formed, which did not survive upon surfactant removal neither by a solvent extraction nor by calcination. Many attempts have been made by other groups to prepare mesostructured stable Zr and SZr by using charged surfactants [87], but the same problem of structural instability in template free samples was encountered. Knowels et al. [88] have synthesized mesoporous zirconia with a broad pore size distribution through cation exchange of hydrous zirconium (IV) oxide with a cationic quaternary ammonium surfactant. The mesostructure has been developed upon calcination at 450^0C. Following the bibliography of the development of synthetic procedures; McIntosh and Kydd [89] have reported the synthesis of the mesoporous SZr through the neutral templating method. Hexadecylammine, hydrochloric acid, water, zirconium propoxide and acetyl acetonate have been combined to form solids after prolonged aging. Theses solids were dried at 100^0C and soaked in aqueous sulfuric acid. After calcination at 650^0C, XRD amorphous materials containing mainly tetragonal ZrO_2 were recovered with low surface areas (46 – 72 m^2/g). Stable mesostructured sulfated zirconia with worm-like pore pattern, crystalline pore walls composed of tetragonal ZrO_2 phase and surface area about 189 m^2/g has been obtained using triblock copolymer, zirconyloxychloride and

ammonia as a catalyst through hydrothermal synthesis at 100^0C for 24 hours [90]. After ethanol extraction and drying it was soaked in aqueous ammonium sulfate. Synthesis mechanism stemming from hydrothermal co-precipitation procedure and leading to formation of mesostructured ZrO_2 was proposed to be scaffolding [87, 91].

Sachtler and coworkers [92] successfully adopted neutral templating route, developed by Tanev and Pinnavaia for mesoporous silicates, to synthesize ZrO_2 with narrow pore size distribution and surface area of 95 m^2/g, while Sayari and Reddy [93] obtained only lamellar zirconium phase by this method. The liquid crystal templating (LCT) method was exploited by Signoretto et al. [94] to synthesize mesoporous zirconia. Here, zirconium propoxide combined with stabilizing agent, acetyl acetonate undergoes condensation-polymerization around the template consisting of a neutral ammine surfactant and water. After aging at hydrothermal conditions and drying, the sulfation of the samples has been achieved by insipient wetness impregnation. The resulting sulfated zirconia has preferentially two phases, amorphous and tetragonal, the particle size of the latter phase was found between 8 and 14 nm. It was observed that the pore size correlates well with the length of co-solvent alkyl chain. Novel one-step non-surfactant alcohothermal route coupled with supercritical drying yielded mesostructured sulfated zirconias with surface areas between 118 and 184 m^2/g composed of tetragonal zirconia walls. The presence of a stabilizer – sulfate was found to be essential in the formation of mesoporosity. ZrO_2/SO_4 mole ratio equal to 4 gave materials with the best textural parameters and at the same time with broader and low in intensity XRD small angle diffraction lines [95].

G.D. Stucky and coworkers [96] have proposed nonhydrolytic block-copolymer templating method for the preparation of non-siliceous oxides from anhydrous inorganic

chloride precursor. The mesoporous ZrO_2 obtained after calcination at 400^0C has pore size between 58 and 62 Å and a semicrystalline framework composed of ~2 nm tetragonal zirconia particles dispersed in the amorphous walls. The morphology is merely determined by the templating agent (e.g. $EO_{75}BO_{45}$ favors cubic phase, P123 – hexagonal phase). Although the resulting materials were highly porous, the surface area was relatively low, 150 m^2/g. Ozin et al. [97] has reported formation of non-silica mesoporous oxides by reacting sodium glycometallate with CTACl in ethanol. The well-organized hexagonal structure, which does not sustain its integrity upon surfactant removal, has been reinforced by post synthesis silanation of dehydrated meso metal oxides with disilane.

The mesostructured silica-zirconia, zirconia and their functionalized analogs are now accessible from a wide range of precursors and synthesis methodologies. Among which the template-directing approach is the most acknowledged for fabrication of materials with predetermined shapes and length scales. Although the general principles to create a mesostructure can be rationalized, but could not be used a priori to predict mesostructure formation from given component precursors. Each new composition needs adoption of the procedures, which, in turn, depends on the chemistry of the system. The unique features of the mesostructures, which first of all allow tunability of their properties, require complexity in their synthesis i.e. more components are combined, more steps a process has before the final product is produced, more sophisticated conditions are applied. The complexity leads to increased problems concerning reproducibility, costs of production and creates obstacles with respect to applications and commercialization of a material.

Here, we exploited a fast hydrolytic one-pot synthesis to synthesize mesoarchitectures, taking advantage in the formation of a stable liquid crystalline template composed of

polyethyle oxide based non-ionic surfactant and Pluronics (triblock copolymers), water and transition metal salts.

1.3. Catalytic Nanoarchitectures

Porous materials have been synthesised and intensively investigated over the decades with regard to technical applications. Porosity (i.e., nothing) is an important part of any system that does catalysis, sensing, energy storage, synthesis or fabrication. The catalytic reactions are most effective when the transport paths through which molecules move into and out of the material is unencumbered. Heterogeneous catalysis has always been an inherently nanoscopic phenomenon. Among the porous materials the family of zeolites has been extensively studied and found industrial applications. Zeolites are crystalline materials composed of silica and alumina with a narrow and uniform micropore size distribution [48]. They have attracted great attention as environmentally friendly acid catalysts, which can substitute harmful liquid acid catalysts and also as redox catalysts, which would diminish the generation of toxic waste, for instance, in petroleum chemistry. However, the application of zeolites is limited, first of all, by their pore sizes < 2 nm, which would complicate mass transfer and prevent catalytic reactions involving large molecules.

An extensive research has been focused on the design of a material, which would overcome the drawbacks of the zeolites. As a result of this effort the MCM family of mesoporous materials with pore sizes in the 2 – 50 nm range has been disclosed by the scientists in Mobil Oil Corporation [7]. Among the remarkable features of these mesoporous silicates a highly ordered hexagonal array of uni-dimensional cylindrical pores with uniform pore size distribution and high surface area have been recognised. Thus, mesoporous

materials have overcome the pore size constraint of the zeolites. However, first attempts in catalytic application have shown that the MCM type mesoporous silicates and alumosilicates are lousy catalysts [98-103]. Hence, mesoscale porosity and high surface area are requisite properties for a potential catalyst, but they do not provide material with catalytic activity. The MCM-41 as such did not find any catalytic application because of its low thermal stability and insufficient acidity. Catalytic tests performed on MCM-41 (hexagonal) and MCM-48 (cubic) have shown that the latter material is more promising as a catalytic support [104]. Periodic porosity is usually uni-dimensional and nanoscopic e.g. MCM-41. It causes diffusion problem and is prone to the pore blockage. Materials with continuous three-dimensional framework e.g. MCM-48 offer the route around blockage [105]. This fact has once more emphasised the importance of morphology in catalytic application. The possibility to control the mesostructure of siliceous framework underlies in the method of its synthesis.

A great research effort has resulted in preparation of thin films [106], fibers [107-108], tubes [109-110], spheres [11-112] or monolith [113]. Poor thermal and hydrothermal stability of the MCM-41 materials is due to their thin walls and incomplete polymerisation of the inorganic framework [114-115]. These disadvantages have been overcome with synthesis of, for example, SBA-n mesoporous materials [18-19].

The detailed research acquired on the zeolites has shown that multifunctionality improves the performance in catalytic processes. Another remarkable feature of ordered mesoporous solids for catalysis is the multitude of possibilities to modify them. Amorphous siliceous framework covered with silanols allows facile incorporation of the large number of active species ranging from a single heteroatom to large organic moieties. A new catalytic function can be introduced to mesoporous material by direct and post-synthesis techniques

[116]: substitution, grafting, immobilisation, surface coating, ion exchange, sililation, encapsulation. For instance, metal ions substituting silicon atoms in the framework can act as acid or redox active site in different catalytic applications. It is important to bear in mind that incorporation of metal centers into the amorphous siliceous framework leads to the formation of vide variety of different sites with various local environments, while in the zeolites a similar substitution results in the formation of defined sites [117]. Therefore, identical modifications performed in mesoporous amorphous framework and crystalline microporous zeolites do not impose the same catalytic properties. For example, the zeolites containing trivalent metal ions (Ba^{3+}, Al^{3+}) possess strong acidity, while mesoporous solids modified with the same heteroatoms bear only mild acidity. It should also be emphasised that the direct synthesis and post-synthesis treatment of initially prepared silica mesoporous material with the same dopant does not induce identical properties. It is because direct synthesis approach introduces heteroelemnt into the framework, similar to the zeolites, while post-synthesis methods primarily modify the surface. Other factors, which strongly influence the catalytic behaviour, are the nature, the local environment and stability of the heteroatom introduced [118-119]. The nature of functional entities and methods of their incorporation into the framework successfully utilised in the zeolites can be used only as a guidance to achieve the similar properties in the mesoporous siliceous solids. Table 1.5 lists the literature data on the potential catalytic application of pure siliceous and heteroelement-silica mesostructured materials.

Table 1.5. Mesostructured materials and their application in catalysis

Materials	Catalytic reaction	Comments
Mesoporous **M**olecular **S**ieves (MMS)[98-103]	Cracking of hydrocarbons, olygomerization, oxidation, acylation, esterification, synthesis of new materials	
Ti-MCM-41[120] Ti-MCM-48[121] Ti-HMS[121] Ti-SBA-15 HyMTS[122] Au/Ti-MCM-41[123] Au/Ti-MCM-48[123] Meso-TiO_2[124]	Oxidation (hydrocarbons), epoxidation (norbornylene, cyclohexene), hydroxylation (1-propanol), peroxidative bromination (phenol red). Oxidation (hydrocarbons, sulfide to salfoxides and sulphones, aromatic compounds), hydroxylation (2,6 –di-tret-butyl phenol, benzene). Oxidation, epoxidation. Epoxidation (olefins) Epoxidation (propene) Photocatalytic reaction (2-propanol)	Brønsted active sites Low activity
Zr-MCM-41[121, 125] Zr-HMS Zr-MMS ZrO_2/SiO_2[126]	Epoxydation (norbornylene), dehydration (isopropyl alcohol), oxydation (cholesterol, substituted amines, cyclohexene), epoxydation (norbornene) Gas phase isomerization (cis-cyclooctane), liquid phase epoxidation (1-butene). Dehydration (alcohol)	Lewis acid sites
Nb-MCM-41[127] Meso-Nb_2O_5[124]	NO decomposition, reduction of NO with NH_3, hydrosulphurisation, oxidation (thioethers) Photocatalytic reaction (2-propanol)	Activity depends on the Nb localisation
V-MCM-41[104, 128] V-HMS	Oxidation of organic substrates in liquid phase (cyclic alkanes, phenol, naphtalene, cyclododecanol)	Low stability
Cr-MCM-41[129] Cr-MCM-41 Cr-HMS Cr-Zr-MMS[130]	Hydroxylation (phenol, 1-naphtol), oxidation (aniline, methyl metacrylate, styrene). Oxydation (trichloro ethylene) Hydroxylation (benzene) Oxidation (methylene chloride)	
Fe-MCM-41[131]	Epoxydation (styrene), hydroxylation (benzene), oxydation (methylene chloride)	
Sn-MCM-41[132] Sn-HMS	Hydroxylation (1-naphtol, phenol), oxydation (aromatics). Hydrxylation (benzene), ring opening & polymerization (lactide)	
Co-MCM-41[133] Co-SBA-15 Co-Zr-MMS[134]	Fischer Tropsch Synthesis (production of hydrocarbons from CO and H_2) SCR of NO with ammonia	low Co content
W-MCM-41[135] W-Zr-TMS14[136] Meso-WO_3/ZrO_2[137]	Epoxidation (cyclooctane), hydroxylation (unsaturated organics). Isomerization&cracking (hydrocarbons). Isomerization	

Table 1.5. Continues

Materials	Catalytic reaction	Comments
Mn-MCM-41[138] Amorphous manganese oxide Mn-Al-O, Mn-La-O, Mn-La-Ce-O[139]	Oxydation (propene) (CO, allylic alcohols, low alkenes), dehydrogenation (hexene), decomposition (H_2O_2, NO_x) Redox reactions (lean de-NO_x and NO-CO conversion)	mesoporous

The advantage of using ordered mesoporous materials in catalysis are the relatively large pores, which facilitate the mass transfer, very high surface area, which allows high concentration of active sites per mass of material, versatile strategies for design and modification of the framework and surface, which generate different properties. The synthesis parameters allow the control over the structure and morphology of the mesomaterials, while the nature of the framework (surface and bulk) can be tuned by incorporation of hetero-species. All these aspects hold much promise for development of novel solid catalysts and catalytic supports.

Conversely, the ordered mesoporus functionalized silicates inherit special features, which rank them as good catalysts and catalytic supports. However, these materials have not found a widespread industrial application yet. Attempts for strong acid catalysts by mesoporous catalysts have failed so far. It has not been rationalised yet how the remarkable properties of the mesoporous materials can be used to better control the catalytic activity of the complex catalyst systems. The process of designing of the decent mesoporous catalyst is, in part, hindered by the lack of understanding of the key parameters, which play a crucial role in the particular catalytic reaction.

1.3.1. Hydrocarbon Selective Catalytic Reduction

Utilisation of catalyst to solve environmental problems in reducing pollution has attracted worldwide attention. The special interest in the environmental catalysis is devoted to the reduction of nitrogen oxides (NO_x) pollution. The nitrogen oxides are known to contribute to the formation of acid rain, smog and ground-level ozone [140]. Traffic is the main source of the total NO_x emissions [141]. Lean-burn and diesel engines, which offer significant fuel economy benefits, operate under highly oxidising conditions. It is, therefore, a big challenge in environmental protection to develop catalytic technologies for removal of NO_x in exhaust gases from vehicle engines operating in lean environments. The catalytic elimination of NO_x under such conditions can be accomplished by using hydrocarbons as "selective" reducing agents, which preferentially react with nitrogen oxides rather than with oxygen [140-141, 143]. This process is the so-called hydrocarbon selective catalytic reduction (HC-SCR) of nitrogen oxides (NO_x). The main advantage of this approach is utilisation of the gas mixture very similar to that found in exhaust (NO_x, C_zH_y, O_2).

The selective reduction of NO with alkanes and alkenes in the presence of O_2 was for the first time demonstrated by Held et al. [144] and Iwamoto et al. [145] on copper-ion-exchanged zeolites. Hamada et al [146] have found that H-zeolites and alumina were also active in the selective reduction of NO, but the required temperatures were much higher. Iwamoto et al. [147] reported that ion-exchanged MFI and mordenite (MOR) structures were active. Li and Armor showed that cobalt-ferrierite (Co-FER) doubles the nitric oxide conversion at temperatures above 500^0C compared to Cu-ZSM5 [148]. It is noteworthy that Co-FER is more selective than Co-ZSM5 when methane is used. The use of methane as a reducing agent presents a special interest, because it offers several advantages. Among these

are low cost, widespread availability (it constitutes 90% of natural gas), utilisation as fuel source in many combustion processes, not corrosive [149]. The selective catalytic reduction of NO with methane occurs according to the following reaction (1.10):

$$2\ NO + CH_4 + O_2 \rightarrow N_2 + CO_2 + 2H_2O \quad (1.10)$$

Inui et al. [150] proved that the activity in the SCR using hydrocarbons should be correlated with the acidity of the catalyst and with the activity for hydrocarbon combustion. This property could also be correlated with the redox properties of the metal-dopant. It is well known that the nature of the reducing agent has a strong influence on the reaction, alkynes are more active than alkanes [151]. The activation of C-H bond in methane necessitates high reaction temperature. Extensive research in SCR of NO_x with hydrocarbons on zeolites as catalytic supports have shown that their resistance to water vapour and SO_2, which are also present in the exhaust gas, should be improved. The leaching of alumina during the reaction poses a strong necessity in the support, which will not suffer the structural damage. The greatest problem is to decrease the temperature of HC-SCR of NO_x below 200^0C [142].

Among transition metal-exchanged zeolites, Co-promoted zeolites, which are active and selective in CH_4-SCR of NO_x, were also reported to be less sensitive to water [152]. The zeolite-based palladium catalysts are more active than cobalt loaded zeolites [153-155], but show low durability to H_2O [156-157]. Hamada and coworkers [158] was the first group, which reported that sulphated metal oxide catalysts (TiO_2, ZrO_2, Al_2O_3) show the activity for SCR with propane. Resasco et al. [159] showed that sulphated zirconia (SZ) is less sensitive to structural damage in comparison to zeolite carriers in the lean SCR of NO by CH_4.

Multifunctionality, which implies that each of the components provides a necessary but different reactive contribution to the end product, is expected to boost catalytic activity and to improve the durability of a catalytic support [160-161]. Zeolite- supported Pd-Co catalysts have been shown to be more efficient and resistant under hydrothermal conditions than either Pd- or Co-containing zeolites for lean reduction of NO by CH_4 [162-165]. The stability of these bifunctional catalysts to water vapour was explained in terms of either high stability of the active sites [163] or nature of the zeolite, MOR based catalysts being the most stable and active [165]. Sulphated zirconia (SZ) was found to stabilise Co^{2+} and Pd^{2+} similar to zeolites [159, 166]. Pd-Co-supported SZ exhibits remarkable performance in the presence of steam [167]. The Pd-Co-alumina catalysts have been found inactive for CH_4-SCR [168].

H_2-TPR data have revealed that cobalt supported on SZ is reduced at lower temperatures [167] as compared to Co-MOR [169]. The temperature required to reduce cobalt is lowered by the presence of Pd in the Pd/Co-HMOR and Pd/Co-SZ [170-171]. Sachtler et al. [164] assumed that palladium particles are covered by a cobalt shell and Co-Pd alloy is formed along the interface between phases of Co and Pd upon reduction with hydrogen.

In summary, despite the lack in structural stability, the zeolite supported metal cation catalysts have superior activity and selectivity as compared to alternative support materials in HC-SCR of NO_x. The zeolite-supported cobalt and palladium catalysts are among the most effective for CH_4-SCR and most resistant to the steam. The reports on Pd-Co supported on other oxides (ZrO_2, TiO_2, mixed oxides etc.) are sparse or lacking.

The idea pursued throughout this work was to extend the “mights” of mesoporous materials towards catalytic reaction, which requires strong acid catalysts. To combine the

wisdom accumulated in the synthetic experience in controlling different parameters into a simple procedure, which will lead to the formation of the aperiodical interconnected 3D framework of nothing (i.e., pores, voids) and provide surface properties essential for the interaction of preadsorbed NO_x species with the methane.

1.4. Thesis Outline

The research described in this thesis is focused on studying the synthesis and characterization of the mesostructured silica-zirconia mixed oxide functionalized with cobalt, palladium and sulfate ions. The potential catalytic ability of the prepared materials was evaluated in methane selective catalytic reduction (CH_4-SCR) of preadsorbed nitrous oxides (NO_x).

In chapter 1 general introduction is given; the development of Nano&Meso science with the special emphases on the importance of functionalized silicates, their synthesis methodologies, mesoporous catalyst properties, achievements in the area of SCR of NO_x with hydrocarbons and the thesis outline are briefly discussed.

In chapter 2 the synthesis mechanism of the zirconia-silica substrate and additionally preparation of transition metal, sulfate supported onto substrate by a relatively easy one-pot procedure will be described. The characterization techniques applied to investigate the materials such as X-ray diffraction, N_2 sorption measurements, TEM, SEM, FTIR spectroscopy, UV-Vis diffuse reflectance spectroscopy are discussed in detail.

Chapter 3 is devoted to the structural and morphological characterisation of the obtained samples. The pore walls and surface properties were investigated on the molecular level using absorption of probe molecules, namely, 2, 6-dimethyl pyridine and NO.

Chapter 4 discusses the catalytic application of the representative samples. It will be shown that the presence of palladium (Pd^{2+}) is crucial for CH_4-SCR of NO_x, and cobalt (Co^{2+}) renders the catalytic performance, apparently, by modification of active centers. Amount of zirconium in the silica framework determines the sulfate coverage.

In chapter 5, the final conclusions, suggestions and drawbacks of investigated materials are addressed.

2. EXPERIMENTAL

2.1. Materials

Tetramethyl orthosilicate ($Si(OCH_3)_4$, TMOS, 99+% Aldrich, Germany), zirconium (IV) propoxide, 70 wt% solution in 1-propanol ($Zr(OC_3H_7)_4$, $Zr(OPr)_4$, Aldrich, Germany), polyethylene 10 lauryl ether, ($CH_3C_{11}H_{25}(CH_2CH_2O)_{10}OH$), $C_{12}EO_{10}$, Sigma, Germany), Pluronic P 85 (PEO_{26}-PPO_{40}-PEO_{26}, BASF, USA), Cobalt (II) nitrate hexahydrate ($Co(NO_3)_2$ $6H_2O$, Sigma-Aldrich, Germany), palladium (II) nitrate dihydrate ($Pd(NO_3)_2$ $2H_2O$, 40% Pd, Merck, Germany), ammonium sulfate ($(NH_4)_2SO_4$, Merck, Germany), nitric acid (HNO_3, 65 % Riedel-de Haën, Germany).

2.2. Synthesis

2.2.1. General Procedure of Silica-Zirconia Synthesis

Typical silica – zirconia (Si-Zr) sample was prepared in the following way. A necessary amount of zirconium (IV) propoxide was acidified with nitric acid to form a yellowish mixture. 1g of surfactant and required amount of TMOS were subsequently added and the mixture was homogenized by shaking. To obtain the samples with 0 – 100 wt% zirconia, the amounts of TMOS and $Zr(OPr)_4$ were varied such that the molar ratio of inorganic precursors to surfactant ($C_{12}EO_{10}$) was kept constant at around 8. Then 0.5 g of deionized water was quickly introduced and all ingredients were instantly shaken. As an example, the mole composition of a mixture with Zr/Si mole ratio of 3 was as follows: 9.97 Zr : 2.96 Si : 0.217 P85 (1.59 $C_{12}EO_{10}$) : 10.3 HNO_3 : 27.7 H_2O. The resulting transparent colorless gel was spread over glass slide to form a film. The film samples were dried at ambient conditions for 1 day, then crushed into powder and subjected to heating under vacuum for 5 hours at 500^0C and then calcined in air at 550^0C for 5 hours.

2.2.2. One-Pot Preparation Technique of Silica – Zirconia Modified with Cobalt and Sulfate

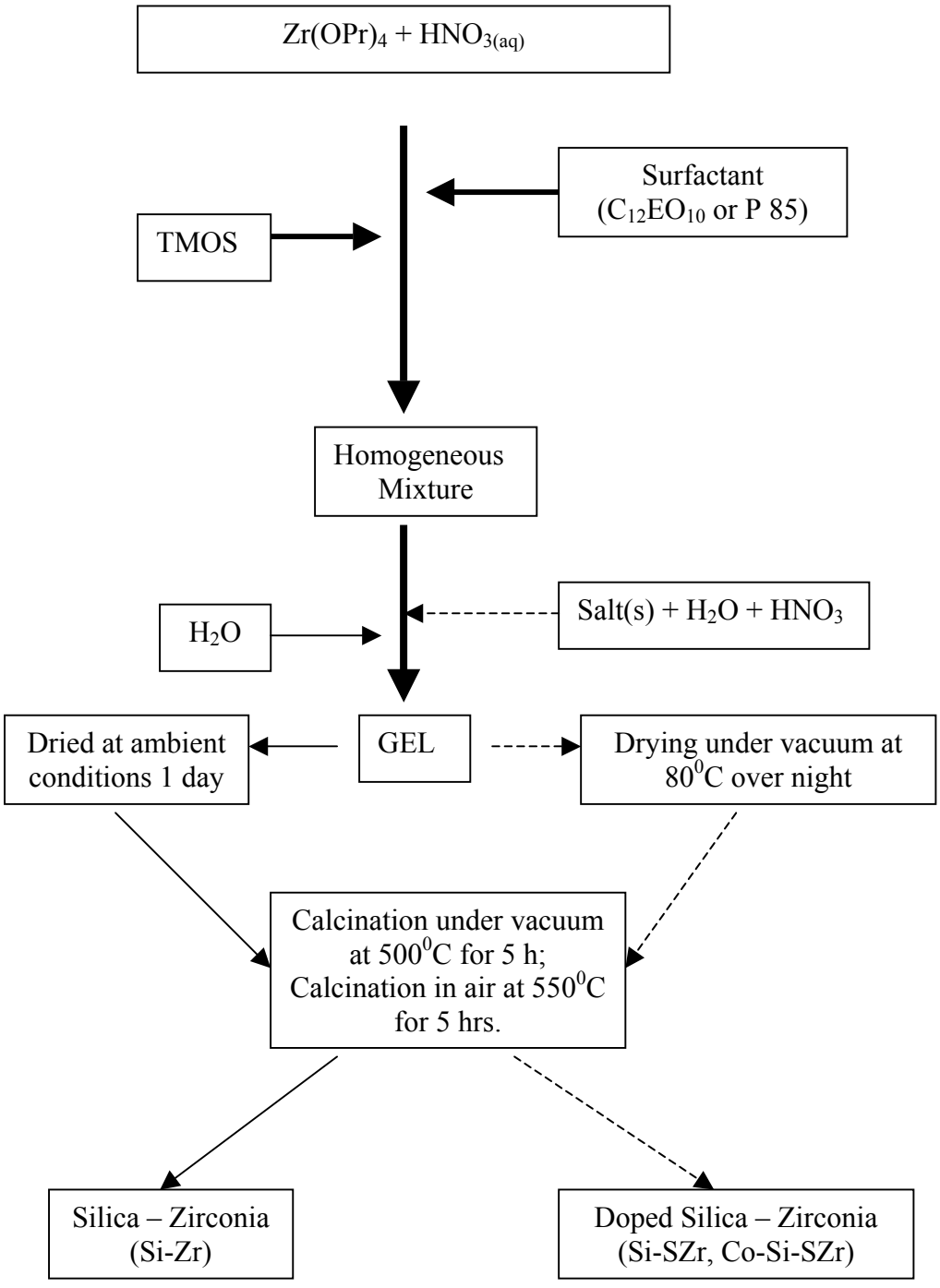

Scheme 1. Schematic diagram illustrating the synthesis procedure of mixed oxides

The zirconium propoxide, nitric acid, 1 g of surfactant, TMOS were mixed using the same procedure as for the synthesis of the Si-Zr. A second mixture composed of necessary amount of $Co(NO_3)_2$ $6H_2O$ salt and 0.186 g of $(NH_4)_2SO_4$, dissolved in minimum amount of water and acidified with nitric acid was added dropwise to the first one upon vigorous stirring. In this case the molar composition of Zr/Si = 3 blend was: 9.97 Zr : 2.96 Si : 0.217 P85 (1.59 $C_{12}EO_{10}$) : 55.5 H_2O : 12.4 HNO_3 : 1.41 SO_4^{2-}: X Co^{2+}. The mixture was stirred for 5 to 10 minutes until clear gel was obtained. The gel was cast as a film to dry at ambient conditions for 1 – 2 hours. The soft immobile samples were transferred to an oven and heated at 80^0C under vacuum over night. The powdered materials were further heated under vacuum at 500^0C for 5 hours with a heating rate of 2 ^{0}/min and then another 5 hours in air at 550^0C.

2.2.3. Introduction of Palladium and Cobalt Ions into Mesoporous Si-SZr

Palladium was impregnated into the calcined samples from an aqueous solution of palladium nitrate. The excess water was evaporated with continuous stirring. The samples were oven-dried at 100^0C over night. Finely grinded samples were calcined stepwise in air: first 2 hours at 350^0C, then 2 hours at 500^0C.

Cobalt ion has also been introduced by post synthesis impregnation method into Si-SZr supports for the sake of comparison with direct approach. The method of cobalt ion incorporation from the aqueous cobalt nitrate solutions is the same as the procedure applied to introduce palladium ion.

2.3. Materials Characterization

2.3.1. Powder X-ray Diffraction

Powder X-ray diffraction (XRD) patterns were acquired on a Rigaku Miniflex diffractometer using a high power Cu-Kα source (λ = 0.15418 nm) operating at 30kV and 15mA. Diffraction patterns were recorded under ambient conditions in the small and wide 2θ angles with a resolution of 0.01^0 to monitor both the mesophase and zirconia structure, respectively. The scan speed was $1\ ^0$/min.

2.3.2. Surface Area Measurements

Quantochrome Corporation, Autosorb-1-C/MS and IGA instruments were used for the nitrogen adsorption/desorption measurements at 77 K. The samples were outgassed at 350^0C under vacuum for 3 hours. The specific surface area was calculated from the BET method.

2.3.3. Diffuse Reflectance UV-Visible Spectroscopy

Diffuse reflectance UV-Visible spectra were obtained under ambient conditions between 200 and1100 nm using a fiber optic spectrometer AvaSpec-2048 (Avantes) from finely crushed samples.

2.3.4. TEM and SEM

TEM images were recorded on a Hitachi HD-2000 STEM operating at 200 kV and Philips 430 microscope with an accelerating voltage of 100 kV. The samples were prepared by dispersing the powder/fragments onto a carbon film-supported 200 mesh copper grid or embedded in epoxy resin and microtome.

2.3.5. FT-IR Spectroscopy

The FT-IR spectra were recorded on a Bomem MB 102 FT-IR (Hartman&Braun) spectrometer equipped with liquid nitrogen cooled MCT detector at resolution of 4 cm^{-1} (128 scans). A standard DTGS detector was used at resolution 2 cm^{-1} (64 scans) for samples pressed with KBr.

2.3.6. Experimental Set-up

A specially designed IR cell (Xenonum Scientific, USA) equipped with BaF_2 windows allowed recording of the IR spectra at high and low temperatures. The sample holder of the cell can be moved up and down relative to the light beam, which gives the possibility to record the gas phase spectra. The cell is connected to a vacuum/adsorption apparatus.

2.3.7. Activation of the Samples

Self-supporting discs (0.025 – 0.030 g/cm^2) were used for the FT-IR studies. These pressed specimens were activated in the three-step procedure: (1) heating for 1 hour at 450^0C under vacuum, (2) keeping the sample in an oxygen (100 Torr) atmosphere at 450^0C for 1 hour, (3) evacuation for 1 hour at the same temperature followed by cooling the cell to room temperature (RT).

The spectra of the activated samples recorded at high and RT temperatures were used as a background references. The background spectrum acquired at high temperature was subtracted from the spectra recorded at the temperatures higher than 250^0C, and, similarly, the RT background spectrum was subtracted from the acquired spectra at temperatures lower than 250^0C.

2.3.8. Adsorption of NO, Co-Adsorption of NO and O_2 and Adsorption of 2, 6 – lutidine

The NO adsorption was performed at RT by introducing 8 Torr NO to the IR cell and evolution of the spectra with time and upon evacuation were followed by using FT-IR spectroscopy.

Co-adsorption of NO and O_2 at RT was performed by introducing a mixture consisting of 8 Torr NO and 8 Torr O_2 for 30 min.

2, 6 – lutidine (1.5 Torr) was subjected to the IR cell and the IR cell was heated at temperatures between 100 and 450^{0}C upon evacuation.

2.3.9. Interaction of CH_4 with the Catalyst

50 Torr methane was added to the IR cell containing activated sample at RT, and then the closed IR cell was heated in the temperature range between 200 and 450^{0}C for 20 min.

2.3.10. Interaction of CH_4 with the NO_x Precovered Catalyst

The NOx surface species were created by co-adsorption of NO and O_2 (1:1 ratio) for 30 min followed by the RT evacuation and then addition of 50 Torr methane. The closed IR cell was heated at elevated temperatures for 20 min.

3. RESULTS AND DISCUSSION

3.1. Synthesis

The roots of mesoporous materials go back to 1992, when M41S family of meso-silicates and aluminosilicates has been disclosed by Mobil group [7]. Over the decade, since the discovery, a wide range of analogous materials has been developed. The nature of inorganic precursors, the type of template used, the variation of synthesis conditions, along with numerous other factors, have been widely studied in order to obtain structural and morphological control over the materials. The success achieved in preparing of such mesoporous solids gave the impetus to the concept to produce materials with potential catalytic applications. The first attempt was to produce mesoporous acidic materials, which would catalyze large molecules whereby to improve size and shape selectivity as well as efficiency of catalytic substrates. In this regard, different kinds of functionalization have been applied to meso-silicates and transition metal-containing mesostructured analogs were recently developed.

The present study involves the synthesis and characterization of functionalised siliceous mixed oxides, namely, silica - zirconia (Si-Zr), silica - sulfated zirconia (Si-SZr) and transition metal M-Si-SZr (M = Co, Pd), with a wide range of heteroatom loading.

We target to prepare Si-Zr and cobalt-, sulfate-containing Si-Zr, which possess structural parameters and surface properties efficient for a catalyst. Among these aspects are (i) three dimensional (3D) mesoporous framework, with poorly defined crystallographic symmetry (which would provide fast and unencumbered diffusion of reactants and products);

(ii) high thermal and hydrothermal stability; (iii) high surface area (implies great accessibility of active sites, high dispersion of active phase); (iv) sufficient Lewis and Brønsted acidity. The Co-Si-SZr composition has been chosen on account of several reasons. The effect of zirconium and cobalt is two-fold. Mixed oxides are reported to be more thermally stable than single oxides [117], the presence of coordinatively unsaturated Zr^{4+} cationic sites brings Lewis acidity to the siliceous matrix [172]. Addition of transition metal, cobalt, is expected to enhance the surface acidity and increase the efficiency of the catalyst towards CH_4-SCR of NO_x [148]. Introduction of the sulfate is known to increase the acidity of zirconia [173].

The synthesis has been limited to the following reagents: inorganic alkoxides (tetramethyl orthosilicate (TMOS) and zirconium propoxide ($Zr(OPr)_4$)), non-ionic surfactants (polyoxiethylene 10 lauryl ether and pluronic P85) as structure directing agents, water as a solvent, nitric acid as hydrolysis catalyst, cobalt salts as cobalt precursor and ammonium sulfate as source of sulfate ions. The one-pot synthesis procedure, which bears similarities with true liquid crystalline templating (TLCT) mechanism, has been developed. This method allows addition of inorganic salts or other additives in a wide range of concentration and results in uniform distribution of the dopant on the internal surface of the support. In contrast to hydrothermal synthesis, all added reagents fully contribute to the final material. The synthesis is carried out on the bench top such that preparation time is short. The design of the desired material requires optimization of the synthetic parameters. In general, mesostructure and porosity are controlled by the type of surfactant, inorganic precursor/surfactant ratio and the nature and concentration of the cobalt salt. The pH value influences the hydrolysis and polycondensation of inorganic source. The primary task in the preparation of intended material is to achieve homogeneous distribution of zirconia in silica matrix. To this end the hydrolysis and polycondensation of silica and zirconia alkoxides should be balanced.

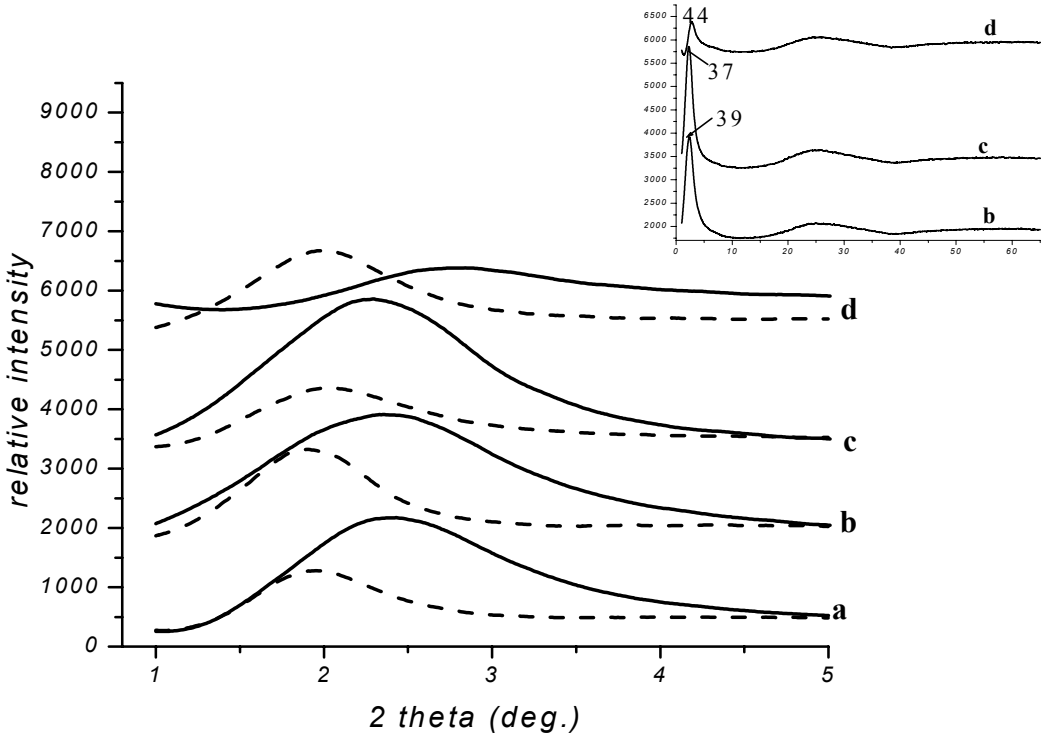

Figure 3.1.1. Powder XRD patterns of silica-zirconia samples prepared at different pH values: 0.28 (a), 0.076 (b), 0.020 (c), -0.13 (d). Dashed line corresponds to as-prepared sample, solid line represents calcined at 500^0C sample.

Powder XRD patterns of Si-Zr synthesized at different pH are shown in Figure 3.1.1. Single broad peak at small 2θ angles confirms mesostructure. The absence of the higher order diffraction peaks implies randomly distributed pores. The d-spacing values slightly increase as the acidity of the medium increases, suggesting the insertion of zirconium into silica framework. The presence and accessibility of Zr^{4+} surface sites is investigated by the adsorption of NO (Fig. 3.1.2). The band at 1912 cm^{-1} attributed to Zr^{4+}-NO gradually rises in intensity as pH in the synthesis is being increased. This experimental fact indicates that there are coordinatively unsaturated Zr^{4+} sites available on the surface and their concentration increases with pH, providing that the surface areas of the samples are comparable.

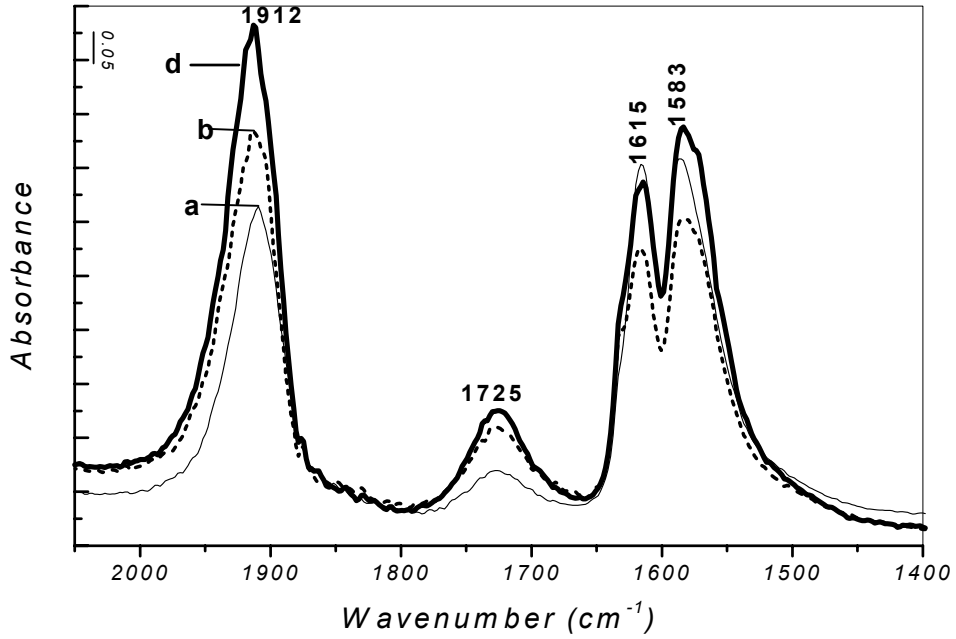

Figure 3.1.2. FT-IR spectra of NO (58 Torr) adsorbed at room temperature on the Si-Zr supports synthesized at various pH values: 0.28 (a), 0.02 (b), -0.13 (c).

The order of addition of the components during the synthesis is a crucial factor for achievement of a homogeneous reaction mixture. In the first attempt to prepare Si-Zr mixed oxide and Co-Si-Zr, the reactants have been mixed in the following order: to cobalt salt dissolved in water and acidified with nitric acid, and then the surfactant is added to form thick liquid crystalline (LC) phase, then methanol is introduced and blend is gently heated to ensure and ease the mixing. TMOS is added to the cooled to room temperature (RT) mixture followed by addition of $Zr(OPr)_4$. This procedure results in weakly mesoporous materials with maximum zirconia concentration ca. 40 wt%. If zirconium content in the mixture exceeds 40 wt% localized condensation of zirconia phase occurs producing heterogeneous translucent or opaque materials without mesostructure.

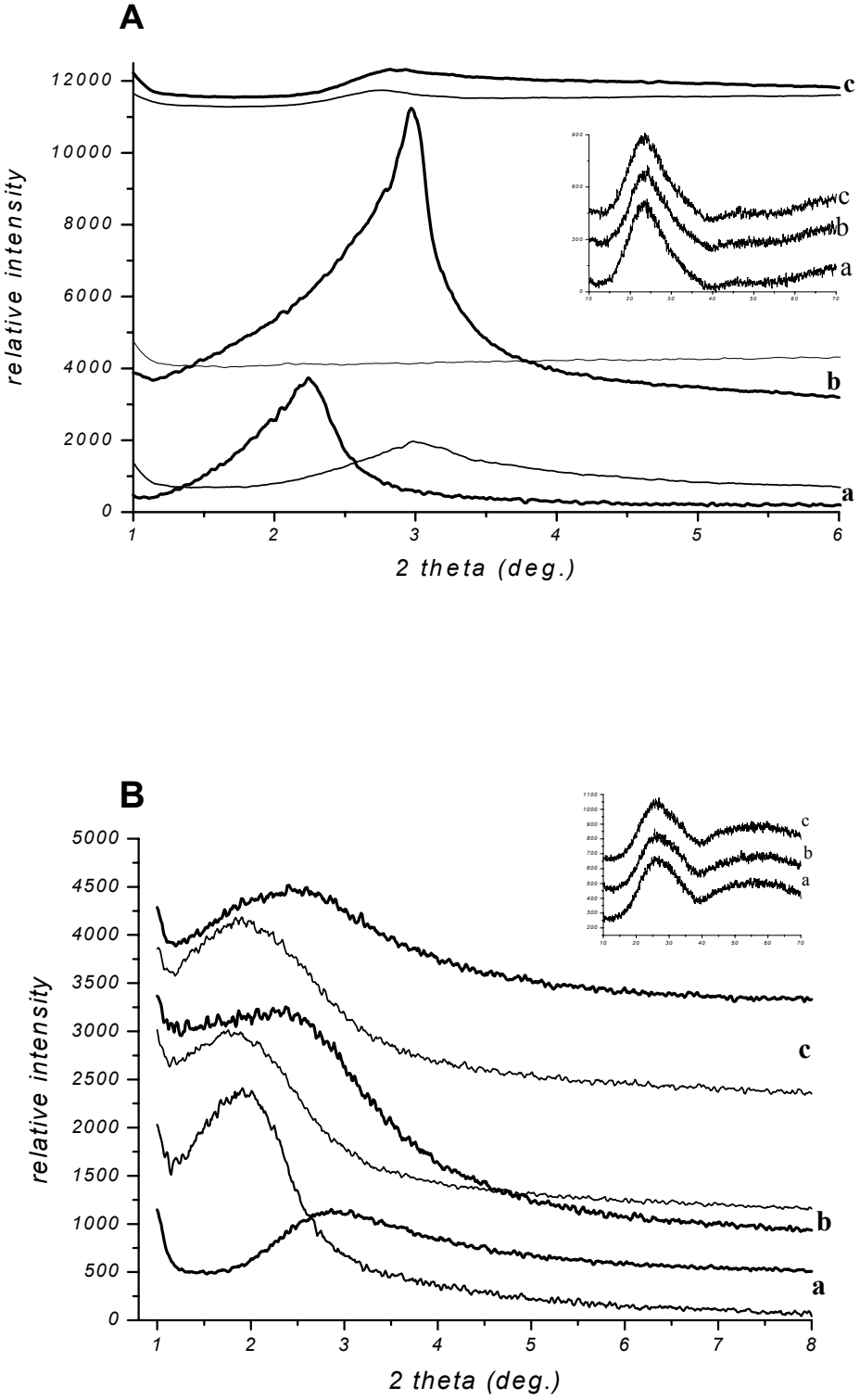

Figure 3.1.3. Powder XRD patterns of (A) SiO_2 and (B) Si-Zr. Inorganic precursor to surfactant molar ratio is (a) 5, (b) 8, (c) 10. Normal line corresponds to as-prepared materials and thick line represents calcined at 500^0C samples.

Another synthesis methodology was developed to prepare mixed oxides with high Zr/Si ratios. This procedure is easier, since it does not require heating and addition of methanol. $Zr(OPr)_4$ is acidified first and then surfactant and TMOS are added. This liquid-like mixture is easy to homogenize by shaking. Cobalt salt is dissolved in water and quickly poured into the first blend. To prevent the precipitation of single ZrO_2 phase from the reaction mixture, zirconia to acid ratio is kept equal to ca. 0.9.

The effect of inorganic precursor/surfactant molar ratio on the structure was studied by means of XRD (Fig. 3.1.3). It can be seen that pores shrink upon calcination as indicated by the shift of the diffraction lines to higher 2θ values. It should be pointed out that the extent of shrinkage decreases as the ratio increases. It means that the materials become more heat resistant, probably, due to increase in the pore wall thickness. Inorganic source to surfactant mole ratio of 8 has been chosen as a condition for further synthesis, since it results in relatively more ordered materials.

Transition metal aqueous salts dissolve easily in the surfactant-water mixture and have been found to affect porosity and morphology of the resulting materials. However, because of multiple and simultaneous effects they induce on a system, the exact mechanism of their action has not been clarified yet. On the bases of XRD data of Co-SiO_2 and Co-Si-Zr samples (Fig. 3.1.4) obtained in the presence of different cobalt precursors, it is difficult to elucidate the anion effect on the structures. Among the cobalt-containing Si-Zr samples, the sample prepared with cobalt nitrate salt shows well-defined mesostructure. However, Co_3O_4 phase is detected at 36.8^0 2θ, when $Co(ClO_4)_2$ has been used as the cobalt source (Fig. 3.1.4, solid line a).

Conversely, on the bases of the results discussed above, the Si-Zr, Si-SZr and Co-Si-SZr materials in this study will be prepared by the one-pot synthesis procedure at highly acidic conditions with inorganic source/surfactant ratio of 8 and cobalt nitrate precursor.

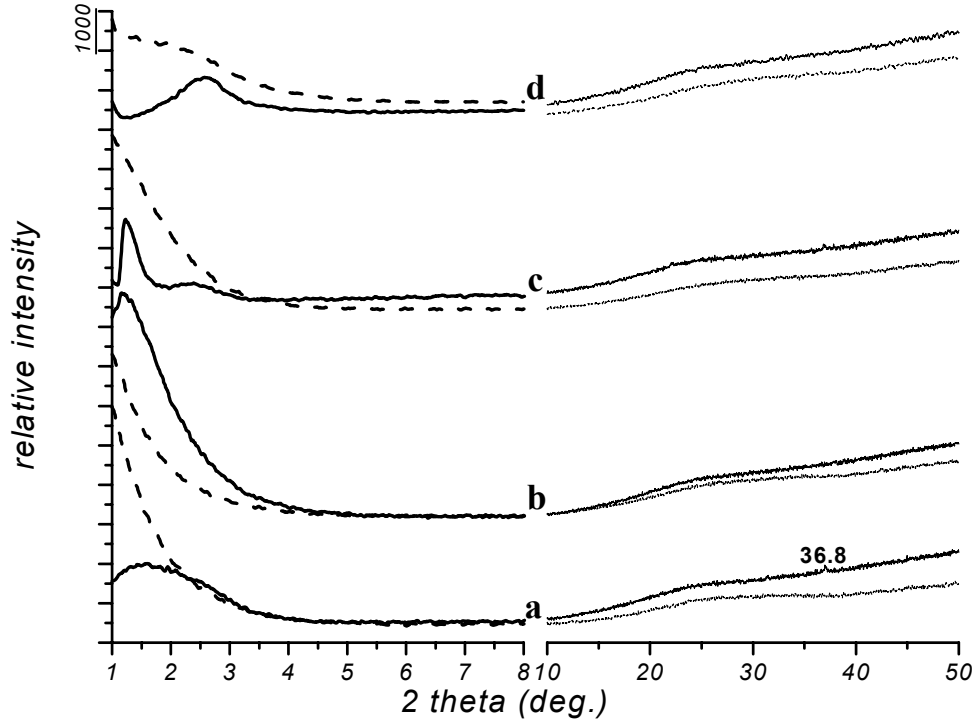

Figure 3.1.4. Powder XRD patterns of cobalt-containing samples calcined at 500^0C. Salts used as cobalt precursors are: (a) $Co(ClO_4)_2$, (b) $Co(Ac)_2$, (c) $Co(Cl)_2$, (d) $Co(NO_3)_2$. Solid line stands for the Co-SiO_2 samples and broken line for the Co-Si-Zr samples.

3.1.1. The Mechanism of the Direct Synthesis of Silica-Zirconia, Silica-Sulfated Zirconia and Cobalt-Silica-Sulfated Zirconia

When one expects that a mixed oxide has been synthesized, a good mixing of heteroelements i.e. formation of M-O-M' linkages rather than segregation of single phases M-

O-M and/or M'-O-M' should be achieved. In contrast to silicon alkoxides $Si(OR)_4$, zirconium (IV) alkoxides due to its lower electronegativity are less stable towards hydrolysis and condensation [174-175], therefore, the introduction sequence and nature of reacting inorganic species are crucial to ensure homogeneous co-precipitation.

In the first procedure to synthesize silica – zirconia mixed oxide, a two-step hydrolysis method has been exploited. TMOS was partially hydrolyzed in water : acid : surfactant mixture, then $Zr(OPr)_4$ was added. This procedure allowed us to prepare homogeneous Si-Zr gels with maximum amount of ZrO_2 up to 35 – 40 wt%. Since addition of zirconium alkoxide to prehydrolized silica results in the formation of mixed oxides with only low Zr/Si ratios, more emphases was given on the second synthetic approach by which samples with zirconia content ranging from 0 to 100 wt% can be prepared.

In the other procedure, $Zr(OC_3H_7)_4$ was first combined with a concentrated nitric acid solution. In a highly acidic medium pH < 0, zirconia moieties are positively charged $ZrO_n^{\delta+}$ and are stabilized by a layer of negatively charged nitrate counteranions [176]. The surfactant and TMOS added to the acidic zirconium solution form a homogeneous mixture. Upon addition of aqueous acidic salt solution, a rapid hydrolysis of the inorganic alkoxides takes place and milky emulsion is observed. Zirconia and silica species are positively charged in the reaction media at pH < 1, which is below the point-of-zero charge of zirconia (~ 4 - 6 [177]) and silica (~ 1.5 - 3 [178]). Depending on the pH, different zirconia polymorphs are formed [179]. Bunker and Keefer [180] have investigated the hydrolysis and condensation of tetravalent Zr(IV) systems. Above pH ~ 0, the $[Zr(OH_2)_6]^{4+}$, $[Zr(OH)_2(OH_2)_4]^{2+}$ ions spontaneously hydrolyze and undergo olation to form $[Zr_4(OH)_8(OH_2)_{16}]^{8+}$ polycations. In this case, the hydrolysis can be considered as the attack and attachment of hydroxyl ions to the

zirconium ion. Acid/base catalyst influences both the hydrolysis and condensation rates. Acid helps to protonate negatively charged alkoxide groups and produces a good leaving group, Eq. (3.1.1):

$$M\text{-}OR + H_3O^+ \rightarrow M^+ \leftarrow :OHR + H_2O \quad (3.1.1.)$$

The blend is opaque or larger white flakes form most likely due to hydrous zirconia species, since silicon alkoxides hydrolyze into transparent solutions containing small oligomeric species.

During 5 – 10 minutes stirring the emulsion turns into a clear gel at sufficiently high pH and avoids precipitation of ZrO_2 species. This experimental observation might be rationalized by complexation of the metal centers with anions produced upon dissolution of the inorganic salts (NO_3^-, HSO_4^- and SO_4^{2-}). The counter anions compete with water for coordination to the metal centers [181]. The nitrates usually bind in monodentate fashion e.g. $[Zr(OH_2)(NO_3)(OH_2)_2]_n^{n+}$, nNO_3 and serve only as terminal ligands [182]. Unlike nitrate, sulfate ion demonstrates quite high complexing ability. According to the literature data, it has no tendency to displace oxo, a negligible tendency to replace hydroxyl, a strong tendency to substitute water, and extremely strong tendency to replace hydronium ligands from zirconium. The sulfate ions act as network forming ligand bridging up to three $Zr(OH_2)^{2n+}$ moieties and remain coordinated to the metal in the final condensation product [182-184]. Ciesla et al. [185] have proposed existence of the following zirconium sulfate species in the aqueous medium: $[Zr(OH)_2(SO_4)_x(OH_2)_y]_n^{-n(2x-2)}$. It is expected that counter anions would interact with silica oligomers in a similar way. Hence, the conversion of zirconium/silicon hydroxo and water bonds into bonds with sulfate and nitrate ions to form zirconium/silicon-aqua-sulfate-nitrate complex ions might be responsible for the formation of the homogeneous clear gel.

Moreover, the formation of inorganic species – ligand complexes slows down the rate of condensation.

In terms of surfactant to water mole ratio (1:1), this synthetic approach can be considered as true liquid crystalline templating (TLCT), which predetermines the formation of a stable liquid crystalline (LC) mesophase. Hydrophobic-hydrophilic interactions are the driving forces for mesophase formation in the nonionic surfactant – water system, where solubilized triblock copolymer aggregates into micelles containing a hydrophobic poly(propylene)oxide (PPO) core and hydrophilic poly(ethylene)oxide PEO corona. The PEO groups can form hydrogen bond with hydrated protons [H_3O^+] under acidic conditions [186]. The cobalt ions in the system are known to hydrogen bond to oxygens of the ethylene oxide units [187-188] through coordinated water molecules. These interactions impose positive charge to the head groups. Evolution of methanol, as a hydrolysis product, helps to dissolve the surfactant and to achieve good mixing of the components.

Thus, inorganic species hydrolyzed in the highly acidic medium acquire positive charge (I^+) and hydrophilic polyethylene oxide head groups (S^0) complexed with cobalt ions and [H_3O^+] also possess a partial positive charge (M^+/H^+S^0), therefore, the interaction at the inorganic/organic interphase is electrostatic and formation of mesostructure occurs through $(I^+)X^-(M^+/H^+S^0)$ ion mediated ($X^- = NO_3^-, HSO_4^-, SO_4^{2-}$) charge interactions.

The sulfate containing samples, dried at RT, are soft materials. The existence of small-angle diffraction line in the XRD pattern is strongly dependent on zirconium and sulfate concentration, which is consistent with literature data [184-185]. As-prepared pure zirconia and zirconia rich silica-sulfated zirconia samples are XRD amorphous, indicating absence of

long-range order. The reasons for this might be (i) poor condensation of $[Zr(OH)_2(SO_4)_x(OH_2)_y]_n^{-n(2x-2)}$ moieties, since sulfate prevents fast condensation, (ii) propanol, which is produced during the hydrolysis of zirconium propoxide, can not be easily removed from the system because it is situated at the hydrophilic/hydrophobic interface of amphiphilic surfactant and may behave as co-solvent or swelling agent affecting the mesophase formation, (iii) electrostatic interaction between numerous charged species (high ionic strength). In the drying step at ambient conditions and at 80^0C under vacuum, the substantial loss of volatile components (methanol, propanol, water) leads to enrichment of the hydrophilic surfactant domains with metal species and stronger interaction between PEO groups and hydrated cobalt cations, which, in turn, results in a very stable liquid crystalline mesophase [189]. Upon heating at 80^0C the inorganic species condense to replicate the template. At this stage mesostructure starts to develop. The samples were further heated under vacuum at 500^0C for 5 hours. The endothermic process occurs during heating, as organics inside the pores undergo pyrolysis. The advantage of this step lays in the fact that the structure-directing power of the template is preserved all time during the framework formation. The carbonaceous residues are removed by high temperature treatment (550^0C) in air. The calcination process increases the structural ordering within the inorganic framework. The high temperature treatment results in deposition of the metal ions onto the internal mesoporous surface. Zirconium atoms introduced during the synthesis are found to be preferentially localised at the pore surface [190]. When the zirconium content is high, tetragonal ZrO_2 is observed along with the amorphous phase. It was suggested that not all of the zirconia can be structured by the template and a part of zirconium oxide crystallizes into tetragonal phase [191].

3.2. The Materials Morphology and XRD Study

Figure 3.2.1 compares the XRD data acquired from silica-zirconia (Si-Zr) samples with zirconia content in the range between 0 and 100 wt% prepared in the presence of oligo(ethylene oxide) $C_{12}EO_{10}$ surfactant. The Si-Zr samples with zirconium content up to 90 wt% show single (100) reflection, usually observed for mixed oxides with three dimensional (3D) wormhole like framework, namely, HMS [20] and MSU types [21]. The peak at low angle broadens with increase in zirconia concentration. It indicates that mesostructural order gradually diminishes. As zirconium content exceeds 40 wt%, the d-spacing values decrease from 35.3 to 26.7 Å. The shift of the d_{100} reflection to lower angles in the case of the sample with 90 wt% zirconia might be an indication for increase in the pore wall thickness. The pure zirconia calcined at 500^0C for 6 hours is 100 % tetragonal (top pattern).

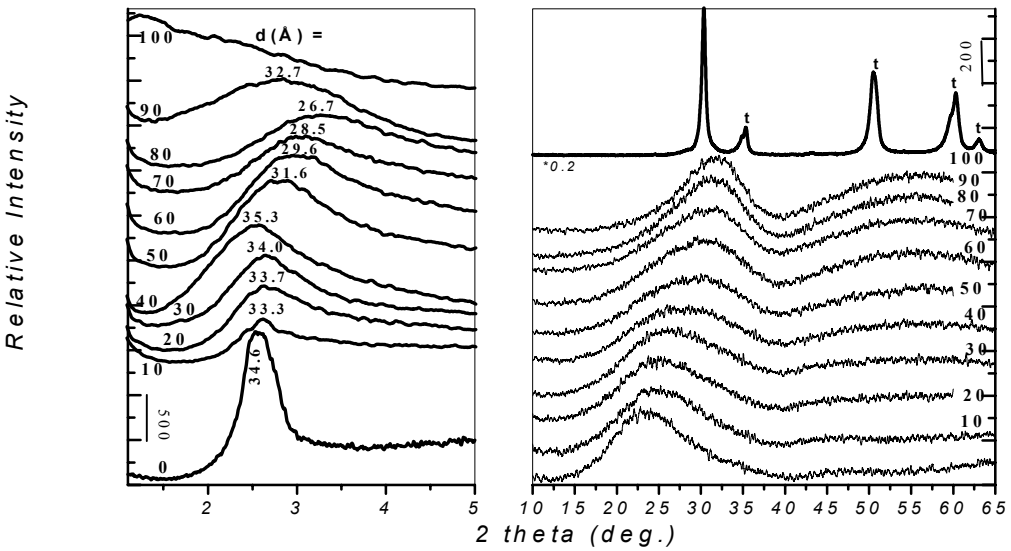

Figure 3.2.1. Powder XRD patterns of calcined at 500^0C Si-Zr samples templated by $C_{12}EO_{10}$. Concentration of ZrO_2 (wt%) is indicated along the lines. The numbers assigned on top of the peaks on the left is the d-spacing values in Å.

The powder XRD data acquired from the Si-Zr samples temlated by the P85 block co-polymer are displayed in Figure 3.2.2. The pure silica shows two diffraction peaks at small 2θ values. The increase in the intensity of the low angle diffraction peak, as concentration of zirconia changes from 60 to 80 wt%, indicates the formation of more ordered structure. In the sample containing only 10 wt% silica the referred (100) diffraction line is weak and broad. It suggests that mesostructure is disrupted at high Zr/Si ratios. It is worth to mention that d-spacing is not affected much by the addition of zirconia in the range between 0 and 90 wt%, which is an indication for the Si-Zr stability and similar structure type. Since there is only one diffraction line in the XRD pattern it is difficult to suggest a space group. However, with the help of TEM images we can suggest that framework is wormlike, which is quite common in the mixed oxides.

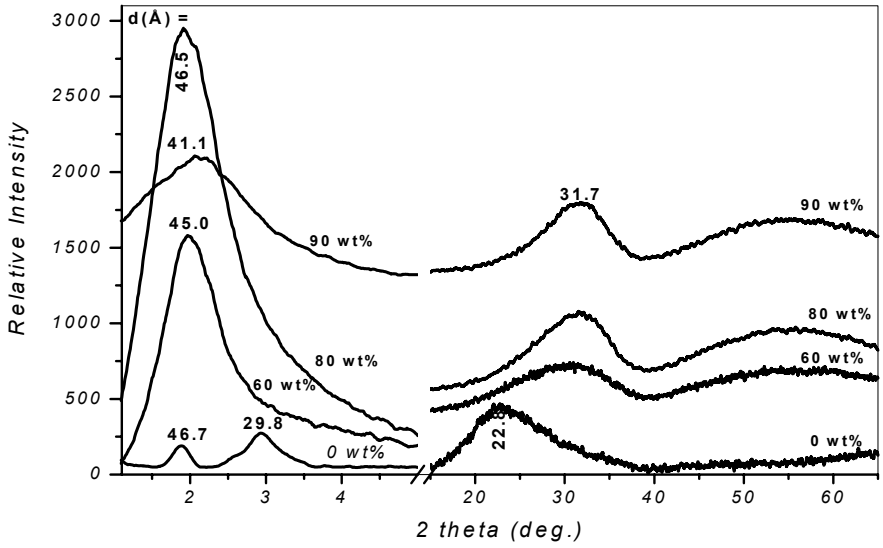

Figure 3.2.2. Powder XRD patterns of calcined at 550^0C Si-Zr samples templated by P85. Concentration of ZrO_2 (wt%) is indicated along the lines. The numbers assigned on top of the peaks on the left is the d-spacing values in Å.

Comparing the data from samples prepared in the presence of $C_{12}EO_{10}$ and P85, Fig. 3.2.1 and Fig. 3.2.2, respectively, it can be inferred that the latter materials possess thicker

walls, since their average pore-pore separation values are noticeably greater than those for the former Si-Zr mesostructured materials. The slight variation in the position of (100) reflection (Fig. 3.2.2) versus gradual shift of the (100) reflection to higher 2θ values (Fig. 3.2.1) as zirconia loading increases implies that Si-Zr synthesized with P85 is more stable than Si-Zr assembled with $C_{12}EO_{10}$. The Si-Zr samples after being heated at 550^0C are all non-crystalline as evidenced by the wide-angle XRD analysis. It can be inferred from the Figure 3.2.1 that equilibrium phase of pure zirconia at 550^0C is tetragonal (t- ZrO_2). These experimental facts suggest that SiO_2 and ZrO_2 are uniformly mixed on the atomic level. This mixing retards the phase transformation of ZrO_2 at elevated temperatures. Silica-sulfated zirconia (Si-SZr) specimens templated by P85 block co-polymer show a single reflection at low angles, consistent with short-range hexagonal order (Fig. 3.2.3).

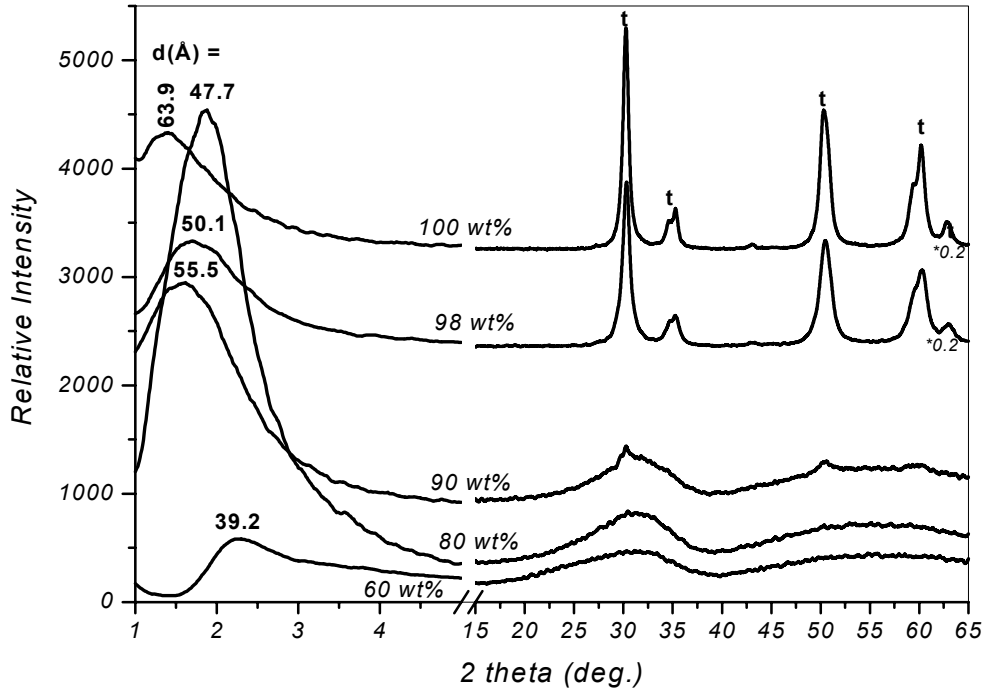

Figure 3.2.3. Powder XRD patterns of calcined at 550^0C silica-sulfated zirconia samples containing ~ 8wt% sulfate, prepared with P85. Concentration of ZrO_2 (wt%) is indicated along the lines. The numbers assigned on top of the peaks on the left is the d-spacing values in Å.

A similar increase in the intensity of the diffraction lines evidenced when the loading of zirconia increases from 60 to 80 wt%. The diffraction peak at about 1.7^0 shifts to the lower 2θ values and broadens as more zirconia is introduced (90 – 100 wt%). The close inspection of the XRD patterns in the wide-angle range reveals the appearance of tetragonal ZrO_2 phase in the sample containing 90 wt% ZrO_2 treated at 550^0C. As amount of silica in the material decreases, the degree of mesostractural order decreases and large tetragonal zirconia particles crystallize out. On the bases of our experimental data from Si-Zr (Fig. 3.2.1 and Fig. 3.2.2) and Si-SZr (Fig. 3.2.3), it can be inferred that the presence of sulfate ions helps aggregation of ZrO_2 species, which crystallize out upon heating the sample with composition 10 wt% SiO_2/90 wt% ZrO_2/ 8 wt% SO_4 at 550^0C, while amorphous zirconia phase is stabilized in the sulfate free sample with matching Zr/Si mole ratio. It is logical to assume that in the presence of sulfate ions, which are more stable on zirconia than on silica [192-193], the surface is enriched with zirconium. It is worth to mention that the d-values for Si-Zr and Si-SZr templated by P85 are comparable up to the point where crystalline ZrO_2 phase is detected.

The powder XRD patterns reported in Fig. 3.2.4 reveal the effect of cobalt on the structure. The broad diffraction at low 2θ values is indexed to (100) reflection of randomly ordered worm-like pores packed into 3D framework. Incorporation of cobalt by one-pot synthesis causes gradual increase in d-spacing values as concentration of transition metal increases (Fig. 3.2.4, patterns a, b, d, e and f). It is interesting to notice that the impregnation of 1 wt% cobalt brings an increase in the d-spacing comparable to that observed in the sample containing 4 wt% cobalt introduced by co-precipitation. It should be also pointed out that the greater shift in the position of (100) diffraction peak is observed for samples containing crystalline ZrO_2 phase (Fig.3.2.4, inset).

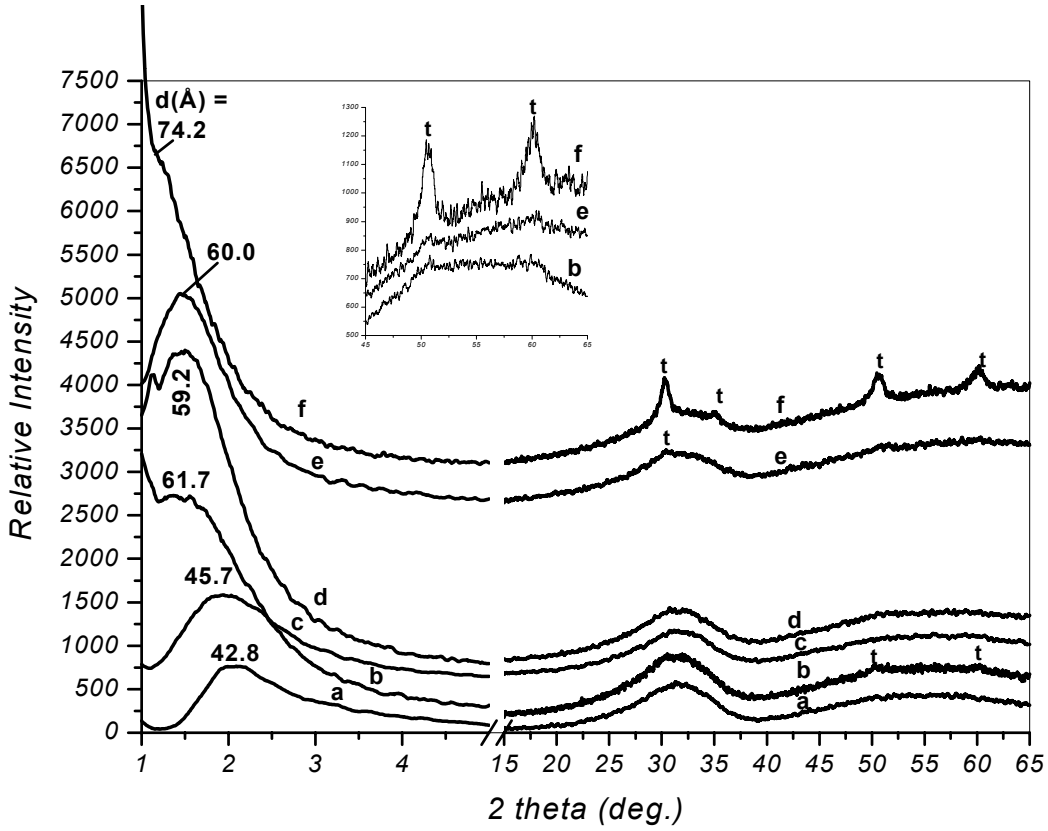

Figure 3.2.4. Powder XRD patterns of calcined at 550^0C X wt% cobalt-silica-sulfated zirconia (Zr/Si = 3) samples containing ~ 8wt% sulfate ion, prepared by one-pot procedure, unless otherwise mentioned, with P85, where X wt% = 0 (a), 1 (Co is impregnated) (b), 1 (c), 2 (d), 4 (e), 6 (f). The numbers assigned on top of the peaks on the left is the d-spacing values in Å. Diffraction lines corresponding to tetragonal ZrO_2 phase are marked by **t**. The inset shows powder XRD patterns in the range between 45 and 65^0 2θ of the corresponding b, c, f samples in the main figure.

The explanation for the shift of the diffraction line to the lower 2θ values can be two-fold: (i) the increase in the pore wall thickness and (ii) phase transformation of the mesostructure. The latter supposition is supported by the appearance of the additional peak at low 2θ angles (Fig. 3.2.4, lines b, d, f), SEM images (Section 3.3, Fig. 3.3.1, B) and N_2 sorption measurements (Section 3.5, Fig. 3.5.4).

The XRD patterns of the Pd-containing Si-SZr, Co-Si-SZr and the parent Si-SZr, Co-Si-SZr are displayed in Figure 3.2.5. The 5 wt% Pd-Co-Si-SZr (Zr/Si =2) and 1 wt% Pd-Si-SZr (Zr/Si = 3) show a peak at $2\theta = 33.9^0$ typical for the [101] plane refraction of PdO [194-195], indicating the presence of large PdO nanoparticles. As the palladium loading in the Co-Si-SZr sample increases the peaks attributed to the tetragonal ZrO_2 phase rise in intensity. It indicates that transformation of zirconia phase from amorphous to crystalline (t-ZrO_2) takes place upon impregnation. No metallic Pd has been detected.

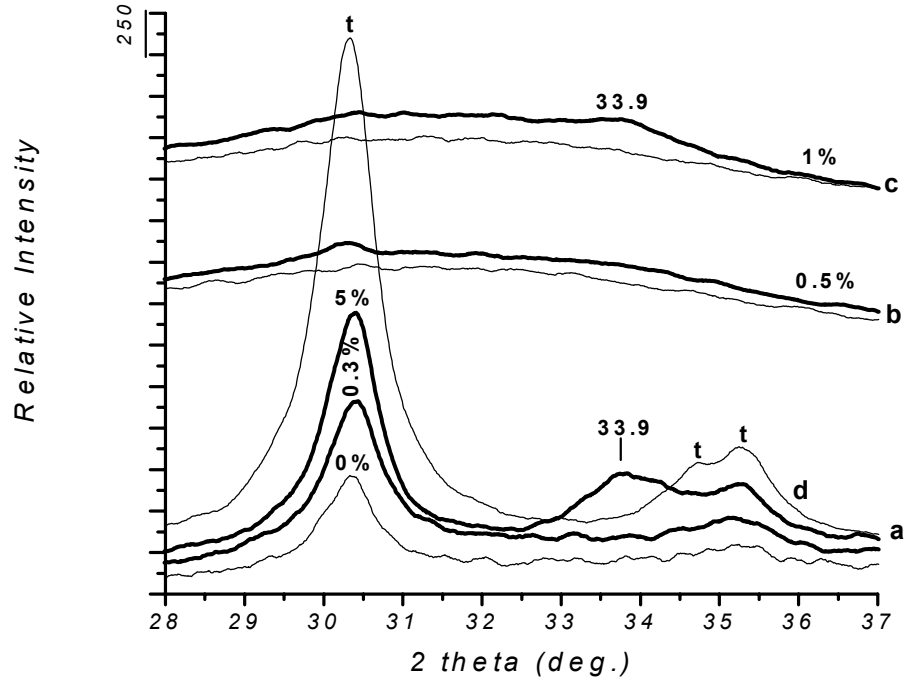

Figure 3.2.5. Powder XRD patterns of calcined at 550^0C Pd-6 wt% Co-Si-SZr (Zr/Si = 2) (a), Pd-Si-SZr (Zr/Si = 2) (b), Pd-Si-SZr (Zr/Si = 3) (c), Si-SZr (Zr/Si = 28) (d). Thick lines correspond to palladium containing samples and normal lines to palladium free samples. Concentration of palladium is indicated along the lines. All samples are templated by P85. **t** stands for tetragonal ZrO_2.

The X-ray diffraction method has been used to study stability of the support upon impregnation with palladium and cobalt. The modification of a material by conventional aqueous impregnation method is a good test for hydrothermal stability of the material. Usually, the hydrothermal stability of mesoporous materials is investigated by boiling them in water for up to 48 hours [196-197]. However, it is important that integrity of the pore structure is retained through repeated adsorption and regeneration cycles. For instance, according to the literature MCM-41 is very stable under hydrothermal conditions [198], but its hexagonal mesostructure is completely lost upon aqueous impregnation [199]. These results confirm that the data obtained with hydrothermal treatment can not be directly used for the evaluation of material's stability through various post-synthesis modifications.

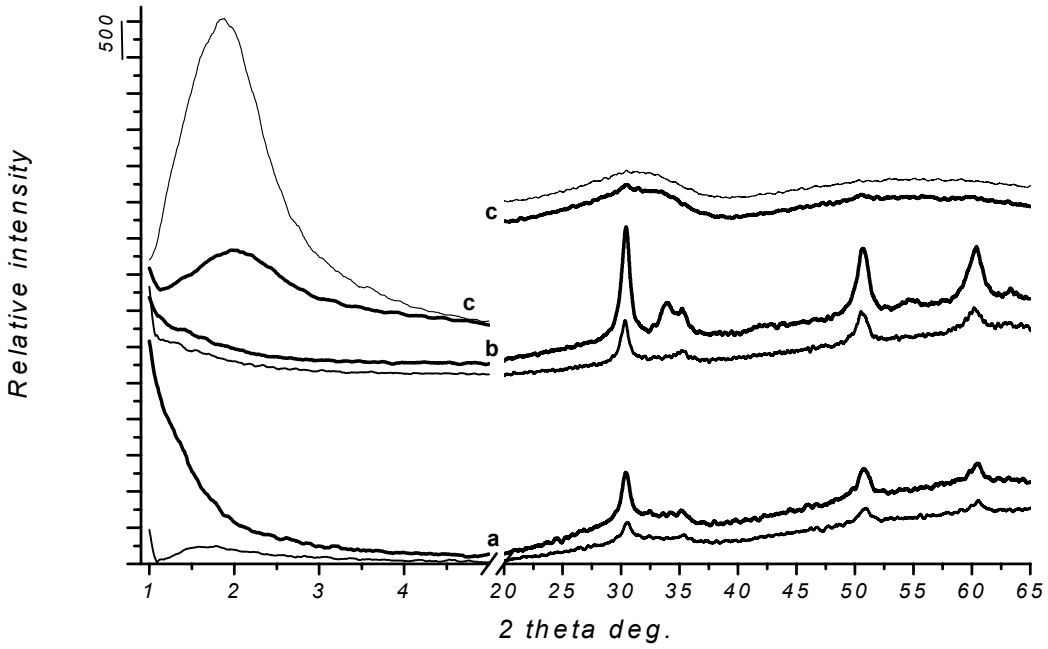

Figure 3.2.6. Powder XRD patterns of calcined at 550^0C 6 wt% Co-Si-SZr (Zr/Si = 2) specimens impregnated with (a) 0.1 wt% Pd, (b) 5 wt% Pd and (c) Si-SZr (Zr/Si = 2) impregnated with 0.5 wt% Pd. Single line represents supports before impregnation, thick line corresponds to modified supports.

Figures 3.2.6 through 3.2.8 show the effect of aqueous impregnation on the mesostructure of the Si-SZr and Co-Si-SZr samples with Zr/Si ratios 2, 3 and 28. The impregnation of the Si-SZr samples (Zr/Si = 2) with palladium leads to a substantial decrease in the intensity of (100) diffraction peak (Fig. 3.2.6, line c). This indicates that the initial mesoporous structure of the Si-SZr is significantly affected by impregnation and drying. The effect of the post-synthesis modification of the cobalt-containing Si-SZr mixed oxides with palladium is less pronounced. Impregnation of 1 wt% Pd onto Si-SZr (Zr/Si = 3) causes slight decrease in the d-spacing and broadening of the small angle peak (Fig. 3.2.7, line b). When 1 wt% cobalt is impregnated, two diffraction peaks with increased intensity are detected in the low 2θ range, indicating formation of more ordered mesostructure.

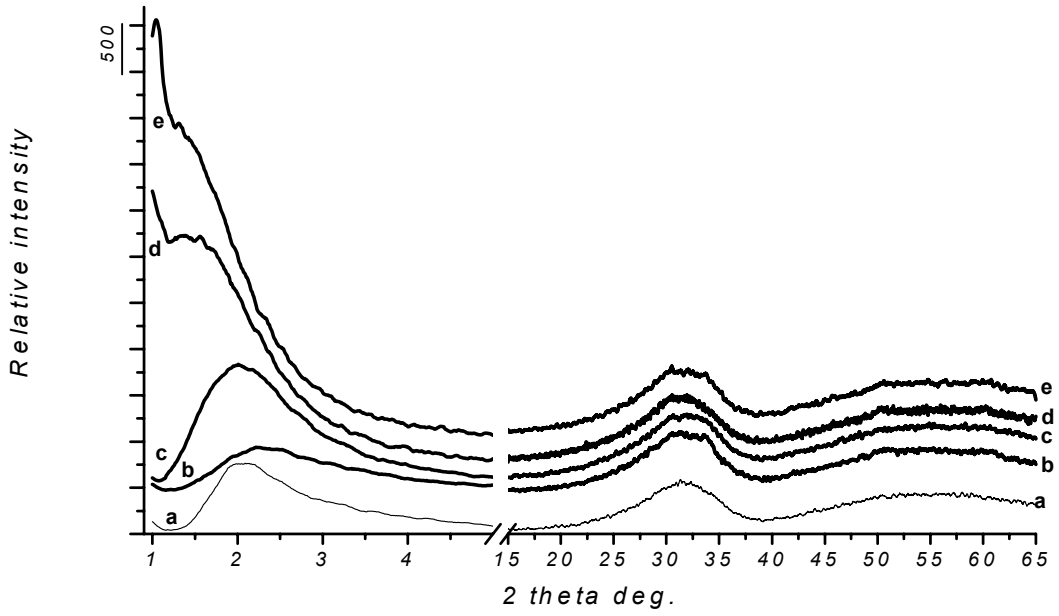

Figure 3.2.7. Powder XRD patterns of calcined at 550^0C Si-SZr (Zr/Si = 3) sample (a) impregnated with (b) 0.1 wt% Pd, (d) 1 wt% Co and (e) 1 wt% Co followed by impregnation with 1 wt% Pd. Line (c) corresponds to 1 wt% Co-Si-SZr (Zr/Si = 3) impregnated with 1 wt% Pd.

Addition of palladium to the Co-Si-SZr samples does not induce substantial changes to the structure. It should be emphasized that Si-SZr sample, which underwent two subsequent impregnation-calcination cycles displays XRD patterns with two well-resolved low-angle reflections (Fig. 3.2.7, line e).

The impregnation of zirconium rich (Zr/Si = 28) mixed oxides with 1 wt% Pd (Fig. 3.2.8, line b) leads to a decrease in the intensity and slight shift to higher 2θ values of the (100) diffraction peak, while the addition of 0.5 wt% Pd by the same procedure does not have a noticeable effect on the mesostructure.

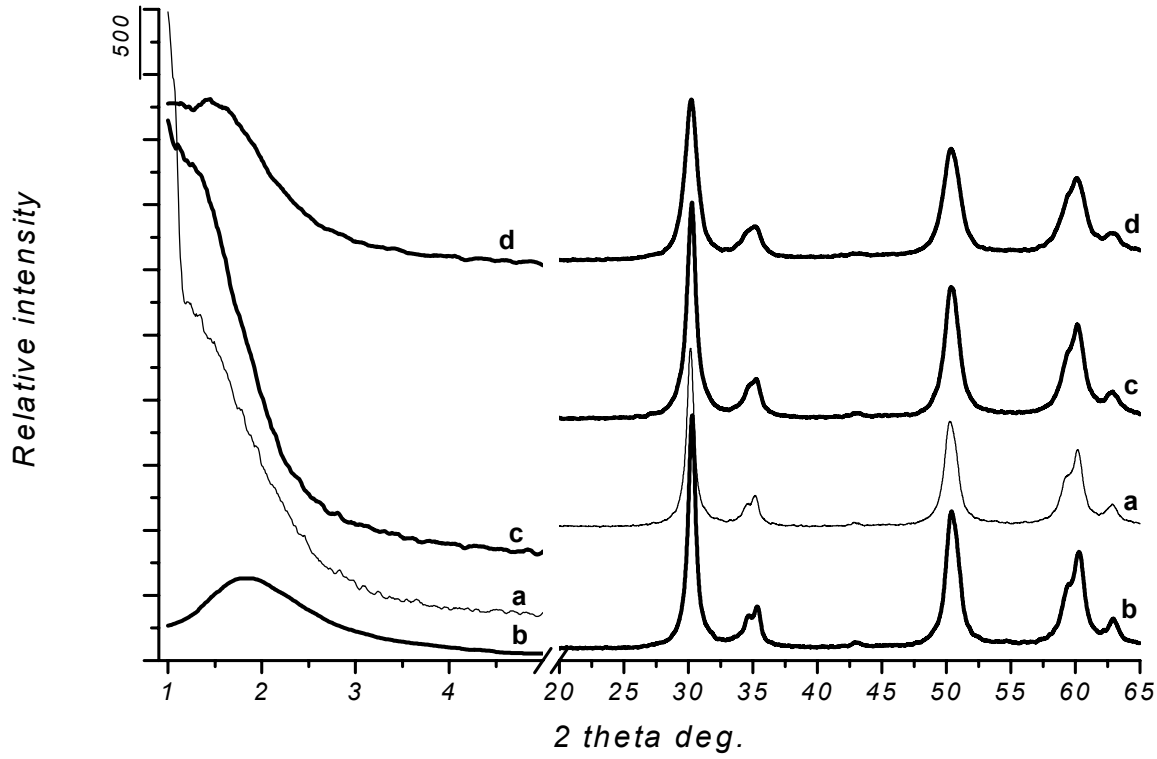

Figure 3.2.8. Powder XRD patterns of calcined at 550^0C Si-SZr (Zr/Si = 28) sample (a) impregnated with (b) 1 wt% Pd, (c) 0.5 wt% Pd and (d) 0.5 wt% Pd followed by impregnation with 1 wt% Co.

The Si-SZr samples impregnated sequentially with palladium and cobalt (Fig. 3.2.8, line d) show two partially overlapped, relatively intense diffraction lines at small 2θ angles confirming that long-range order and mesoporosity are preserved. It is worth to notice that the lines in the wide-angle region attributed to t-ZrO_2 become broader and lose their intensity after cobalt impregnation. The t-ZrO_2 crystallite sizes estimated from the diffraction line at 30.2^0 2θ by Scherrer's equation are shown in Table 3.2.1.

Table 3.2.1. Variation of the t-ZrO_2 crystallite sizes upon impregnation of Si-SZr (Zr/Si = 28) samples with Pd or Co.

Sample	t-ZrO_2 crystallite size, nm
Si-SZr	12.9
0.5 wt% Pd	10.5
1 wt% Pd	12.7
1 wt% Co-0.5 wt% Pd-Si-SZr	7.4

The deterioration of the original structure in siliceous mesoporous materials is mainly attributed to the hydrolysis of ≡Si-O-Si≡ bonds [200-201]. On the other hand, the structure and stability can be improved by the hydrothermal treatment due to enhancement of silica surface condensation at elevated temperatures [201-203]. The experimental results reported in Figures 3.2.6 through 3.2.8 show that the impregnation with cobalt improves the structure, while impregnation with palladium has opposite effect on the structure. Moreover, the impregnation of the Co(II)-containing Si-SZr materials with Pd(II) does not have a significant effect on the structural order. These experimental facts lead to a conclusion that the incorporation of cobalt increases the order of silica condensation, presumably, due to formation of ≡Si-O-Co-O-Si≡ or ≡Si-O-Co-O-Zr-/Zr-O-Co-O-Zr- linkages at the surface. This surface is more resistant to the hydrolysis and high temperature treatments. The Si-SZr framework with greater zirconium content shows high stability in the post-synthesis functionalization with inorganic salts, probably, due to thicker walls, the higher order of

condensation of the framework building species and resistance of the Zr-O-Zr bonds to the hydrolysis.

Overall, the Si-SZr and Co-, Pd-containing Si-SZr possess 3D wormhole framework with short-range order. Silica stabilizes amorphous zirconia phase at elevated temperatures. The formation of the tetragonal zirconia phase is induced by (i) the presence of sulfate ions, (ii) the impregnation of Co(II) and/or Pd(II), (iii) higher Co(II) loadings introduced by co-precipitation. The Si-SZr (Zr/Si = 3, 28) and Co-Si-SZr samples are stable upon aqueous impregnation and calcination processes.

3.3. SEM Images of Silica and Silica-Zirconia Oxides

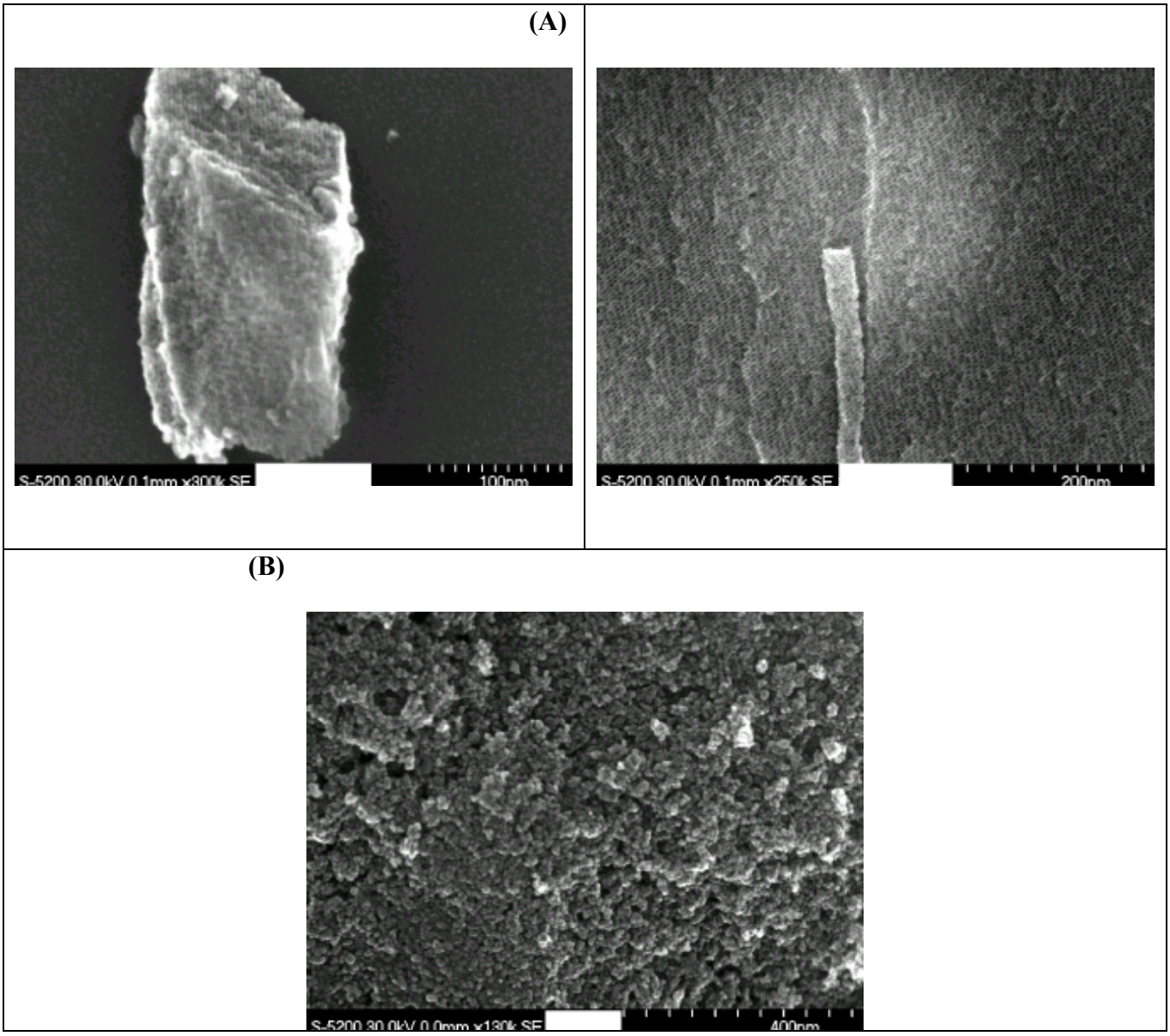

Figure 3.3.1. SEM images of (A) SiO_2 calcined at 700^0C with different magnification, (B) Si-Zr (Zr/Si = 2) calcined at 650^0C.

The scanning electron micrographs of the pure silica (Fig. 3.3.1, A) confirm the presence of regular mesopores arranged in a honeycomb pattern. The silica-zirconia mixed oxide consists of spherical particles, which are aggregated into rope-like macrostructures (Fig. 3.3.1, B). The SEM images reveal clear morphological differences among the samples. The

well-ordered structure of the single silica is changed to the less uniform structure in the mixed oxide.

3.4 TEM Investigation

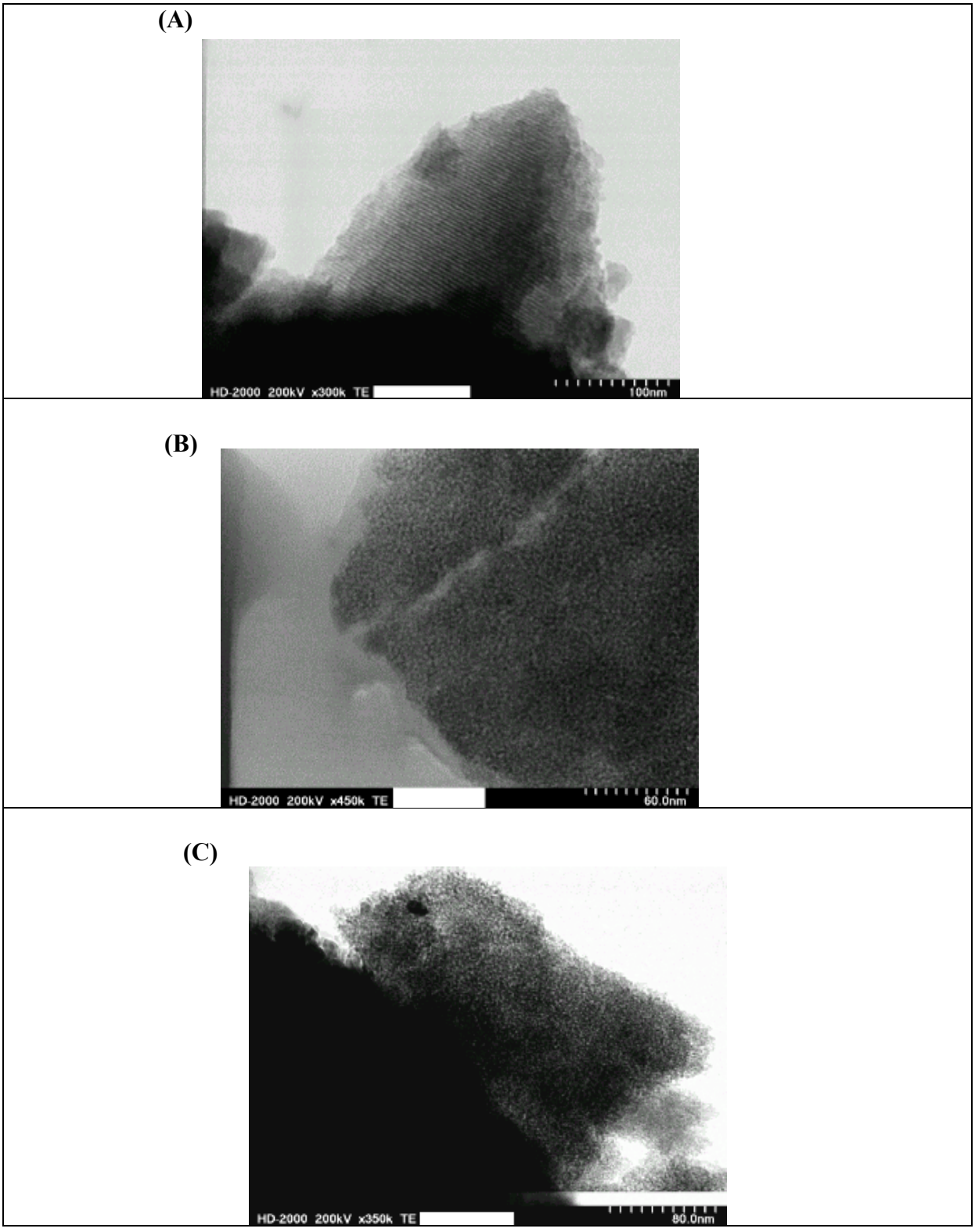

Figure 3.4.1. TEM images of (A) Co-SiO_2, (B) Co-Si-Zr (Zr/Si = 0.1), (C) Co- Si-Zr (Zr/Si = 2) samples calcined at 500^0C

The transmission electron microscopy (TEM) is used to elucidate the pore structure of the materials. The exact analysis of the pore sizes and thickness of the pore walls is, however, very difficult from the images presented in Figures 3.4.1 and 3.4.2. Figure 3.4.1 shows the effect of zirconia on the pore structure of cobalt-silica-zirconia (Co-Si-Zr) substrates. The cobalt containing silica (Fig. 3.4.1, A) features two-dimensional (2D) hexagonally arranged uniform pores. However, the TEM image of Co-Si-Zr with Zr/Si = 0.1 shows randomly oriented, shorter, interconnected channels comprising three-dimensional (3D) worm-like framework. The size of the ordered domains becomes even smaller (Fig. 3.4.1, C), when zirconia content is increased to 80 wt% (Zr/Si = 2), but 3D framework is preserved. Thus, addition of zirconia disrupts the order and leads to 3D framework of wormhole like pores.

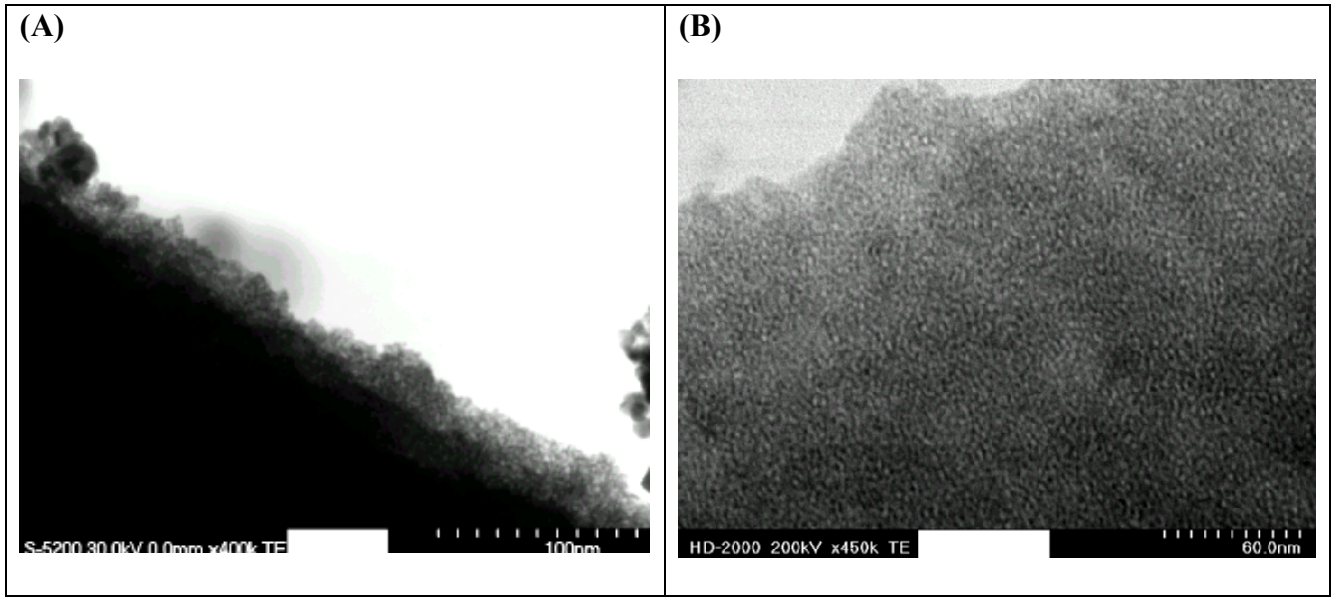

Figure 3.4.2. TEM images of (A) Si-Zr (Zr/Si = 2), (B) Co- Si-Zr (Zr/Si = 2) materials calcined at 650^0C

Figure 3.4.2 compares cobalt-free (section A) and cobalt containing (section B) Si-Zr (Zr/Si = 2) materials. The silica-zirconia support has a disordered 3D framework. Introduction of cobalt salt during the synthesis significantly improves the structure. Randomly oriented,

relatively long worm-like pores are clearly visible in the TEM micrograph. Several reasons can be proposed to explain this experimental result: (i) cobalt-containing template has higher resistance to drying and mild heat treatment, and, therefore, assists the condensation-polymerization of inorganic moieties in a longer time and at higher temperatures, (ii) cobalt ion prevents formation of micropores, which collapse at high temperatures and disrupt the order, (iii) during calcination cobalt ion may diffuse in bulk (silica, silica-zirconia) and becomes part of the matrix. The Co-Si-Zr framework is more resistant to heat treatment (compare Fig. 3.4.1, C and 3.4.2, B) than Si-Zr one.

From the TEM results it can be inferred that Si-Zr and Co-Si-Zr are mesostructured materials, which exhibit three-dimensional randomly packed worm-like channels and can be regarded as a type of HMS materials [20]. The pore structure is regular over the whole material.

3.5. Mesoporosity and Its Tuning

Physical gas adsorption is a prominent technique to study the pore characteristics of solid materials. The technique accurately determines the amount of gas adsorbed on a solid material, which is a direct measure for the pore properties and structure. The isotherm obtained from these adsorption measurements gives insight on the structure of the material and provides information on the specific surface area, pore volume and pore size distribution (PSD) [204-205]. The latter values are important in the area of catalysis, namely, large surface area is crucial for a solid catalyst since it determines accessibility of the active sites and is therefore usually related to catalytic activity, the pore architecture controls transport phenomena and governs selectivity in catalyzed reactions.

According to the IUPAC classification [206], the mesoporous materials show type IV adsorption-desorption isotherm, where a sharp increase in adsorption uptake at higher relative pressure ($p/p_0 \sim 4$) and hysteresis loop are the peculiar features. It is believed that the hysteresis loop arises from thermodynamic and network effects [207-208]. The thermodynamic effects are related to the delayed capillary condensation and/or evaporation that may take place at higher or lower pressures, respectively, in comparison to the pressure of coexistence of gas like and liquid like phases in the pores. The network or pore connectivity effects play an important role in desorption processes. It occurs when larger pores can only be emptied through the smaller pores or pore openings ("inkbottle" pores). In spite of all shortcomings and limitations present in the method, Brunauer-Emmet-Teller (BET) method [204, 206, 209] is currently used to evaluate specific surface area in mesoporous materials. The monolayer-multilayer adsorption data at relative pressure below 0.3 are used to determine monolayer capacity, which is multiplied by the cross-sectional area of the adsorbed molecule (0.162 nm^2 for N_2) to obtain the specific surface area [210]. Determination of pore volume

and PSD from gas adsorption data is based on the capillary condensation and evaporation. The total pore volume can be calculated from the amount of adsorbed gas at a relative pressure close to the saturation vapor pressure, whereas the relation between the capillary condensation or evaporation pressure and the pore size can be used to estimate PSD from either branch of the isotherm. Barret, Joyner and Hallenda (BJH) method [211], which is based on the Kelvin equation and assumes cylindrical pores, is widely used to estimate PSD in the mesoporous materials. The shape and position of the descending branch of isotherm provides potential information on the pore connectivity [208, 212-213]. It can be rationalized in the following way: the capillary evaporation pressure from a given pore depends on both the size of the pore and the pore accessibility to the surrounding gas phase. This accessibility is dependent on whether pores that connect the given pore with the surrounding gas have their cores filled or empty at the particular pressure, which, in turn, depends on the size and shape of the connecting pore.

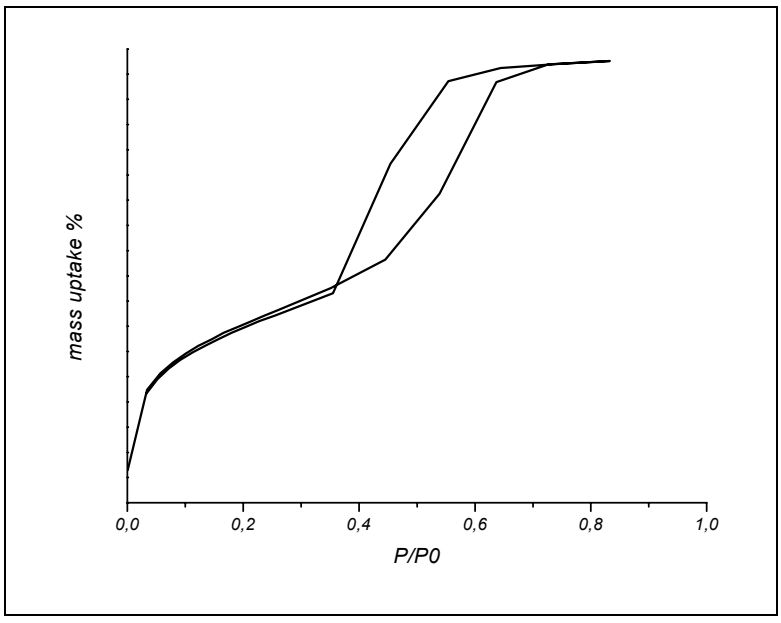

Fig. 3.5.1. Nitrogen adsorption-desorption isotherm for SiO_2 templated by P85 and calcined at 550^0C

The nitrogen adsorption-desorption isotherm of the pure mesoporous SiO_2 (Fig.3.5.1) templated by P85 is a superposition of a type IV and type I isotherms with H1 type hysteresis loop, which is confined to the relative pressure between 0.35 and 0.7. The ascending and descending boundary curves of the hysteresis loop are nearly parallel. It suggests that isotherm is governed by delayed condensation, i.e., pore filling and empting appear to occur in a narrow range of uniform near-cylindrical pores. A considerable adsorption at low relative pressure is associated with the microporosity, which arises from the ability of PEO moieties to intervene with the silica oligomers during synthesis [214-216]. The values of specific surface area of the analyzed samples are reported in the Table 3.5.1. The BET surface area gradually vanishes as the zirconium content in the material increases. The samples prepared with oligo(ethylene oxide) ($C_{12}EO_{10}$) surfactant have substantially higher surface areas than the materials templated by block co-polymer P85.

Table 3.5.1. The specific surface areas of the samples studied

Si, wt%	Zr, wt%	Surfactant	Co, wt%	Pd, wt%	SO_4^{2-}, wt%	S_{BET}, m^2/g
100	-	P85	-	-	-	505
100	-	$C_{12}EO_{10}$	6	-	-	925
90	10	$C_{12}EO_{10}$	6	-	-	573
70	30	$C_{12}EO_{10}$	6	-	-	443
40	60	P85	-	-	~8	208
20	80	P85	-	-	~8	234
10	90	P85	-	-	~8	145
2	98	P85	-	-	~8	99
-	100	P85	-	-	~8	37
2	98	P85	-	1	~8	49
2	98	P85	1	-	~8	61
2	98	P85	6	-	~8	47
2	98	P85	1	0.5	~8	68

The formation of denser framework with thicker walls in the latter case accounts for this difference. Addition of transition metal salts either in one-pot synthesis or by impregnation furnishes the surface of the pores and, consequently, decreases the surface area. Figures 3.5.2 through 3.5.4 compare the obtained isotherms. Addition of cobalt salt to pristine silica in one-step synthesis leads to a reversible isotherm with prominent absorption at low relative pressure between 0.1 and 0.3 (Figure 3.5.2, a). Although the adsorption-desorption hysteresis is a characteristic feature of the mesoporous materials, the reversible isotherms were reported for MCM-41 [14-16] with cylindrical pores of around 4 nm. A distinct increase in adsorbate amount at low p/p_0 values is associated with substantial adsorption in the micropores. In mixed silica-zirconia (Si-Zr) oxides incorporation of the non-siliceous component causes the change in the shape of isotherm to reversible and then to type IV isotherm with a triangular hysteresis loop.

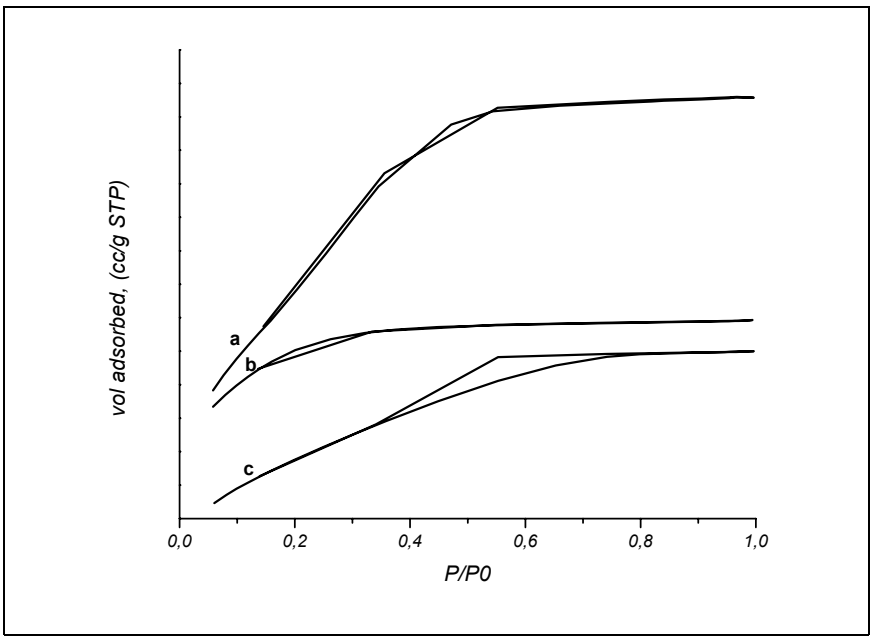

Fig. 3.5.2. N_2 sorption isotherms of calcined mesoporous siliceous mixed oxides synthesized in the presence of $C_{12}EO_{10}$ surfactant and 6wt% cobalt: a) SiO_2, b) 90 wt% SiO_2/10 wt% ZrO_2, c) 70 wt%SiO_2/30 wt% ZrO_2.

The triangular shape of the adsorption-desorption hysteresis indicates that the capillary evaporation (at relative pressure of 0.45 – 0.5) was significantly delayed with respect to the capillary condensation [220-221]. This type of hysteresis loop has been reported for either the so-called cage-like mesopores, where the pore entrance is much narrower than the pore interiors or to the channel-like pores with constrictions. A similar trend is observed in the case of silica-sulfated zirconia (Si-SZr) materials with an increase in zirconia loading, Figure 3.5.3. The isotherms **a** and **b** in Fig. 3.5.3 display monotonic shape without any characteristic changes. According to IUPAC [206] these isotherms would be classified as type I and associated with the microporous materials. In the light of concept of mesoporosity, the type I isotherms that do not level off below the relative pressure 0.1 correspond to materials with pore sizes close to the micropore range [208], which are called supermicroporous materials, or to the samples which exhibit a considerable amount of mesoporosity together with microporosity.

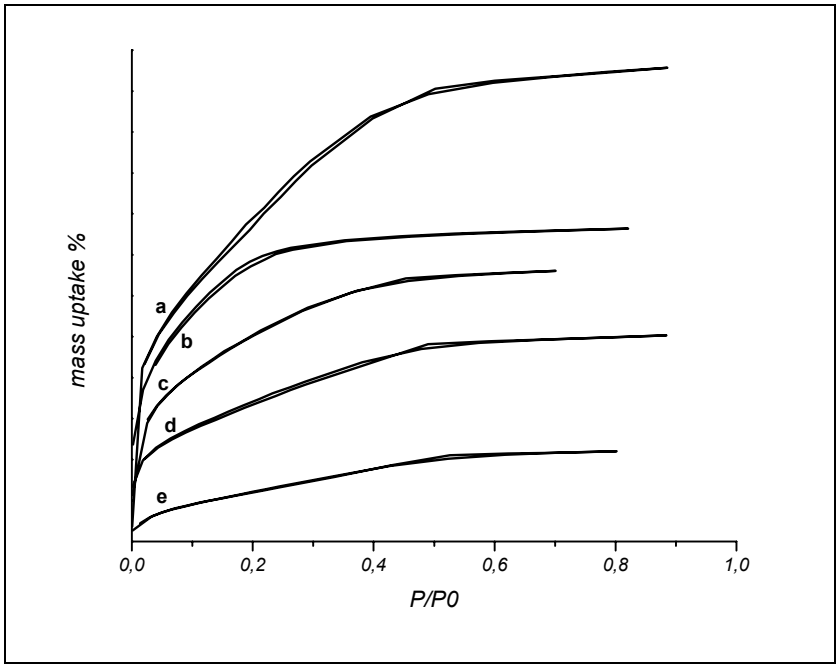

Fig. 3.5.3. N_2 sorption isotherms of calcined silica-sulfated zirconia samples with different zirconia content wt% (a) 80, (b) 60, (c) 90, (d) 98, (e) 100 templated by P85.

The supermicroporous materials possess pore sizes ≥ 2 nm, narrow pore size distribution and ordered structures [222]. On the bases of the N_2 adsorpion-desorption data presented in Figure 3.5.3, it can be inferred that as the amount of zirconium in the framework increases, there is a tendency to the following changes: (i) the adsorption at low p/p_0 decreases, which is directly related to the decrease in the degree of microporosity; (ii) the triangular hysteresis loop with the desorption brunch much steeper than the adsorption one evolves, indicating the presence of non-uniform pores (iii) the decrease in textural parameters (Table 3.5.1). The change in the pore shape could be rationalized by the appearance of ZrO_2 crystallites, which modify the pore walls and semi block the pores.

Figure 3.5.4 shows the N_2 sorption isotherms illustrating the effect of transition metal ions on the structure of the Si-SZr (Zr/Si = 28) support.

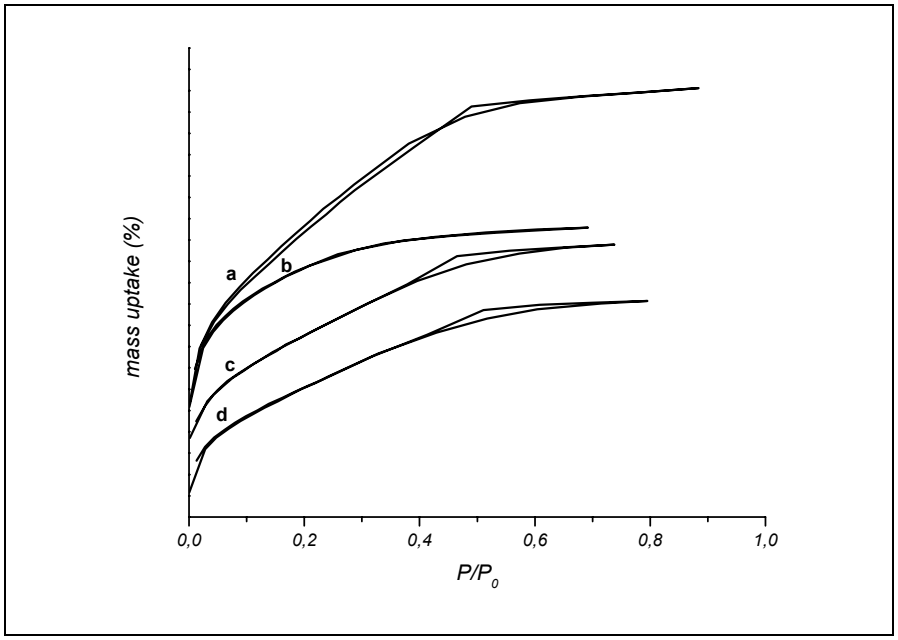

Fig. 3.5.4. N_2 sorption isotherms of calcined transition metal functionalized Si-SZr (Zr/Si = 28) materials: (a) transition metal free, (b) 1 wt% $Pd_{(impr)}$, (c) 1 wt% $Co_{(co\text{-}prec)}$, (d) 6 wt% $Co_{(co\text{-}prec)}$

The impregnation of palladium does not affect the shape of the isotherm (Fig. 3.5.4, c), but leads to lower surface area. Cobalt(II) introduced by co-precipitation causes flattening of the isotherm branches at low relative pressure, i.e. the amount of micropores decreases, and formation of the pronounced triangular shaped hysteresis loop. The isotherms **c** and **d** in Fig. 3.5.4 can be tentatively classified as type IV isotherms with type H4 adsorption-desorption hysteresis. Increase in cobalt ion concentration (1 – 6 wt%) leads to decrease in the surface area, therefore, it is expected that most of the cobalt ions are on the surface of the pores rather than in the bulk. From the data presented above, it is noteworthy to notice that increase in the concentration of both Zr(IV) and Co(II) leads to decrease in the microporosity and modification of the pore shape. It might be suggested that the degree of mixing of the PEO units with inorganic moieties, which according to the literature data is the cause of microporosity, decreases. It may also support the idea that cobalt ions are solubilized in the hydrophilic head groups and prevents their penetration into the forming framework.

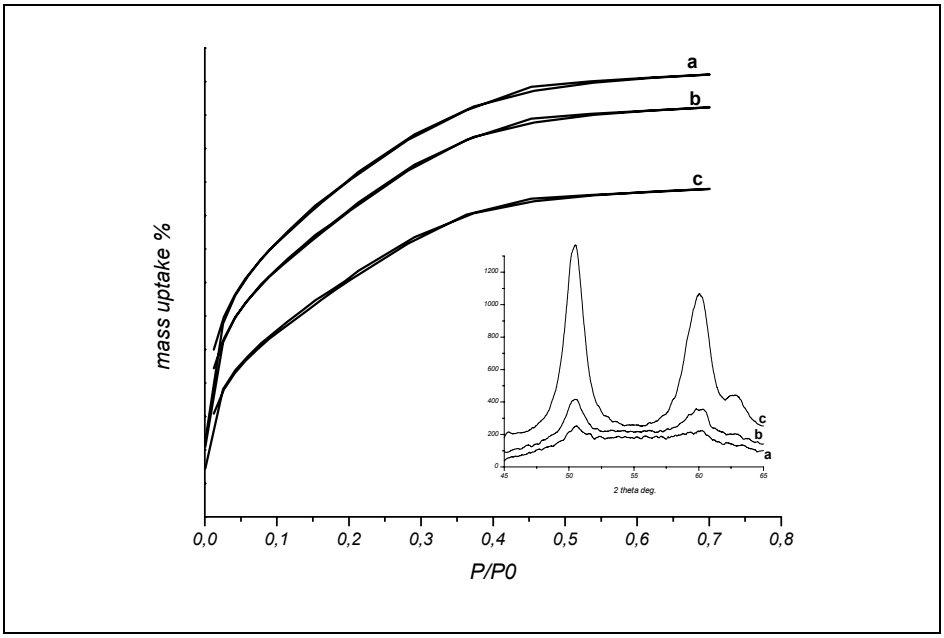

Fig. 3.5.5. N_2 sorption isotherms of Si-SZr (Zr/Si = 4) sample heated stepwise at a) 550^0C, b) 600^0C, c) 650^0C dwelling at each temperature for 3 hrs. Inset shows corresponding powder XRD patterns.

Thermal treatment of the silica-sulfated zirconia samples with Zr/Si mole ratio equal to 4 between 550 and 650^{0}C leads to formation of tetragonal zirconia phase (Fig. 3.5.5, inset) and concomitant decrease in the surface area from 145 m^2/g at 550^{0}C to 127 m^2/g at 600^{0}C to 97 m^2/g at 650^{0}C, while the nitrogen sorption data exhibit superimposed type I and type IV isotherms.

3.6. Coordination Environment of Cobalt and Palladium in Si-SZr Materials: DR UV-Vis Spectroscopic Study

The UV-Visible-NIR absorption spectroscopy is a valuable tool to study the oxidation state and location of cobalt and palladium centers.

The samples dried in air are pink and display characteristic UV-Vis-NIR absorption spectrum (Fig. 3.6.1, curve a) due to Co^{2+} species coordinated octahedrally as either $[Co(H_2O)_6]^{2+}$ or $[Co(H_2O)_5(OH)]^{+}$ [119, 223]. The diffuse reflectance spectrum of the Si-SZr sample exposed to air after calcination at 550^0C (Fig. 3.6.1, curve b) exhibits a broad poorly resolved peak with a maximum at about 550 nm. The broadening is probably due to the presence of octahedrally coordinated Co^{2+} in different environments.

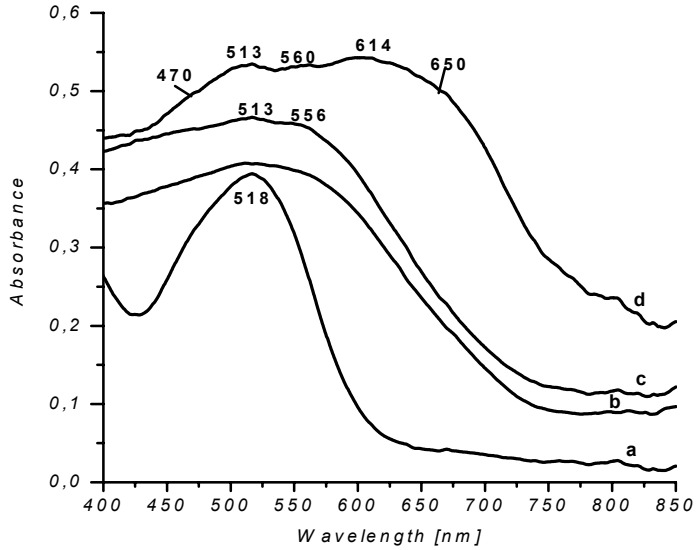

Figure 3.6.1. DR UV-Vis absorption spectra of 1 wt% Co-SZr (a) dried at ambient conditions, (b) calcined at 550^0C, and calcined at 550^0C (c) 1 wt% Co-Si-SZr (Zr/Si = 28), (d) 6 wt% Co-Si-SZr (Zr/Si = 28).

Addition of silica does not change the spectrum significantly. Unlike other spectra shown in Fig. 3.6.1, the spectrum corresponding to 6 wt% Co-Si-SZr (Zr/Si = 28) sample consists of a broad absorption, which can be deconvoluted into five peaks at 470 513, 560, 614 and 650 nm. The peaks at 560, 614 and 650 nm are representative of Co^{2+} ion in a tetrahedral environment [223, 224-225]. The peaks at 470 and 513 nm indicate the presence of the octahedrally coordinated Co^{2+} ions, which is supported by the pale pink color of the sample. It was reported in the literature that exposure of the calcined Co-ZSM samples to air leads to the hydration of the surface tetrahedral cobalt sites and formation of the pseudo octahedral sites as evidenced by a band observed at 520 nm [226]. Figure 3.6.2 shows the diffuse reflectance (DR) spectra of calcined Co-containing Si-SZr (Zr/Si = 3) samples with different cobalt loadings, indicating the presence of octahedral (high energy) and tetrahedral (low energy) Co(II) sites.

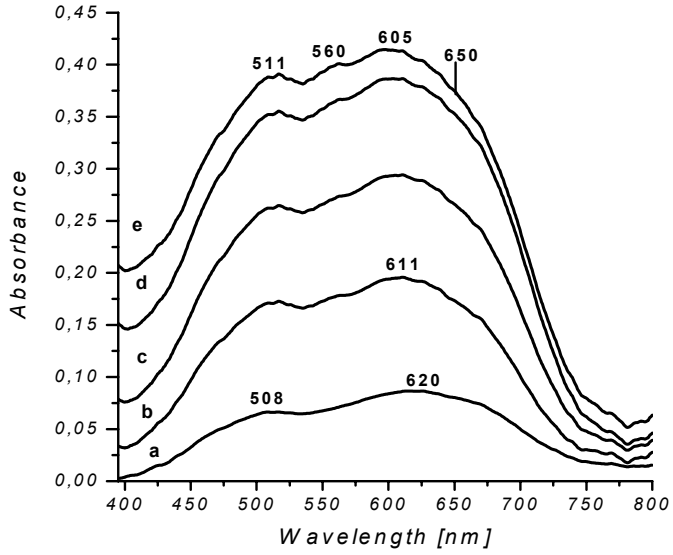

Figure 3.6.2. UV-Visible diffuse reflectance spectra of the calcined at 550^0C X wt% Co-Si-SZr (Zr/Si = 3) samples, where X = 1 wt%, cobalt is impregnated (a), 1 wt % (b) 2 wt % (c), 4 wt % (d), 6 wt % (e) cobalt is introduced during the synthesis.

The bands at 560 nm (green region), 605 nm (yellow-orange region) and 650 nm (shoulder) (red region) are ascribed to the $^4A_2(F) \rightarrow {}^4T_1$ (P) transitions of high spin Co^{2+} in tetrahedral environments and give rise to the blue color. As the amount of cobalt ion increases, all the bands simultaneously rise in intensity (curves b through e) indicating that the coordination of cobalt ions in the concentration range between 1 and 6 wt% introduced during the synthesis does not change.

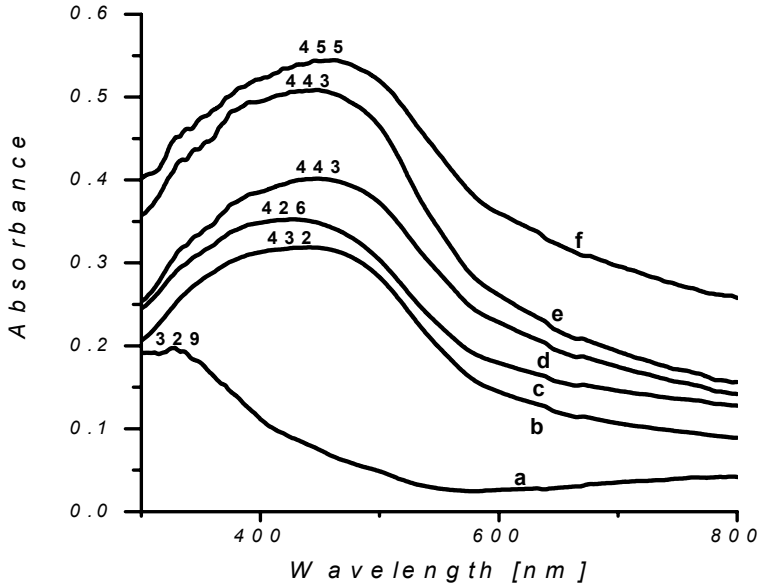

Figure 3.6.3. DR UV-Vis absorption spectra of (a) Si-SZr (Zr/Si = 28), (b) 0.25 wt% Pd-Si-SZr (Zr/Si = 28), (c) 0.5 wt% Pd-Si-SZr (Zr/Si = 28), (d) 0.5 wt% Pd-Si-SZr (Zr/Si = 2), (e) 1 wt% Pd-Si-SZr (Zr/Si = 28), (f) 1 wt% Pd-Si-SZr (Zr/Si = 3). All samples were calcined at 550^0C.

The DR UV-Vis spectra obtained from the palladium containing Si-SZr with different Zr/Si mole ratios and various palladium concentrations are compared in Fig. 3.6.3. The maximum absorption in the visible region at 426 - 455 nm corresponds to a d-d transition of isolated Pd^{2+} ions linked to surface oxygen atoms of the support or to small $(PdO)_x^{2+}$ moieties [227]. Similar bands at 460 - 480 and 450 nm due to the d-d transition of the isolated Pd^{2+} ions or $(PdO)_x^{2+}$ entities were observed on Pd-zeolites [228-229] and Pd-tungstated zirconia

[230], respectively. Increase in the palladium content leads to the increase in intensity of the band at 426 - 443 nm (Fig. 3.6.3, curves b, c and e), while the position of the band does not change significantly. It is interesting to notice that the absorption maximum slightly shifts to higher wavelength as the amount of silica in the support increases (compare curves c and d, and curves e and f) indicating the presence of smaller $(PdO)_x^{2+}$ aggregates on silica reach samples i.e., better dispersion.

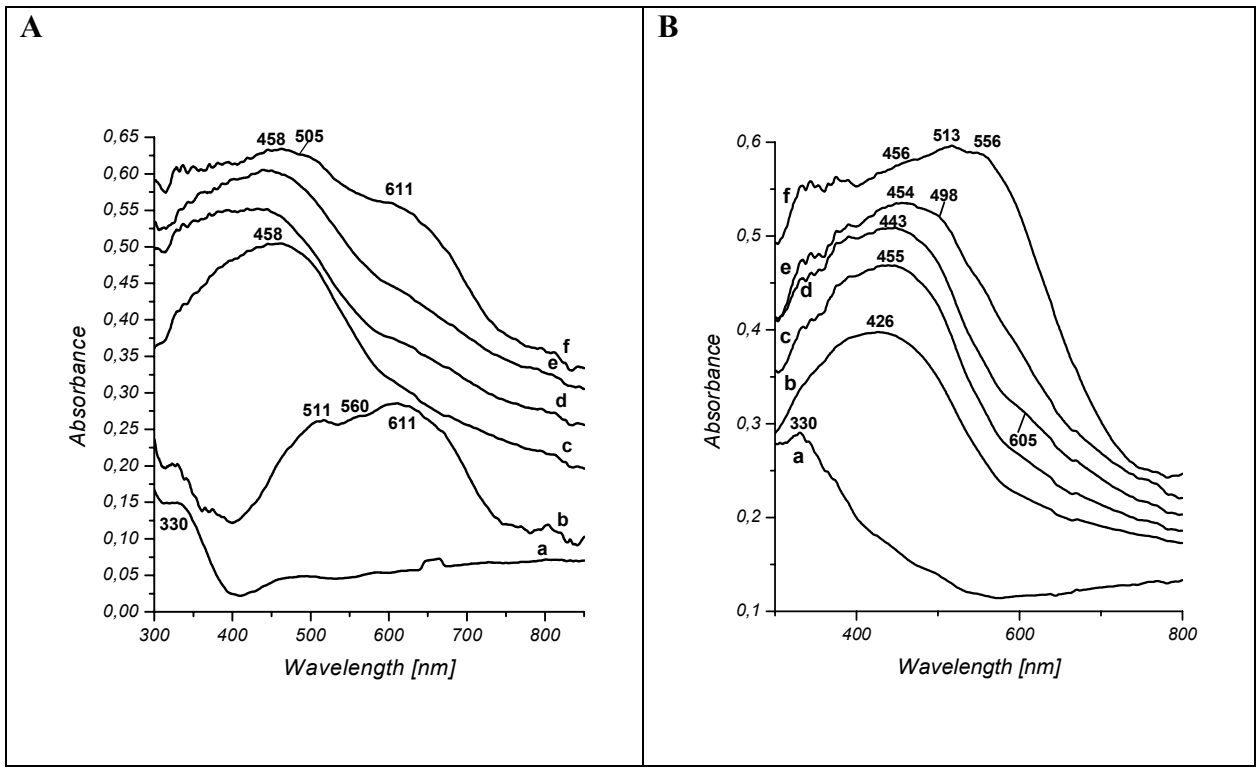

Figure 3.6.4. DR UV-Vis absorption spectra of calcined at 550^0C **(A)** (a) Si-SZr (Zr/Si = 3), (b) 1 wt% Co-Si-SZr (Zr/Si = 3) cobalt is co-precipitated, (c) 1 wt% Pd-Si-SZr (Zr/Si = 3), and X wt% Co-1 wt% Pd-Si-SZr (Zr/Si = 3), where X = 1 wt% cobalt is impregnated (d), 1 wt% cobalt is co-precipitated (e), 6 wt% cobalt is co-precipitated. **(B)** (a) Si-SZr (Zr/Si = 28), (b) 0.5 wt% Pd-Si-SZr (Zr/Si = 28), (c) 0.25 wt% Co-0.5 wt% Pd-Si-SZr (Zr/Si = 28) cobalt is impregnated, (d) 1 wt% Co-0.5 wt% Pd-Si-SZr (Zr/Si = 28) cobalt is impregnated, (e) 1 wt% Co-0.5 wt% Pd-Si-SZr (Zr/Si = 28) cobalt is co-precipitated, (f) 1 wt% Co-Si-SZr (Zr/Si = 28) cobalt is co-precipitated.

All the palladium-containing samples are brownish in color. It suggests the formation of the $(PdO)_x^{2+}$ entities, since the isolated Pd^{2+} ions observed in zeolite matrix are pink colored [229].

Figure 3.6.4 shows the DR UV-Vis spectra of the Pd-Co-Si-SZr samples, where Zr/Si = 3 (Fig. 3.6.4, A) and 28 (Fig. 3.6.4, B). All the detected bands are broad with maxima close to those observed in the corresponding Pd-Si-SZr DR UV-Vis-NIR absorption spectra (Fig. 3.6.3). The growing band at 611 nm (Fig. 3.6.4, A) indicates the presence of tetrahedrally coordinated Co^{2+} ions, the other two bands of the tetrahedral cobalt at 511 and 560 nm are superimposed to the band at 458 nm. A similar broadening of the band at 443 nm and protruding of the shoulder at about 605 nm associated with increase in cobalt content is observed from the Pd-Si-SZr (Zr/Si = 28) samples (Fig. 3.6.4, B).

In summary, since intensities of the detected bands due to octahedral Co^{2+} and tetrahedral Co^{2+} are comparable, it is concluded that cobalt ions are predominantly in octahedral coordination in the Si-SZr (Zr/Si = 3) support. It is well known fact that the absorption intensities of the tetrahedral species are almost 10 times more intense than that of the octahedral species [231]. In the case of the support with composition Zr/Si = 28, the majority of the Co^{2+} ions are in octahedral position, however, tetrahedrally coordinated cobalt is detected at high cobalt loadings. On the bases of these experimental results it can be inferred that cobalt in the tetrahedral environment is stabilized in the silica rich samples, whereas the octahedral Co(II) sites furnish the zirconia enriched surface. Palladium is stabilized on the surface of Si-SZr and Co-Si-SZr in the form of isolated Pd^{2+} ions and/or small $(PdO)_x^{2+}$ aggregates.

3.7. FT-IR Spectra of the Activated Samples

Figure 3.7.1 shows the FT-IR spectra of the activated samples. The unmodified Si-SZr supports display two-band spectra with maxima at 1380-1370 cm^{-1} and shoulder at about 1322 cm^{-1} typical of the ν(S=O) vibration of highly covalent multibridged sulfates coordinated preferentially to Zr^{4+} sites [232] (Fig. 3.7.1, B - C, spectra a). The weak broad adsorption at ~1605 cm^{-1} is attributed to residual water. Residual carbonate species give rise to the strong band at 1523 cm^{-1} on Co-SZr (Fig. 3.7.1, A) and according to the literature are stable on zirconia surface [233-234]. The presence of silica prevents the formation of surface carbonates as is evidenced from the negligible intensity of the band at 1605 cm^{-1} and absence of the band at 1523 cm^{-1}. Impregnation of palladium ions has no significant effect on the sulfate groups (Fig. 3.1.1, B - C, curve b). It indicates that sulfate species are not the anchoring sites for the palladium ions. The variation of the intensities of the sulfate related bands of the cobalt-containing samples relative to those of the pure supports indicates the coordination of the cobalt ion to the sulfate groups.

Impregnation of the 0.7 wt% cobalt on Si-SZr (Zr/Si = 3) causes a slight shift and drastic decrease in the intensity of the ν (S=O) vibration, whereas the addition of 1 wt% cobalt during the co-precipitation leaves the sulfate bands practically intact (Fig. 3.1.1, B, curves c and d, respectively). Increasing the cobalt loading up to 6 wt% by co-precipitation method causes similar changes in the spectra of sulfate groups as has been observed after cobalt impregnation. These experimental data correlate with the results detected on the Co-Si-SZr (Zr/Si = 28) samples (Fig. 3.1.1, C curves d-e). Sequential impregnation of palladium ion onto cobalt-containing samples, where the cobalt salt has been introduced during the synthesis, also causes decrease in the intensities of the sulfate bands.

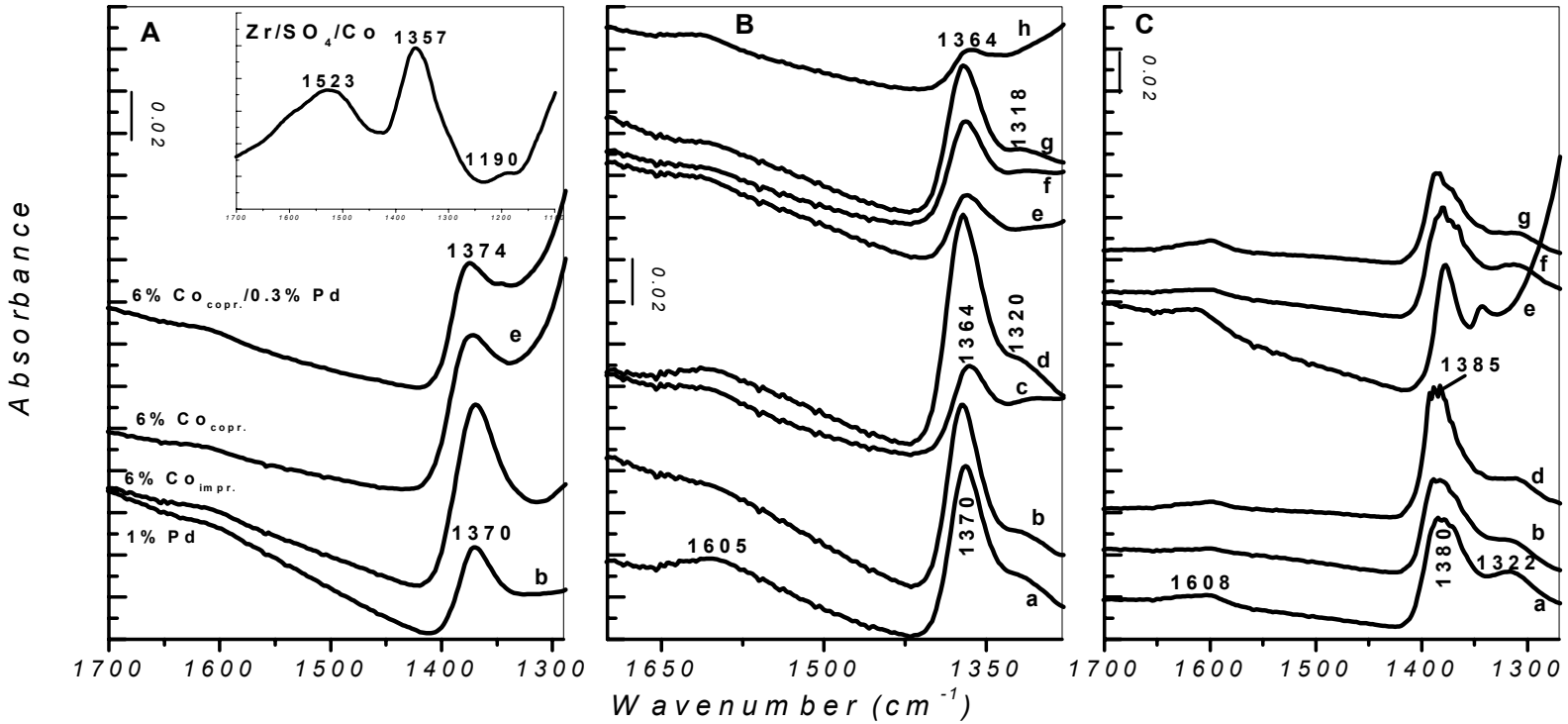

Figure 3.7.1. FT-IR spectra of activated Si-SZr supports (a) with Zr/Si mole ratio equal to (A) 2, (B) 3, (C) 28 and modified supports after (b) impregnation of 1 wt% Pd, (c) impregnation of 0.7 wt% Co, (d) co-precipitation with 1wt% Co, (e) coprecipitation with 6 wt% Co, (B) impregnation of 1 wt% Pd onto (f) sample c, (g) sample d, (h) sample e, (C) impregnation of 0.5 wt% Pd onto (f) sample impregnated with 1 wt% Co, (g) sample d. The spectra are taken at ambient temperature.

This experimental fact suggests that redistribution of the surface cobalt ions takes place upon impregnation followed by calcination.

Kantcheva et al. [235] observed a similar decrease in the intensity of the ν (S=O) band on the Co-SZr to be accompanied by the appearance of the absorption at 1163 cm^{-1} due to more ionic sulfates [236] attached to cobalt(II). The band at 1190 cm^{-1} detected on the Co-SZr (Fig. 3.1.1, A inset) can be assigned to sulfate compounds with high ionic character. On the Co-Si-SZr samples, however, this band cannot be observed because of a strong absorption of the support.

Addition of cobalt ion to Si-SZr causes transformation of the covalent sulfates to more ionic sulfate species, complexed with cobalt ions. Incorporation of cobalt by the post-synthesis technique results in the deposition of cobalt ions mainly on the surface of the support, whereas the one-pot coprecipitation method leads to functionalization of both the surface and the framework. The intensity of the ν(S=O) band is affected depending on (i) the amount of ZrO_2, (ii) the method of introduction of M^{2+} ion, impregnation or co-precipitation (see Fig. 3.7.1, B spectra c, d), (iii) the amount of M^{2+} present.

3.8. Adsorption of 2,6-Dimethyl Pyridine onto Functionalized Si-SZr (Zr/Si = 3)

2,6-Dimethyl pyridine (2, 6-DMP, lutidine) is used as a probe molecule to test the acidic properties of oxides, especially, Brønsted acidity. It is because, in comparison with pyridine, lutidine has two substituent groups, which hinder the chemisorption of the molecule on the Lewis acid sites [237-238]. Schema 3.8.1 [239] shows the spectral positions of ring

stretching modes, 8A, 8B and 19A, 19B and δ (CH_3) deformation modes of free and adsorbed 2,6-DMP.

Schema 3.8.1. Spectral location of mid-IR vibrational modes of free and adsorbed 2,6-DMP [239]

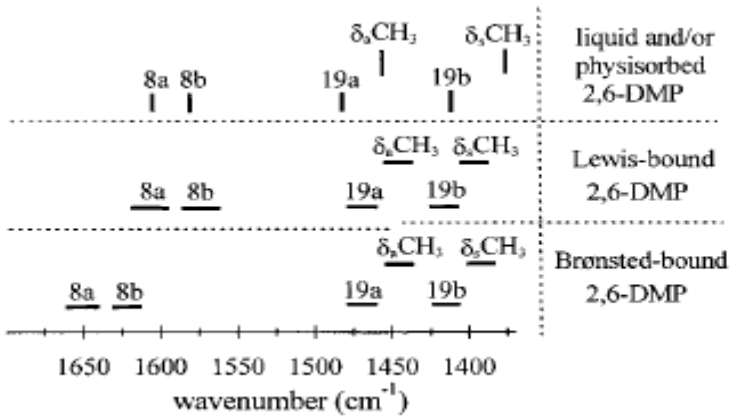

Figure 3.8.1, A displays a series of FT-IR spectra in the analytical range between 1700 and 1400 cm^{-1} obtained after evacuation at 150^0C. 2,6-DMP adsorbs on the Brønsted acid sites as lutidinium ion (2,6-$DMPH^+$) [232] giving rise to the doublet with maxima at 1630 and 1640 cm^{-1} ascribed to 8A and 8B vibrational modes, respectively, (Fig.3.8.1, A, a). The weak absorption at lower frequency, 1580 cm^{-1} due to 8B mode signifies the presence of the Lewis acid sites. These sites originate from the Zr (IV) cationic centers. Impregnation of palladium brings about little increase in the Lewis acidity. The band at 1580 cm^{-1} becomes more pronounced and intense as the concentration of cobalt increases (Fig. 3.8.1, A, spectra b through d and f through h). The sample with 6 wt% cobalt possesses the strongest Lewis acid sites, which are evidenced from the appearance of the 8A band at 1614 cm^{-1} [240-241]. This band is partially overlapped with the band due to protonated 2,6-DMP species. The intensities of the bands at 1630 and 1640 cm^{-1} are observed to decrease on Si-SZr (Zr/Si = 3) after impregnation with 0.7 wt% cobalt (Fig. 3.8.1, A, spectrum b), incorporation of 6 wt% cobalt (Fig. 3.8.1, A, spectrum d) and impregnation of palladium onto cobalt-containing samples

(spectra f through h). The decrease in the intensity correlates with concentration of strongly covalent sulfate groups coordinated to Zr^{4+} sites (Fig. 3.8.1, B).

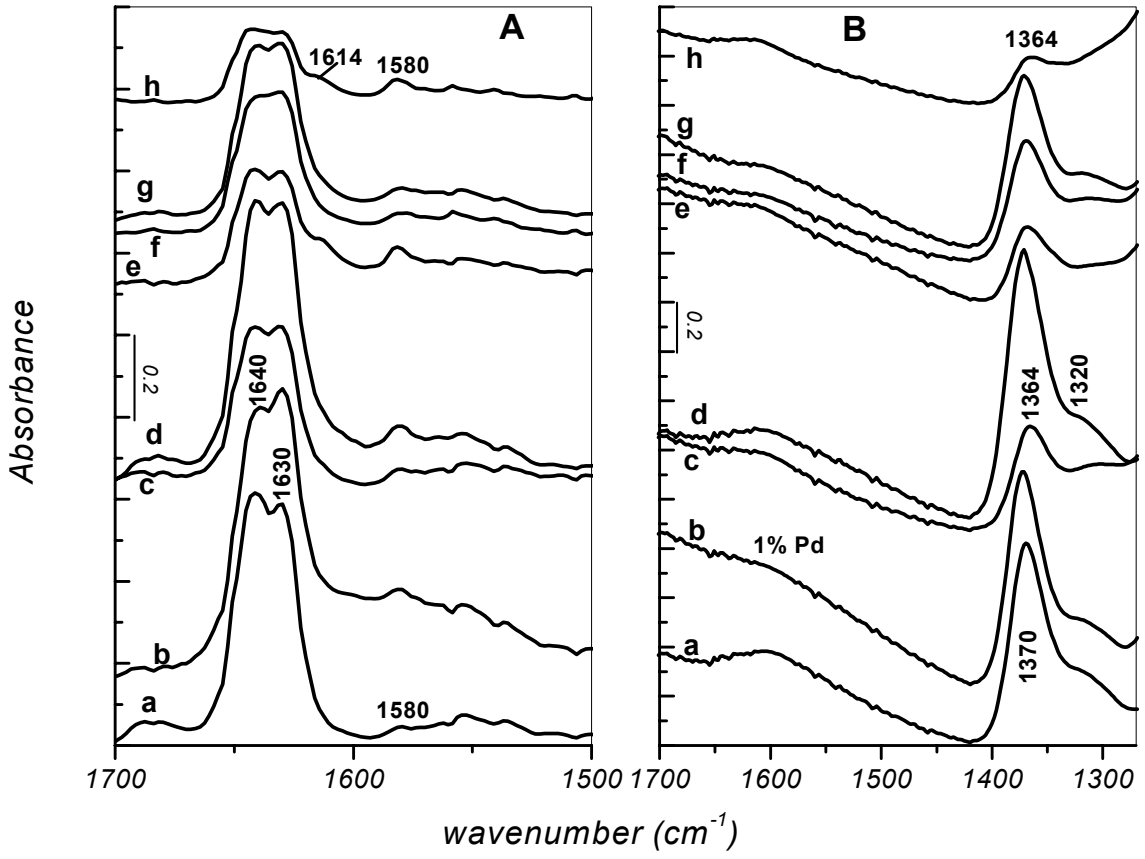

Figure 3.8.1. FT-IR spectra at 150^0C in dynamic vacuum (A) in the analytical range of the 8a, 8b modes (1700-1500 cm^{-1}) of 2, 6 DMP adsorbed onto Si-SZr (Zr/Si = 3) (a), after (b) impregnation with 1 wt% Pd, (c) impregnation with 0.7 wt% Co, (d) co-precipitation with 1 wt% Co, (e) co-precipitation with 6 wt% Co, 1 wt% Pd impregnated onto (f) sample c, (g) sample h. The spectrum of activated sample is used as reference. (B) Activated Si-SZr (Zr/Si = 3) support (a) modified with (b) 1 wt% Pd, (c) 0.7 wt% Co, (d) 1 wt% Co, (e) 6 wt% Co, (f) 0.7 wt% Co and 1 wt% Pd, (g) 1 wt% Co and 1 wt% Pd, (h) 6 wt% Co and 1 wt% Pd. The spectra are taken at ambient temperature.

This experimental result is in agreement with the literature [242-243], where it was reported on the bases of adsorption of strong bases, pyridine and ammonia that surface sulfates generate Brønsted (protonic) acidity. It is also known that sulfation of the oxide surfaces modifies their intrinsic Lewis acidic properties [244]. The overall Lewis acidity is expected to decrease, since the sulfate groups screen part of the coordinatively unsaturated surface cations, and the residual Lewis acidity has sometimes been observed to increase in strength due to inductive effect from the charge-withdrawing sulfate groups. The 2, 6-$DMPH^+$ ions are stable on the surface of single and modified Si-SZr even at 450^0C.

The Si-SZr samples possess strong Brønsted acidity, which is associated with sulfate groups and weak Lewis acidity, which originates from the coordinatively unsaturated Zr^{4+} cations. In-situ incorporation of cobalt enhances Lewis acidity. The 6 wt% Co-Si-SZr shows the strongest Lewis acidity.

3.9. Adsorption of NO

During adsorption of 8 Torr NO, a broad band positioned at 1931 cm^{-1} develops immediately in the IR spectrum of the Si-SZr samples (Fig, 3.9.1, A) and is most probably due to a superposition of several support-NO_x complexes such as Zr(IV)-NO, which have sulfate ions in their closest coordination sphere i.e., ($Zr^{4+}(SO_4^{2-})$-NO) [245] and/or (NO)-Zr^{4+}-(NO_3^-) [246-247] species. The adsorption of NO (10 Torr) on cobalt containing silica (Fig. 3.9.1, B, spectrum a, 1) gives rise to a pair of bands with maxima at 1884 and 1801 cm^{-1} typical of cobalt (II)-nitrosyls [248-250]. The band at 1884 cm^{-1} has asymmetric shape and contains a component at about 1900 cm^{-1}. The latter band is removed by room temperature (RT) evacuation and can be attributed to cobalt (II) nitrosyls. The bands at 1882 and 1801

cm^{-1} resist evacuation and are ascribed to ν_s (symmetric, lower in intensity) and ν_{as} (asymmetric, higher in intensity) stretching modes of Co(II)-$(NO)_2$ complexes, respectively [248, 251].

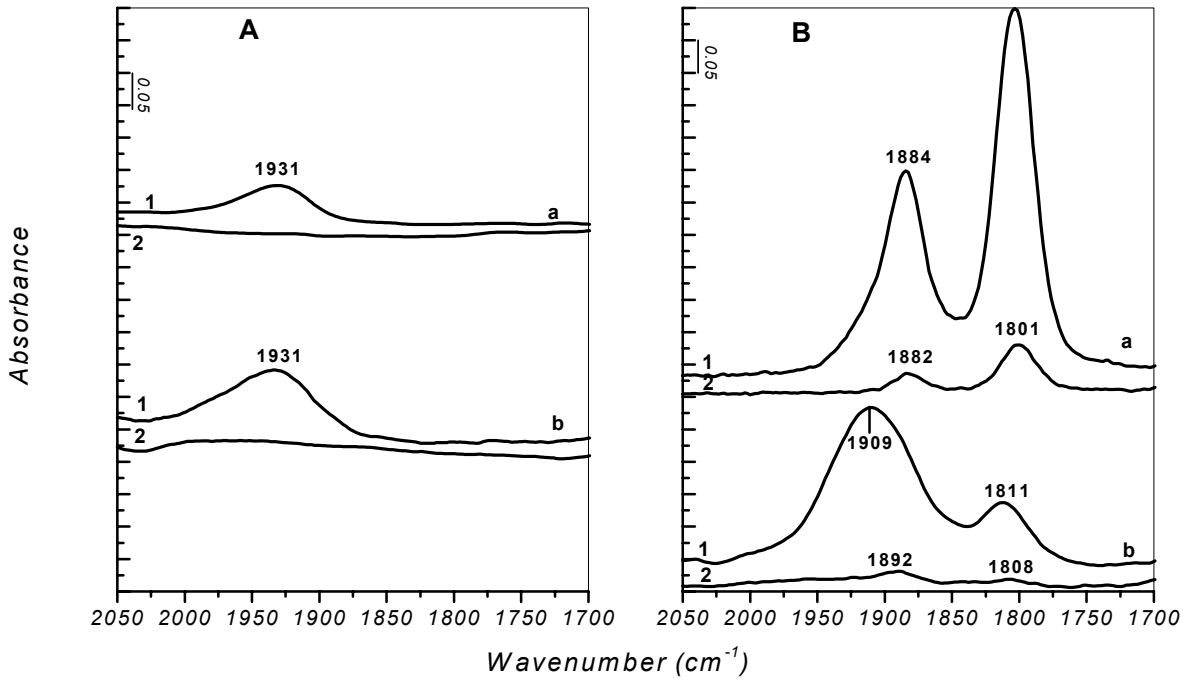

Figure 3.9.1. FT-IR spectra of (A) Si-SZr (a) Zr/Si = 3, (b) Zr/Si = 28 after adsorption of 8 Torr NO (1) and room temperature evacuation (2); (B) Co-SiO_2 (a) after adsorption of 10 Torr NO (1) and subsequent evacuation at RT (2), Co-SZr (b) in the atmosphere of 8 Torr NO (1) followed by room RT (2). The spectrum of the activated sample is used as a reference.

Exposure of the cobalt-SZr sample to NO (8 Torr) leads to a two-band spectrum with maxima at 1909 and 1811 cm^{-1} (Fig. 3.9.1, B, spectrum b, 1). The band shape at 1909 cm^{-1} resembles that, observed from the cobalt free Si-SZr sample and consists of overlapped bands of Zr(IV)-NO_x and Co(II)-nitrosyl species. Evacuation results in the disappearance of the band at 1909 cm^{-1} and two weak bands at 1892 and 1808 cm^{-1} are detected that are assigned to Co(II)-$(NO)_2$. The behavior of the former band is similar to that observed earlier for support-

NO_x compounds, however, Pietrogiaconi and co-workers [248] have attributed this band to Co(II)-mononitrosyl.

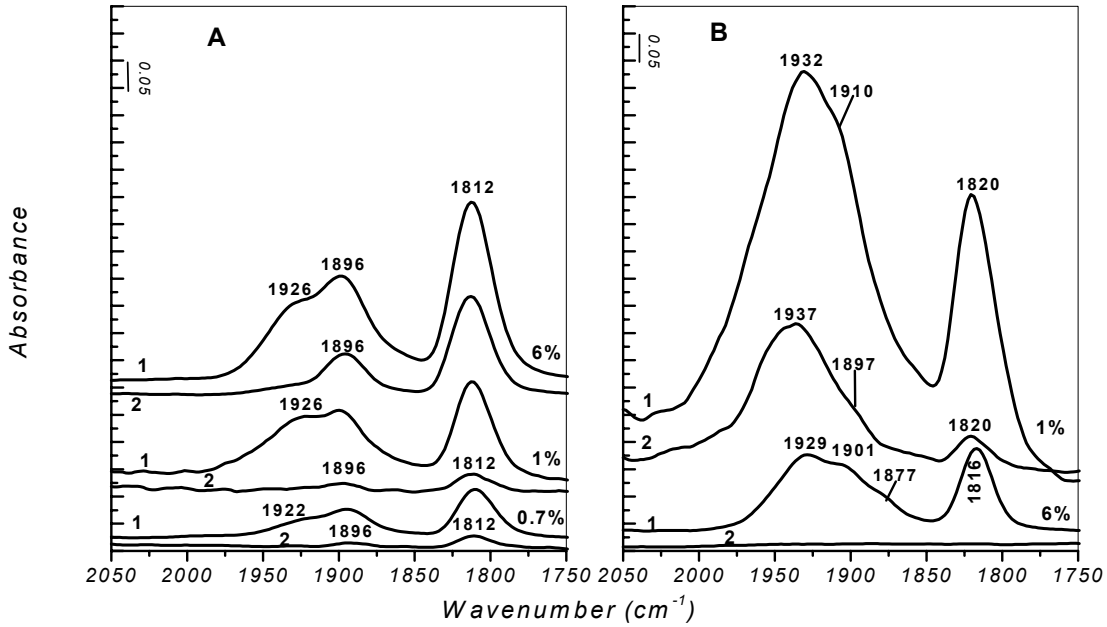

Figure 3.9.2. FT-IR spectra of (1) adsorbed NO (8 Torr) and (2) after room temperature evacuation on the X wt% Co-Si-SZr samples with Zr/Si = 3 (A) and Zr/Si = 28 (B), concentration of the cobalt is indicated along the spectra. The spectra of corresponding activated samples are used as reference.

The RT adsorption of NO (8 Torr) on the cobalt-silica-sulfated zirconia with different cobalt content yielded a band at 1896 cm^{-1} with a component at 1926 cm^{-1} and a strong absorption at 1812 cm^{-1} (Fig. 3.9.2, A). All the bands increase in intensity as cobalt loading increases. This experimental fact suggests that these bands arise from the adsorption of NO preferentially on Co(II) sites. Thus, the band at 1926 cm^{-1}, which partially overlaps with the band at 1896 cm^{-1} and disappears upon RT evacuation, is attributed to cobalt (II)-nitrosyl. The careful examination of the spectra and fitting show that the band at 1926 cm^{-1} has a high frequency contribution at about 1940 cm^{-1}. The behavior of this band resembles that of the

band detected on the pure support, therefore it is assigned to NO adsorbed on the Zr^{4+} centers of the support.

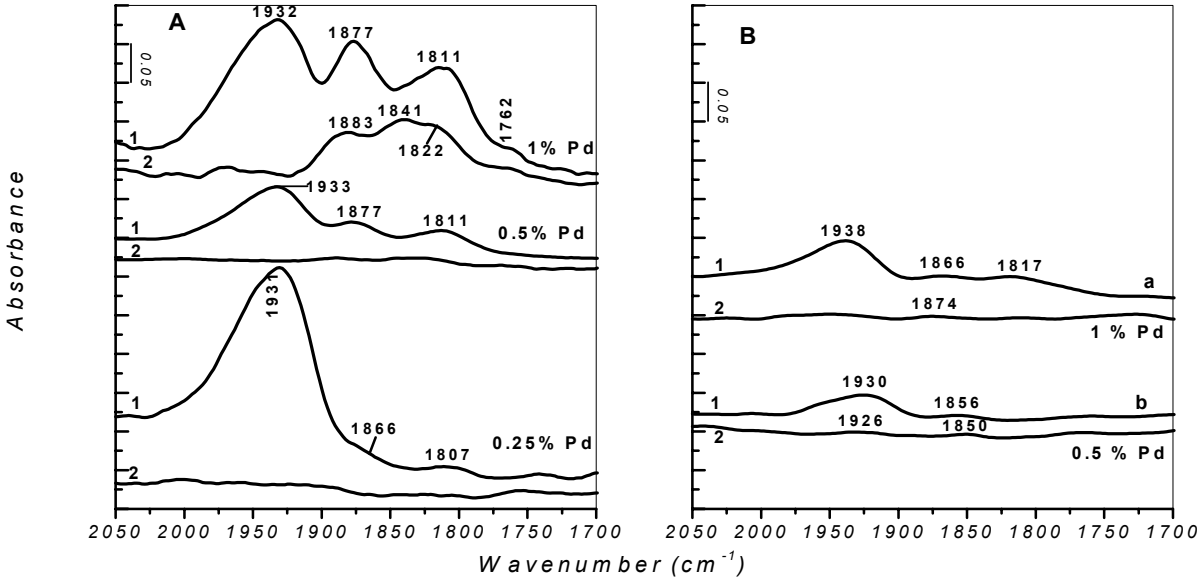

Figure 3.9.3. FT-IR spectra of (1) adsorbed NO (8 Torr) and (2) after RT evacuation on the X wt% Pd-Si-SZr samples, where (A) Zr/Si = 28, (B) Zr/Si = 3 (a), Zr/Si = 2 (b); amount of palladium is indicated along the spectra. The spectra of corresponding activated samples are used as a reference.

The bands at 1896 and 1812 cm^{-1} (Fig. 3.9.2, A) synchronously decrease in intensity as the pressure of NO decreases. Moreover, the intensity of the former band is always lower than that of the latter one. This supports the assignment of the bands to symmetric and asymmetric stretching vibration of cobalt-dinitrosyls, respectively. Figure 3.9.2, B shows NO adsorption on the Co-Si-SZr (Zr/Si = 28) samples. In this case, conversely to the results obtained in Fig. 3.9.2, A on the Co-Si-SZr (Zr/Si = 3), the overall intensities of the bands decrease as cobalt loading increases from 1 to 6 wt%, moreover, the bands have more complex nature. A very strong band at 1932 cm^{-1} with a shoulder at 1897 cm^{-1} are formed as a result of NO adsorption on the 1 wt% Co-Si-SZr (Zr/Si = 28) sample. Adsorption of the same amount of NO on the

sample with higher cobalt content yields less intense absorbance between 1960 and 1850 cm^{-1} containing at least three overlapped bands. Since this variation in the intensity is related to the cobalt coverage, it is assumed that the band at 1932 cm^{-1} is due to support-NO_x complexes. Species adsorbed on the 1 wt% Co-Si-SZr sample are surprisingly stable upon evacuation and the corresponding bands can not be resolved, therefore, we assume that cobalt (II)-dinitrosyls have been formed as is evidenced by the ν_{as} (NO) mode at 1820 cm^{-1}, but the symmetric counterpart overlaps with the bands in the region between 1960 and 1880 cm^{-1}. The complex nature of the bands observed from the NO adsorption on the 6 wt% cobalt –Si-SZr (Zr/Si = 3) sample suggests the presence of the several types of cobalt (II)-nitrosyl compounds. It was reported [248] that the presence of sulfate ions induces heterogeneity of the cobalt species and this effect is stronger in the samples with high cobalt content. This proposition is also supported by the spectra of the activated samples (Fig. 3.7.1, B - C), which show substantial modification of the sulfate related bands with the increase of cobalt concentration. In summary, adsorption of NO on the Co-Si-SZr supports reveals the presence of Co^{2+} sites on the surface.

The contact of NO (8 Torr) with all the Pd-Si-SZr samples studied yields broad absorption at around 1932 cm^{-1}, which is removed by evacuation and is ascribed to the support-NO_x compounds and a pair of bands with maxima at 1877-1856 and 1817-1811 cm^{-1} (Fig. 3.9.3). The latter bands are assigned to different types of palladium (II)-nitrosyls. Nitrosyls adsorbed on Pd(II) are stable upon evacuation [230, 252-253]; however, they lose their intensities under dynamic vacuum. An increase in the intensity and greater complexity of the palladium (II)-nitrosyl bands are observed at higher palladium loading. For example, the RT evacuation reveals three Pd (II)-NO bands at 1883, 1841 and 1822 cm^{-1} as well as a band at 1762 cm^{-1} due to Pd^{+}-NO [254] (Fig. 3.9.3 A). On the bases of the data acquired during NO

adsorption on Pd-Si-SZr, it might be concluded that palladium is dispersed on the surface of the Si-SZr supports mainly in the form of Pd (II) ions or small $(PdO)_x^{2+}$ clusters.

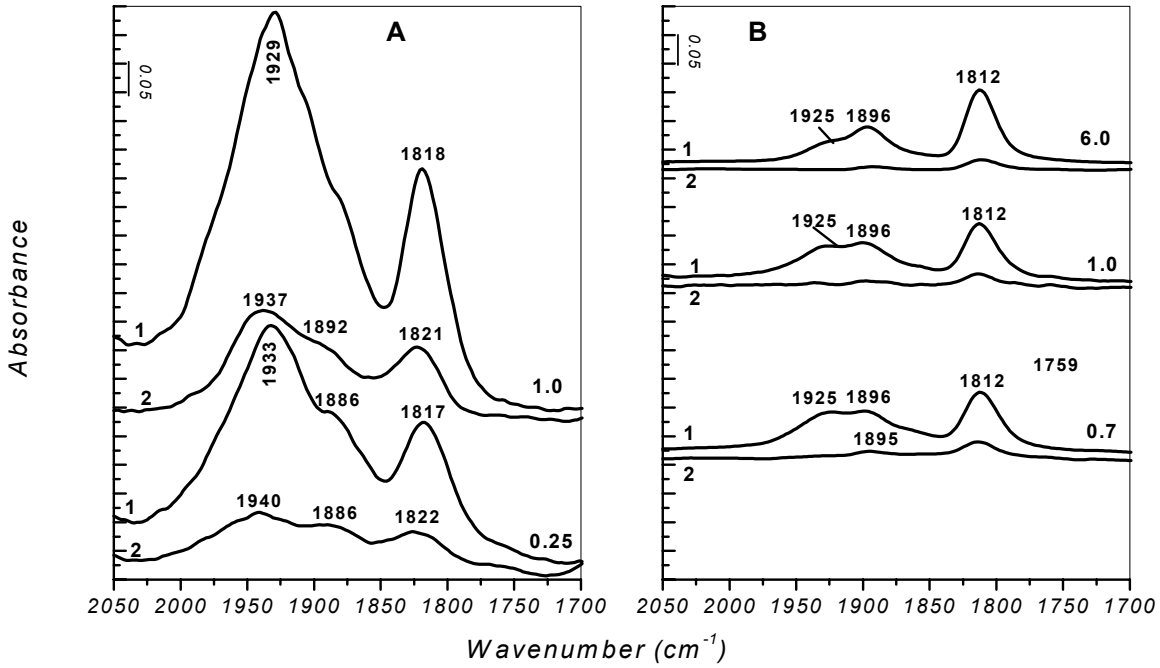

Figure 3.9.4. FT-IR spectra of (1) adsorbed NO (8 Torr) and (2) after RT evacuation on the (A) X wt% Co-0.5 wt% Pd-Si-SZr (Zr/Si = 28) samples, (B) X wt% Co-1 wt% Pd-Si-SZr (Zr/Si = 3); concentration of cobalt is shown along the spectra. The spectra of corresponding activated samples are used as a reference.

Adsorption of NO (8 Torr) on the Si-SZr containing both cobalt and palladium is displayed in Figure 3.9.4. Impregnation of the cobalt containing samples with palladium does not bring significant changes to the spectra detected on the Si-SZr functionalized with cobalt only, even the increase in the resistance of the bands to evacuation is not evidenced (compare with Fig. 3.9.2). Since the formation of new bands is not clearly visible, it is expected that the broad absorption between 1960 and 1840 cm^{-1} and the strong band at 1812-1822 cm^{-1} consist of overlapped palladium- and cobalt-nitrosyl compounds identical to those observed on Pd-

and Co-support alone. It is difficult to resolve Pd(II)- and Co(II)-nitrosyl compounds becase they have close ν(NO) stretching frequencies, as evidenced from the adsorption of NO on only cobalt and only palladium-supported samples and, probably, because the peaks originating from the Pd(II)-NO species are weaker in intensity than those from Co(II)-nitrosyls.

4. IN-SITU FT-IR MEASUREMENTS

The selective catalytic reduction of NO with hydrocarbons implies the following reaction (4.1):

$$aNO + C_bH_c \rightarrow bCO_2 + (a/2)\ N_2 + (c/2)\ H_2O, \text{ where } a = 2b + c/2 \quad (4.1)$$

This reaction occurs in several steps. In general, intermediates formed upon partial oxidation of the hydrocarbon are capable of selectively reducing NO species to N_2.

Effective selective catalytic reduction of NO_x with methane has been reported over cobalt containing zeolites [255-258]. Recently, bimetallic catalysts have received an increased attention due to a cooperative effect between the metal cations [259-292]. For example, Pd-Co loaded zeolites were found appreciably active for methane selective catalytic reduction (CH_4-SCR) [263-265]. Several reaction mechanisms have been reported in the literature for CH_4-SCR of NO_x on cobalt- and palladium-promoted catalysts. In the mechanism proposed by Kantcheva et al., [266] for SCR of NO_x by methane on Co-sulfated zirconia, the key intermediate is formic acid, which dissociates to formates. These formate ions reduce the surface nitro-nitrato species to dinitrogen being oxidized to CO_x and H_2O. Sun et al. [267] assumed the formation of nitromethane on the Co-ZSM-5 as a primary intermediate in the CH_4-SCR of NO in the presence of oxygen. Nitromethane decomposes to yield HNCO and H_2O [268-271]. The produced HNCO hydrolyses to NH_3 and the latter reduces NO to N_2 [268-270, 272]. The reported intermediates in the CH_4-SCR of NO_x over Co- and Pd-H-ZSM-5 according to Lobree et al. [273] are CH_2NO, which decomposes releasing H_2O and CN. The latter species react with NO to form N_2 and CO. Shimizu and co-workers [274] suggest that Pd^{2+}- NO and NH_4^+ are the important intermediates on Pd-H-MOR. Recently, Kantcheva et

al. [275] have observed formation of nitromethane as a primary intermediate in the surface reaction of methane with NO_2 on the Pd-tungstated zirconia. The nitromethane decomposes through the intermediacy of cis-methyl nitrite to produce Pd^{+}-NO and formate ions. These compounds react further to N_2, CO_3^{2-}, HCO_3^{-}.

In this work the surface interaction of methane with NO_x species has been studied on transition metal-promoted silica-sulfated zirconia (Si-SZr) mixed oxides. Samples with three different Zr/Si ratios, different Pd/Co ratios and constant sulfate content (~ 8 wt%) have been investigated. The phase of zirconia is a function of the Zr/Si ratio and cobalt content (Table 4.1). The choice of sample's compositions is contemplated by the literature data, which report that surface acidity as well as activity of a catalyst are directly dependent on the amount of zirconium and are also affected by zirconia phase [276-277].

Table 4.1. Physico-chemical characterization of the samples investigated by in-situ FT-IR spectroscopy

Zr/Si	Si wt%	Zr wt%	Co wt%	Pd wt%	XRD, ZrO_2 phase	Density of the self-supporting discs, g/cm^2
2	20	80	-	-	Amorphous	0.0218
			-	0.5	Amorphous	0.0215
			6	0.3	Amorphous	0.0208
			6	-	Amorphous	0.0210
3	22	88	-	-	Amorphous	0.0229
			-	1	Amorphous	0.0275
			0.7	1	Amorphous	0.0201
			1	1	Amorphous	0.0193
			6	1	Amorph/tetragonal	0.0169
			6	-	Amorph/tetragonal	0.0169
28	2	98	-	-	Tetragonal	0.0182
			-	0.5	Tetragonal	0.0164
			-	1	Tetragonal	0.0278
			0.25	0.5	Tetragonal	0.0235
			1	0.5	Tetragonal	0.0302
			1	-	Tetragonal	0.0290

The behavior of NO_x species adsorbed on the surface of a catalyst in the presence of methane at elevated temperatures has been investigated by in-situ FT-IR spectroscopy in three subsequent steps:

(i) The so-called "blank NO_x" experiment, in which co-adsorption of NO and O_2 followed by evacuation leads to formation of NO_x compounds stable at room temperature. Then the closed IR cell containing NO_x-precovered catalyst is heated at various temperatures for 20 min.

(ii) "Blank CH_4 experiment" aims to investigate the interaction of activated catalyst with methane at elevated temperatures.

(iii) "CH_4 - NO_x" experiment consists of interaction of the catalyst containing pre-adsorbed NO_x compounds with methane at temperatures in the range between 150 and 450^0C with 50^0C ramp. It is expected that intermediates containing C-N-O will form in the course of the reaction leading to the N_2, CO_x and H_2O end products.

4.1. Interaction of Preadsorbed NO_x Species with Methane

The results of in-situ FT-IR "CH_4 - NO_x" experiments performed on the Pd-Si-SZr catalysts with different Zr/Si mole ratios are described below. The "blank NO_x" and "blank CH_4" experiments are invoked where it is necessary. By comparing of the experimental results on the series of Pd-Si-SZr catalysts, it is expected to elucidate the reaction intermediates and to investigate the effect of the composition of the Si-SZr support.

4.1.1. 1 wt% Pd-Si-SZr (Zr/Si = 3) Catalyst and 0.5 wt% Pd-Si-SZr (Zr/Si = 2) Catalyst.

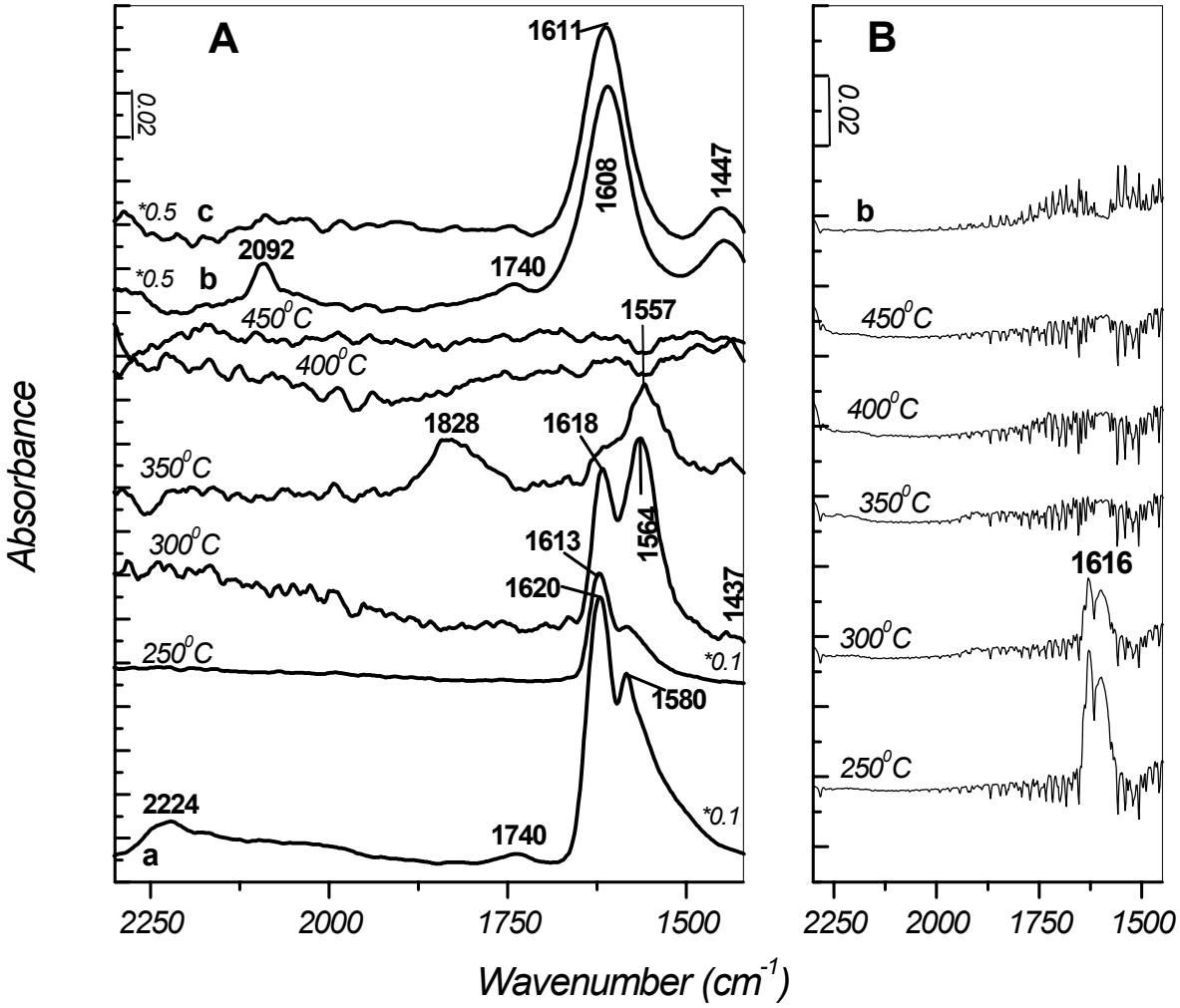

Figure 4.1.1.1. FT-IR spectra of 1 wt% Pd-Si-SZr (Zr/Si = 3) catalyst taken after addition of NO/O_2 mixture (16 Torr, $NO:O_2$ = 1:1) for 30 min at RT followed by evacuation and addition of 50 Torr methane (a), after heating of the closed IR cell for 20 min and then cooling to RT (b), subsequently evacuation of the gas phase at RT (c). The spectrum of the activated sample is used as a background reference. Gas phases are subtracted from spectra. (B) Gas phase spectrum of the corresponding spectrum shown on panel A.

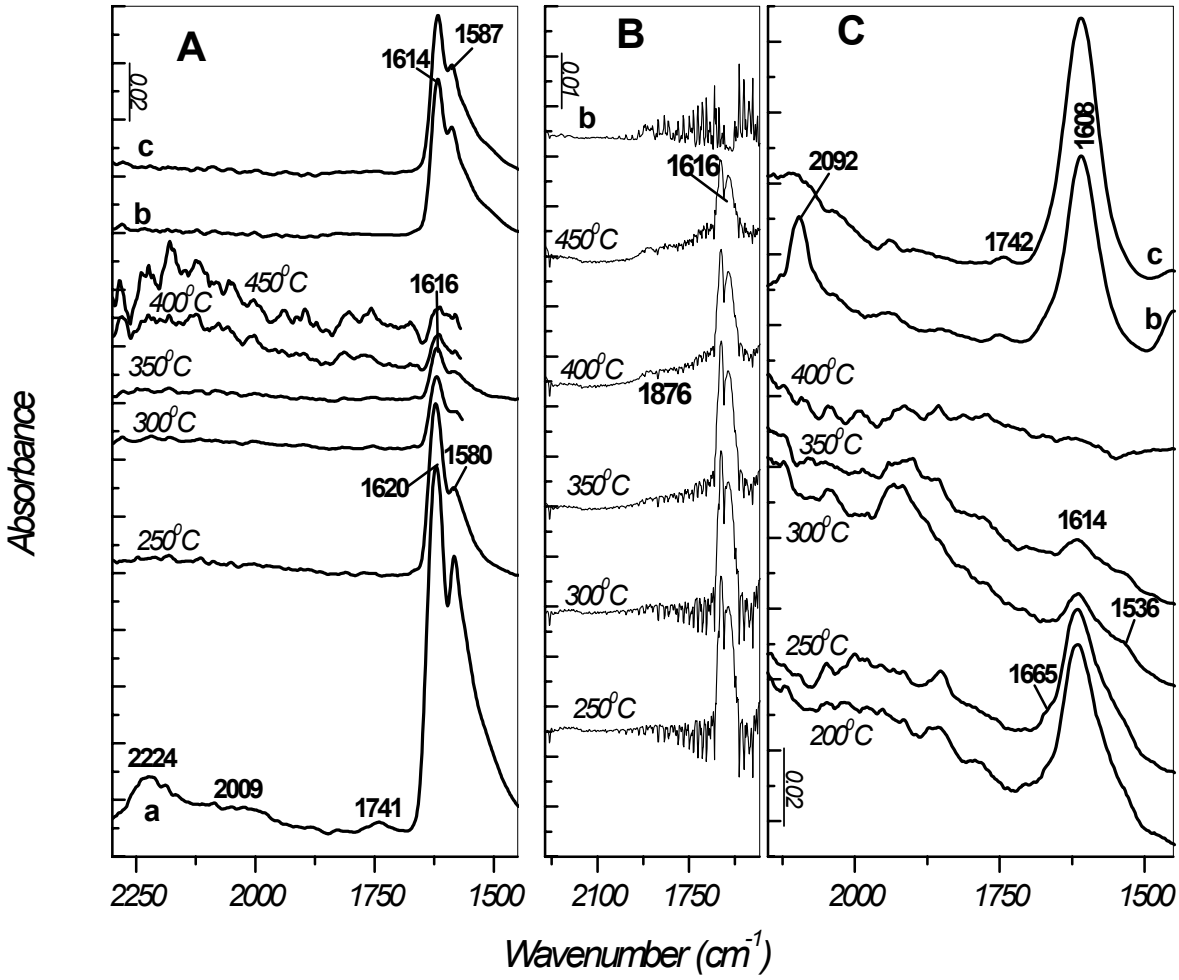

Figure 4.1.1.2. (A) FT-IR spectra of 1 wt% Pd-Si-SZr (Zr/Si = 3) catalyst taken after adsorption of NO/O_2 mixture (16 Torr, $NO:O_2$ = 1:1) for 30 min at RT followed by evacuation (a) and after heating of the closed IR cell for 20 min, then cooling to RT (b), and evacuation of the gas phase (c). (B) Gas phase spectrum of the corresponding spectrum shown on panel A. (C) FT-IR spectra of 1 wt% Pd-Si-SZr (Zr/Si = 3) catalyst taken after addition of 50 Torr methane at RT, followed by heating of the closed IR cell for 20 min and then cooling to room temperature (b), and evacuation of the gas phase (c). The spectrum of the activated sample is used as a background reference. Gas phases are subtracted from spectra.

The surface NO_x species are formed at RT by co-adsorption of NO/O_2 mixture (16 Torr, $NO:O_2$ = 1:1) for 30 min followed by evacuation. Methane (50 Torr) is added and the closed IR cell is heated at different temperatures. The nitro-nitrato bands (at 1620 and 1580 cm^{-1} [247]) decrease in intensity up to 250^0C (Fig. 4.1.1.1, A). At 300^0C the bands shift to 1613 and 1564 cm^{-1}. The intensity of the band at 1564 cm^{-1} increases relative to that at 1613 cm^{-1}. This behavior is not observed in the "blank NO_x" experiment (Fig. 4.1.1.2, A). Hence, it can be concluded that new species at 1564 cm^{-1} is formed. Since the concentration of NO_2 gas at 300^0C decreases, it is reasonable to assume that CH_3NO_2 is formed and the band at 1564 cm^{-1} corresponds to the ν_{as} (NO_2) mode. The other characteristic bands of CH_3NO_2 fall below 1400 cm^{-1} [269, 278-280] and can not be observed. At 350^0C a broad absorption at 1838 cm^{-1} and a weak band at 1437 cm^{-1} appear, the band at 1613 cm^{-1} decreases in intensity and the band at 1564 cm^{-1} shifts to 1557 cm^{-1}. It is worth to notice that NO_2 is completely consumed at this stage. No adsorbed species are detected after heating at 400^0C. Bands at 2092, 1740, 1608 and 1447 cm^{-1} are observed in the spectrum after cooling to RT (Fig. 4.1.1.1, A). These bands could be attributed to the following species: the band at 2092 cm^{-1} is due to Pd^0-CO [281], the band at 1608 cm^{-1} is a superposition of carbonate-carboxylate species [282] and water and the band at 1447 cm^{-1} is due to monodentate carbonates [282] or together with the absorption at 1608 cm^{-1} belongs to $HCOO^-$. The bands at 2092 and 1740 cm^{-1} vanish upon RT evacuation, while the band at 1608 cm^{-1} shifts slightly to 1611 cm^{-1}. The nature of the band at 1740 cm^{-1} is ambiguous. On one hand, it can be attributed to organic-like carbonates [282], since this band has also been detected in the "blank CH_4" experiment (Fig. 4.1.1.2, C). According to the literature [282] organic-like carbonate compounds are stable and can not be removed by RT evacuation. In our case, however, the absorption resulting upon cooling to RT in the "CH_4-NO_x" experiment vanishes during RT evacuation (compare spectra b and c in Fig. 4.1.1, A). The band at 1740 cm^{-1} can also arise from Pd^0-NO species [283-285], which do not resist

evacuation. Figure 4.1.1.3 compares the results of the "CH_4 - NO_x", "blank NO_x" and "blank CH_4" experiments obtained after evacuation at RT. Similar bands form upon interaction of NO_x-precovered and NO_x-free 1% Pd-Si-SZr (Zr/Si = 3) catalyst with methane indicating that carbonate-carboxylate species are the main products of interaction.

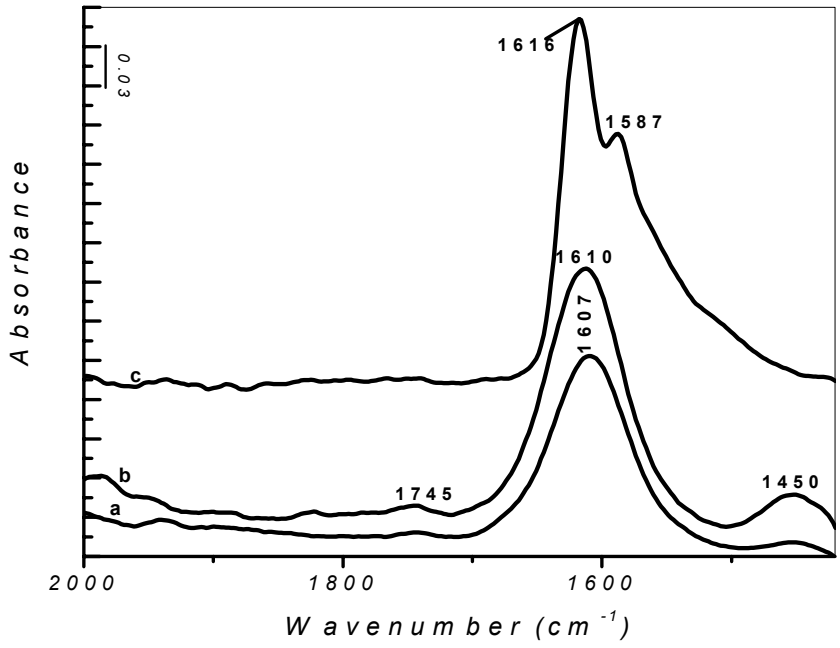

Figure 4.1.1.3. FT-IR spectra of the 1% Pd-Si-SZr (Zr/Si = 3) catalyst taken from the "blank CH_4" (a), the interaction of the CH_4 with NO_x (b) and the "blank NO_x" experiments after the final evacuation at RT. The spectrum of the activated sample is used as a background reference. Gas phases are subtracted from spectra.

The adsorbed NO_x species were created on the 0.5 wt% Pd-Si-SZr (Zr/Si = 2) catalyst as described above and are heated in the methane atmosphere in the closed IR cell between 150 and 450^0C. As the temperature rises, the preadsorbed NO_x compounds (bands at 1616 and 1582 cm^{-1} (shoulder)) gradually leave the surface to produce NO_2 gas (Fig. 4.1.1.4, A-B).

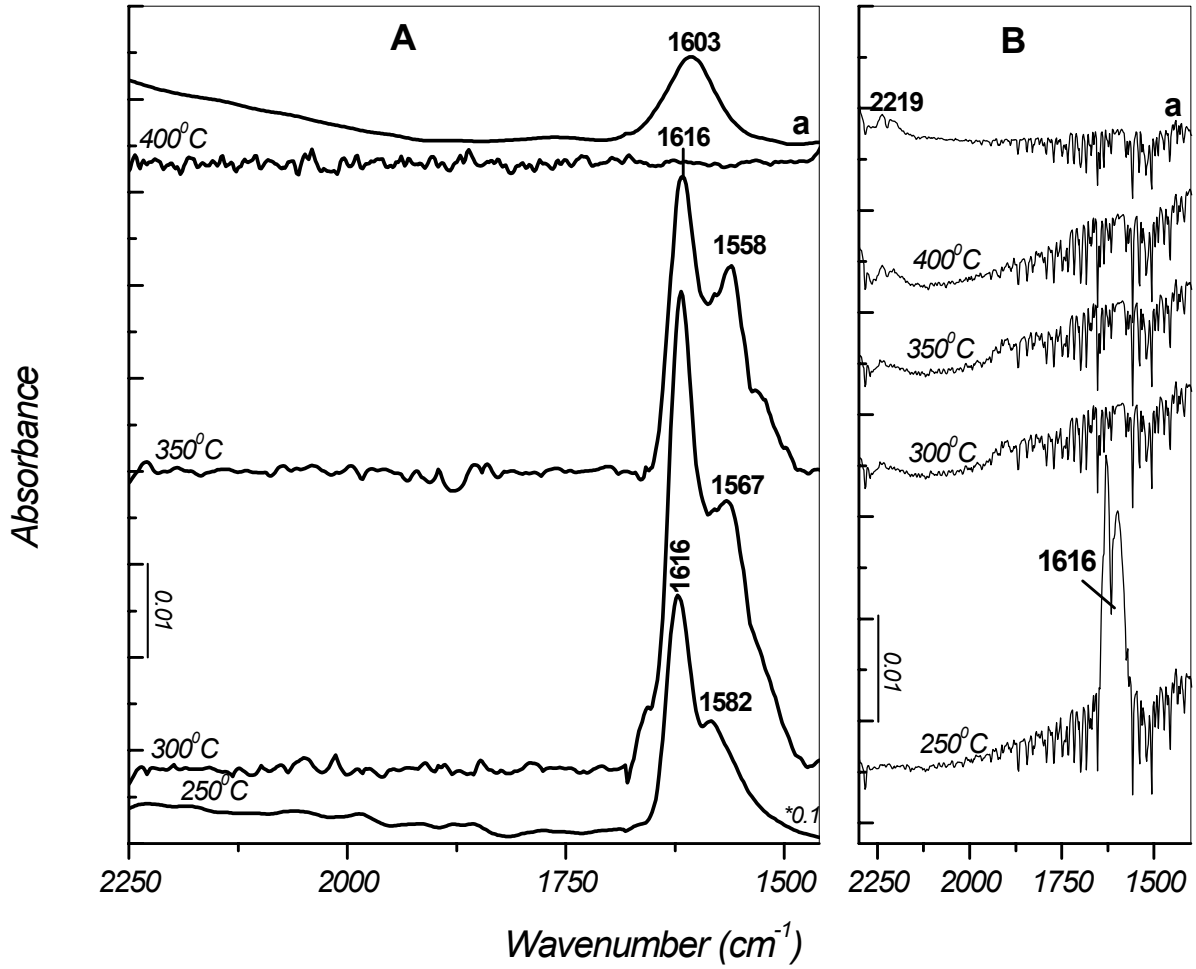

Figure 4.1.1.4. FT-IR spectra of 0.5 wt% Pd-Si-SZr (Zr/Si = 2) catalyst taken after addition of NO/O_2 mixture (16 Torr, $NO:O_2$ = 1:1) for 30 min at RT followed by evacuation and addition of 50 Torr methane, after heating of the closed IR cell for 20 min and then cooling to RT (a). The spectrum of the activated sample is used as a background reference. Gas phases are subtracted from spectra. (B) Gas phase spectrum of the corresponding spectrum shown on panel A.

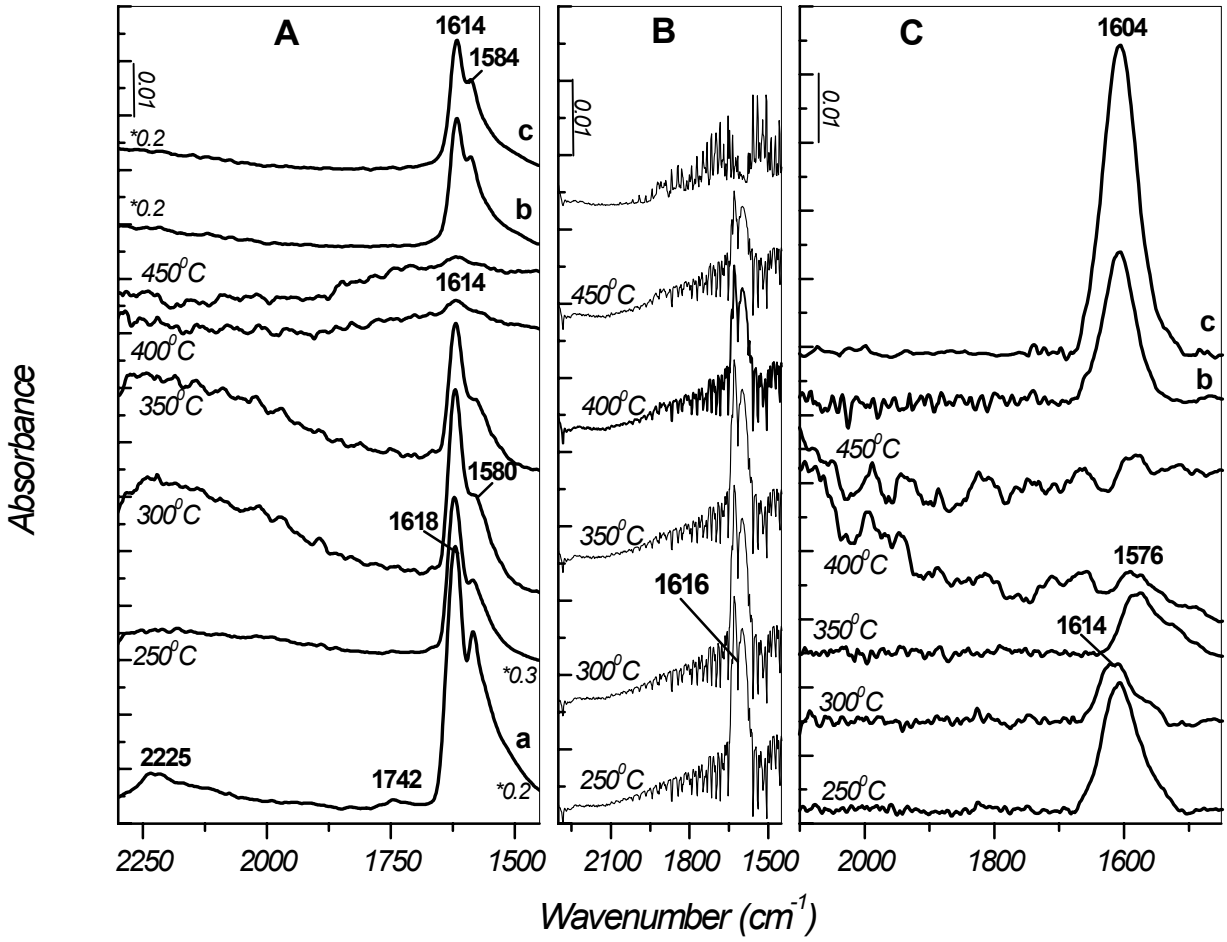

Figure 4.1.1.5. (A) FT-IR spectra of 0.5 wt% Pd-Si-SZr (Zr/Si = 2) catalyst taken after adsorption of NO/O_2 mixture (16 Torr, $NO:O_2$ = 1:1) for 30 min at RT followed by evacuation (a) and after heating of the closed IR cell for 20 min, then cooling to RT (b), and evacuation of the gas phase (c). (B) Gas phase spectrum of the corresponding spectrum shown on panel A. (C) FT-IR spectra of 0.5 wt% Pd-Si-SZr (Zr/Si = 2) catalyst taken after addition of 50 Torr methane at RT, followed by heating of the closed IR cell for 20 min and then cooling to RT (b), and evacuation of the gas phase (c). The spectrum of the activated sample is used as a background reference. Gas phases are subtracted from spectra.

The NO_2 disappears after heating at 300^0C. In the sample spectrum recorded at this temperature, the same bands appear with lower intensities relative to those observed at the same conditions in the absence of methane, in the "blank NO_x" experiment (Fig.4.1.1.5, A). Moreover, NO_2 gas is detected in the latter case. After heating to 350^0C (Fig.4.1.1.4, A), the intensity of the band at 1616 cm^{-1} further decreases and new distinct band at 1558 cm^{-1}, which does not appear in the corresponding spectrum Fig. 4.1.1.5, B, is detected. At 400^0C no adsorbed species are detected in the case of the CH_4-NO_x interaction (Fig. 4.1.1.4, A), while residual nitrates are present in the spectrum in Fig.4.1.1.5, A. Cooling the cell to RT leads to restoration of the NO_x species (strong band at 1616 cm^{-1} with a shoulder at 1585 cm^{-1}) (Fig. 4.1.1.5, A), whereas new band at 1602 cm^{-1} is detected in Fig. 4.1.1.4, A. Hence, by comparing of the corresponding spectra recorded upon heating of the adsorbed NO_x compounds in methane atmosphere (Fig. 4.1.1.4, A) and in the absence of methane (Fig. 4.1.1.5, A) and after cooling to RT it can be concluded that surface reaction between the methane and decomposition product of the NO_x compounds have taken place. Since NO_2 gas was consumed after heating at 300^0C, this is a supposed interaction temperature. The most likely products of CH_4 – NO_x interaction are CO_x (band at 1602 cm^{-1} falls in the carbonate-carboxylate region [282]), water (band at 1602 cm^{-1}) and N_2, N_2O (gas, at 2219 cm^{-1}). Disappearance of NO_2 between 250 and 300^0C and formation of the same end products as in the case of 1 wt% Pd-Si-SZr (Zr/Si = 3) leads to supposition that CH_4 – NO_x interaction on the 0.5 wt% Pd-Si-SZr (Zr/Si = 2) catalyst went through the same steps. The intermediates were not resolved, because they overlap with, apparently, more stable on the silica rich-sulfated zirconia residual nitrates.

4.1.2. Pd-Si-SZr catalyst, Zr/Si = 28

Figure 4.1.2.1 shows the spectra recorded during the heating of preadsorbed NO_x species on the 0.5 wt% Pd-Si-SZr in the presence of 50 Torr methane in the closed IR cell.

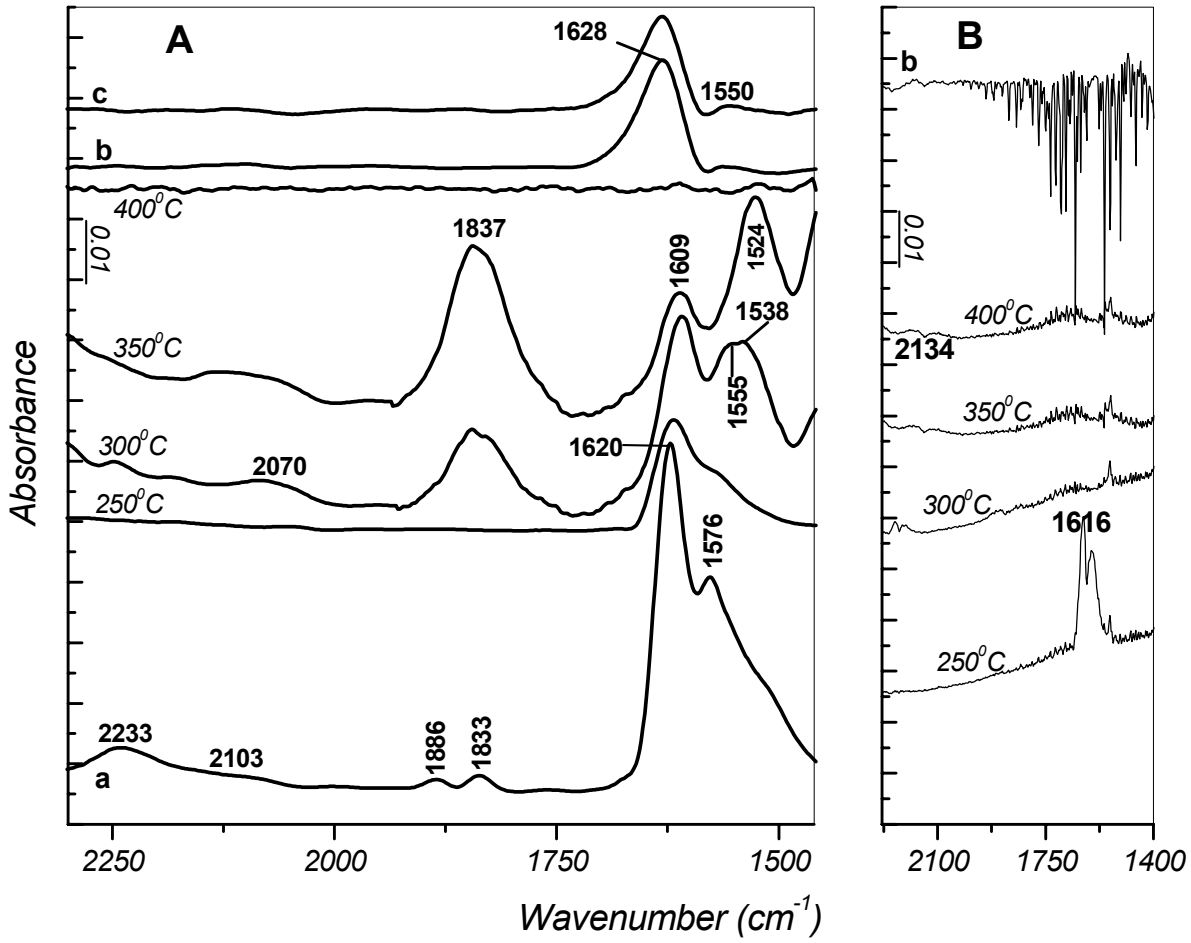

Figure 4.1.2.1. FT-IR spectra of 0.5 wt% Pd-Si-SZr (Zr/Si = 28) catalyst taken after addition of NO/O_2 mixture (16 Torr, $NO:O_2$ = 1:1) for 30 min at RT followed by evacuation and addition of 50 Torr methane (a), after heating of the closed IR cell for 20 min and then cooling to RT (b), subsequently evacuation of the gas phase at RT (c). The spectrum of the

activated sample is used as a background reference. Gas phases are subtracted from spectra. (B) Gas phase spectrum of the corresponding spectrum shown on panel A.

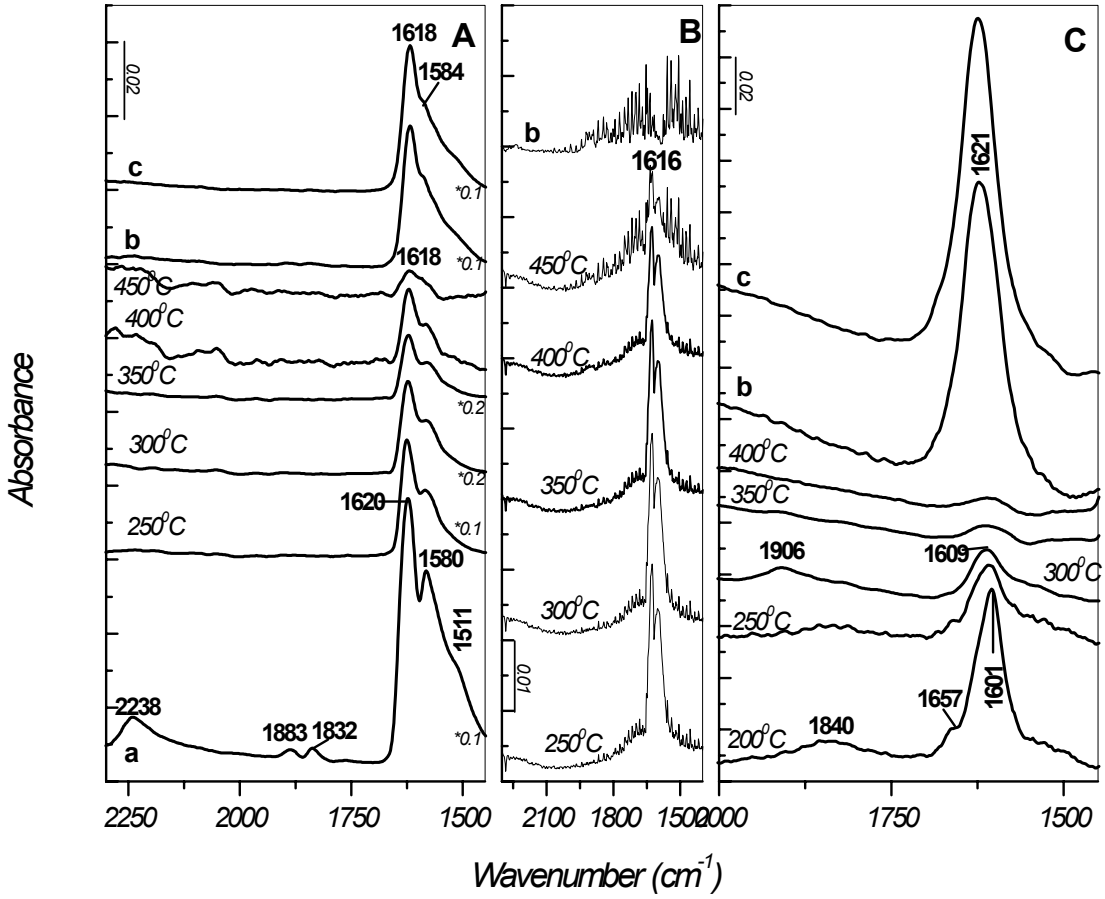

Figure 4.1.2.2. (A) FT-IR spectra of 0.5 wt% Pd-Si-SZr (Zr/Si = 28) catalyst taken after adsorption of NO/O_2 mixture (16 Torr, $NO:O_2$ = 1:1) for 30 min at RT followed by evacuation (a) and after heating of the closed IR cell for 20 min, then cooling to RT (b), and evacuation of the gas phase (c). (B) Gas phase spectrum of the corresponding spectrum shown on panel A. (C) FT-IR spectra of 0.5 wt% Pd-Si-SZr (Zr/Si = 28) catalyst taken after addition of 50 Torr methane at RT, followed by heating of the closed IR cell for 20 min and then cooling to RT (b), and evacuation of the gas phase (c). The spectrum of the activated sample is used as a background reference. Gas phases are subtracted from spectra.

Desorption of the NO_x compounds at elevated temperatures results in the formation of NO_2 (Fig. 4.1.2.1, B). At 300^0C NO_2 disappears, while NO (1786 cm^{-1}) and N_2O (2224 cm^{-1}) are evidenced in the gas phase. The broad absorption at 2070 cm^{-1} as well as bands at 1837, 1609, 1555 and 1536 cm^{-1} appear in the spectrum at this temperature. The intensity of the overlapped 1555 and 1536 cm^{-1} bands has increased relative to that of the band at 1609 cm^{-1}. In the absence of methane, in the "blank NO_x" experiment (Fig. 4.1.2.2, A), heating at 300^0C for 20 min leads to the decrease in intensities of the bands at 1620 and 1580 cm^{-1}, whereas the concentration of NO_2 in the gas phase does not change. These experimental observations are in accordance with those obtained on the 1 wt% Pd-Si-SZr (Zr/Si = 3) catalyst and lead to the conclusion that a surface interaction of CH_4 with NO_2 has taken place to produce CH_3NO_2 characterized by the band at 1555 cm^{-1} [26-28]. Nitromethane rearranges on the surface to cis-methyl nitrite isomer ascribed by the ν (N=O) vibration at 1609 cm^{-1}. Increasing the temperature by 50^0C results in increase in the intensity of the band at 1837 cm^{-1} and appearance of the strong band at 1524 cm^{-1}, while the bands at 1609 and 1555 cm^{-1} significantly decrease in intensity. Note also that N_2O and NO are not detected in the gas phase. On the bases of the considerations above the bands at 2070, 1837, 1524 cm^{-1} are attributed to the products of decomposition of primary intermediates. After cooling to RT a strong band at 1628 cm^{-1} and weak absorption at 1550 cm^{-1} are observed in Fig. 4.1.2.1, A, spectrum b. The same experiments have been performed on 1 wt% Pd-Si-SZr catalyst. Figure 4.1.2.3 compares the results of "CH_4-NO_x" experiment on the catalyst activated by the standard procedure (Fig. 4.1.2.3, A) and methane pretreated catalyst (Fig. 4.1.2.3, C). The latter catalyst was pre-reduced in methane atmosphere at elevated temperatures and then reoxidized before the "CH_4-NO_x" experiment. NO_2 gas disappears between 250 and 300^0C (Fig. 4.1.2.3, B).

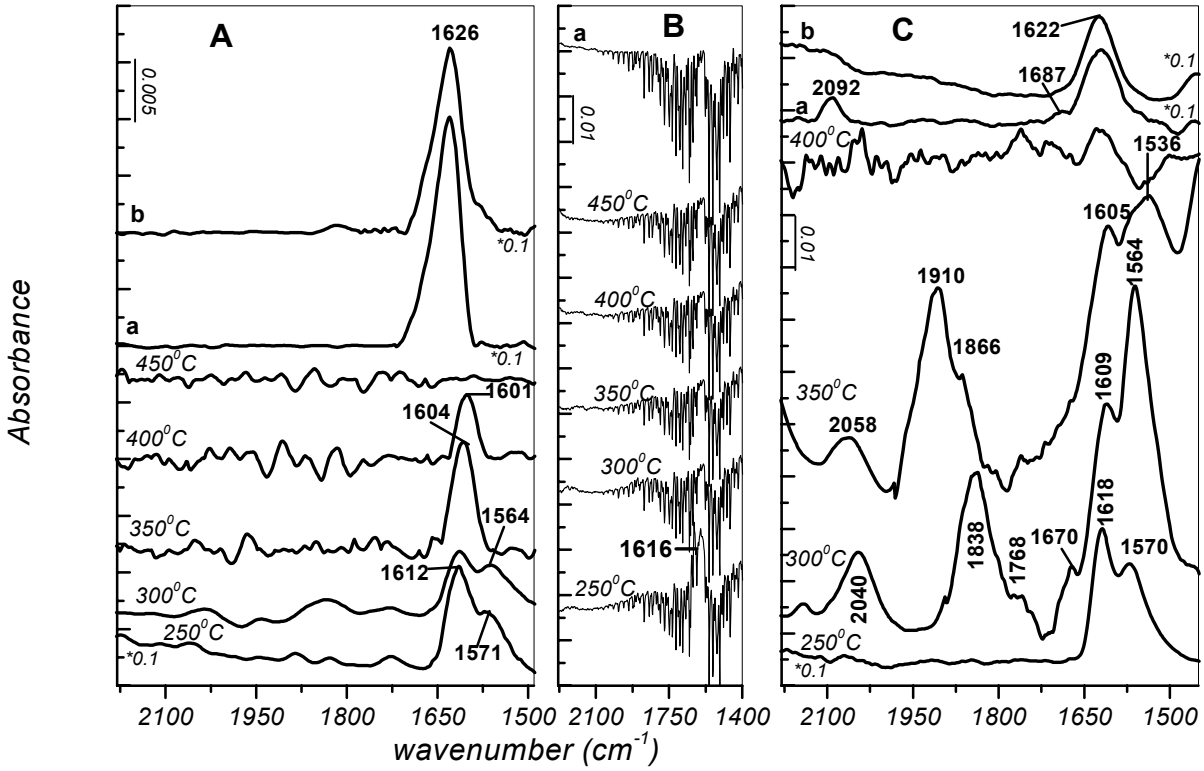

Figure 4.1.2.3. FT-IR spectra of the 1 wt% Pd-Si-SZr (Zr/Si = 28) catalyst activated by the standard procedure (A) and pretreated with CH_4 (C) taken after addition of NO/O_2 mixture (16 Torr, $NO:O_2$ = 1:1) for 30 min at RT followed by evacuation and addition of 50 Torr methane, after heating of the closed IR cell for 20 min and then cooling to RT (a), subsequently evacuation of the gas phase at RT (b). The spectrum of the activated sample is used as a background reference. Gas phases are subtracted from spectra. (B) Gas phase spectrum of the corresponding spectrum shown on panel A.

At 300^0C, two-band spectrum with maxima at 1612 and 1564 cm^{-1} and a weak absorption at 1838 cm^{-1} are detected. The intensity of the latter band has increased relative to that of the former one. Such change has not been observed in the "blank NO_x" experiment (Fig.4.1.2.2, A). In the spectrum acquired at 350^0C a single band at 1604 cm^{-1} ascribed to carbonate-carboxylate species [282] is observed, which slightly shifts to 1601 cm^{-1} and loses intensity at 400^0C. The carbonate-carboxylate species superimposed with water reappear on the surface of

the cooled to RT catalyst at 1626 cm^{-1} (Fig. 4.1.2.3, A curve a). The consumption of NO_2 and formation of CO_x and water indicate that CH_4 has interacted with nitrogen dioxide, however no intermediates have been detected. The Fig. 4.1.2.3, C shows FTIR spectra of the same sample subjected to reduction with methane followed by reoxidation prior to the "CH_4-NO_x" experiment. All NO_2 is consumed after heating at 300^0C. Intense bands at 1609 and 1564 cm^{-1} previously ascribed to cis-CH_3ONO and CH_3NO_2, respectively, [278-280] are observed in the spectrum (Fig.4.1.2.3, C) together with bands at 2040, 1838, 1768 and 1670 cm^{-1}. The behavior of the former two bands upon heating is the same as that observed for the other Pd-promoted catalysts. New absorption at 1910 cm^{-1} with a low frequency component at 1866 cm^{-1} form and the band at 1838 cm^{-1} disappears at 350^0C. Pd^0 – carbonyl (2092 cm^{-1}) [281], carbonate-carboxylate compounds (1622 cm^{-1}) [282] and water (1622 cm^{-1}) have formed as a result of the CH_4-NO_x interaction. Experimental data presented in Fig. 4.1.2.3 suggest that interaction of CH_4 with NO_2 to CO_x, H_2O and N_2 takes place very fast between 300 and 350^0C on the catalyst activated by the standard procedure, therefore, intermediates have not been detected (Fig. 4.1.2.3, A). After reduction with CH_4 and reoxidation the reaction slows down and intermediates are illustrated in the spectrum at 300^0C in Fig. 4.1.2.3, C. At 350^0C the formation of the strong bands at 1910, 1866 cm^{-1} (shoulder) due to $(Pd^0)_2$-CO [286], at 1768 cm^{-1} corresponding to Pd^+-NO [230, 269, 280] and at 1670 cm^{-1} ascribed to $(Pd^0)_2$-NO [247] is observed. Note that at the same conditions no such bands were detected on the catalyst activated by the standard procedure. Formation of carbonyls and nitrosyls on metallic palladium at 350^0C leads to assumption that it is easier to reduce larger clusters of palladium present on the surface. Thus, the dispersion of palladium has a crucial effect on the course of the CH_4-NO_x reaction.

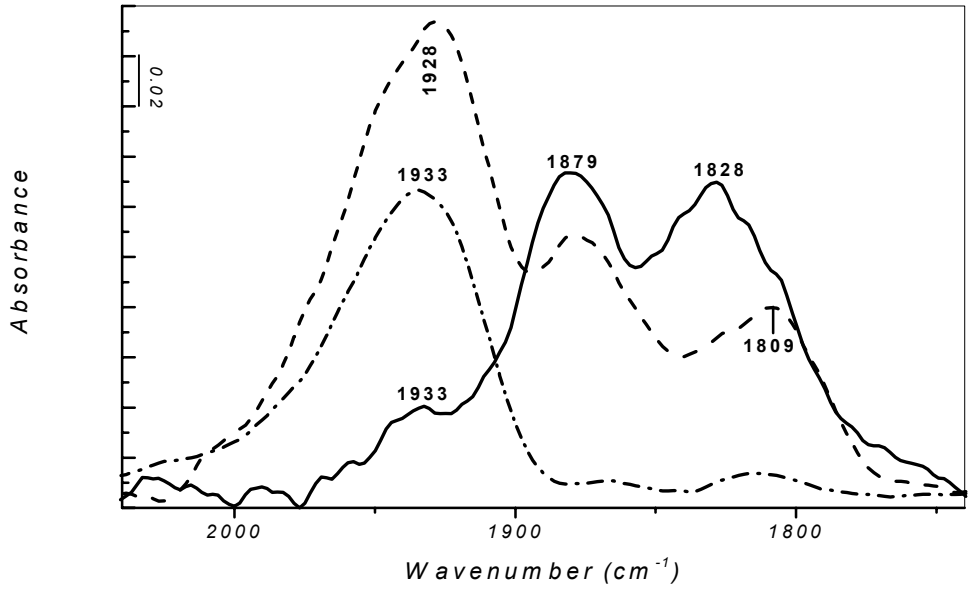

Figure 4.1.2.4. The FT-IR spectra of adsorbed NO (8 Torr) on the Si-SZr (Zr/Si = 28) support (dash-dot line), Pd-Si-SZr catalyst activated by the standard procedure (solid line), and (dash line) Pd-Si-SZr catalyst pretreated with methane.

To rationalize the aggregation of PdO_x species after the reduction with methane the adsorption of NO (8 Torr) on the Si-SZr and Pd-Si-SZr both catalysts activated by the standard procedure and catalyst pretreated with methane is compared (Fig. 4.1.2.4). The band at 1933 cm^{-1} is ascribed to the Zr^{4+}-nytrosils on the support, the bands at 1879 and 1828-1809 cm^{-1} are due to Pd^{2+}-NO (see Section 3.3). The intensity of the band ascribed to nytrosils adsorbed on the support is expected to be a function of the surface coverage with palladium (since the introduced palladium will occupy the support sites for NO adsorption and the intensity of the band at 1933 cm^{-1} will decrease). Negligible intensity of the band at 1933 cm^{-1} observed on the Pd-Si-SZr catalyst activated by the standard procedure relative to that on the pure support indicates that the dispersion of palladium on the surface is high. On the other hand, the intensity of the same band detected on the Pd-Si-SZr sample pretreated with CH_4 is comparable to that on the palladium-free sample. It implies that palladium ions have

agglomerated liberating surface Zr^{4+} sites for NO adsorption. These results are coherent with X-ray diffraction patterns acquired after the methane oxidation over the Pd-Si-SZr catalysts at 450^0C shown in Figure 4.1.2.5. It can be seen that palladium undergoes reduction, when the Pd-Si-SZr catalyst with 1 wt% Pd loading is subjected to the methane at elevated temperatures (Fig. 4.1.2.5, line c) the peaks appear at $2\theta = 40^0$ and 46.7^0 correspond to Pd^0 (111) and (200) planes, respectively [287-288].

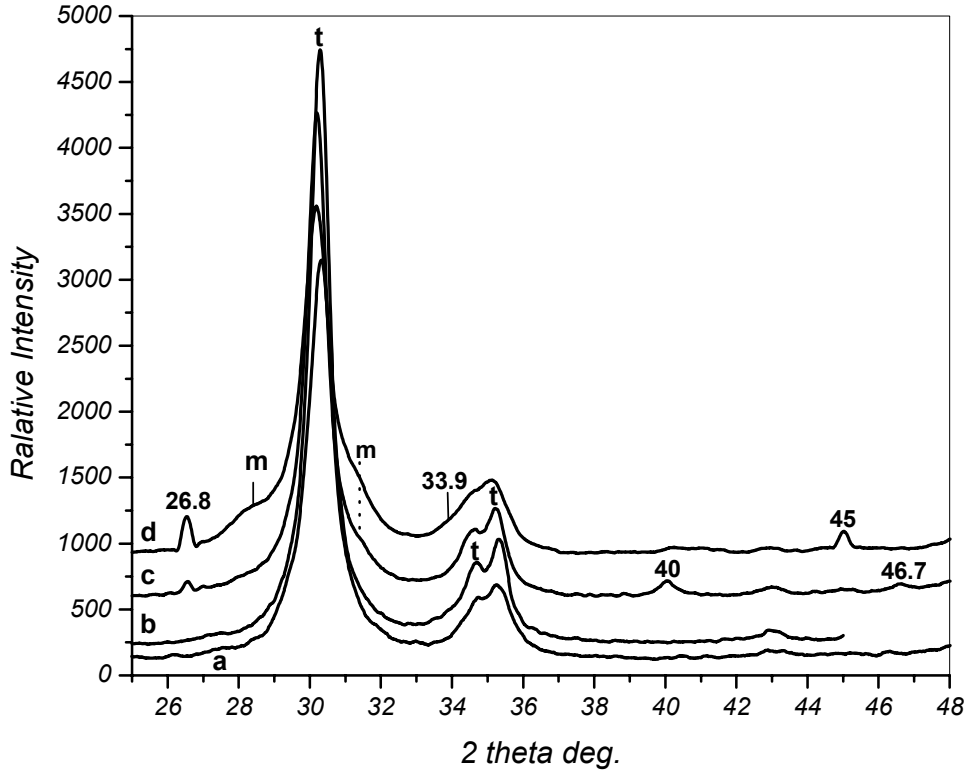

Figure 4.1.2.5. Powder XRD patterns of Si-SZr (Zr/Si = 28) support (a), 1 wt% Pd-containing support before reaction with CH_4 (b), after reaction with CH_4 (c) and 0.5 wt% Pd-Si-SZr (Zr/Si = 28) after reaction with CH_4 (d).

Whereas the catalyst containing 0.5 wt% Pd after treatment with methane shows broadening in the XRD pattern between 33.5^0 and 35.0^0 2θ values (Fig. 4.1.2.5, line d), indicating the formation of PdO nanoparticles, which diffract at about 33.9^0 2θ [194-195]. It is also important to point out that transformation of tetragonal zirconia (t-ZrO_2) to monoclinic ZrO_2 (m-ZrO_2) phase takes place upon high temperature treatment with methane.

Overall, the structure of the Pd-Si-SZr (Zr/Si = 28) catalyst after reaction with methane at anaerobic conditions is quite different from that of unreacted catalyst. It shows that both $Pd^{2+}/(PdO)_x^{2+}$ and t-ZrO_2 have been transformed in the reaction medium. These findings correlate well with literature. Duprez et al., [289] have observed similar transformation in the palladium oxidation state on Pd-supported Al_2O_3 in alkene and alkyne oxidations reactions. Ohtsuka and Tabata [161] proposed that agglomeration of palladium on Pd-MOR in the NO_x reaction with CH_4 is promoted by water. It was also shown [281] that redistribution of palladium takes place in the NO atmosphere and Pd^{2+} is stabilized on the surface.

By comparing the results of "CH_4-NO_x" experiment on the palladium-promoted catalysts with low and high zirconium content, it is evident that the surface reaction of CH_4 with NO_2 occurs faster in the latter case. The detailed assignment of the detected bands is compiled in the Table 4.1.2.1.

The common features observed during the interaction of CH_4 with preadsorbed NO_x species on the Pd-Si-SZr catalysts independently on the Zr/Si mole ratio are as follows:

1. Gradual decomposition of the surface nitro-nitrato compounds to NO_2 at elevated temperatures;

2. Significant or complete consumption of NO_2 after heating at 300^0C;
3. Formation of CO_x (carbonate-carboxylate), H_2O and N_2 after cooling to RT;
4. Absence of Pd nytrosils after cooling to RT;

Table 4.1.2.1. Assignments of the FT-IR bands observed during interaction of methane with NO_x species adsorbed on Pd-Si-SZr catalysts with Zr/Si = 2, 3, 28 at elevated temperatures

Temperature, ^{0}C	Species	Band, cm^{-1}	Mode
25	NO^+	2233	ν (NO)
	Pd^{2+}-NO (two types)	1886, 1833	ν (NO)
	NO_3^- (bidentate)(two types)	1620-1616	ν (N=O)
		1585-1570	ν (N=O)
	NO_3^- (monodentate)	1516	ν_{as} (NO_2)
250	NO_2 (gas)	1616	ν_{as} (NO_2)
	NO_3^- (bidentate)(two types)	1620-1616	ν (N=O)
		1585-1570	ν (N=O)
300	N_2O (gas)	2224	ν (NN)
	NO (gas)	1876	ν (NO)
	Pd^0-CO (linear)	2070-2040	ν (CO)
	Pd^0-NO	1768	ν (NO)
	Pd^+-NO	1838, 1760	ν (NO)
	HCOOH	1670	ν (C=O)
	cis- CH_3ONO	1616-1609	ν (N=O)
	CH_3NO_2	1564-1555	ν_{as} (NO_2)
	$HCOO^-$	1555, 1538	ν_{as} (CO_2)
	CO_3^{2-} (bidentate)	1538	ν (C=O)
350	Pd^0-CO (linear)	2070-2060	ν (CO)
	$(Pd^0)_2$-CO (bridged)	1910	ν (CO)
	Pd^+-NO	1838-1828, 1768	ν (NO)
	$(Pd^0)_2$-NO	1670	ν (NO)
	cis- CH_3ONO	1616-1605	ν (N=O)
	CH_3NO_2	1558	ν_{as} (NO_2)
	$HCOO^-$	1557	ν_{as} (CO_2)
	CO_3^{2-} (bidentate)	1536	ν (C=O)
	CO_3^{2-} (monodentate)	1524	ν_{as} (COO^-)
	$HCOO^-$ (bidentate)	1524	ν_{as} (CO_2)
400	N_2O (gas)	2219	ν (NN)
Room temperature (RT)	N_2O (gas)	2219	ν (NN)
	Pd^0-CO	2092-2090	ν (CO)
	CO_3^{2-} (organic-like)	1762-1740	ν (C=O)
	Pd^0-NO	1762-1740	ν (NO)
	CO_3^{2-} (bidentate)	1622-1602	ν (C=O)
	CO_2^{2-}	1622-1602	ν_{as} (COO^-)
	H_2O	1622-1602	δ (HOH)

Experimental facts outlined in 2, 3 and 4 are necessary and sufficient criteria to conclude that methane has reacted with adsorbed NO_x compounds.

By examining the experimental results accumulated in the "CH_4 - NO_x" experiments on the Pd-Si-SZr catalysts with Zr/Si = 3 and 28 the reaction intermediates can be elucidated. Formation of Pd^+-NO (strong absorption at 1838-1828 cm^{-1} [230, 269, 278-280]), hydrogencarbonates (bands at 1610-1524 cm^{-1} [282]) and water (1610 cm^{-1}) takes place at the expense of the bands at 1613-1609 and 1564 cm^{-1}, and is accompanied by the consumption of NO_2 gas.

4.2. Interaction of Methane with NO_x Precovered Co-Si-SZr Samples.

In this section in situ FT-IR investigation of Co-Si-SZr catalysts with Zr/Si mole ratios equal to 2, 3 and 28 and different cobalt loading is presented. The so-called "blank NO_x", "blank CH_4" and "CH_4-NO_x" experiments have been performed to gain information on the role of cobalt in the reaction of surface NO_x compounds with hydrocarbon.

The interaction of CH_4 with surface NO_x compounds over 1 wt% Co-Si-SZr (Zr/Si = 28) (Fig. 4.2.1) can be summarized as follows:

1. Nitro-nitrato species characterized by the bands at 1620 and 1581 cm^{-1} decompose to NO_2 up to 300^0C;
2. In the temperature range between 300 and 350^0C the concentration of NO_2 significantly decreases. New bands at 1883, 1779, 1618 and 1546 (shoulder) cm^{-1} are detected after heating at 350^0C;
3. Rising the temperature to 400^0C leads to complete disappearance of NO_2 and desorption of surface species. Formation of NO and N_2O (at 450^0C) in the gas phase is evidenced.
4. After cooling the closed IR cell to RT bands at 1912, 1815 and 1602 cm^{-1} are detected. The latter band is not symmetric and accommodates a shoulder at about 1640 cm^{-1}. Only the band at 1610 cm^{-1} is detected after evacuation.

On the bases of these experimental results it can be concluded that the interaction of methane with pre-adsorbed NO_x compounds has occurred at 350^0C. The "blank NO_x" (Fig. 4.2.2, A) and "blank CH_4" (4.2.2, C) experiments confirm this conclusion. The "blank CH_4" experiment shows that NO_x-free catalyst can activate methane at 200^0C. The valuable information in the "blank NO_x" experiment is that NO_2 is present in the gas phase at all temperatures studied. The bands obtained in the sample spectrum at 350^0C (Fig. 4.2.1, A) can

be assigned to multicarbonyls of cobalt in zero oxidation state (1883 and 1779 cm^{-1}) [286] and carbonates (1618 and 1546 cm^{-1}) [282].

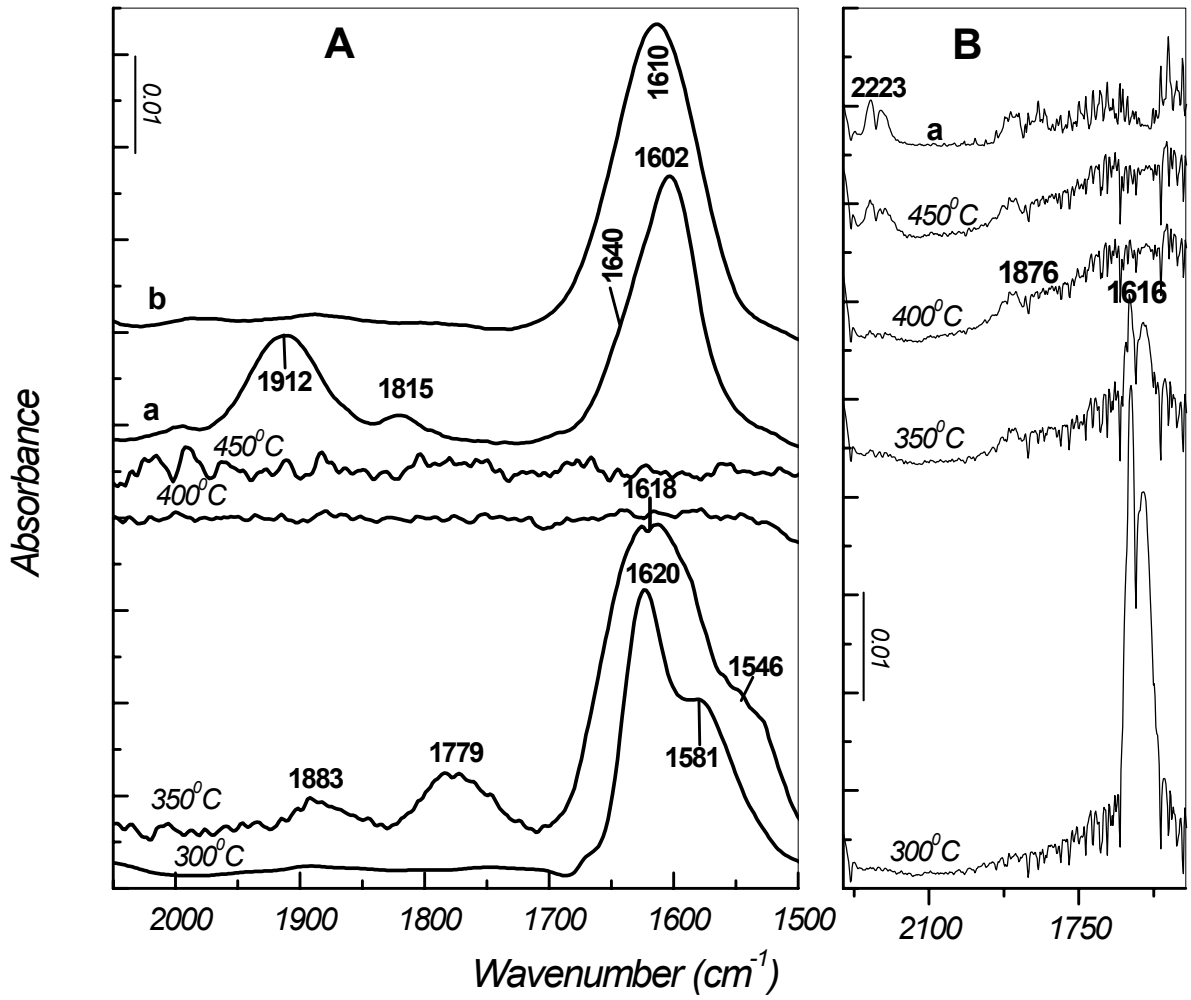

Figure 4.2.1. FT-IR spectra of 1 wt% Co-Si-SZr (Zr/Si = 28) catalyst taken after addition of NO/O_2 mixture (16 Torr, $NO:O_2$ = 1:1) for 30 min at RT followed by evacuation and addition of 50 Torr methane, after heating of the closed IR cell for 20 min and then cooling to RT (a), subsequently evacuation of the gas phase at RT (b). The spectrum of the activated sample is used as a background reference. Gas phases are subtracted from spectra. (B) Gas phase spectrum of the corresponding spectrum shown on panel A.

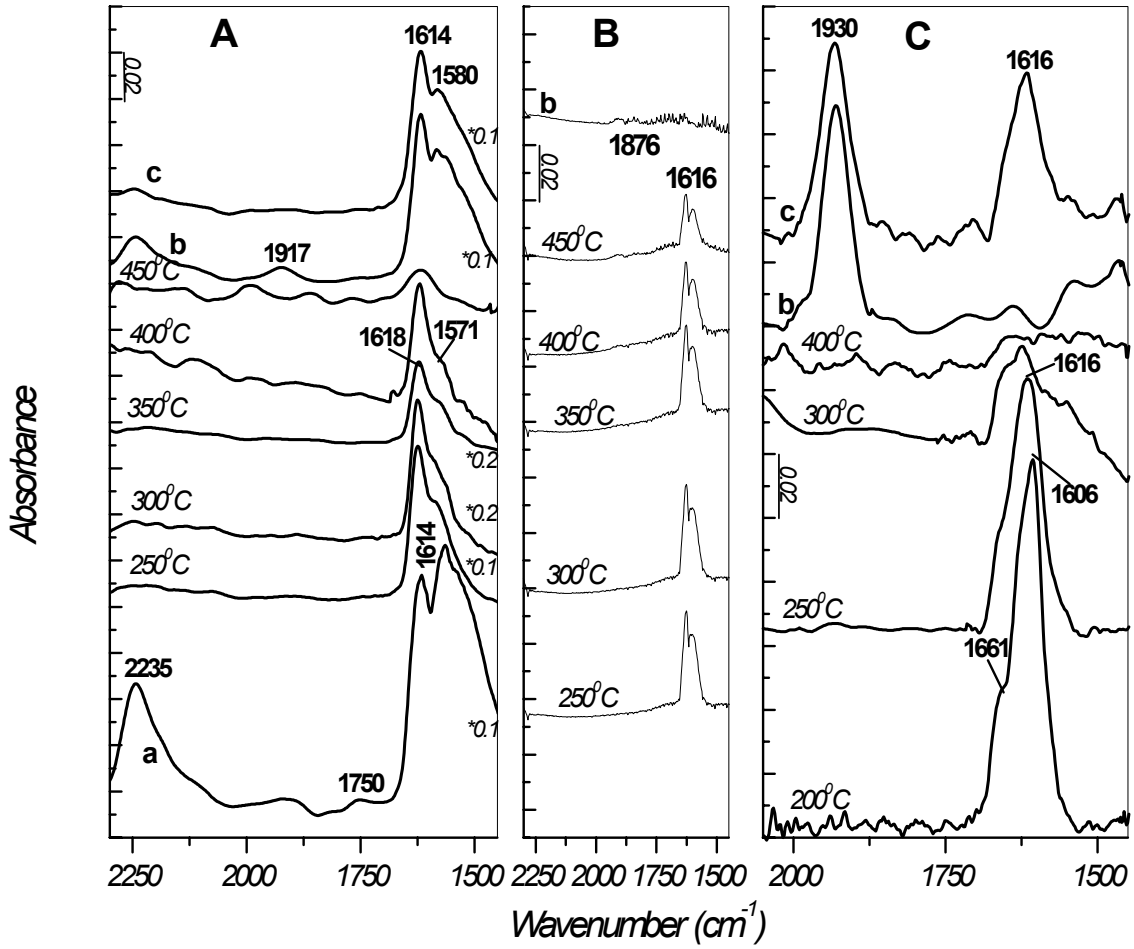

Figure 4.2.2. (A) FT-IR spectra of 1 wt% Co-Si-SZr (Zr/Si = 28) catalyst taken after adsorption of NO/O_2 mixture (16 Torr, $NO:O_2$ = 1:1) for 30 min at RT followed by evacuation (a) and after heating of the closed IR cell for 20 min, then cooling to RT (b), and evacuation of the gas phase (c). (B) Gas phase spectrum of the corresponding spectrum shown on panel A. (C) FT-IR spectra of 1 wt% Co-Si-SZr (Zr/Si = 28) catalyst taken after addition of 50 Torr methane at RT, followed by heating of the closed IR cell for 20 min and then cooling to RT (b), and evacuation of the gas phase (c). The spectrum of the activated sample is used as a background reference. Gas phases are subtracted from spectra.

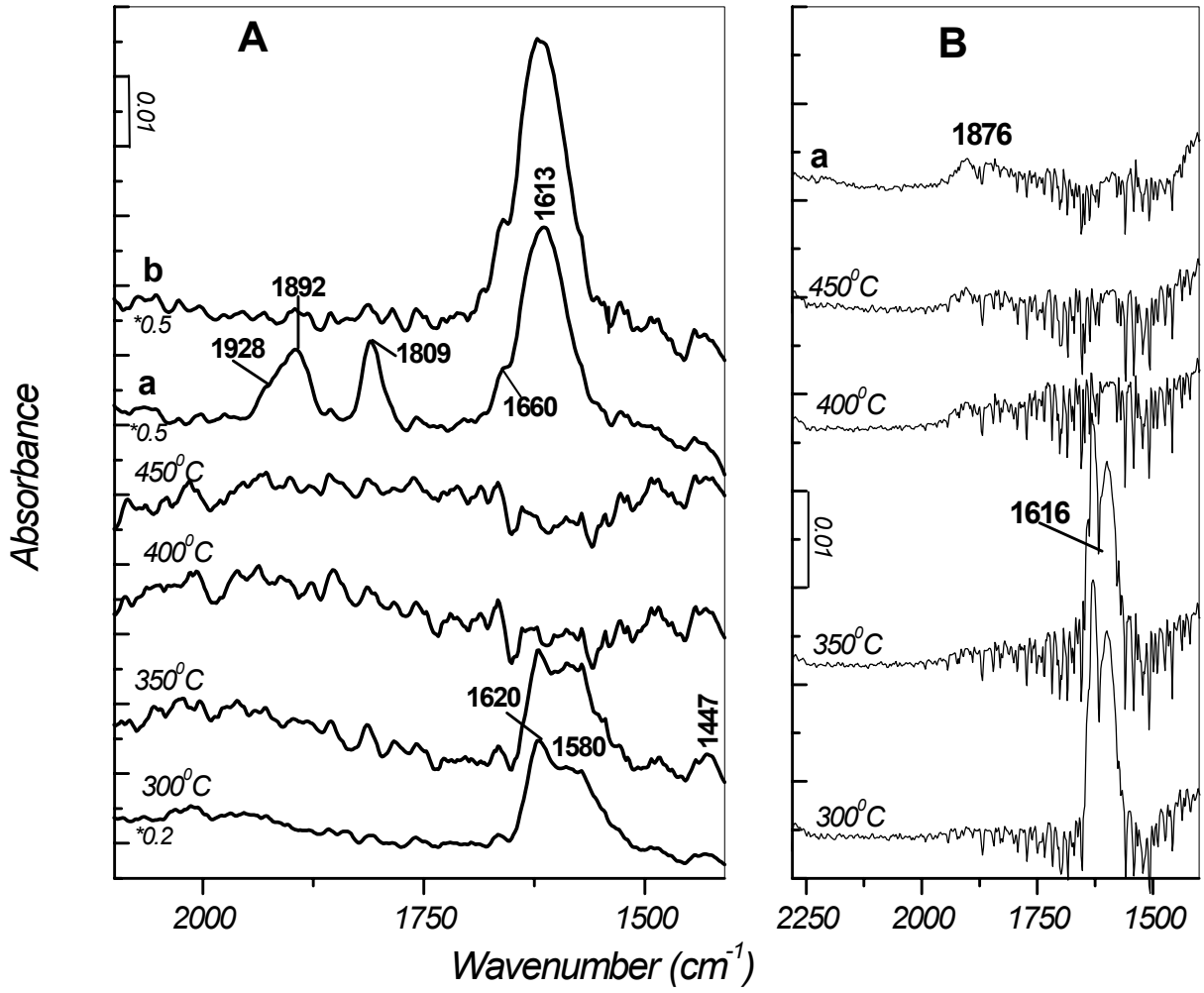

Figure 4.2.3. FT-IR spectra of 6 wt% Co-Si-SZr (Zr/Si = 3) catalyst taken after addition of NO/O_2 mixture (16 Torr, $NO:O_2$ = 1:1) for 30 min at RT followed by evacuation and addition of 50 Torr methane, after heating of the closed IR cell for 20 min and then cooling to RT (a), subsequently evacuation of the gas phase at RT (b). The spectrum of the activated sample is used as a background reference. Gas phases are subtracted from spectra. (B) Gas phase spectrum of the corresponding spectrum shown on panel A.

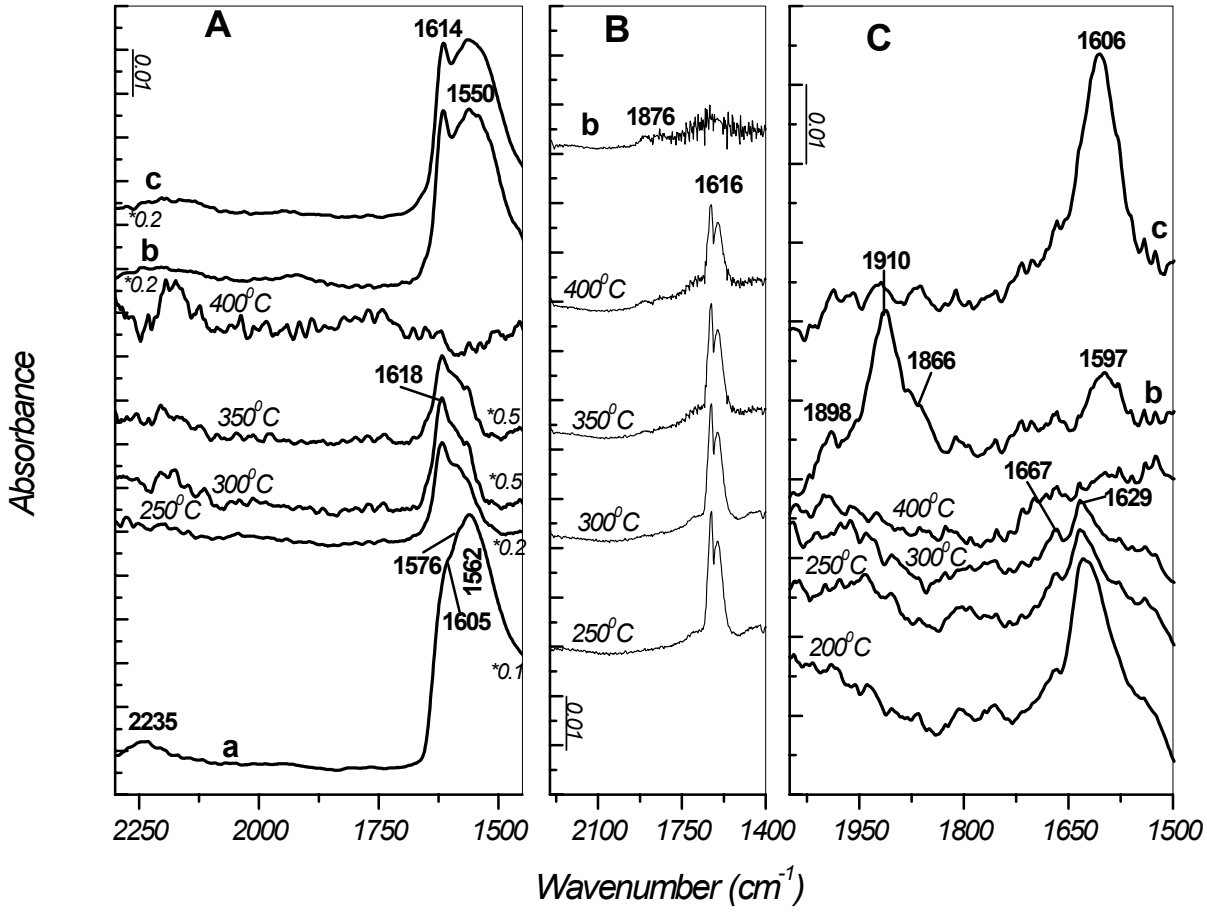

Figure 4.2.4. (A) FT-IR spectra of 6 wt% Co-Si-SZr (Zr/Si = 3) catalyst taken after adsorption of NO/O_2 mixture (16 Torr, $NO:O_2$ = 1:1) for 30 min at RT followed by evacuation (a) and after heating of the closed IR cell for 20 min, then cooling to RT (b), and evacuation of the gas phase (c). (B) Gas phase spectrum of the corresponding spectrum shown on panel A. (C) FT-IR spectra of 6 wt% Co-Si-SZr (Zr/Si = 3) catalyst taken after addition of 50 Torr methane at RT, followed by heating of the closed IR cell for 20 min and then cooling to RT (b), and evacuation of the gas phase (c). The spectrum of the activated sample is used as a background reference. Gas phases are subtracted from spectra.

The bands at 1912 and 1815 cm^{-1}, which appear upon cooling to RT, could be attributed to both nitrosyls of Co(II) and/or two-, tribriged carbonyls of metallic cobalt. The latter assignment can be ruled out by the fact that multicoordinated carbonyl complexes are stable upon evacuation [282]. This is also confirmed by the stability of the band at 1932 cm^{-1} obtained after final evacuation in the "blank CH_4" experiment (Fig.4.2.2, C). Thus, the bands in question correspond to Co(II)-nitrosyls [248-250] as has been observed earlier in the Section 3.9. The strong band at 1602 cm^{-1} is due to superimposed carbonates, formate (1640 cm^{-1}) and water. The formate species can appear as a result of nucleophilic attack of the surface hydroxyls by CO [290].

Analysis of the in situ FT-IR data acquired during heating of NO_x precovered 6 wt%-Co-Si-SZr , where Zr/Si = 3 (Fig. 4.2.3) and 2 (Fig. 4.2.5), in the presence of methane show similar trends, but several differences should be pointed out. The consumption of NO_2 takes place at higher temperatures. In the case of sample with Zr/Si = 3, NO_2 disappears between 350 and 400^0C, when Zr/Si = 2, the concentration of NO_2 decreases in the same temperature range, but the complete consumption takes place between 400 and 450^0C. The bands assigned to Co(II)-nitrosyls are more complex indicating the presence of cobalt sites in different environment. This correlates well with the data reported in the Section 3.9 and the literature [248]. No N_2O is detected, when cobalt loading is high.

In summary, CH_4 interaction with NO_2 over Co-Si-SZr catalysts occurs at elevated temperatures (i) 350^0C on the zirconia rich catalyst with 1 wt% cobalt loading; (ii) between 400 and 450^0C on the Si-SZr supports with low Zr/Si ratios and high cobalt loading. Interaction of NO_2 with methane suggests the formation of C-N-O (organonitrogen) intermediate, as, for instance, nitromethane in the case of Pd-Si-SZr catalysts.

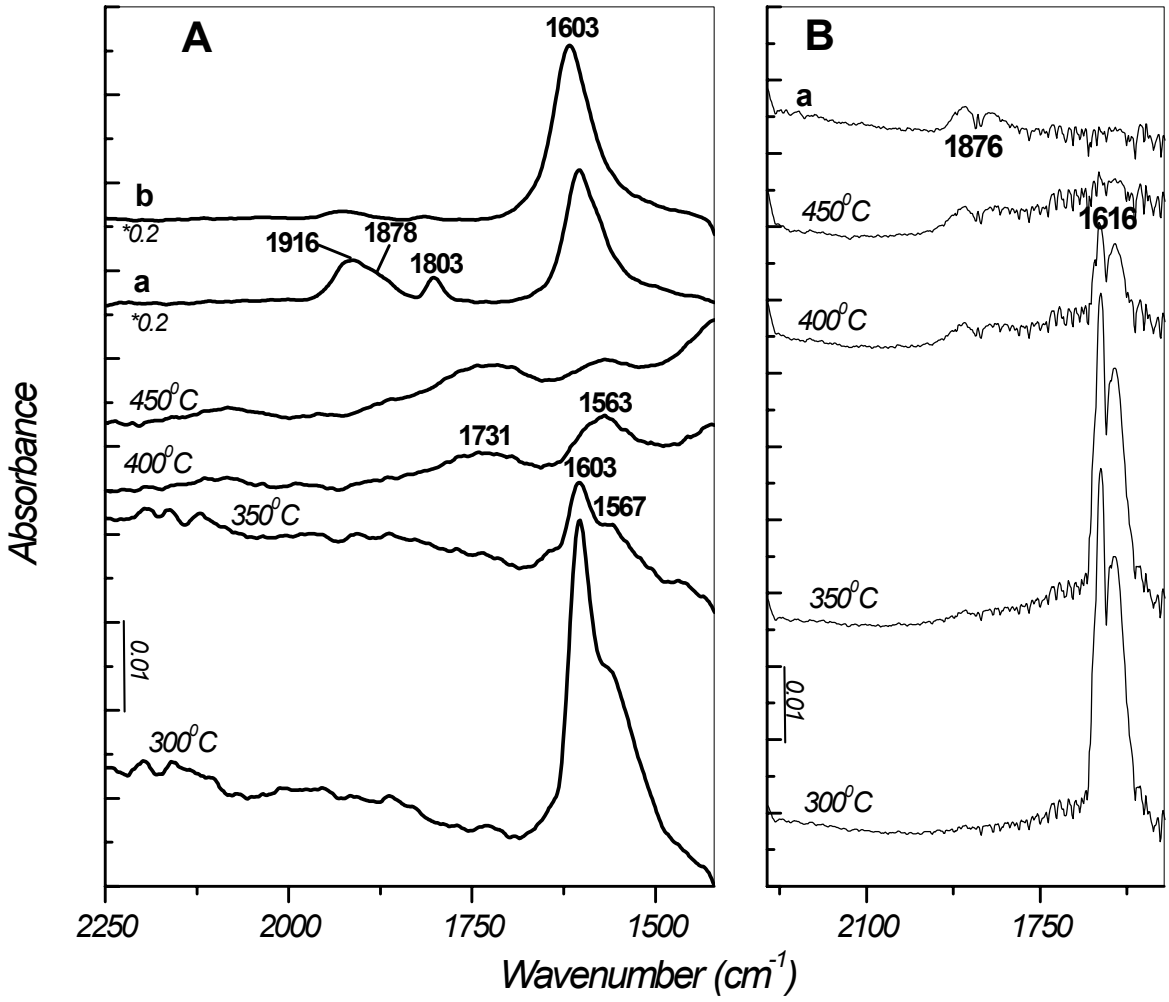

Figure 4.2.5. FT-IR spectra of 6 wt% Co-Si-SZr (Zr/Si = 2) catalyst taken after addition of NO/O_2 mixture (16 Torr, $NO:O_2$ = 1:1) for 30 min at RT followed by evacuation and addition of 50 Torr methane, after heating of the closed IR cell for 20 min and then cooling to RT (a), subsequently evacuation of the gas phase at RT (b). The spectrum of the activated sample is used as a background reference. Gas phases are subtracted from spectra. (B) Gas phase spectrum of the corresponding spectrum shown on panel A.

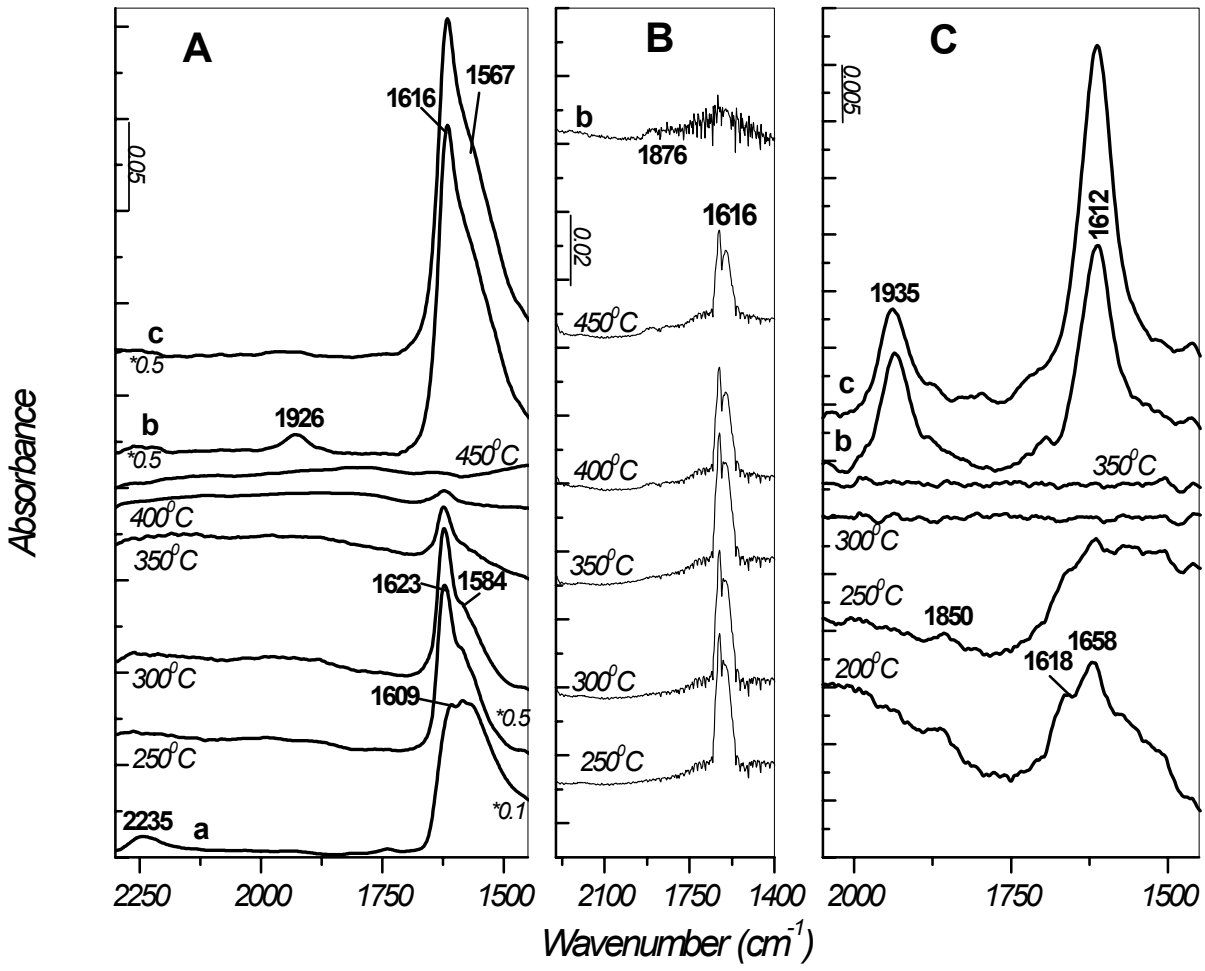

Figure 4.2.6. (A) FT-IR spectra of 6 wt% Co-Si-SZr (Zr/Si = 2) catalyst taken after adsorption of NO/O_2 mixture (16 Torr, $NO:O_2$ = 1:1) for 30 min at RT followed by evacuation (a) and after heating of the closed IR cell for 20 min, then cooling to RT (b), and evacuation of the gas phase (c). (B) Gas phase spectrum of the corresponding spectrum shown on panel A. (C) FT-IR spectra of 6 wt% Co-Si-SZr (Zr/Si = 2) catalyst taken after addition of 50 Torr methane at RT, followed by heating of the closed IR cell for 20 min and then cooling to RT (b), and evacuation of the gas phase (c). The spectrum of the activated sample is used as a background reference. Gas phases are subtracted from spectra.

However, no such species have been detected in the course of the "CH_4-NO_x" reaction on the Co-Si-SZr catalysts. It might be due to several reasons: low concentration of organonitrogen species, their instability on the surface at high temperatures, the interaction takes place so fast that only end products (CO_x, H_2O, NO) can be detected in our set-up, the reaction proceeds through the different paths or homogeneous interaction between CH_4 and NO_2 occurs. The question whether catalyzed homogeneous or surface reaction occurs has attracted a great attention in the literature. Homogeneous reactions in CH_4-O_2-NO_2 [257, 291-292], CH_4-O_2-NO [257], CH_4-O_2 mixtures were studied to monitor gas phase activation of methane. The interaction between CH_4 and NO_2 in the gas phase occurred between 450 and 500^0C [257], formation of partial oxidation products of methane - methanol and formaldehyde were detected at 460 and 480^0C, respectively [292]. According to theoretical study [291] the onset temperature for CH_4-O_2-NO_2 reaction was 427^0C and 487^0C for CH_4-O_2 mixture. It was proposed that NO_2 is stronger oxidizing agent than O_2 [257, 293], therefore the interaction temperature of CH_4 with NO_2 is lowered. Hall et al. [257] pointed out that CH_4-NO_2 reaction took place in the empty reactor between 400 and 450^0C, while in the presence of Co-ZSM-5 the reaction was catalysed between 350 and 400^0C. The authors have observed NO as a main product of NO_2 reduction, while the simultaneous conversion to N_2 was low. Busca et al. [294] reported that CH_4-SCR activity of Co-H-MFI appears mostly above 400^0C, when competing reaction of NO oxidation to NO_2 becomes less thermodynamically favored. On the other hand, Co-SA catalyst was inactive in CH_4-SCR.

The preliminary tests performed at our experimental conditions in the empty IR cell are shown in Figure 4.2.7.

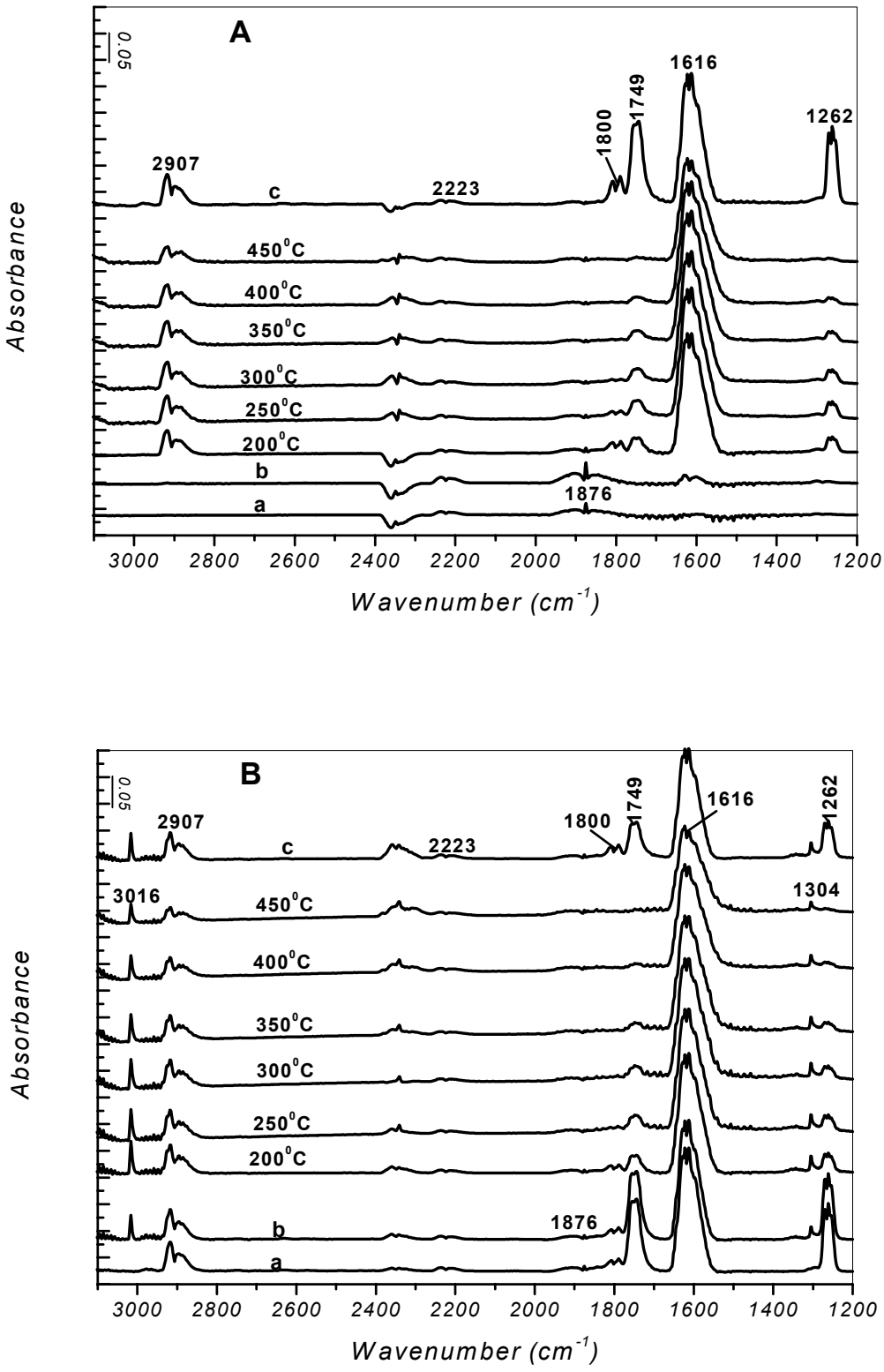

Figure 4.2.7. Gas phase FTIR spectra of (A) 8 Torr NO (a), NO/O_2 (16 Torr, 1:1 ratio) (b), heated at elevated temperatures, then cooled to RT (c); (B) NO/O_2 (16 Torr, 1:1 ratio) (a), after addition of 50 Torr CH_4 (b), heated at different temperatures, then cooled to RT (c).

It can be seen that spectra obtained during heating of the $NO-O_2-CH_4$ mixture (Fig. 4.2.7, B) in the absence of a catalyst closely resemble those obtained for the $NO-O_2$ mixture (Fig. 4.2.7, A). Only negligible amount of CO_2 is detected in the former case, which might suggest, but does not prove that combustion of methane takes place.

4.3. Interaction of Methane with NO_x Compounds Adsorbed on Pd-Promoted Co-Si-SZr Catalysts.

In this section transformation of NO_x complexes adsorbed on Pd-Co-Si-SZr in the presence of methane is investigated. In an attempt to envisage the effect of cobalt in the interaction of CH_4 with NO_x species pre-adsorbed on the bimetallic catalyst the concentration of cobalt is varied. The experimental results have shown that methane interacts with the NO_x precovered Pd-Si-SZr catalysts. The interaction temperature is indicated by the consumption of NO_2 gas, which takes place at ca. 250^0C. The products of the hydrocarbon oxidation are carbonate-carboxylate species and water, while NO_2 is reduced to N_2. In the case of Co-Si-SZr catalysts the light off temperature is also matched to the temperature of NO_2 disappearance, which lay between 350 and 400^0C. Among the reaction products Co^{2+}-nitrosyls, carbonate-carboxylate species and water have been detected.

4.3.1. Pd/Co > 1

The surface NO_x species are created at room temperature by co-adsorption of NO and O_2 in the 1:1 ratio for 30 min followed by evacuation. Then 50 Torr methane is added and the closed IR cell is heated for 20 min at different temperatures. NO_2 gas is produced at elevated temperatures as preadsorbed NO_x species start to decompose (Fig. 4.3.1.1, B). Heating of the closed IR cell containing 1 wt% Pd-0.7 wt% Co-Si-SZr (Zr/Si = 3) catalyst at 300^0C leads to complete disappearance of NO_2. This result suggests that the NO_2 is consumed interacting with the methane. In the spectrum recorded at 300^0C (Fig. 4.3.1.1, A) bands at 2067, 1838, 1608, 1563 and 1443 cm^{-1} have formed. Simultaneous increase in intensity of the band at 1838 cm^{-1} and decrease in intensities of the bands at 1608 and 1563 cm^{-1} is observed after

heating between 300 and 350^{0}C. The absorption between 1650 and 1520 cm^{-1} is complex and difficult to resolve (see spectrum at 350^{0}C Fig. 4.3.1.1, A).

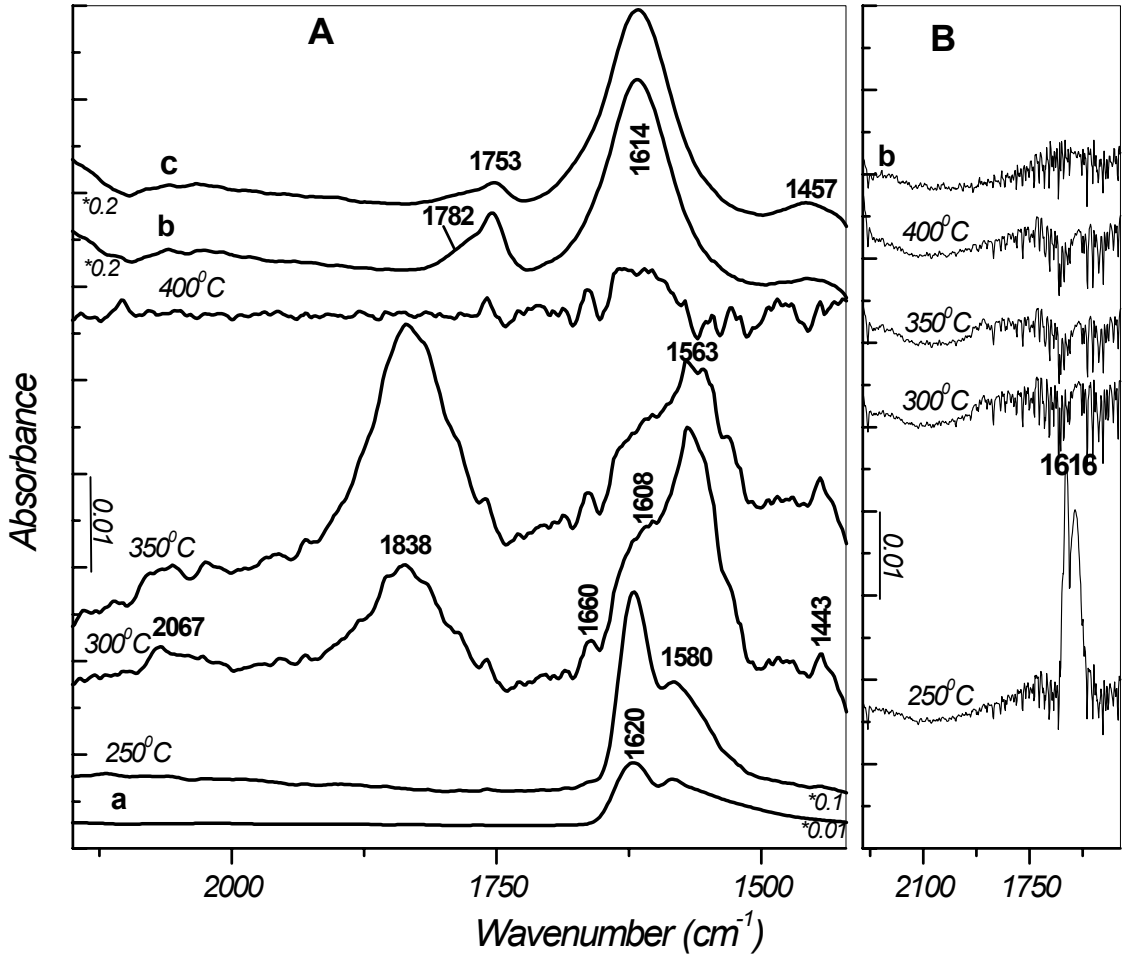

Figure 4.3.1.1. FT-IR spectra of the 1 wt% Pd-0.7 wt% Co-Si-SZr (Zr/Si = 28) catalyst taken after addition of NO/O_2 mixture (16 Torr, $NO:O_2$ = 1:1) for 30 min at RT followed by evacuation and addition of 50 Torr methane (a), after heating of the closed IR cell for 20 min and then cooling to RT (b), subsequently evacuation of the gas phase at RT (c). The spectrum of the activated sample is used as a background reference. Gas phases are subtracted from spectra. (B) Gas phase spectrum of the corresponding spectrum shown on panel A.

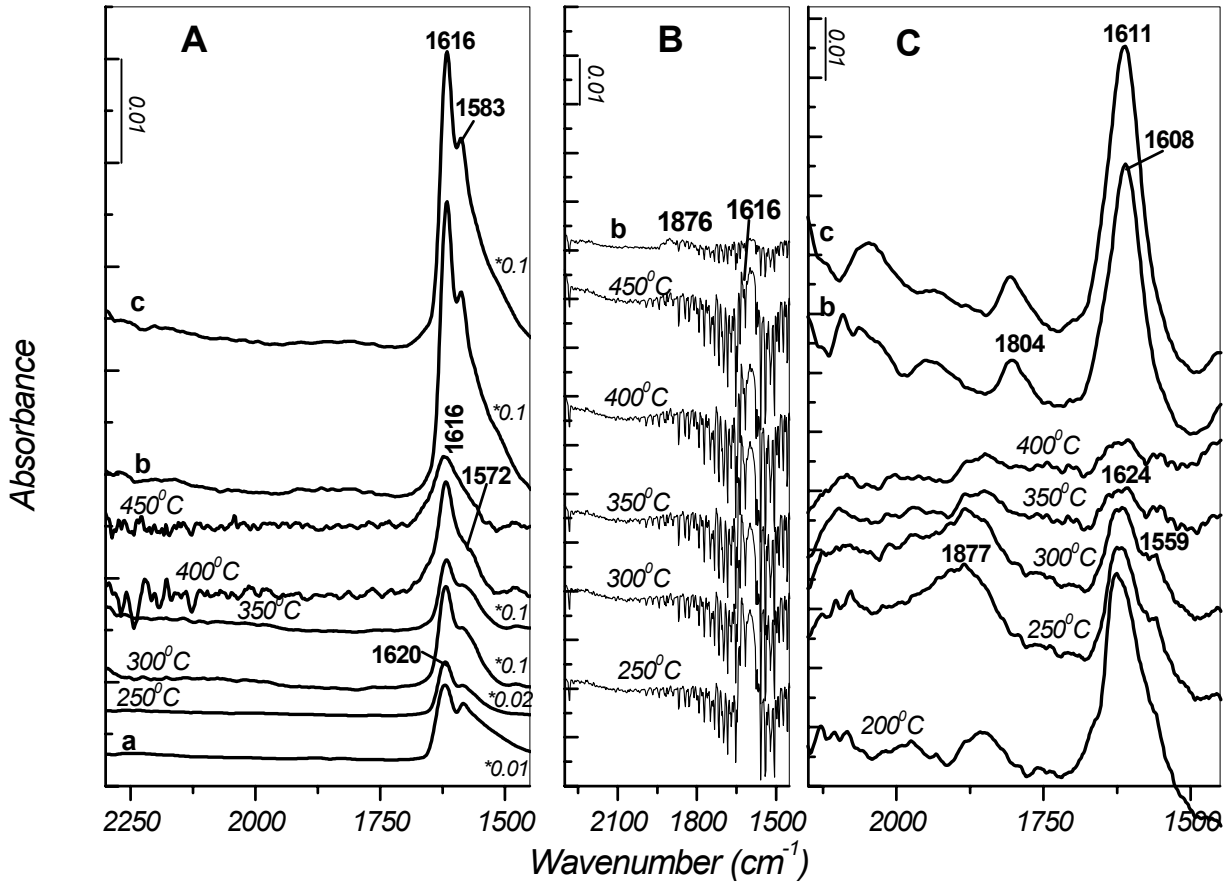

Figure 4.3.1.2. (A) FT-IR spectra of 1 wt% Pd-0.7 wt% Co-Si-SZr (Zr/Si = 3) catalyst taken after adsorption of NO/O_2 mixture (16 Torr, $NO:O_2$ = 1:1) for 30 min at RT followed by evacuation (a) and after heating of the closed IR cell for 20 min, then cooling to RT (b), and evacuation of the gas phase (c). (B) Gas phase spectrum of the corresponding spectrum shown on panel A. (C) FT-IR spectra of 1wt% Pd-0.7 wt% Co-Si-SZr (Zr/Si = 3) catalyst taken after addition of 50 Torr methane at RT, followed by heating of the closed IR cell for 20 min and then cooling to RT (b), and evacuation of the gas phase (c). The spectrum of the activated sample is used as a background reference. Gas phases are subtracted from spectra.

Comparing the spectra acquired at 300 and 350^{0}C it can be concluded that decomposition products adsorbed at 1838 cm^{-1} and between 1650 and 1520 cm^{-1} of compounds defined by the peaks at 1608 and 1563 cm^{-1} are present already at 300^{0}C. The bands at 1608 and 1563 cm^{-1} can best be assigned to the organonitrogen intermediates i.e. cis-methyl nitrite and nitro methane, respectively [269, 278-280]. The Pd^+-NO (at 1838 cm^{-1}) [278-280] is one of the decomposition products of cis-methyl nitrite. Heating to 400^{0}C causes disappearance of all adsorbed species. Bands detected after cooling to RT appear at 1782 (shoulder), 1752 cm^{-1} due to Pd^+-NO and Pd^0-NO, respectively, [247, 283-285] or organic-like carbonates [282] and strong band at 1614 cm^{-1} attributed to superimposed carbonate-carboxylate compounds [282] and water. Recalling the data accumulated on the cobalt-free Pd-Si-SZr catalyst (Fig. 4.1.1.1), it should be pointed out that in the latter case the depletion of NO_2 in the gas phase starts between 250 and 300^{0}C and it is no longer observed at temperatures higher than 350^{0}C. Subsequently, the spectrum of adsorbed species at 300^{0}C looks different, namely, only two distinct bands at 1613 and 1564 cm^{-1} ascribed to the organonitrogen compounds are observed. These experimental facts lead to supposition that processes of the formation of the primary intermediates and their decomposition occurs faster on the cobalt-containing Pd-Si-SZr catalyst. The results of the "CH_4-NO_x", "blank NO_x" and "blank CH_4" experiments are compared in Figure 4.3.1.3. The spectra obtained after the methane interaction with the NO_x-precovered and NO_x-free 1 wt% Pd-0.7 wt% Co-Si-SZr (Zr/Si = 3) catalyst are similar, which shows that the main products in both cases are adsorbed carbonate-carboxylate species and water. The higher intensity of the bands in the case of "CH_4-NO_x" experiment implies that more methane has been oxidized.

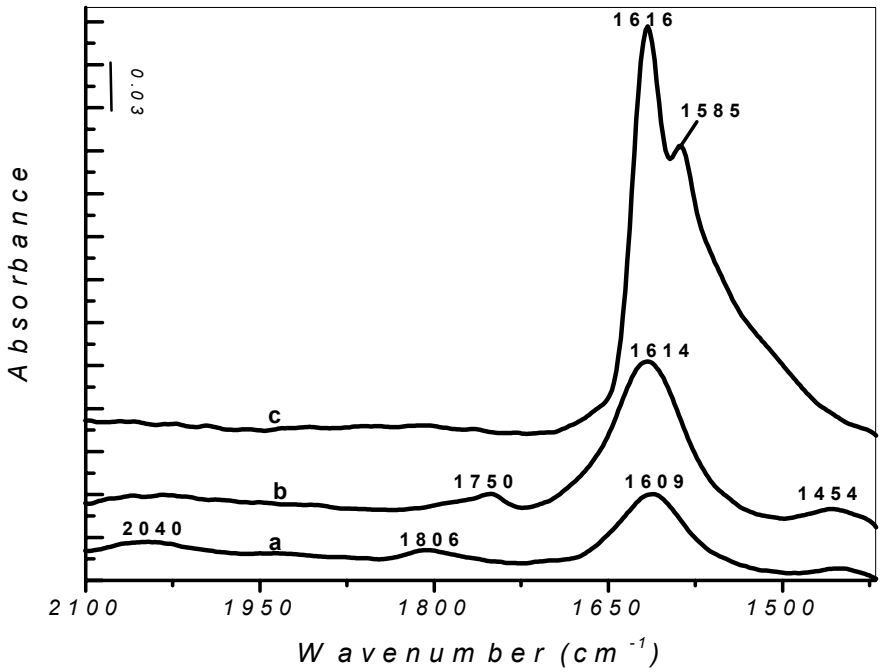

Figure 4.3.1.3. The FT-IR spectra of the1 wt% Pd-0.7 wt% Co-Si-SZr (Zr/Si=3) catalyst taken from the "blank CH_4" (a), the interaction of the preadsorbed NO_x with methane (b) and "blank NO_x" (c) experiments after cooling to RT followed by evacuation. The spectrum of activated sample is used as a reference. Gas phases are subtracted from spectra.

The results of "CH_4-NO_x" experiment on the 0.5 wt% Pd-0.25 wt% Co-Si-SZr catalyst are displayed in Fig. 4.3.1.4. Gaseous phase spectra show decrease in intensity of the NO_2 band at 1616 cm^{-1} and simultaneous appearance of NO (1876 cm^{-1}) and N_2O (2220 cm^{-1}) at temperature as low as 250^0C. The shape of the sample spectrum at 250^0C (Fig. 4.3.1.4, A) resembles that of nitro-nitrato species observed at 200^0C. After the next heating step (300^0C) broad intense absorption at 1840 cm^{-1} and complex bands centered at 1609 and 1555 cm^{-1} are evidenced together with disappearance of NO_2 gas. In the spectrum at 350^0C formation of carbonyls on metallic cobalt at 1966 cm^{-1} [286], Pd^0-NO at 1752 cm^{-1} [283-285], $(Pd^0)_2$-NO at 1677 cm^{-1} [286], carbonate-carboxylate compounds at 1616 cm^{-1} and monocoordinated carbonate at 1514 cm^{-1} [282, 295] as well as disappearance of NO and N_2O strongly suggest

that primary intermediates have completely decomposed and selective conversion of NO/N_2O to dinitrogen has occurred.

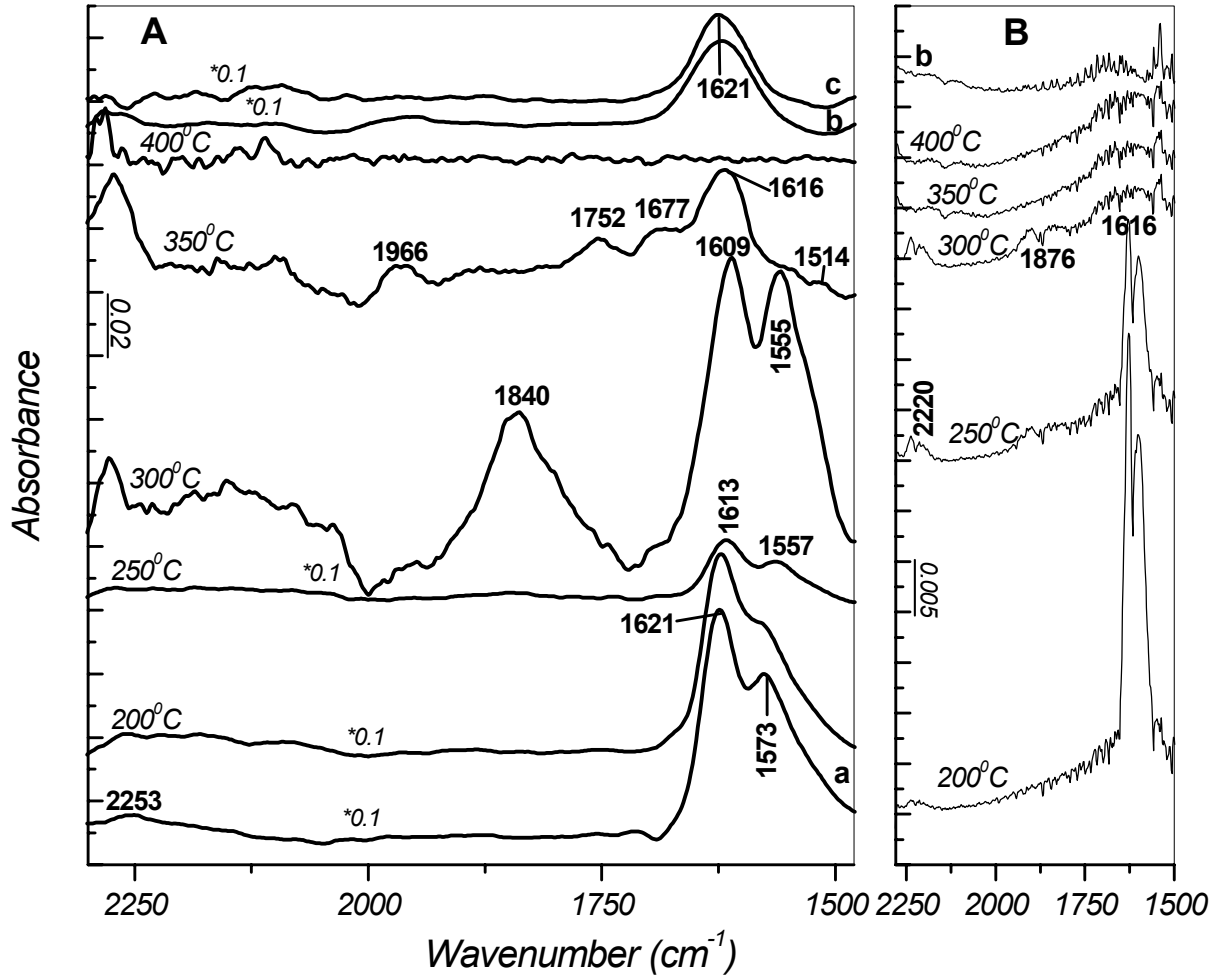

Figure 4.3.1.4. FT-IR spectra of the 0.5 wt% Pd-0.25 wt% Co-Si-SZr (Zr/Si = 28) catalyst taken after addition of NO/O_2 mixture (16 Torr, $NO:O_2$ = 1:1) for 30 min at RT followed by evacuation and addition of 50 Torr methane (a), after heating of the closed IR cell for 20 min and then cooling to RT (b), subsequently evacuation of the gas phase at RT (c). The spectrum of the activated sample is used as a background reference. Gas phases are subtracted from spectra. (B) Gas phase spectrum of the corresponding spectrum shown on panel A.

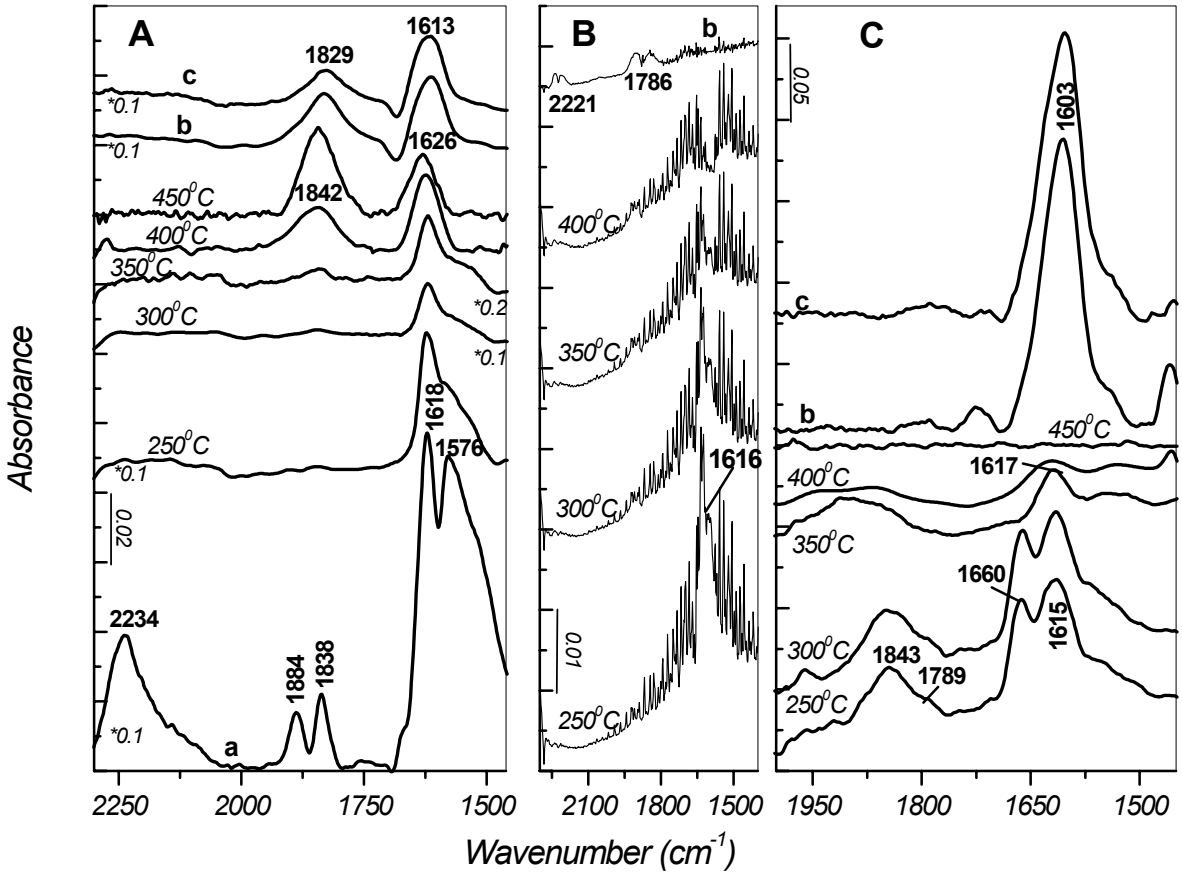

Figure 4.3.1.5. (A) FT-IR spectra of 1 wt% Pd-0.25 wt% Co-Si-SZr (Zr/Si = 3) catalyst taken after adsorption of NO/O_2 mixture (16 Torr, $NO:O_2$ = 1:1) for 30 min at RT followed by evacuation (a) and after heating of the closed IR cell for 20 min, then cooling to RT (b), and evacuation of the gas phase (c). (B) Gas phase spectrum of the corresponding spectrum shown on panel A. (C) FT-IR spectra of 1wt% Pd-0.25 wt% Co-Si-SZr (Zr/Si = 3) catalyst taken after addition of 50 Torr methane at RT, followed by heating of the closed IR cell for 20 min and then cooling to RT (b), and evacuation of the gas phase (c). The spectrum of the activated sample is used as a background reference. Gas phases are subtracted from spectra.

All species desorb after heating at 400^0C. Strong band at 1621 cm^{-1} has formed, when sample is cooled to RT. It can be attributed to superimposed carbonate-carboxylate species and water.

By comparing the results obtained in the "CH_4-NO_x" experiment on the cobalt-free and cobalt-containing Pd-Si-SZr (Zr/Si = 28) catalysts between 250 and 400^{0}C it can be outlined that the interaction of methane with NO_2 begins at 250^{0}C, CH_3NO_2 and cis-CH_3ONO have completely decomposed and CO_x and N_2 have formed at 350^{0}C in the case of cobalt-supported Pd-promoted catalyst, whereas on the Pd-Si-SZr catalyst these processes occur at higher temperatures. In conclusion, surface interaction of methane with NO_x compounds on the Pd-Co-Si-SZr with low cobalt loading occurs in the same way as on the Pd-Si-SZr, but at slightly lower temperatures.

4.3.2. Pd/Co ≤ 1

Figure 4.3.2.1 displays the results obtained during the heating of the preadsorbed NO_x species on 1wt% Pd-1 wt% Co-Si-SZr (Zr/Si = 3) in the atmosphere of methane. The spectral changes in the each heating step are outlined below:

150 – 250^{0}C: the surface nitro-nitrato compounds (bands at 1621 and 1582 cm^{-1}) gradually decompose and NO_2 gas is produced;

250 – 300^{0}C: decrease in concentration of NO_2 is accompanied by the formation of new bands at 1619 and 1567 cm^{-1}. The intensity of the latter band is slightly higher than that of the former one, whereas in the "blank NO_x" experiment (Fig. 4.3.2.2, A) the ratio of the relative intensities of the bands at 1618 and 1567 cm^{-1} is reverse;

300 – 350^{0}C: broad band at 1806 cm^{-1} and complex absorption with maxima at about 1613 and 1561 cm^{-1} are observed. NO_2 is completely consumed;

350 – 400^{0}C: all adsorbed species leave the surface;

Back to RT: carbonate-carboxylate compounds superimposed with water appear at 1618 cm^{-1} and a weak band at 1760 cm^{-1} is formed. These bands resist evacuation.

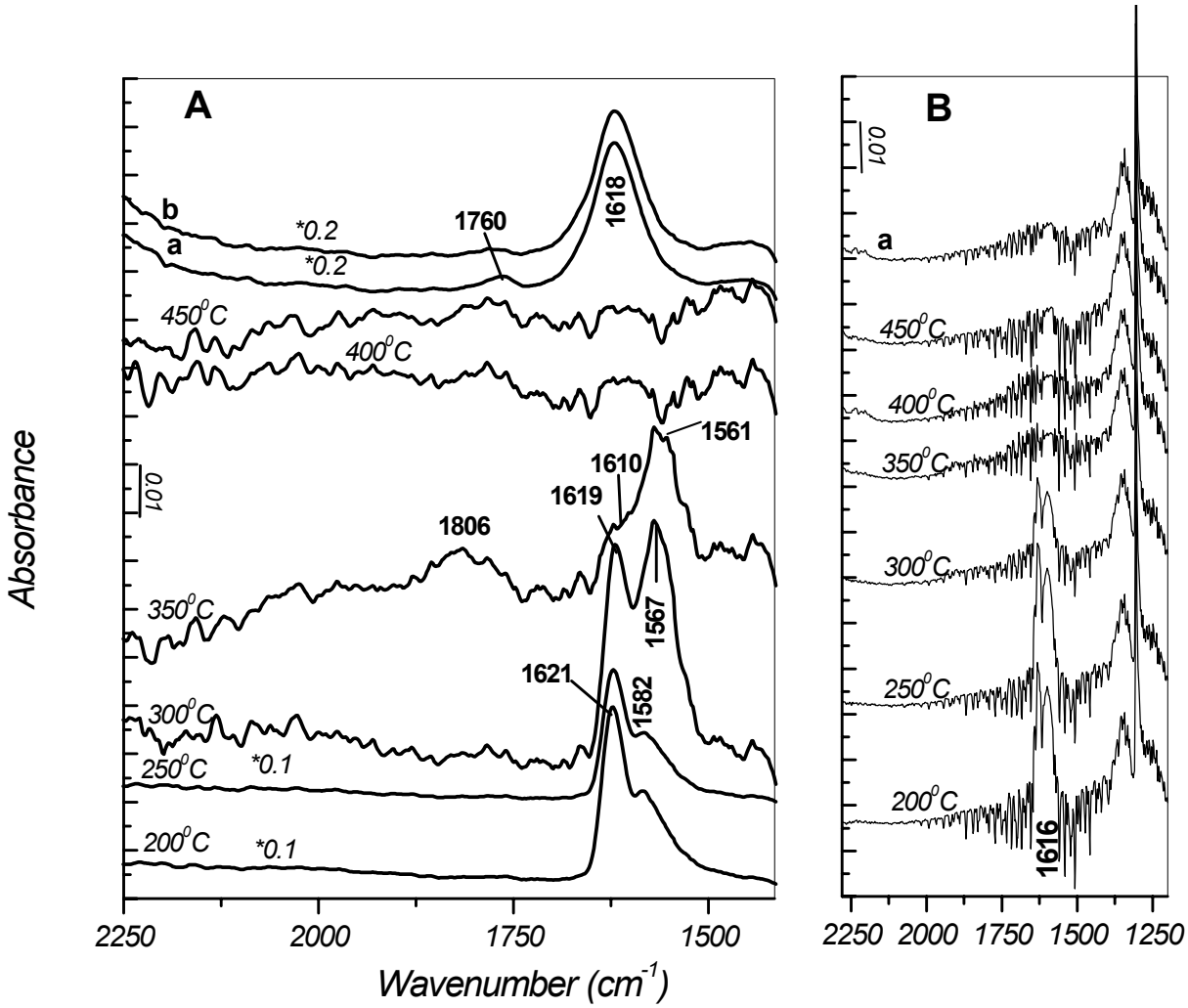

Figure 4.3.2.1. FT-IR spectra of 1 wt% Pd-Si-SZr (Zr/Si = 3) catalyst taken after addition of NO/O_2 mixture (16 Torr, $NO:O_2$ = 1:1) for 30 min at RT followed by evacuation and addition of 50 Torr methane, after heating of the closed IR cell for 20 min and then cooling to RT (a), subsequently evacuation of the gas phase at RT (b). The spectrum of the activated sample is used as a background reference. Gas phases are subtracted from spectra. (B) Gas phase spectrum of the corresponding spectrum shown on panel A.

The trend of this experiment closely resembles that observed on the cobalt-free 1 wt% Pd-Si-SZr catalyst (Figure 4.1.1.1). It is interesting to notice that the results of the "blank NO_x" and "blank CH_4" experiments are alike on both samples.

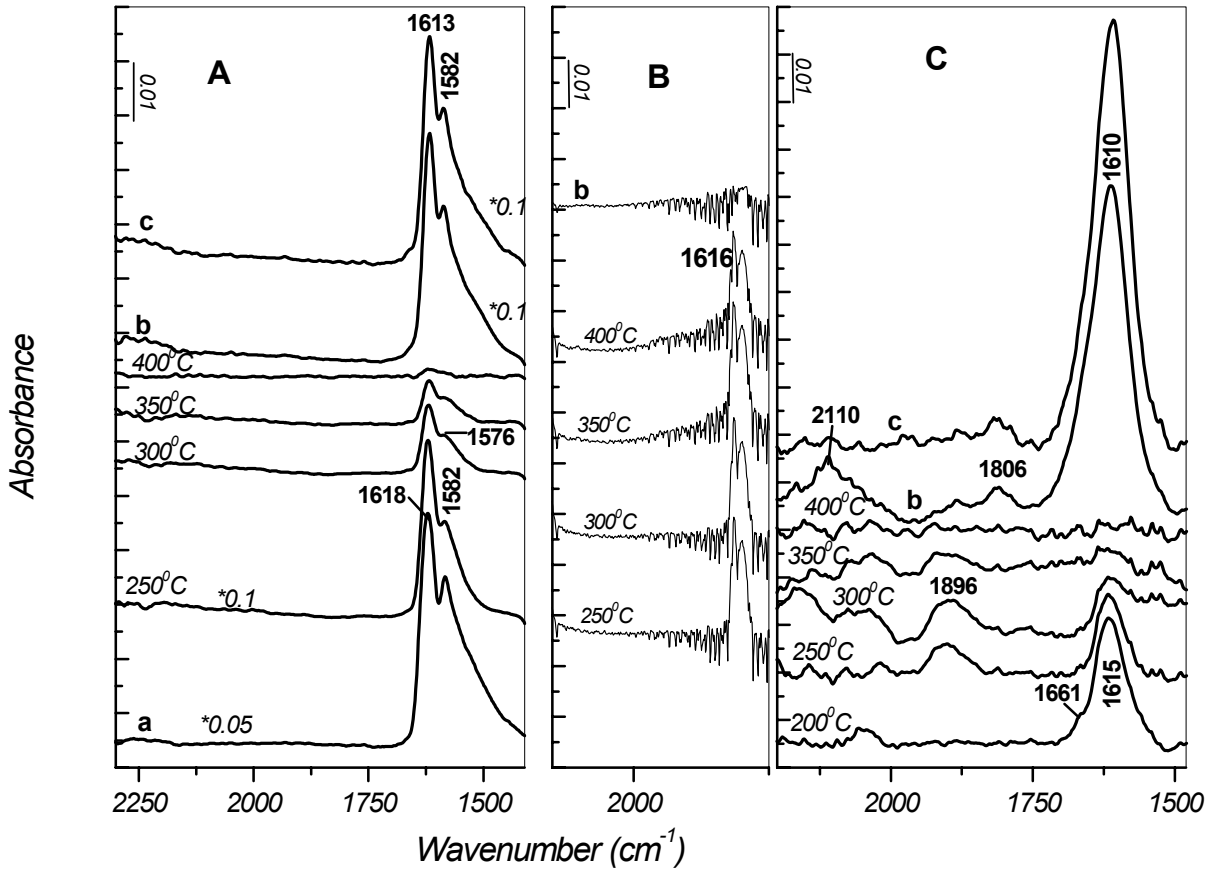

Figure 4.3.2.2. (A) FT-IR spectra of 1 wt% Pd-1 wt% Co-Si-SZr (Zr/Si = 3) catalyst taken after adsorption of NO/O_2 mixture (16 Torr, $NO:O_2$ = 1:1) for 30 min at RT followed by evacuation (a) and after heating of the closed IR cell for 20 min, then cooling to RT (b), and evacuation of the gas phase (c). (B) Gas phase spectrum of the corresponding spectrum shown on panel A. (C) FT-IR spectra of 1wt% Pd-1 wt% Co-Si-SZr (Zr/Si = 3) catalyst taken after addition of 50 Torr methane at RT, followed by heating of the closed IR cell for 20 min and then cooling to RT (b), and evacuation of the gas phase (c). The spectrum of the activated sample is used as a background reference. Gas phases are subtracted from spectra.

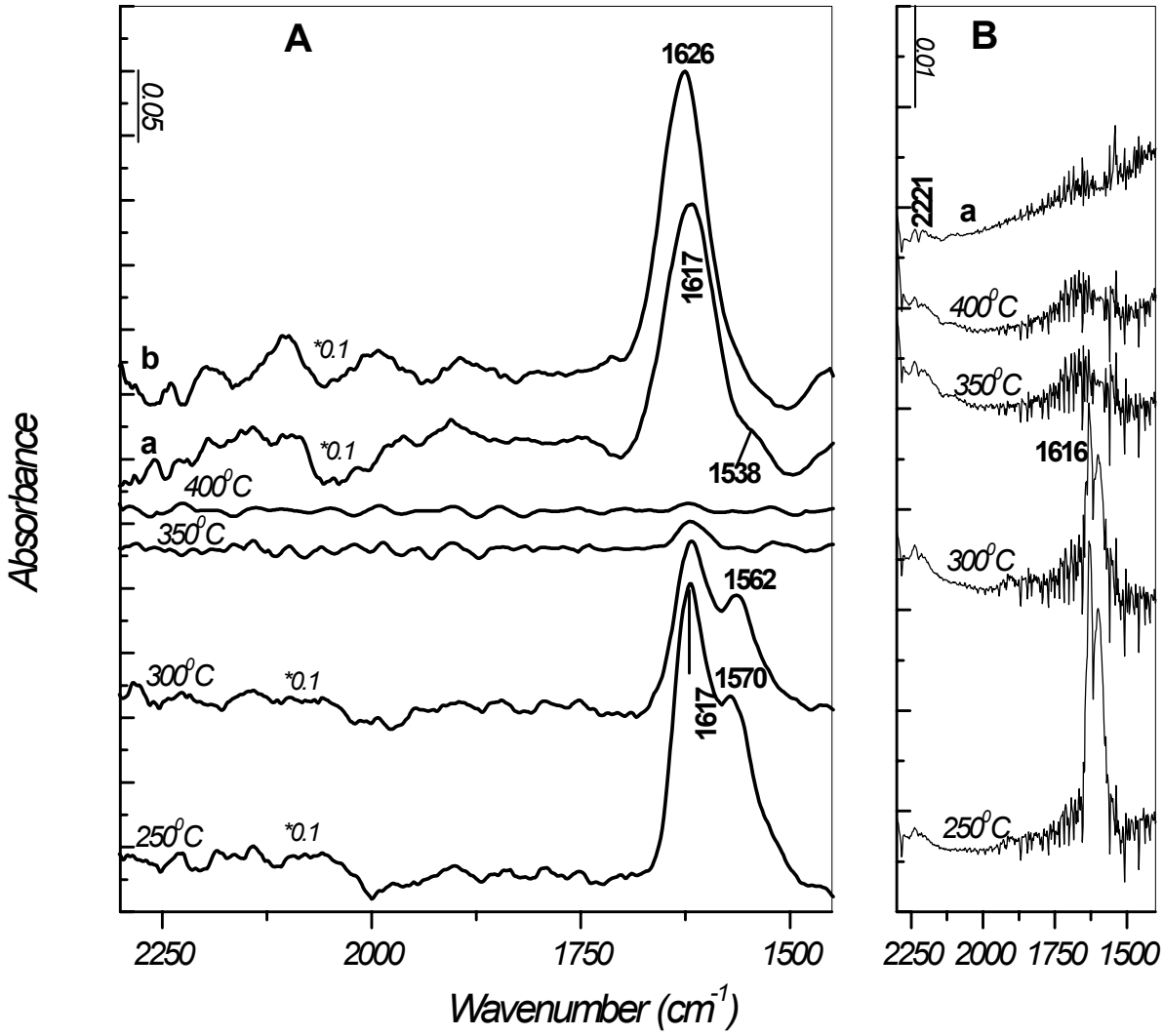

Figure 4.3.2.3. FT-IR spectra of 0.5 wt% Pd-1 wt% Co-Si-SZr (Zr/Si = 28) catalyst taken after addition of NO/O_2 mixture (16 Torr, $NO:O_2$ = 1:1) for 30 min at RT followed by evacuation and addition of 50 Torr methane, after heating of the closed IR cell for 20 min and then cooling to RT (a), subsequently evacuation of the gas phase at RT (b). The spectrum of the activated sample is used as a background reference. Gas phases are subtracted from spectra. (B) Gas phase spectrum of the corresponding spectrum shown on panel A.

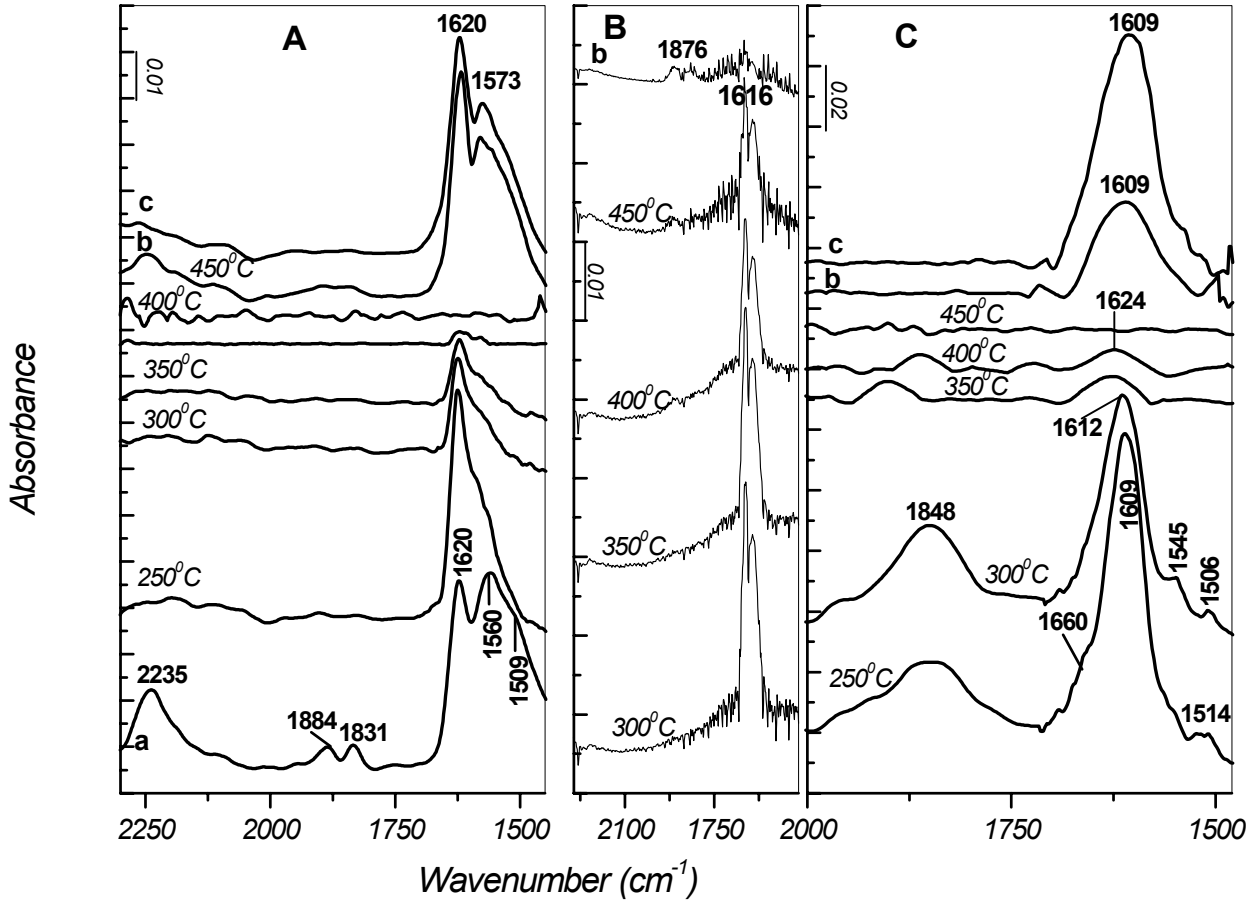

Figure 4.3.2.4. (A) FT-IR spectra of 0.5 wt% Pd-1 wt% CoSi-SZr (Zr/Si = 28) catalyst taken after adsorption of NO/O_2 mixture (16 Torr, $NO:O_2$ = 1:1) for 30 min at RT followed by evacuation (a) and after heating of the closed IR cell for 20 min, then cooling to RT (b), and evacuation of the gas phase (c). (B) Gas phase spectrum of the corresponding spectrum shown on panel A. (C) FT-IR spectra of 0.5 wt% Pd-1 wt% Co-Si-SZr (Zr/Si = 28) catalyst taken after addition of 50 Torr methane at RT, followed by heating of the closed IR cell for 20 min and then cooling to RT (b), and evacuation of the gas phase (c). The spectrum of the activated sample is used as a background reference. Gas phases are subtracted from spectra.

FT-IR spectra displayed in the Figure 4.3.2.3 show the behavior of NO_x compounds adsorbed on 0.5 wt% Pd-1 wt% Co-Si-SZr (Zr/Si = 28) catalyst in the presence of methane. The decrease in intensity of the NO_2 band between 250 and 300^{0}C (Fig. 4.3.2.3, A) suggests that

interaction with methane has taken place. N_2O is also detected at 300^0C. The spectrum of the catalyst resembles that of the residual nitro-nitrato species. Heating to 350^0C results in the complete disappearance of NO_2 gas and formation of carbonate-carboxylate compounds (bands at 1617 and 1520 cm^{-1} [282]). These bands desorb, when further heated to 400 and 450^0C. A single strong band at 1617 cm^{-1} appears after cooling to RT. Thus, when Si-SZr (Zr/Si = 28) support is modified with 1 wt% cobalt followed by impregnation of 0.5 wt% palladium, the consumption of NO_2 begins at temperature by ~50^0C higher than on the cobalt-free palladium-promoted support.

4.3.3. Pd/Co « 1

Figure 4.3.3.1 displays FT-IR spectra of the "CH_4-NO_x" experiment performed on the 1wt% Pd-6 wt% Co-Si-SZr (Zr/Si = 3). The amount of NO_2 is noticed to decrease at 300^0C and to completely disappear at 350^0C. The sample spectrum at 300^0C shows two intense poorly resolved bands centered at 1611 and 1582 cm^{-1} with low frequency component at 1660 cm^{-1} and a weak band at 1475 cm^{-1}. At 350^0C the absorption between 1670 and 1500 cm^{-1} broadens and the intensity of the band at 1621 cm^{-1} decreases relative to that of the band at 1582 cm^{-1}, barely noticeable absorption appears at around 1830 cm^{-1}. After cooling to RT bands at 1762 cm^{-1} and at 1623 cm^{-1} are observed. The latter band due to water superimposed with carbonate-carboxylate species resists evacuation.

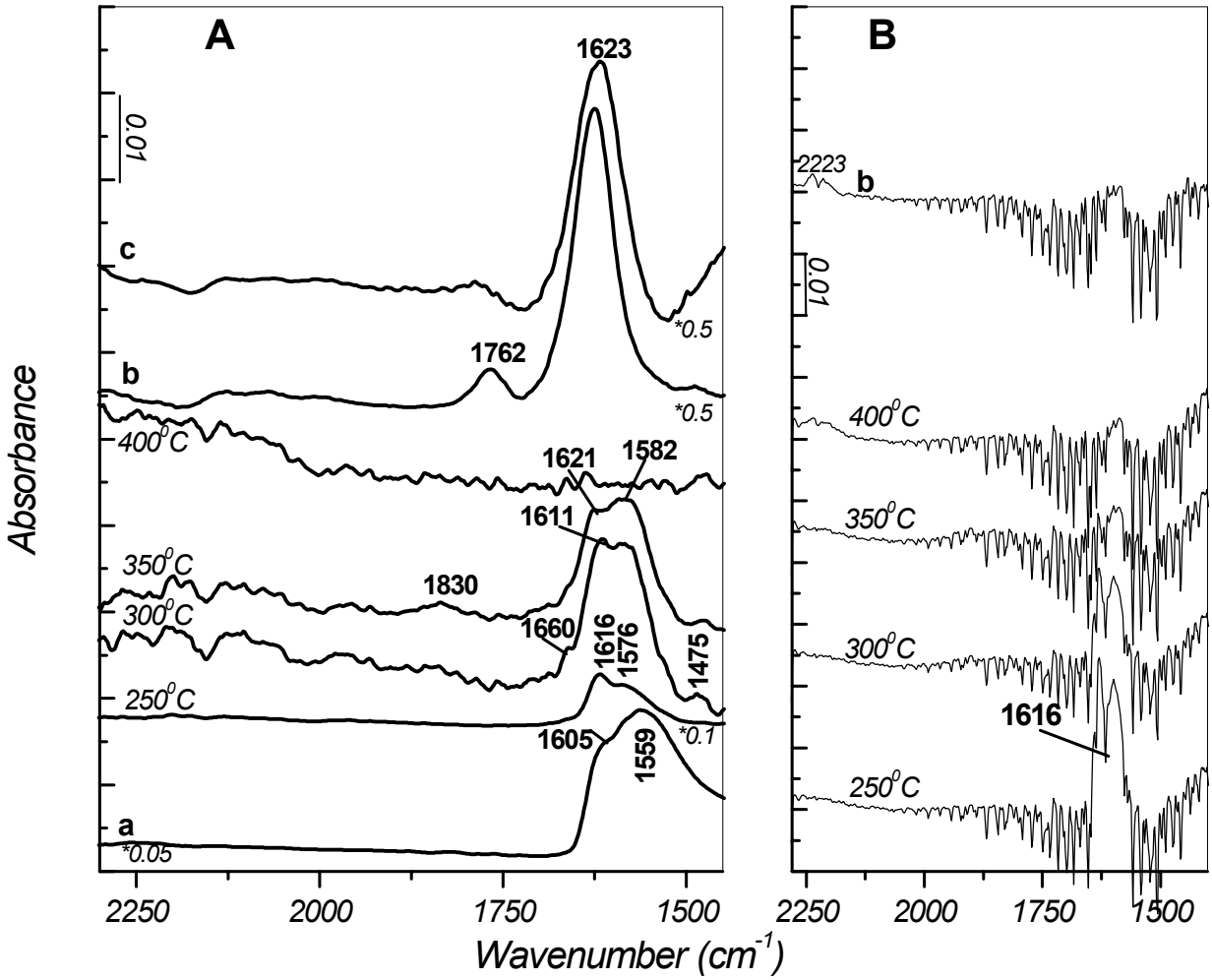

Figure 4.3.3.1. FT-IR spectra of 1 wt% Pd-6 wt% Co-Si-SZr (Zr/Si = 3) catalyst taken after addition of NO/O_2 mixture (16 Torr, $NO:O_2$ = 1:1) for 30 min at RT followed by evacuation and addition of 50 Torr methane (a), after heating of the closed IR cell for 20 min and then cooling to RT (b), subsequently evacuation of the gas phase at RT (c). The spectrum of the activated sample is used as a background reference. Gas phases are subtracted from spectra. (B) Gas phase spectrum of the corresponding spectrum shown on panel A.

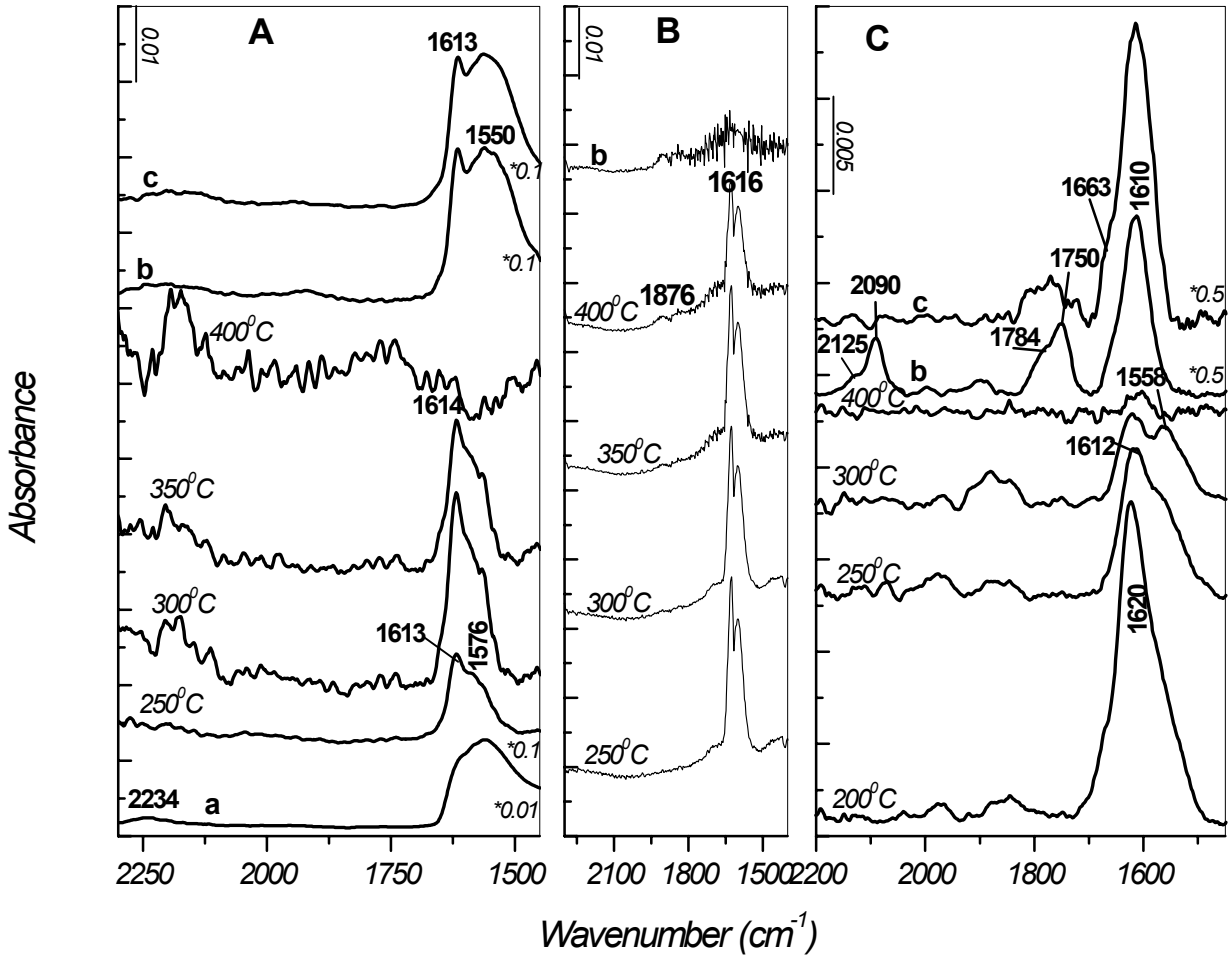

Figure 4.3.3.2. (A) FT-IR spectra of 1 wt% Pd-6 wt% CoSi-SZr (Zr/Si = 3) catalyst taken after adsorption of NO/O_2 mixture (16 Torr, $NO:O_2$ = 1:1) for 30 min at RT followed by evacuation (a) and after heating of the closed IR cell for 20 min, then cooling to RT (b), and evacuation of the gas phase (c). (B) Gas phase spectrum of the corresponding spectrum shown on panel A. (C) FT-IR spectra of 1 wt% Pd-6 wt% Co-Si-SZr (Zr/Si = 3) catalyst taken after addition of 50 Torr methane at RT, followed by heating of the closed IR cell for 20 min and then cooling to RT (b), and evacuation of the gas phase (c). The spectrum of the activated sample is used as a background reference. Gas phases are subtracted from spectra.

On the whole, the temperature range of NO_2 consumption and spectral features obtained after cooling to RT are identical for all Pd-Si-SZr catalysts independently on the presence of cobalt and its concentration. It indicates that the reaction of the preadsorbed NO_x species with methane follows the same paths. However, as cobalt loading increases the intermediate reaction products are not resolved. One of the possible explanations of this fact can be that the concentration of intermediates is scares and they are covered by the residual nitro-nitrato compounds at 350^0C. The actual reactions leading to the end products occur at higher temperatures, apparently, between 350 and 400^0C, when all preadsorbed NO_x species leave the surface liberating active sites (see the "blank NO_x" experiment Fig. 4.3.3.2, A).

The interaction of methane with surface NO_x compounds over the 0.3wt% Pd-6 wt% Co-Si-SZr (Zr/Si = 2) has also been investigated (Fig. 4.3.3.3). NO_2 gas is firstly produced by decomposition of nitro-nitrato species, then its concentration decreases upon heating between 300 and 350^0C and it is eventually completely consumed at 400^0C. The spectrum detected at 350^0C displays two bands with comparable intensities at 1607 and 1537 cm^{-1}.Comparison of the corresponding spectra acquired in the "blank NO_x" and "blank CH_4" experiments (Fig. 4.3.3.4, A and C, respectively) suggests that new species have been formed. Moreover, absence of the bands at the same frequencies in the "blank CH_4" experiment rules out the possibility of assigning these species to formates. The new compound can best be assigned to ν_{as} (NO) of CH_3NO_2 (1537 cm^{-1}) and ν (N=O) of cis-CH_3ONO (1607 cm^{-1}) [269, 278-280]. At 450^0C no adsorbed species are detected, but N_2O is present in the gas phase. Cooling to RT leads to appearance of the band at 1598 cm^{-1}, while the gas phase spectrum does not change. The intensity of the band increases upon evacuation. This band is tentatively assigned to bidentate formate species, which form on the surface of oxides as a result of nucleophilic attack of the basic OH groups on the coordinated CO molecule [290].

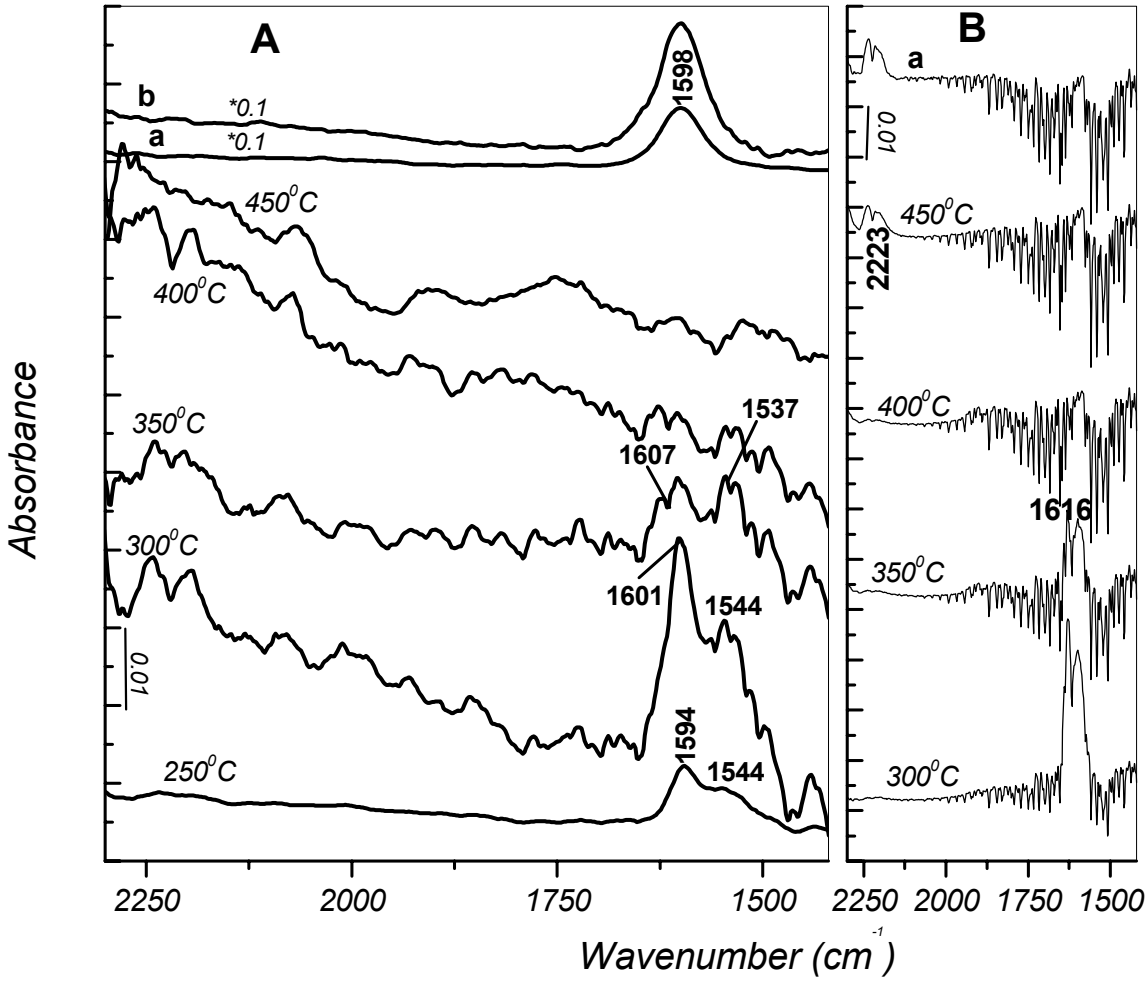

Figure 4.3.3.3. FT-IR spectra of 0.3 wt% Pd-6 wt% Co-Si-SZr (Zr/Si = 2) catalyst taken after addition of NO/O_2 mixture (16 Torr, $NO:O_2$ = 1:1) for 30 min at RT followed by evacuation and addition of 50 Torr methane, after heating of the closed IR cell for 20 min and then cooling to RT (a), subsequently evacuation of the gas phase at RT (b). The spectrum of the activated sample is used as a background reference. Gas phases are subtracted from spectra. (B) Gas phase spectrum of the corresponding spectrum shown on panel A.

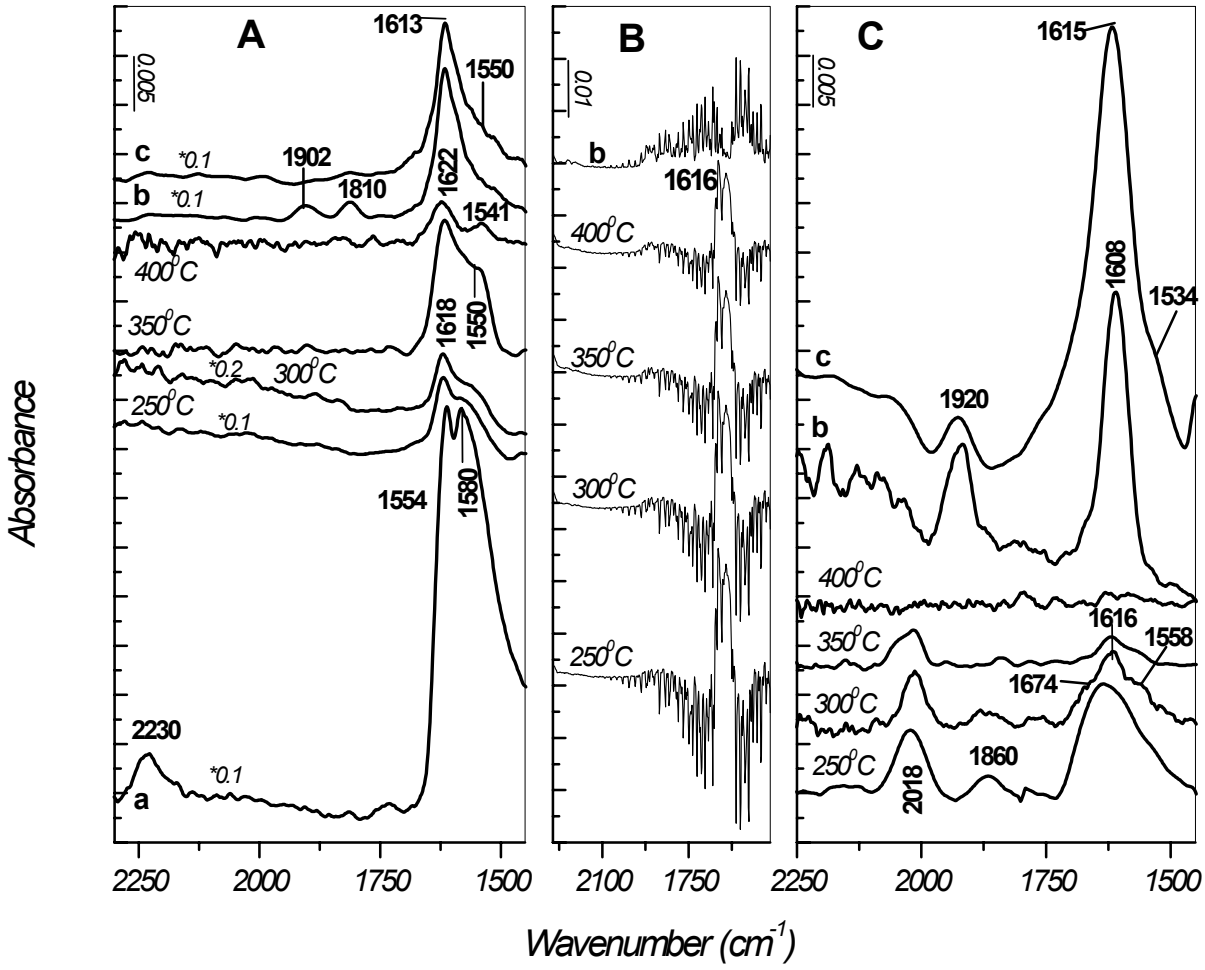

Figure 4.3.3.4. (A) FT-IR spectra of 0.3 wt% Pd-6 wt% CoSi-SZr (Zr/Si = 2) catalyst taken after adsorption of NO/O_2 mixture (16 Torr, $NO:O_2$ = 1:1) for 30 min at RT followed by evacuation (a) and after heating of the closed IR cell for 20 min, then cooling to RT (b), and evacuation of the gas phase (c). (B) Gas phase spectrum of the corresponding spectrum shown on panel A. (C) FT-IR spectra of 0.3 wt% Pd-6 wt% Co-Si-SZr (Zr/Si = 2) catalyst taken after addition of 50 Torr methane at RT, followed by heating of the closed IR cell for 20 min and then cooling to RT (b), and evacuation of the gas phase (c). The spectrum of the activated sample is used as a background reference. Gas phases are subtracted from spectra.

Addition of 6 wt% cobalt to Pd-Si-SZr catalyst shifts the CH_4-NO_x reaction to higher temperature relative to that detected on the cobalt-free 0.5 wt% Pd-Si-SZr (Zr/Si = 2) catalyst (Fig. 4.1.1.4). This experimental fact indicates that cobalt suppresses the catalytic activity of palladium sites. In general, addition of cobalt to Pd-Si-SZr catalysts affects the onset temperature of CH_4 interaction with NO_2. According to Pd/Co ratio the following trend has been observed: (i) Pd/Co > 1 interaction occurs at about 200 - 250^0C, (ii) Pd/Co ≤ 1 interaction temperature shifts to 300^0C, (iii) Pd/Co « 1 the light off temperature is between 300 and 350^0C.

4.4. Effect of Cobalt and Zirconia on the Efficiency of the Catalyst

In this subsection the results obtained by in-situ FTIR spectroscopic measurements on all catalysts studied are compared. The experimental results acquired in the "CH_4-NO_x" experiment are summarized in Table 4.4.1 and Figure 4.4.1.

The temperatures of NO_2 consumption for each catalyst investigated are schematically displayed in Figure 4.4.1. This temperature is considered to be the onset temperature at which nitrogen dioxide interacts with hydrocarbon. The interaction of NO_2 with CH_4 takes place in the following temperature ranges: between 250 and 300^0C over the Pd-Si-SZr catalysts; between 300 and 450^0C over the Co- Si-SZr catalysts and between 200 and 400^0C over the Pd-Co-Si-SZr catalysts. NO_2 is believed to be a key species in the selective oxidation of methane. All of the catalysts studied have high activity for NO_2 formation. In the case of Pd-Si-SZr catalysts, the occurrence of interaction between CH_4 and NO_2 is evidenced from the presence of organonitrogen (C-N-O) intermediate (Table 4.4.1).

Table 4.4.1. Intermediates and products detected by in-situ FT-IR spectroscopy in the "CH_4-NO_x" experiment on the catalysts studied.

Sample M, wt% / Zr/Si	**Intermediates**						**Products**			
	NO_2[a]	Organonitrogen	nitrosyl	Oxygenates	NO	N_2O	CO_3^{2-} /COO^-	H_2O	nitrosyl	N_2O
0.5 Pd / 2	250[b]	300 (?)[c]	-	350			+	+	-	+
1 Pd / 3	300	300	350	350			+	+	-	-
0.5 Pd / 28	250	300	300, 350	300, 350	300	300	+	+	-	-
1 Pd / 28	250	300 (?)	300	300			+	+	-	-
1 Co /28	350	-	-	350 (?)	400	450	+	+	+	-
6 Co / 2	400	-	-	400 (?)	400, 450		+	+	+	-
6 Co / 3	450	-	-	-	450		+	+	+	-
1 Pd-0.7 Co / 3	250	300	300,350	(?)	-	-	+	+	-	-
0.5 Pd-0.25 Co / 28	250	300 (?)	300,350	300 (?)	250, 300	250, 300	+	+	-	-
1Pd-1 Co / 3	300	300	350	350	-	-	+	+	-	+
0.5 Pd-1 Co / 28	300	(?)	-	(?)	-	300	+	+	-	+
0.3 Pd-6 Co / 2	350	-	-	350 (?)	-	450	+	+	-	+
1Pd-6 Co / 3	300	300 (?)	350	350 (?)	-	-	+	+	-	+

[a]) the temperature above which NO_2 is no longer observed; [b]) temperature, ^{0}C; [c]) bands are weakly resolved; [d]) bands are not resolved
"-" – a species has not been detected; "+" – a species has been observed.

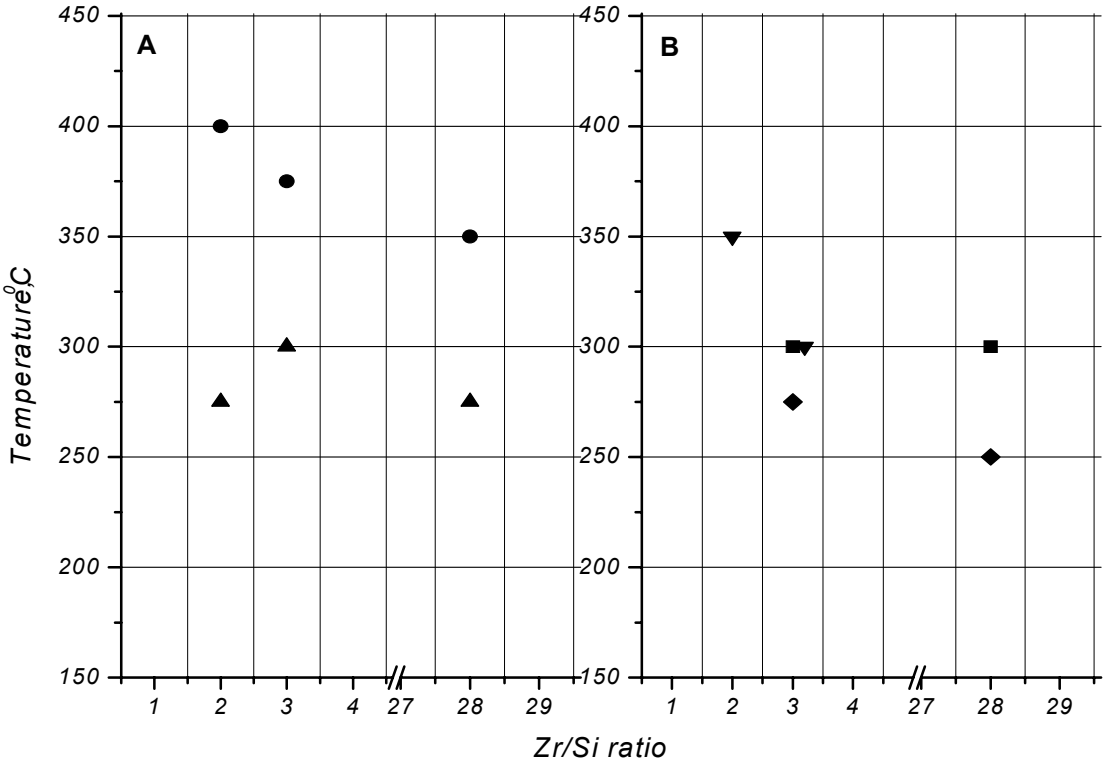

Figure 4.4.1. Temperatures of the NO_2 gas consumption obtained by in-situ FTIR spectroscopy in the "CH_4-NO_x" experiment on the catalysts studied: (A) ▲ - stands for Pd-Si-SZr catalysts, ● - represents Co-Si-SZr catalysts; (B) Pd-Co-supported on Si-SZr, wt% ◆ - represents [Pd] > [Co], ■ - represents [Pd] ≤ [Co] and ▼ - corresponds to [Pd] « [Co]. The mark on the line indicates that concentration of NO_2 has decreased at the temperature below than that indicated by the line, and the complete NO_2 disappearance takes place at temperature above that indicated by the line. The mark inside the rectangular means that NO_2 has completely disappeared in the temperature range limited by the lower and upper lines.

The formation of CO_x, H_2O and absence of nitrogen containing compound in the FTIR spectra taken after cooling to RT implies that the NO_x-precovered catalysts oxidize the methane and can have high activity for NO reduction to N_2. The interaction of CH_4 with NO_2 over the Co-Si-SZr catalysts is evidenced mainly on the bases of the reaction products. These are CO_x,

H_2O and NO. Surface interaction of methane with NO_2 on the Co-Pd-supported Si-SZr samples with low cobalt loading follows the same route as in the case of Co-free catalyst. Hence, the catalysts with cobalt concentrations lower than that of palladium are active and selective for the CH_4-NO_x interaction reaction.

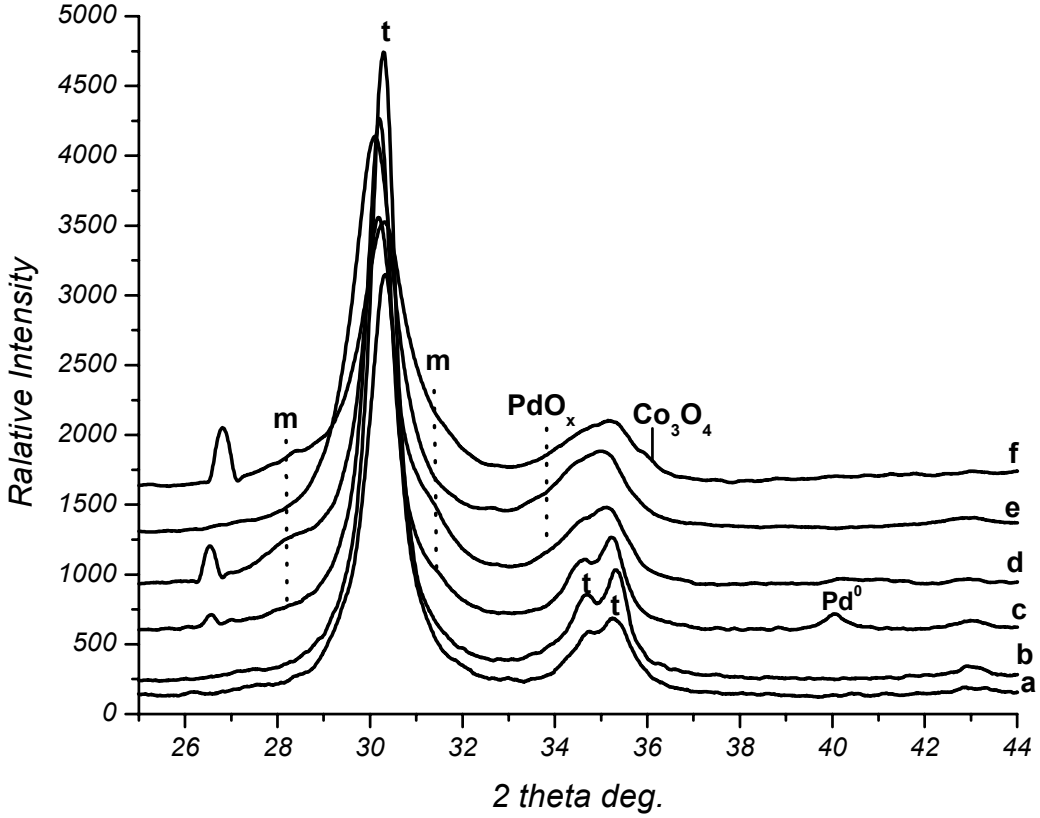

Figure 4.4.2. Powder XRD patterns of calcined (at 550^0C) Si-SZr (Zr/Si = 28) support (a) functionalized with 1 wt% Pd (b), 0.5 wt% Pd-1 wt% Co (e); M-Si-SZr catalyst after the reaction of CH_4 oxidation, where M is 1 wt% Pd (c), 0.5 wt Pd (d), 0.5 wt% Pd-1 wt% Co (f).

When cobalt content is comparable to that of palladium or higher the reaction intermediates are difficult to resolve. Final products are CO_x, H_2O and N_2O. On the bases of the FTIR data it is not possible to say whether N_2 has also formed along with NO and N_2O as

a result of CH_4-NO_x interaction on the cobalt-promoted catalysts. However, the presence of NO and N_2O signals indicate that the efficiency of the catalyst diminishes as cobalt loading in the sample increases. It should be emphasized that transition metal-supported Si-SZr catalyst with the highest Zr/Si ratio of 28 shows the lowest temperatures of NO_2 consumption, when compared with other catalysts studied. In the case of silica rich supports, where amorphous zirconia is stabilized, the efficiency of the catalyst to N_2 decreases. For example, N_2O is formed in the "CH_4-NO_x" experiment over Pd-Si-SZr (Zr/Si = 2) catalyst (Table 4.4.2).

Table 4.4.2. The effect of cobalt loading on the activity and selectivity of the catalysts studied

Pd/Co, wt%	CH_4-NO_2 interaction temperature, ^0C	Selectivity
∞	250	N_2
> 1	200-250	N_2
≤ 1	250	N_2/ N_2O
« 1	250-300	N_2O
0	300-350	NO

The results of the "blank CH_4" experiment have shown that all NO_x-free catalysts investigated activate methane between 200 and 250^0C. NO_x species preadsorbed on the catalyst have similar stability on all samples studied and leave the surface at elevated temperatures between 400 and 450^0C (see the "blank NO_x" experiment).

The XRD data obtained before and after the reaction of methane oxidation (Fig. 4.4.2) show that palladium, cobalt and zirconia have been transformed in the reaction medium. This fact may explain the greater activity of the catalyst with high Zr/Si ratio, where substantial amount of zirconia is in the tetragonal phase.

To the best of our knowledge, no study on Pd-Co-supported oxides in the wide range of Pd/Co ratios has yet been reported in the literature.

5. CONCLUSIONS

1. The facile one-pot synthesis procedure has been developed to prepare silica-zirconia (Si-Zr) mixed oxides through $(I^+)X^-(H^+S^0)$ ion-mediated interaction from the inorganic alkoxides and non-ionic surfactant in a highly acidic aqueous medium. This procedure successfully combines the ideas of the true liquid crystalline templating (TLCT) and sol-gel methodologies. The method allows (i) relatively fast synthesis of the mesostructured materials on the bench top; (ii) variation of the zirconia content between 0 and 100 wt%; (iii) the direct one-step functionalization with inorganic salts in a wide concentration range. We have exploited this procedure to modify Si-Zr with cobalt and sulfate ions, however, it can be readily extended to other precursors. The olygo(ethylene oxide) type non-ionic surfactant or Pluronics mixed with cobalt nitrate systems are highly stable at ambient conditions and upon water evaporation system. It is therefore an excellent structure-directing agent to assemble the inorganic framework.

2. This synthetic method leads to (I) the pure siliceous materials possessing ordered hexagonal bimodal framework with thick walls and large surface area; (II) the silica-zirconia mixed oxides, which are supermicroporous materials with 3D wormlike aperiodical framework of open interconnected pores; (III) an easy incorporation of zirconia into the silica matrix to the large extent; (IV) the uniform distribution of Co^{2+} and SO_4^{2-} ions predominantly on the inner surface of the silica-zirconia (Si-Zr).

3. The amorphous zirconia phase can be stabilized in the calcined (at 550^0C) Si-Zr mixed oxides up to 98 wt% of zirconia loading, whereas the addition of sulfate (~ 8 wt%) induces segregation and crystallization of the tetragonal ZrO_2 nanoparticles upon calcination in the silica-sulfated zirconia (Si-SZr) samples containing above 90 wt% zirconia. The direct incorporation (co-precipitation) of large amounts of Co(II) or impregnation with Co(II) and Pd(II) also causes similar transformation in the ZrO_2 phase. The Co^{2+} is incorporated into the silica rich Si-Zr matrix predominantly in the tetrahedral environment. However, the amount of octahedral Co^{2+} sites gradually increases with increasing zirconia content in the Si-SZr materials. The palladium ions can be stabilised on the Si-SZr support in the form of Pd^{2+} ions and PdO nanoparticles.

4. The stability, structure, morphology and surface properties of the siliceous mesoporous material are controlled by the modification with hetero-species (such as zirconia, cobalt and sulfate). The Si-SZr and, especially, Co-Si-SZr supports show high stability during post-synthesis treatments. Incorporation of Zr(IV) and Co(II) into the matrix cause a change in the framework structure from ordered hexagonal to 3D disordered as well as modification of pore morphology from longer channels to spherical-like voids and reduces the extent of microporosity. The adsorption of 2,6 - lutidine has revealed that the Si-SZr support possesses strong Brønsted acidity and negligible Lewis acidity. However, the modification with Co(II) and Pd(II) enhances Lewis acidity. For example, the Co-Si-SZr and Pd-Co-Si-SZR samples containing 6 wt% cobalt have the strongest Lewis acidity. The presence of accessible Lewis sites (Zr^{4+}, Co^{2+}, Pd^{2+}) is confirmed by the RT NO adsorption and consecutive FTIR measurements.

5. The Si-SZr supports promoted with Pd(II), Co(II) and bifunctional, Co(II)-Pd(II) have been tested for the reaction of preadsorbed NO_x species with methane by in-situ FTIR spectroscopy. All the investigated NO_x-free catalysts readily activate the methane at 250^0C in absence of molecular oxygen. All the NO_x precovered catalysts show high activity for NO_2 formation. Addition of cobalt is found to affect both the onset temperatures of the NO_2 and CH_4 surface interaction and the selectivity of the catalyst. High cobalt loading has a negative effect, namely, it shifts the reaction window to higher temperatures and leads to the formation of N_2O or NO rather than N_2. The Si-SZr (Zr/Si = 28) supported Pd(II), Co(II) and Pd-Co(II) catalysts show the lowest CH_4-NO_2 interaction temperatures among the samples studied.

6. The transformation of the Co^{2+} and Pd^{2+} to large Co_mO_n and PdO nanoparticles, respectively, and the amorphous Si-Zr framework to t-ZrO_2 to m-ZrO_2 phase takes place upon treatment of the Pd-, Co- and Pd-Co-supported Si-SZr samples with the methane at elevated temperatures under anaerobic conditions. These structural changes lead to deactivation of the catalyst.

6. REFERENCES

[1] J. Rouqerol, D. Avnir, C.W. Fairbridge, D.H. Everett, J.H. Haynes, N. Pernieone, J.D. Ramsay, K.S.W. Sing, K.K. Unger, Pure Appl. Chem. 66 (1994) 1739.

[2] S. Förster, M. Antonietti, Adv. Mater. 10 (1998) 195.

[3] H. Gölfen, M. Antonietti, Angew. Chem. Int. Ed. 44 (2005) 2.

[4] M. Antonietti, G.A. Ozin, Chem. Eur. J. 10 (2004) 28.

[5] Jacques Livage, New J. Chem. 25 (2001) 1.

[6] a) S. Mann, Biomineralization and Biomimetic Materials Chemistry, VCH Publishers, New York. 1996. b) S. Mann, Nature 365 (1993) 499.

[7] a) C.T. Kresge, M.E. Leonowicz, W.J. Roth, C.J. Vartulli, J.S. Beck, Nature, 359 (1992) 710, b) J.S. Beck, J.C. Vartulli, W.J. Roth, M.E. Leonowicz, C.T. Kresge, K.D. Schmitt, C. T-W. Chu, D.H. Olson, E.W. Sheppard, S.B. McCullen, J.B. Higgins, J.L. Schlenker, J.Am. Chem. Soc. 114 (1992) 10834.

[8] S.M. Yang, H. Yang, N. Coombs, I. Sokolov, C.T. Kresge, G.A. Ozin, Adv. Mater. 11 (1999) 52.

[9] a) I. Sokolov, H. Yang, G.A. Ozin, C.T. Kresge, Adv. Mater., 11, (1999), 634-646, b) Hong Yang, Geoffrey A. Ozin, Charles T. Kresge, Adv. Mater. 10 (1998) 883.

[10] C.J. Brinker, Yunfeng Lu, A. Sellinger, Hongyou Fan, Adv. Mater. 11 (1999) 579.

[11] Charl F.J. Faul, Markus Antonietti, Adv. Mater. 15 (2003) 673.

[12] N.K. Raman, M.T. Anderson, C.J. Brinker, Chem. Mater. 8 (1996) 1682.

[13] Q. Huo, D.I. Margoles, G.D. Stucky, Chem. Mater. 8 (1996) 1147.

[14] R.L. Ballar, S.J. Tuman, D.J. Fouquette, W. Stegmiller, M.D. Soucek, Chem. Mater. 11 (1999) 726.

[15] S.W. Keller, H.N. Kim, T.E. Mallouk, J. Am. Chem. Soc. 116 (1994) 8817.

[16] a) T. Yanagisawa, T. Shimizu, K. Kuroda, C. Kato, Bull. Chem. Soc. Jpn. 63 (1990) 988, b) S. Inagaki, Y. Fukushima, K. Kuroda, J. Chem. Soc. Chem. Commun. (1993) 680.

[17] a) Q. Huo, D.I. Margoles, C.P. Feng, T.E. Gier, P. Sieger, R. Leon, P.M. Petroff, F. Schüth, G.D. Stucky, Nature 368 (1994) 317; b) Q. Huo, D.I. Margoles, U. Ciesla, D.K. Demuth, P. Feng, T.E. Gier, P. Sieger, A. Firouzi, B.F. Chmelka, F. Schüth, G.D. Stucky, Chem. Mater. 6 (1994) 1176.

[18] D. Zhao, Q. Huo, J. Feng, B.F. Chmelka, G.D. Stucky, J. Am. Chem. Soc. 120 (1998) 6024.

[19] D. Zhao, J. Feng, Q. Huo, N.Melosh, G.H. Fredrikson, B.F. Chmelka, G.D. Stucky, Science 279 (1998) 548.

[20] a) P.T. Tanev, T.J. Pinnavaia, Science, 267 (1995) 865; b) W. Zhang, T.R. Pauly, T.J. Pinnavaia, Chem. Mater.9 (1997) 2491.

[21] a) S.A. Bagshaw, E. Prouzet, T.J. Pinnavaia, Science 269 (1995) 1242; b) E. Prouzet, F. Cot, G. Nabias, A. Larbort, P. Kooyman, T.J. Pinnavaia, Chem. Mater. 11 (1999) 1498; c) Boissiere, A. Larbort, E. Prozet, Chem. Mater. 12 (2000) 1937.

[22] a) Chengzhong Yu, Yonghao Yu, Dongyuan Zhao, Chem. Commun. (2000) 575; b) J.R. Matos, M. Kruk, L.P. Mercuri, M. Jaroniec, L. Zhao, T. Kamiyama, O. Terasaki, T.J. Pinnavaia, Yu Liu, J. Am. Chem. Soc. 125 (2003) 821.

[23] J.S. Jansen, Z. Shan, L. Marchese, W. Zhou, N. van der Puil, T. Maschmeyer, Chem. Commun. 8 (2001) 713.

[24] R. Ryoo, J.M, Kim, C.H. Ko, C.H. Shin, J. Phys. Chem. 100 (1996) 17718.

[25] P. Schmidt-Winkel, W.W. Lukens, J.D. Zhao, P. Yang, B.F. Chmelka, G.D. Stucky, J. Am. Chem. Soc. 121 (1999) 254.

[26] a) T. Asefa, M.J. MacLachlan, N. Coombs, G.A. Ozin, Nature 402 (1992) 867; b) B.J. Melde, B.T. Holland, C.F. Blandford, A. Stein, Chem. Mater. 11 (1999) 3302; c) T. Asefa, M.J. MacLachlan, H. Grondley, N. Coombs, G.A. Ozin, Angew. Chem., Int. Ed. 39 (2000) 1808; d) S. Inagaki, S. Guan,Y. Fukushima, T. Ohsuna, O. Terasaki, J. Am. Chem. Soc. 121 (1992) 9611.

[27] a) S.A. El-Safty, T. Hanaoka, Adv. Mater. 15 (2203) 1893; b) S.A. El-Safty, T. Hanaoka, F. Mizukami, Adv. Mater. 17 (2005) 47.

[28] A. Firouzi, D. Kumar, L.M. Bull, T. Besier, P. Sieger, Q. Huo, S.A. Walker, J.A. Zasadzinski, C. Glinka, J. Nocol, D. Margolese, G.D. Stucky, B.F. Chmelka, Science 267 (1995) 1138.

[29] A. Steel, S.W. Caar, M.W. Anderson, J. Chem. Soc. Chem. Commun. (1994) 1571.

[30] C.-Y. Chen, S.L. Burkett, H.-X. Li, M.E. Davis, Microporous Mater. 2 (1993) 27.

[31] A. Monnier, F. Schüth, Q. Huo, D. Kumar, D. Margolese, R.S. Maxwell, G.D. Stucky, M. Krishnamurty, P. Petroff, A. Firouzi, M. Janicke, B.F. Chmelka, Science 261 (1993) 1299.

[32] F. Schüth, Chem. Mater. 13 (2001) 3184.

[33] G.S. Attard, J.C. Giyde, C.G. Göltner, Nature 378 (1995) 366.

[34] G.W. Scherer, C.J. Brinker, Sol-Gel Science, Academic Press, New York, 1990.

[35] G.J.d.A. Soler-Illia, E.L. Crepaldi, D. Grosso, C. Sanchez, Curr. Opin. Colloid Interf. Sci. 8 (2003) 109.

[36] a) J.M. Kim, Y.J. Han, B.F. Chmelka, G.D. Stucky, Chem. Commun. (2000) 2437; b) E. Leontidis, Curr. Opin. Colloid Interf. Sci. 7 (2002) 81.

[37] L. Sierra, J.-L. Guth, Microp. Mater. 27 (1999) 243.

[38] J.S. Beck, J.C. Vartulli, G.J. Kennedy, C.T. Kresge, W.J. Roth, S.E. Schramm, Chem. Mater. 6 (1994) 1816.

[39] a) J.N. Israelachvili, D.J. Mitchel, B.W. Niham, J.Chem. Soc., Faraday Trans. 2, 72 (1976) 1525; b) J.N. Israelachvili, Intermolecular and Surface Forces, 2nd ed.; Ed. Academic Press: New York, 1992.

[40] S.T. Hyde, Pure Appl. Chem. 64 (1992) 1617.

[41] a) B. Chu, Langmuir 11 (1995) 414; b) G. Wanka, H. Hoffmann, W. Ulbricht, Macromolecules 27 (1994) 4145.

[42] a) D. Khushalani, A. Kuperman, N. Coombs, G. Ozin, Chem. Mater. 8 (1996) 2188; b) Suman K. Jana, Atsushi Mochizuki, Seitaro Namba, Catal. Surveys from Asia 8 (2004) 1.

[43] a) P. Di Renzo, F. Testa, J.D. Chen, H. Cambon, A. Galarnean, D. Plee, F. Fajula, Microporous Mesoporous Mater. 28 (1994) 437; b) P. Feng, X. Bu, D.J. Pine, Langmuir 16 (2000) 5304.

[44] a) S.A. Bagshaw, Mesoporous Molecular Sieves; Studies in Surface Science and Catalysis vol. 117, Elseveir: Amsterdam, 1998; b) T.R. Pauly, T.J. Pinnavaia, Chem. Mater. 13 (2001) 987; c) M. Kruk, J.R. Matos, M. Jaroniec, Colloids and Surfaces A: Physicochem. Eng. Aspects 241 (2004) 27.

[45] N.A. Melosh, P. Lipic, F.A. Bates, F. Wudl, G.D. Stucky, B.F. Chmelka, Macromolecules 32 (1999) 4332.

[46] M. Imperor-Clerc, P. Davidson, A. Davidson, J. Am. Chem. Soc.122 (2000) 11925.

[47] a) S.M. de Paul, J.W. Zwanziger, R. Ulrich, U. Wiesner, H.W. Spiess, J. Am. Chem. Soc. 121 (1999) 5727; b) C.G. Göltner, B. Smarsley, B. Berton, M. Antonietti, Chem. Mater. 13 (2001) 1617; c) C. Göltner-Spickermann, Curr. Oppin. Colloid Interf. Sci. 7 (2002) 173.

[48] G.J.A.A. Soller-Illia, E. Crepaldi, D. Grosso, C. Sanchez, Chem. Commun. (2002) 2298.

[49] R. Ivanova, P. Alexandridis, B. Lindmann, Colloids Surf. A (2001) 183.

[50] C.J. Brinker, G.W. Scherer, Sol – Gel science: The Physics and Chemistry of Sol-Gel Processing. Academic Press: San Diego, 1990.

[51] a) L.L. Hench and J.K. West, Chem Rev. 90 (1990) 33 b) J. Livage, N. Henry, C. Sanchez, Prog. Solid State Chem. 18 (1988) 259.

[52] J.A. Anderson, C.A. Fergusson, J. Non-Cryst. Solids 246 (1999) 177.

[53] a) M. Hino, S. Kabayashi, K. Arata, J. Am. Chem. Soc. 101 (1979) 6439, b) C. Morterra, G. Gerrato, C. Emanuel, V. Bolis, J. Catal. 142 (1993) 349, c) G. Pecchi, P. Reyes, F. Orellana, T, Lopez, R. Gomez, J.L.G. Fierro, J. Chem. Tech. and Biotechnol. 74 (1999) 897.

[54] D.G. Rosenberg, F. Coloma, J.A. Anderson, J. Catal. 210 (2002) 218.

[55] a) J.M. Miller, L.J. Lakshmi, J. Phys. Chem. B, 102 (1998) 6465 – 6470, b) Q. Zhuang, J.M. Miller, Appl. Catal. A 209 (2001) L1 – L6, c) J. Europ. Ceram. Soc. 25 (2005) 283.

[56] ZHi-Gang Wu, Yong-Xiang Zhao, Dian-Sheng Liu, Micropor. Mesopor. Mater. 68 (2004) 127.

[57] C. Flego, L. Carluccio, C. Rizzo, C. Perego, Catal. Commun. 2 (2001) 43.

[58] A. Parafdar, A.B. Panda, P. Paramanik, Micropor. Mesopor. Mater. 84 (2005) 223.

[59] I. Hasegawa, K. Hibino, K. Takei, Appl. Organometal, Chem. 13 (1999) 549.

[60] a) X.X. Wang, F. Lefebvre, J. Patarin, J.M. Basset, Micropor. Mesopor. Mater. 42 (2001) 269, b) J.I. Haskouri, S. Cabrera, C. Guilem, J. Latorre, A, Beltran, D. Beltran, M.D. Marcos, P. Amoros, Chem. Mater. 12 (2002) 5015.

[61] M.S. Morey, G.D. Stucky, S. Schwarz, M. Froba, J. Phys. Chem. B 103 (1999) 2037.

[62] B.L. Newalkar, J. Olanrewaju, S. Komarneni, J. Phys. Chem. B 105 (2001) 8356.

[63] J-H. Chou, J-B. Yoon, H. Jung, J-H. Park, J. Por. Mater. 11 (2004) 123.

[64] E. Rodriguez-Castellon, A. Jimenez-Lopez, P. Maireles-Torres, D.J. Jones, J. Roziere, M Trombetta, G. Busca, M. Lenarda, L. Storaro, J. Solid State Chem. 175 (2003) 159.

[65] a) L.F. Chen, L.E. Norena, J. Navarette, J.A. Wang, Mater. Chem. Phys. 97 (2006) 236, b) K. Chaudhari, R. Bal, T.K. Das, A. Chandwadkar, D. Srinivas, S. Sivasanker, J. Phys. Chem. B 104, (2000) 11066, c) M.L. Occelli, S. Biz, A. Aurox, Appl. Catal. A 183 (1999) 231.

[66] a) M.S. Wong, H.C. Huang, J.Y. Ying, Chem. Mater. 14 (2002) 1961, b) A. Infantes-Molina, J. Merida-Robles, P. Maireles-Torres, E. Finocchio, G. Busca, E. Rodriguez-Castellon, J.L.G. Fierro, A. Jemenez-Lopez, Micropor. Mesopor. Mater. 75 (2004) 23, c) A.V. Ivanov, S.V. Lysenko, S.V. Baranova, A.V. Sungurov, T.N. Zangelov, E.A. Karakhanov, Micropor. Mesopor. Mater. 91 (2006) 254.

[67] M. Wei, K. Okabe, H. Arakawa, Y. Teraoka, Catal. Commun. 5 (2004) 597.

[68] J.E. Haskouri, S. Cabrera, C. Guillem, J. Latorre, A. Beltran, D. Beltran, M. D. Marcos, P. Amoros, Chem. Mater. 14 (2002) 5015.

[69] W-H. Zhang, J-L. Shi, L-Z. Wang, D-S. Yan, Mater. Lett. 46 (2000) 35.

[70] Q.-H. Xia, K. Hidajat, S. Kawi, J. Catal. 205, (2002) 318.

[71] a) Y. Sun, L. Zhu, H. Lu, R. Wang, S. Lin, D, Jiang, F-S. Xiao, Appl. Catal. A 237 (2002) 21-31, b) H. Matsuhashi, M. Tanaka, H. Nakamura, K. Arata, Appl. Catal. A 208 (2001) 1.

[72] Q.-H. Xia, K. Hidajat, S. Kawi, Chem. Commun. (2000) 2229.

[73] a) L.M. Eshelman, A.M. de Jong, J.W. Neimantsverdriet, Catal. Lett. 10 (1991) 201.

[74] H. Chen, J. Gao, M. Ruan, J. Shi, D. Yan, Microp. Mesopor. Mater. 76 (2004) 209.

[75] W. Hua, Y. Yue, Z. Gao, J. Mol. Catal., A 170 (2002) 195.

[76] a) Y. Sun, L. Zhu, H. Lu, R. Wang, S. Lin, D. Jiang. F.S. Xiao, Appl. Catal. A 237 (2002) 21, b) M.A. Ecormier, A.F. Lee, K.Wilson, Micropor. Mesopor. Mater. 80 (2005) 301, c) Y. Du, Y. Sun, Y. Di, L. Zhao, S. Liu, F.S. Xiao, J. Porous Mater. 13 (2006) 163.

[77] a) T. Lopez, F. Tzompantzi, J. Navarette, R. Gomez, J.L. Boldu, E. Munoz, O. Novaro, J. Catal.181 (1999) 285, b) D.J. Rosenberg, F. Coloma, J.A. Anderson, J. Catal. 210 (2002) 218.

[78] C.L. Chen, S. Cheng, H.P. Lin, S.T. Wong, C.Y. Mou, Appl. Catal. A 215 (2001) 21.

[79] C.L. Chen, T. Li, S. Cheng, H.P. Lin, C.J. Bhongale, C.Y. Mou, Micropor. Mesopor. Mater. 50 (2001) 201.

[80] D.J. Rosenberg, B. Bachiller-Baeza, T.J. Dines, J.A. Anderson, J. Phys. Chem. B 107 (2003) 6526.

[81] P. Salas, L.F. Chen, J.A. Wang, H. Armendariz, M.L. Guzman, J.A. Montoya, D.R. Acosta, Appl. Surf. Sci. 252 (2005) 1123.

[82] a) K. Arata, Adv. Catal. 37 (1990) 165, b) M. Hino, S. Kobayashi, K. Arata, J. Am. Chem. Soc. 101 (1979) 6439, c) K. Arata, M. Hino, Mater. Chem.Phys. 26 (1990) 213.

[83] a) B.H. Davis, R.A. Keogh, R. Srinivason, Catal. Today 20 (1994) 219, b) X. Song, A. Sayari, Catal. Rev. Sci. Eng. 38 (1996) 329.

[84] a) C. Morterra, G. Cerrato, F. Pinna, M. Signoretto, G. Strukul, J. Catal 149 (1994) 181, b) S. Mellado, S.A. Ardizzone, C.I. Bianchi, Micropor. Mesopor. Mater. 73 (2004) 203.

[85] a) M.A. Risch, E.E. Wolf, Appl. Catal. A 172 (1998) L1, b) S. Melada, M. Signoretto, F. Somma, F. Pinna, G. Sirrato, G. Meligrana, C. Morterra, Catal. Lett. 94 (2004) 193.

[86] M.S. Wong, J.Y. Ying, Chem. Mater. 10 (1998) 2067.

[87] a) X. Song, A. Sayari, Catal. Rev. 38 (1996) 329, b) P.D.L. Mercera, J.G. Van Ommen, E.B.M. Doesburg, A.J. Burggraaf, J.R.H. Ross, Appl. Catal. 57 (1990) 127.

[88] M.J. Hudson, J.A. Knowels, J. Mater. Chem. 6 (1) (1996) 89.

[89] D.J. McIntosh, R.A. Kydd, Micropor. Mesopor. Mater. 37 (2001) 281.

[90] Y. Sun, L. Yuan, C.L. Chen, F.S. Xiao, Catal. Lett. 87 (2003) 57.

[91] V.I. Parvulescu, H. Bonnemann, V. Parvulescu, U. Endruschat, A. Rufinska, Ch. W. Lehmann, B. Tesche, G. Poncelet, Appl. Catal A 214 (2001) 273.

[92] Y. Huang, T.J. McCarthy, W.M.H. Sachtler, Appl. Catal. A 148 (1996) 135.

[93] J.S. Reddy, A. Sayari, Catal. Lett. 38 (1996) 219.

[94] M. Signoretto, A. Breda, F. Somma, F. Pinna, G. Cruciani, Micropor. Mesopor. Mater. 91 (2006) 23.

[95] N. Yi, Y. Cao, W.L. Feng, W.L. Dai, K.N. Fan., Catal. Lett. 99 (1-2) (2005) 73.

[96] P. Yang, D. Zhao, D.I. Margolese, B.F. Chmelka, G.D. Stucky, Chem. Mater. 11 (1999) 2813.

[97] D. Khushalani, Ö. Dag, G.A. Ozin, A. Kuperman, J. Mater. Chem. 9 (1999) 1491.

[98] Z.S. Seddegi, V. Budrthumal, A.A. Al-Amer, S.A.I. Barri, Appl. Catal. A 225 (2002) 167.

[99] B. Chiche, E. Sauvage, F.D. Renzo, I.I. Ivanova, F. Fajula, J. Mol. Catal. A 134 (1998) 145.

[100] T. Yu. Stoilkova, C. D. Chanev, H.T. Lechert, C.P. Bezouhanova, Appl. Catal. A 203 (2000) 121.

[101] E.A. Gunnewegh, S.S. Gopie, H. Bekkum, J. Mol. Catal. A 106 (1996) 151.

[102] R. Koster, E. Poels, A. Bliek, J. Catal. 204 (2001) 333.

[103] P. Baltrame, F. Demartin, G. Zuretti, Appl. Catal. A 232 (2002) 265.

[104] M. Morey, A. Davidson, H. Eckert, G. Stucky, Chem. Mater. 8 (1996) 486.

[105] K.M. Reddy, I. Monrakouski, A. Sayari, J. Chem. Soc., Chem. Commun. (1994) 1059.

[106] H. Yang, A. Kuperman, N. Coombs, S. Mamiche-Afara, G.A. Ozin, Nature 379 (1996) 703.

[107] Q. Huo, D. Zhao, J. Feng, K. Weston, S.K. Burrato, G.D. Stucky, S. Schacht, F. Schuth, Adv. Mater. 9 (1997) 974.

[108] F. Marlow, F. Kleitz, Microp. Mesop. Mater. 44-45 (2001) 671.

[109] H.P. Lin, C.Y. Mou, Science, 273 (1996) 765.

[110] W.-H. Chen, Q. Zhao, H.-P. Lin, Y.-S. Yang, S.-Y. Mou, S.-B. Liu, Micropor. Mesopor. Mater. 66 (2003) 209.

[111] P.J. Bruinsma, A.Y. Kim, J. Liu, S. Baskaran, Chem. Mater. 9 (1997) 2507.

[112] Y.F. Lu, H.Y. Fan, A. Stump, T.L. Ward, T. Rieker, C.J. Brinker, Nature 398 (1999) 223.

[113] S.H. Tolbert, A. Firouzi, G.D. Stucky, B.F. Chmelka, Science 278 (1997) 264.

[114] K. Cassiers, T. Linssen, M. Mathieu, M. Benjelloun, K. Schrijnemakers, P. Van Der Voort, P. Cool, E.F. Vansant, Chem. Mater. 14 (2002) 2317.

[115] N. Igarashi, K.A. Koyano, Y. Tanaka, S. Nakata, K. Hashimoto, T. Tatsumi, Micropor. Mesopor. Mater. 59 (2003) 43.

[116] K. Moller, T. Bein, Chem. Mater. 10 (1998) 2950.

[117] A. Taguchi, F. Schuth, Micropor. Mesopor. Mater. 77 (2005) 1.

[118] M. Inaba, Y. Kintaichi, M. Haneda, H. Hamada, Catal. Lett. 39 (1996) 269.

[119] D. Pietrogiacomi, S. Tuti, M.C. Campa, V. Indovina, Appl. Catal. B 28 (2002) 43.

[120] J. Jarupatrakorn, T.D. Tilley, J. Am. Chem. Soc. 124 (2002) 8380.

[121] K. Chaudnari, R. Bal, D. Srinivas, A.J. Chandvadkar, S. Sivasanker, Micropor. Mesopor. Mater. 50 (2001) 209.

[122] F. Fiqueras, H. Kockar, S. Caldarelli, Micropor. Mesopor. Mater. 39 (200) 249.

[123] B.S. Uphade, T. Akita, T. Nakamura, M. Haruta, J. Catal. 209 (2002) 331.

[124] V.F. Stone, J. Davis, R. Davis, Chem. Mater. 10 (1998) 1468.

[125] K. Chaudhari, R. Bal, T.K. Das, A. Chandwadkar, D. Srinivas, S. Sivasanker, J. Phys. Chem. B 104 (2000) 11066.

[126] Q. Zhuang, J.M. Miller, Appl. Catal. A 209 (2001) L1.

[127] M. Ziolek, I. Sobezak, I. Nowak, P. Decyk, A. Lawandowska, J. Kujawa, Micropor. Mesopor. Mater. 35 (2002) 195.

[128] P. Van Der Voort, M. Morey, G. Stucky, M. Mathiey, E.F. Vansant, J. Phys. Chem. B 102 (1998) 585.

[129] E. Zhu, M. Hartmann, E.M. Moes, R.S. Gernuszewicz, L. Kevan, J. Phys. Chem. B 104 (2000) 4690.

[130] J. Janas, J. Janik, T. Machej, E.M. Serwicka, E. Bielanska, W. Janes, Catal. Today, 59 (2000) 241.

[131] Y. Wang, Q. Zhang, T. Shishiclo, K. Takenira, J. Catal. 209 (2002) 186.

[132] T.M. Abdel-Fatah, T.J. Pinnavaia, J. Chem. Soc., Chem. Commun. (1996) 665.

[133] A.Y. Khodakov, A. Gribobal-Contant, R. Bechara, V.L. Zholobenko, 209 (2002) 230.

[134] R. Moreno-Tost, J. Santamaria-Gonzalez, P. Maireles-Torres, E. Rodriguez-Castellon, A. Jimenez-Lopez, Appl. Catal. B 38 (2002) 51.

[135] D. Zhang, J. Suo, X. Zhang, S. Li, Appl. Catal. A 179 (1999) 11.

[136] M.S. Wong, E.S. Jeng, J.Y. Ying, Nano Lett. 1 (2001) 637.

[137] O.V. Melezhyk, S.V. Prudius, V.V. Brei, Micropor. Mesopor. Mater. 49 (2001) 39.

[138] R. Bruch, N.A. Cruise, D.G. Seeson, S.C. Tsang, J. Mater. Chem. 8 (1999) 107.

[139] C.E. Salmas, V.N. Stathopoulos, P.J. Pomonis, G.P. Androutsopolous, Langmuir, 18 (2002) 423.

[140] Y. Traa, B. Burger, J. Weitkamp Micropor. Mesopor. Mater. 30 (1999) 13.

[141] J.N. Armor, Catal. Today, 26 (1995) 99.

[142] F. Klingstedt, K. Arve, K. Eranen, D. Yu. Murzin, Acc. Chem. Res. 39 (2006) 273.

[143] V.I. Parvulescu, P. Grange, B. Delmon, Catal. Today 46 (1998) 233.

[144] W. Held, A. Koenig, T. Richter, L. Puppe, SAE paper 900496 13-20.

[145] M. Iwamoto, H. YahiroS. Shundo, Y. Yu-u, N. Mizuno, Shokubai 32 (1990) 430.

[146] H. Hamada, Y. Kintaichi, M. Tabata, M. Sasaki, T. Ito, Catal. Lett. 6 (1990) 239.

[147] S. Sato, H. Hirabayashi, H. Yahiro, N. Mizuno, M. Iwamoto, Catal. Lett. 12 (1992) 193.

[148] Y. Li, J.N. Armor, Appl. Catal. B 3 (1993) L1.

[149] M.D. Fokema, J.Y. Ying, Catal. Rew. 43 (2001) 1.

[150] T. Inui, S. Iwamoto, S. Koja, S. Shimizu, T. Hirabayashi, Catal. Today 22 (1994) 41.

[151] J. Siera, P. Gobden, K. Tanaka, B.E. Nieuwenhuys, Catal. Lett. 10 (1991) 335.

[152] J.N. Armor, T.S. Farris, Appl. Catal. B 4 (1994) L 11.

[153] Y. Nizaka, M. Misono, Chem. Lett. (1993) 1295.

[154] C.J. Loughran, D.E. Resasco, Appl. Catal. B 17 (1995) 113.

[155] M. Ogura, Y. Sugiura, M. Hayashi, E. Kikuichi, Catal. Lett. 42 (1996) 185.

[156] C. Discorme, P. Geling, C. Lecuyer, M. Primet, Appl. Catal. B 13 (1997) 185.

[157] M. Suzuki, J. Amano, M. Niwa, Micropor. Mesopor. Mater. 21 (1998) 541.

[158] H. Hamada, Y. Kintaichi, M. Tabata, M. Sasaki, T. Ito, Chem. Let. (1991) 2179.

[159] Y.-H. Chin, A. Pisanu, L. Serventy, W.E. Alvarez, D.E. Resasco, Catal. Today 54 (1999) 419.

[160] Y. Traa, B. Burger, J. Weitkamp Micropor. Mesopor. Mater. 30 (1993) 185.

[161] H. Ohtsuka, T. Tabata, Appl. Catal. B 21 (1999) 133.

[162] M. Ogura, S. Kage, M. Hayashi, M. Matsukata, E. Kikuchi, Appl. Catal. B 27 (2000) 213.

[163] M. Ogura, S. Kage, T. Shimujo, J. Oba, M. Hayashi, M. Matsukata, E. Kikuchi, J. Catal. 211 (2002) 75.

[164] B. Wen, J. Jia, S. Li, T. Liu, L.X. Chen, W.M.H. Sachtler, Phys. Chem. Chem. Phys. 4 (2002) 1983.

[165] J.A.Z. Pieters, R.W. van den Brink, S. Booneveld, F.A. de Bruijn, Appl. Catal. B 46 (2003) 239.

[166] N. LiA. Wang, J. Tang, X. Wang, D. Liang, T. Zhang, Appl. Catal. B 43 (2003) 195.

[167] L.F. Cordoba, W.M.H. Sachtler, C. Montes de Correa, Appl. Catal. B 56 (2005) 269.

[168] F. Bustamante, F. Cordoba-Castrillon, M. Yates, C. Montes de Correa, Appl. Catal. A 234 (2002) 127.

[169] L.F. Cordoba, G.A. Fuentes C. Montes de Correa, Micropor. Mesopor. Mater. 2-3 (2005) 193.

[170] L. Guezi, Z. Schay, G. Stefler, F. Mizukami, J. Mol. Catal, A 141 (1999) 177.

[171] N. Tsubaki, S. Sun, K. Fujimoto, J. Catal. 199 (2001) 617.

[172] R. Mokaya, W. Jones, J. Mater. Chem. 9 (1999) 555.

[173] K. Arata, H. Matsuhashi, M. Hino, H. Nakamura, Catal. Today 81 (2003) 17.

[174] D.C. Bradley, D.G. Carter, Can. J. Chem. 40 (1962) 15.

[175] B.E. Yoldas, J. Am. Seram. Soc. 65 (1982) 387.

[176] M.S. Wong, E.S. Jeng, J.Y. Ying, Nano Lett. 11 (2001) 637.

[177] G.A. Parks, Chem. Rev. 65 (1965) 177.

[178] R.J. Hunter, Zeta Potential in Colloid Science, Academic Press, New York, 1981.

[179] J. Livage, M. Henry, C. Sacher, Prog. Solid State Chem. 18 (1988) 259.

[180] B.C. Bunker, K.D. Keefer, unpublished results.

[181] E. Matijević, R.S. Sapieszko, J.B. Melville, J. Colloid Interface Sci. 50 (1975) 567.

[182] D.B. McWhan, G. Lundgren, Acta Cryst. 16 (1963) A36.

[183] C.J. Brinker, G.W. Scherer, Sol-Gel Science: The Physics and Chemistry of Sol-Gel Processing, Academic Press, INC., San Diego, 1990.

[184] M.S. Wong, H.C. Huang, J.Y. Ying, Chem. Mater. 14 (2002) 1961.

[185] U. Ciesla, M. Froba, G. Stucky, F. Schuth, Chem. Mater. 11 (1999) 227.

[186] F.E. Baily, R.W. Callard, J. Appl. Polym. Sci. 1 (1959) 56.

[187] Ö. Dağ, S. Alayoglu, I. Unsal, J. Phys. Chem. B, 108 (24) (2004) 439.

[188] Ö. Dağ, O. Samarskaya, G. Tura, A. Gunay, Ö. Celik, Langmuir, 19 (2003) 3671.

[189] Ö. Celik, Ö. Dağ, Angew. Chem. Int. Ed. 40 (2001) 3799.

[190] A. Infantes-Molina, J. Merida-Robles, P. Maireles-Torres, E. Finocchio, G. Busca, E, Rodriguez-Castellon, J.L.G. Fierro, A. Jimenez-Lopez, Micropor. Mesopor. Mater. 75 (2004) 23.

[191] J.L. Blin, R. Flamant, B.L. Su, Int. J. Inorg. Mater., 3, 2001, 959.

[192] M.A. Ecormier, A.F. Lee, K. Wilson, Mesopor. Micropor. Mater. 80 (2005) 301.

[193] S.M. Jung, P. Grange, Appl. Catal. A 228 (2002) 65.

[194] B. Wen, Q. Sun, W.M.H. Sachtler, J. Catal. 204 (2001) 314.

[195] Y.-F. Han, D. Kumar, D.W. Goodman, J. Catal. 230 (2005) 353.

[196] L. Chen, T. Horiuchi, T. Mori, K. Maeda, J. Phys. Chem. B 103 (1999) 1216.

[197] H.-P. Lin, C.-Y. Mou, Micropor. Mesopor. Mater. 55 (2002) 69.

[198] C.F. Ceng, W.Z. Zhao, D.H. Park, J. Klinowki, M. Hargreaves, F. Gladden, J. Chem. Soc., Faraday Trans. 93 (1997) 359.

[199] A.Y. Khodakov, V.L. Zholobenko, R. Bechara, D. Duran, Micropor. Mesopor. Mater. 79 (2005) 29.

[200] S.C. Shen, S. Kawi, J. Phys. Chem. B 103 (1999) 8870.

[201] J.M. Kim, R. Ryoo, Bull. Korean Chem. Soc. 17 (1996) 66.

[202] V.M. Bermudez, J. Phys. Chem. 74 (1970) 4160.

[203] F. Zhang, Y. Yan, H. Yang, Y. Meng, C. Yu, B. Tu, D. Zhao, J. Phys. Chem. B 109 (2005) 8723.

[204] S.J. Gregg, K.S.W. Sing, Adsorption Surface Area and Porosity, second ed., Academic Press, London, 1982.

[205] F. Rouquerol, J. Rouquerol, K.S.W. Sing, Adsorption by Powder and Porous Solids, Academic Press, London, 1999.

[206] K.S.W. Sing, D.H. Everett, R.A.W. Haul, L. Moscou, R.A. Pierotti, J. Rouquerol, T. Siemieniewska, Pure Appl. Chem. 57, 1958, 603.

[207] G.C. Groen, L.A.A. Peffer, J. Perez-Ramirez, Microporous Mesoporous Mater. 60 (2003) 1.

[208] M. Kruk, M. Jaroniec, Chem. Mater. 13 (2001) 3169.

[209] S. Brunauer, P.H. Emmett, E. Teller, J. Am. Chem. Soc. 60 (1938) 309.

[210] J. Rouquerol, D. Avnir, C.W. Fairbridge, D.H. Everett, J.H. Haynes, N. Pernicon, J.D.F. Ramsay, K.S.W. Sing, K.K. Unger, Pure Appl. Chem. 66 (1994) 1739.

[211] E.P. Barrett, L.G. Joyner, P.P. Halenda, J. Am. Chem. Soc. 73 (1951) 373.

[212] P.I. Ravikovich, A.V. Neimark, Langmuir 18 (2002) 9830.

[213] Y. Sakamoto, I. Diaz, O. Terasaki, D. Zhao, J. Perez-Pariente, J.M. Kim, G.D. Stuky, J. Phys. Chem. B 106 (2002) 3118.

[214] C.G. Goltner, B. Smarsley, B. Berton, M. Antonietti, Chem. Mater. 13 (2001) 1617.

[215] S. Storck, H. Bretinger, W.F. Maier, Appl. Catal. A 174 (1998) 137.

[216] M. Kruk, M. Jaroniec, Chem. Mater. 12 (2000) 1961.

[217] J. Choma, M. Jaroniec, W. Burakiewitcz-Motka, M. Kloske, Appl. Surf. Sci. 196 (2002) 216.

[218] V.B. Fenelonov, V.N. Romannikov, A. Yu. Derevyankin, Microporous Mesoporous Mater. 28 (1999) 57.

[219] U. Ciesla, F. Schuth, Microporous Mesoporous Mater., 27 (1999) 131.

[220] J.R. Matos, L.P. Mercuri, M. Kruk, M. Jaroniec, Langmuir 18 (2002) 884.

[221] M. Kruk, M. Jaroniec, Chem. Mater. 15 (2003) 2942.

[222] A. Infantes-Molina, J. Merida-Robles, P. Maireles-Torres, E. Finochio, G. Busca, E. Rodriguez-Castellion, J.L.G. Fierro, A. Jimenez-Lopez, Microporous Mesoporous Mater. 75 (2004) 23.

[223] C. Chupin, A.C. Van Veen, M. Konduru, J. Despres, C. Mirodatos, J. Catal., 241 (2006) 103.

[224] S. Cava, S.M. Tebcherani, S.A. Pianaro, C.A. Paskocimas, E. Longo, J.A. Varela, Mater. Chem. Phys., 97 (2006) 102.

[225] S.S. Bhoware, S. Shylesh, K.R. Kamble, A.P. Singh, J. Mol. Catal. A, 255 (2006) 123.

[226] G.A.H. Mekhemer, H.M.M. Abd-Allah, S.A.A. Mansour, Colloids and Surface A, 160 (1999) 251.

[227] A. Rakai, D. Tessier, F. Bozon-Verduraz, New J. Chem., 16 (1992) 869.

[228] K. Shimizu, f. Okada, Y. Nakamura, A. Satsuma, T. Hattori, J. Catal. 195 (2000) 151.

[229] Z. Zhang, G. Mestl, H. Knözinger, W.M.H. Sachtler, Appl. Catal. A, 89 (1992) 155.

[230] M. Kantcheva, I. Cayirtepe, J. Mol. Catal. A, 247 (2006) 88.

[231] A.B.P. Lever "Studies in physical and theoretical chemistry 33; Inorganic Electronic Spectroscopy" ELSEVIER 1984.

[232] C. Morterra, G. Serrato, F. Pinna, M. Signoretto, J. Phys. Chem. 98 (1994) 12373.

[233] V. Bolis, G. Magnacca, G. Cerrato, C. Morterra, Top. Catal. 19 (2002) 259.

[234] C. Morterra, E. Giamello, G. Cerrato, G. Centi, S. Parathoner, J. Catal. 179 (1998) 111.

[235] M. Kantcheva, S. Vakkasoglu, J. Catal. 223 (2004) 352.

[236] E. Laperdix, A. Sahibed-dine, G. Kostentin, O. Saur, M. Bensitel, C. Nedez, A.B. Mohamed Saad, J.C. Lavalley, Appl. Catal. B 26 (2000) 71.

[237] H. A. Benesi, J. Catal. 28 (1973) 176.

[238] P.A. Jacobs, C.F. Heylen, J. Catal. 34 (1974) 276.

[239] C. Morterra, G. Cerrato, G. Meligrana, Langmuir 17 (2001) 7053.

[240] T. Onfroy, G. Clet, M. Houalla, Microporous Mesoporous Mater. 82 (2005) 99.

[241] C. Morterra, G. Magnacca, Catal. Today 27 (1996) 497.

[242] C. Morterra, V. Bolis, G. Cerrato, G. Magnacca, J. Catal. 307-309 (1993) 1206.

[243] M. Waqif, J. Bachelier, O. Saur, J-C. Lavalley, J. Mol. Catal. 722 (1992) 127.

[244] K. Tanabe, Mater. Chem. Phys. 13 (1985) 347.

[245] K. Hadjiivanov, D. Panayotov, V. Avreyska, B. Tsynsarski, D. Klissurski, Ts. Marinova, Surf. Interf. Anal. 34 (2002) 88.

[246] M. Kantcheva, E.Z. Ciftlikli, J. Phys. Chem. 106 (2002) 3941.

[247] K. Hadjiivanov, Catal Lett. 68 (2000) 157.

[248] D. Pietrogiacomi, M.C. Kampa, S. Tuti, V. Indovina, Appl. Catal. B 41 (2003) 301.

[249] X. Wang, H.Y. Chen, W.M.H. Sachtler, J. Catal.197 (2001) 281.

[250] B. Djonev, B. Tsynsarski, D. Klissurski, K. Hadjiivanov, J. Am. Chem. Soc., Faraday Trans. 93 (1997) 4055.

[251] Y. Li, T. L. Slager, J.N. Armor, J. Catal. 150 (1994) 388.

[252] L.J. Lobree, A.W. Aylor, A.J. Reimer, A.T. Bell, J. Catal. 181 (1999) 189.

[253] S. Descorme, P. Gelin, M. Primer, C. Lecuyer, Catal. Lett. 41 (1996) 319.

[254] M. Valden, R. Keiski, N. Xiang, J. Pere, J. Aaltonen, M. Pessa, T. Maunula, A. Savimaki, A. Lahti, M. Harkonen, J. Catal. 161 (1996) 614.

[255] Y. Li, J.N. Armor, Appl. Catal. B 1 (1992) L31.

[256] M.C. Campa, S.D. Rossi, G. Ferraris, V. Indovina, Appl. Catal. B 8 (1996) 315.

[257] D.B. Lukyanov, G.A. Sill, J.L.d'Itri, W.K. Hall, J. Catal. 153 (1995) 265.

[258] W. Zhang, H. Yahiro, N. Mizuno, J. Izumi, M. Iwamoto, Chem. Lett. (1992) 851.

[259] H. Ohtsuka, T. Tabata, T. Hino, Appl. Catal. B 28 (2000) 73.

[260] H. Ohtsuka, Appl. Catal. B 33 (2001) 325.

[261] N. Li, A. Wang, J. Tang, X. Wang, D. Liang, T. Zhang, Appl. Catal. B 43 (2003) 195.

[262] S. Descorme, P. Gelin, M. Primet, C. Lecuyer, J. Caint-Just, in L. Bonneviot, S. Kalliaguine (Eds.), Zeolites: A Refined Tool for Designing Catalytic Sites, Studies in Surface Science and Catalysis Vol. 97, Elsvier, Amsterdam, 1995.

[263] Y. Traa, B. Burger, J. Weitkamp, Micropor. Mesopor. Mater. 30 (1999) 3.

[264] Y. Nishizaka, M. Misono, Chem. Lett. (1993) 1295.

[265] K. Kagawa, Y. Ichikawa, S. Iwamoto, T. Inui, Catal. Lett. 52 (1998) 145.

[266] M. Kantcheva, A.S. Vakkasoglu, J. Catal, 223 (2004) 364.

[267] T. Sun, M.D. Fokema,J.Y. Ying, Catal. Today, 33 (1997) 251.

[268] A.D. Kowan, N.W. Cant, B.S. Haynes, P.F. Nelson, J. Catal. 176 (1998) 329.

[269] M. Yamaguchi, J. Chem. Soc. Faraday Trans. 93 (1997) 3581.

[270] V. Zuzaniuk, F.C. Meunier, J.R.H. Ross. J. Catal. 202 (2001) 340.

[271] A.A. Kheir, J.F. Haw, J. Am.Chem. Soc. 116 (1994) 817.

[272] C.J. Blower, T.D. Smith, Zeolites 13 (1993) 394.

[273] L.J. Lobree, A.W. Aylor, J.A. Leimer, A.T. Bell, J. Catal. 181 (1999) 189.

[274] K. Shimizu, F. Okada, Y. Nakamura, A. Satsuma, T. Hattori, J. Catal. 195 (2000) 151.

[275] M. Kantcheva, I. Cayirtepe, J. Catal. Submitted

[276] R.A. Boyse, E.I. Ko, J. Catal. 179 (1998) 100.

[277] E. Rodriguez-Castellon, A. Jimenez-Lopez, P. Maireles-Torres, D.J. Jones, J. Roziere, M. Trombetta, G. Busca, M. Lenarda, L. Storaro, J. Solid State Chem. 175 (2003) 159.

[278] J.R. Hill, D.S. Moor, S.C. Schmidt, C.B. Storm, J. Phys. Chem. 95 (1991) 3037.

[279] Y.H. Yeom, B. Wen, W.M.H. Sachtler, W. Weitz, J. Phys. Chem. B, 108 (2004) 5386.

[280] Y.H. Yeom, M.Li, W.M.H. Sachtler, W. Weitz, J. Catal, 238 (2006) 100.

[281] A.W. Aylor, L.J. Lobree, J.A. Reimer, A.T. Bell, J. Catal. 172 (1997) 453.

[282] G. Busca, V. Lorenzelli, Mater. Chem. 7 (1982) 89.

[283] X. Xu, P. Chen, D.W. Goodman, J. Phys. Chem. 98 (1994) 9242.

[284] A.El Hadaoui, G. Bergeret, J. Massardier, M. Primet, A. Renouprez, J. Catal. 148 (1994) 47.

[285] Y.-H. Chin, A. Pisanu, L. Serventi, W.E. Alvarez, D.E. Resasco, Catal. Today 54 (1999) 419.

[286] K.I. Hadjiivanov, G.N. Vayssilov, Adv. Catal. 47 (2002) 307.

[287] Z. Kaszkur, J. Appl. Cryst. 33 (2000) 1262.

[288] Z. Kaszkur, J. Appl. Cryst. 33 (2000) 87.

[289] Z. Ferhat-Hamida, J. Barbier Jr., S. Labruquere, D. Duprez, Appl. Catal. 29 (2001) 195.

[290] M. Kantcheva, E.V. Albano, G. Ertl, H. Knözinger, Appl. Catal. 8 (1983) 71.

[291] T. Tabata, Y. Teng, Y. Yamaguchi, H. Sakurai, E. Suzuki, J. Phys. Chem. A 104 (2000) 2648.

[292] Z. Yan, C.-X. Xiao, Y. Kou, Catal. Lett. 3-4 (2003) 135.

[293] A. Sen, M. Lin, Topics in Catal. 3-4 (2005) 175.

[294] G. Bagnasco, M. Turco, C. Resini, T. Montanari, M. Bevilaqua, G. Busca, J. Catal. 225 (2004) 536.

[295] A. Davydov “Molecular Spectroscopy of Oxide Catalyst Surfaces” J. Wiley&Sons, Ltd., 20.